IMPERIAL

Novel Thin Film Composite Membranes for Solvent-based Molecular Separation

Submitted by

Dezhi Liu

Thesis supervisor: Dr. Qilei Song, Prof. Andrew Livingston

Department of Chemical Engineering

South Kensington Campus

In submission for PhD degree at Imperial College London

Abstract

Membranes are semi-permeable filter materials that are broadly used in separation industries. Polyamide thin film composite membranes can be massively produced via interfacial polymerization directly on porous supporting substrates. Over the past decade, facilitated mass transport in microporous membranes and minimizing transport resistance by reducing membrane thickness have drawn great interests. Alas, ultra-thin membranes have poor mechanical properties. Additional gutter layer and backing substrate must be used in composite membrane production which raises greater costs and technical challenges in the process.

Here in this thesis, a new interfacial synthesis mechanism was revealed to prepare microporous polyamide thin film membranes. This work shows crosslinked asymmetric membranes with well-defined separate pore structures can be prepared from singular independent interfacial polymerization. This new mechanism takes advantage of microporosity in the synthesized solid polymer film, and could achieve one-piece integrated membranes with sub-100nm selective skin layer with autonomous micron-level porous support layer, coupled with superior solvent permeability and selectivity in organic solvent nanfiltration.

PIM-type amine-functionalized molecules with tetra-planar contortion were used to react with acyl chlorides. From singular interfacial synthesis of self-supported polyamide (SPA) membranes, selective skin layer and a porous supporting layer can be prepared through one-step reaction and one set of reagents. This represents a benchmark discovery to prepare asymmetric crosslinked membranes.

Further, enantiomeric separation in static diffusion was achieved using DBMPA-TPC thin film composite membrane functionalized by (R)-binaphthalene diamine (RBA). ~16% enantiomeric excess was stable in the permeate over 196 hour operation. In addition, thin film composite membranes with semi-crystalline TAPA-TFP skin layers have been prepared from templated growth method. TAPA-TFP and PPD-TFP thin film composite membranes show promising performances in neutral pH redox flow batteries.

Declaration

I certify that figure and text materials which did not originate from my own works have been properly acknowledged.

By Dezhi Liu

March 2024

Copyright Declaration

The copyright of this thesis rests with the author. Unless otherwise indicated, its contents are licensed under a Creative Commons Attribution-Non-Commercial 4.0 International Licence (CC-BY-NC). Under this license, you may copy and redistribute the material in any medium or format. You may also create and distribute modified versions of the work. This is on the condition that: you credit the author and do not use it, or any derivative works, for a commercial purpose. When reusing or sharing this work, ensure you make the license terms clear to others by naming the licence and linking to the licence text. Where a work has been adapted, you should indicate that the work has been changed and describe those changes. Please seek permission from the copyright holder for used of this work that are not included in this licence or permitted under UK Copyright Law.

By Dezhi Liu

March 2024

Copyright permissions

Figure	Origin of published work	Copyright holder	Approval status
1	Ref (65)	Springer Nature	Y
2	Ref (73)	ACS	Y
3	Ref (96), Ref (100)	Elsevier	Y
4	Ref (96), Ref (101) Energy-efficient polymeric gas separation membranes for a sustainable future: A review David F. Sanders, Zachary P. Smith, Ruilan Guo, Lloyd M. Robeson, Polymer 54(18):4729-4761	Elsevier, ACS	**Y**
5	Ref (126)	ACS	Y
6	Ref (66), Ref (123), Ref (124), Ref (128), Ref (129)	Springer Nature, Wiley, AAAs	Y
7	Ref (66), Ref (124), Ref (126)	ACS, AAAs	Y
8	Ref (132)	ACS	Y
9	Ref (136)	Elsevier	Y
10	Ref (104)	Elsevier	Y
12	Ref (183)	ACS	Y
13	Ref (188), Ref (190), Ref (193)	ACS, Elsevier	Y
14	Ref (201)	Wiley	Y
15	Ref (201), Ref (202)	Wiley	Y
16	Ref (206), Ref (211), Ref (215)	Springer Nature	Y
17	Ref (67), Ref (229)	Wiley	Y
18	Novel thin film nanocomposite membranes incorporated with functionalized TiO_2 nanoparticles for organic solvent nanofiltration, Majid Peyravi, Mohsen Jahanshahi et al. Chemical Engineering Journal 241 (2014) 155-166	Elsevier	Y
19	Novel thin film nanocomposite membranes incorporated with	Elsevier	Y

	functionalized TiO_2 nanoparticles for organic solvent nanofiltration, Majid Peyravi, Mohsen Jahanshahi et al. Chemical Engineering Journal 241 (2014) 155-166		
20	Ref (239), Ref (241)	Elsevier	Y
21	Ref (248)	Elsevier	Y
22	Ref (253)	Springer Nature	Y

Acknowledgement

To start with, I would like to whole-heartedly thank Dr. Qilei Song and Prof. Andrew Livingston for supervision of this thesis and research works. In addition, I would like to thank Prof. Kang Li for mentoring me throughout my PhD program. I would also like to especially thank Prof. Andrew Livingston for supervision of my research directions, Dr. Zhiwei Jiang for insights and guidance in experimental works, Dr. Adam Oxley for providing ultrafiltration support membranes and intellectual input, Dr. Anqi Wang and Dr. Rui Tan for intellectual input in battery separator membranes, plus all of my colleagues at Imperial College London as well as Queen Mary University who supported me throughout my PhD program. I appreciate Maria Burggraef and Dr. Adam Oxley who helped with proof-reading of my thesis.

I would like to acknowledge credits for Imperial College London which primarily provided me with laboratory training, working places and resources. I would like to acknowledge Queen Mary University of London who provided me with working places and resources. I would like to thank my sponsor China Scholarship Council (CSC) for all of the support and funding so that I can complete my PhD program oversea.

Additionally I would like to thank Prof. Neil B. Mckeown and Dr. Richard Malpass-evans for contributions regarding chemical synthesis, Dr. Zhiming Feng for high resolution SEM images, Dr. Richard Thorogate for AFM training and assistance at London Centre of Nanotechnology. I would like to thank Patricia who is head of analytical services at Imperial college London who helped me learn instrumental operation of characterization facilities, and Kaho who also was of great help in the processes. I would like to thank all my contributors and collaborators who made great works possible.

In the end I would like to thank my parents and loved ones who dedicated to supporting me throughout my PhD program and COVID period. I want to thank my friends and colleagues who kept me company and helped me throughout difficult times over the past nearly 5 years. My PhD journey is fantastic. There is an old saying roaming in my homeland that goes, if you are sick for long enough you become a doctor. We can't foresee the future but we can always start changing the present.

Declaration of authenticity

This thesis was written by author Dezhi Liu who is a PhD student at Imperial College London. The author declares authenticity of design and execution of experimental works and writing in this thesis.

By Dezhi Liu

Claimed at submission of this thesis March 2024

Publications and conference abstracts associated with this PhD program

Conference abstracts and presentations:

1. **Dezhi Liu,** Richard Malpass-Evans, Tianyin Liu, Neil B. Mckeown, Qilei Song, Andrew G. Livingston, "Ultra-thin Microporous Polyamide Membranes for Molecular Separations" International Congress on Membranes and Membrane Processes, London, UK, Dec 7th, 2020.
2. **Dezhi Liu**, Richard Malpass-Evans, Tianyin Liu, Neil B. Mckeown, Qilei Song, Andrew G. Livingston, "Highly permeable polyamides of intrinsic microporosity (PAIMs) with tunable molecular weight cut-offs for organic solvent nanofiltration (OSN)" Euromembrane 2022 C onference, Sorrento, Italy, November 20-24, 2022.
3. **Dezhi Liu**, Richard Malpass-Evans, Tianyin Liu, Neil B. Mckeown, Qilei Song, Andrew G. Livingston, "Highly permeable polyamides of intrinsic microporosity (PAIMs) with tunable molecular weight cut-offs for organic solvent nanofiltration (OSN)" SynHiSel BP patenting workshop, London, UK, Feb 2nd, 2023.
4. **Dezhi Liu,** "Inversing film formation in interfacial polymerization" SynHiSel progress meet ing, Manchester, UK, 17th Oct, 2023

Academic papers published:

1. Anqi Wang, Rui Tan, **Dezhi Liu**, Jiaxin Lu, Xiaochu Wei, Alberto Alvarez-Fernandez, Chunchun Ye, Charlotte Breakwell, Stefan Guldin, Anthaony R. Kucernak, Kim E. Jelfs, Nigel P. Brandon, Neil B. Mckeown, and Qilei Song*. "Ion-selective Microporous Polymer Membranes with Hydrogen-Bond and Salt-bridge Networks for Aqueous Organic Redox Flow Batteries" Advanced Materials. 2023, 35, 2210098.
2. Rui Tan, Anqi Wang, Chunchun Ye, Jiaxi Li, **Dezhi Liu**, Barbara Primera Darwich, Luke Petit, Zhiyu Fan, Toby Wong, Alberto Alvarez-Fernandez, Mate Furedi, Stefan Guldin, Charlotte E. Breakwell, Peter A. A. Klusener, Anthony R. Kucernak, Kim E. Jelfs, Neil B. Mckeown, and Qilei Song*. "Thin Film Composite Membranes with Regulated Crossover and Water Migration for Long-life Aqueous Redox Flow Batteries" Advanced Science. 2023, 10, 2206888
3. Rui tan, Anqi Wang, Irene Bechis, Charlotte Breakwell, Mengnan Wang, Zhiyu Fan, **Dezhi Liu**, Joshua M. Tuffnell, Alberto Alvarez-Fernandez, Shengming Zhang, Tomas Juergensen, Hannah L. Pilsworth, Tongchao Liu, Stefan Guldin, John V. Hanna, Ifan E. L. Stephens, Maria Magdalena Titirici, Wei Li, Anthony K. Cheetham, Kim E. Jelfs, Thomas D. Bennett, Qilei Song*. Pressure-sintered monolithic metal-organic framework membranes for selective ionic and molecular transport, submitted to Natural Sustainability.

Academic manuscripts to submit:

1. **Dezhi Liu**, Adam Oxley, Zhiming Feng, Seok Ju Han, Neil B. Mckeown, Richard Malpass-evans, Zhiwei Jiang*, Qilei Song*, and Andrew G. Livingston*. 'Self-supported Polyamide Membranes from Interfacial Polymerization' manuscript to submit.
2. **Dezhi Liu**, Tobias Wong, Anqi Wang, Rui Tan, Zhiyu Fan, Qilei Song*. 'Self-standing Semi-crystalline membranes as redox flow battery separator' manuscript in preparation.

Award

1. Royal Society of Chemistry Horizon Prize. 2023

Table of abbreviation and symbols

AAO: Alumina Oxide

BET: Brunauer-Emmett-Teller

CE: Columbic efficiency

COF: Covalent Organic Frameworks

CSP: Chiral stationary phase

DCM: Dichloromethane

DFT: Density-functional theory

ee: Enantiomeric excess

EE: Energy efficiency

EtOH: Ethanol

FFV: Fractional Free Volume

IP: Interfacial polymerization POC: Porous Organic Cages

MeOH: Methanol

MP: Mobile phase

MOF: Metal Organic Frameworks

MF: Microfiltration

MW: Molecular weight

MWCO: Molecular Weight Cut-off

NF: Nanofiltration

PA: Polyamide

PAN: Polyacrylonitrile

PBI: Polybenzimidazole

PF: Pressurized filtration

PIMs: Polymers of Intrinsic Microporosity

PVDF: Polyvinylidene fluoride

RFB: Redox flow battery

RO: Reverse Osmosis

TFC: Thin film composite

Tg: Glass transition temperature

UF: Ultrafiltration

Contents

Chapter 1. Introduction **20**

1.1 Background 20

1.2 Motivation of research 20

1.3 Outline of thesis and post-graduate research 21

Chapter 2. Literature review and objectives **24**

2.1 Introduction to membrane separation processes 24

2.2 Porous polymeric membranes 27

2.2.1 Polymers of intrinsic microporosity (PIMs) 29

2.2.2 Covalent organic frameworks (COF) 34

2.2.3 Porous organic cages (POC) 35

2.2.4 Interfacially-polymerized microporous polymers 36

2.3 Organic solvent filtration membranes 40

2.3.1 Molecular mass transport in organic solvents 41

2.3.2 Phase inverted membranes 44

2.3.3 Composite membranes 50

2.4 Chiral separation membranes 51

2.4.1 Organic chiral molecule mass transport through membranes 52

2.4.2 Grafting chiral side chains onto backbones 54

2.4.3 Direct assembly of optically active building blocks 55

2.4.4 Filler incorporation and enantiomer templating 56

2.4.5 Chiral porous polymers 59

2.5 Flow battery separator membranes 61

2.6 Thin film composite membranes 63

2.6.1 Interfacial polymerization 63

2.6.2 Monomer species used in reactions 66

2.6.3 Composite membrane selective layers with fillers 70

2.6.4 Synthesis condition effects 73

2.6.5 Gutter layer effects 75

2.7 Challenges, scientific question and research objectives 79

Chapter 3. Methods **83**

3.1 Materials 83

3.2 Experimental characterizations 83

3.3 Nanofiltration and diffusion testing methods 90

3.4 Flow battery performance testing methods 92

Chapter 4. Self-supported polyamide membranes from interfacial polymerization **93**

4.1 Research motivation 93

4.2 Self-supported microporous polyamide films from IP 95

4.3 Asymmetry of polyamide and layer properties 104
4.4 Enhanced solvent permeability from SPAs 111
4.5 Clean rejections for charged solutes in organic solvents 115
Chapter 5. Functionalized SPA membranes for chiral separation **121**
5.1 Research motivation 121
5.2 Chiral SPAs with bi-naphthalene structures (RBA-SPA-1) 122
5.3 Stable permeate enantiomer excess under static diffusion 124
Chapter 6. Semi-crystalline thin-film composite membranes for energy storage devices **128**
6.1 Research motivation 128
6.2 Free-standing polyimide film formation 129
6.3 Semi-crystalline TFC membrane for neutral pH RFB 133
Chapter 7. Conclusion and future perspectives **136**
7.1 Summary of project conclusions 136
7.2 Future research directions 138
References: **140**
Appendix. **158**

List of figures and tables

Figure .1 Distinct separation mechanisms in liquid-phase separation and gas separations. And existing representative thicknesses of membranes with disordered or ordered structures. (reprinted from reference 65) 26

Figure 2. Fractional free volume dependence against temperatures in crosslinked polymers. Under decreasing temperature free volumes in crosslinked polymers shrink, while with increasing temperatures fractional free volumes increase. (reprinted from reference 73) 28

Table. 1 Examples of reported linear pristine PIMs and contorted monomer structures used in synthesis. ... 31

Figure 3. 3-D structures of most popular PIM-1 and novel type of Trip-PIM synthesized from tri-planar triptycene structures. (referred from Neil et al) 32

Figure 4. Chemical structures of chosen linear PIMs, and novel polyimide PIMs using triptycene structures as part of polymer backbones. TPI-1 through TPI-8 were designed and prepared using di-functional triptycene with one inert plane, increasing the bulkiness of inert side chain segments increased BET surface area which was concluded to be due to enhanced inefficient packing. 33

Figure 5. Well-defined and ideal COF ordered structures can be prepared from reacting symmetric monomers under controlled conditions. Recently Banerjee and others revealed COF thin film formation via fibre-to-film or sphere-to-film mechanism. 2-D polymeric materials with uniform micropores or even mesopores can now prepared into thin films via interfacial polymerization. 35

Figure 6. Microporous polymer thin films prepared from interfacial polymerization by applying, a. contorted monomers such as TTSBI and BHPF, b. commercial MPD and triptycene acyl chloride, c. connected cage molecules, d. cyclodextrins with asymmetric hydrophilicity, e. commercial COF precursors synthesized into 2-D ordered COF structures. 37

Figure 7. Separation performances and pore sizes of 2-D thin films and 3-D networked PIM membranes. a. Dye rejections in MeOH solvent using MPD-TMC, MPD-Triptycene, TTSBI-TMC polyester, BHPF-TMC polyester membranes in nanofiltration. b. BET pore size distributions derived from CO2 adsorption isotherms of MPD-TMC and contorted MPD-Triptycene polymers. c. CO2 gas adsorption isotherms. d. Dye rejections of 2-D TAPA-TFP and TAPA-TFB self-standing COF films in acetonitrile solvent in dead-end filtration. e. Solvent permeances of 2-D TAPA-TFP and TAPA-TFB COF films in nanofiltration. f. XRD spectrums of reported TAPA-TFP and TAPA-TFB COF thin films. g. Molecular structures 2-D COF membranes reported by Banerjee group. h and i, Pore size distributions of Tp-Azo COF films synthesized from fibre-to-film and sphere-to-film methods. 38

Figure 8. Organic solvent filtration can be divided into a few categories including concentration, solvent exchange and purification applications. 41

Figure 9. Swelling degrees of membranes in organic solvents. Swelling of membranes does not necessarily restricted to polar solvents, but is rather dependent on solubility of the membrane materials in solvents. (reprinted from reference 136) 43

Figure. 10 Left: PEG rejections of TB-OH PIM membrane in water and PEG rejections of same membrane after 5 days of water treatment. Right: PEG rejection comparison of crosslinked TB-OH membranes with different crosslinker weight percentage and uncrosslinked TB-PH membranes. (reprinted from reference 104) 45

Table.2 Popular organic solvent nanofiltration membranes directly prepared on backing support or on ultrafiltration supporting substrates. 47

Figure 11. a. Chiral separation using columns and chiral stationary phase. Mobile phase will carry both enantiomers through the chiral column, each enantiomer has different retention time in the column hence high purity enantiomers can be collected from the permeate side of the column. b. Racemates are first dissolved in solvents, a resoling agent is added into the solution which will selectively bind with one

enantiomer forming diastereomeric complex. Diastereomeric complex usually have low solubility in the chosen solvents, thus can be removed by filtration or methods alike. Pure counter enantiomer can be obtained dissolved in the solution. 52

Figure 12. Chiral separation mechanism based on selective binding of guest enantiomers and separation media. Due to different spatial orientation one enantiomer interacts strongly with selector surface while the counter enantiomer interaction is weak. This was interpreted by Berthod resembling a 'LEGO' fitting process. 53

Figure 13. Cyclodextrin-based chiral separation membranes can be designed and prepared via several methods. CD can be grafted onto existing functionalized nanochannels to create chiral nanochannels. CD can also be grafted to functionalized membrane surfaces to create chiral surfaces to promote chiral -selective adsorption. In addition natural chiral polymers such as DNA can also be grafted into bulk of chitosan membranes to create chiral pores due to bulkiness of DNA molecules. 55

Figure 14. Chiral MOF crystals can be doped into PES membranes to prepare Mixed Matrix Membranes (MMM). (reprinted from reference 201) 57

Figure 15. Cross-sectional morphology of chiral MMMs prepared from doping amorphous polymers with chiral MOF or ZIF crystals. As can be seen from cross-sectional SEM images of MMMs doped with different weight percentages of MOF/ZIF crystals, phase separation between amorphous phase and crystal phase is very obvious but within ~ 25 wt% crystal loading membranes were still defect free. Doped crystals were not uniformly distributed in the amorphous polymer matrix. 58

Figure 16. Intrinsically chiral porous polymers synthesized using chiral molecules as direct building blocks. a. Chiral PIMs synthesized from TTSBI enantiomer. b. Amino acids can usually be directly used as reagents due to their natural chirality and abundance in nature. D/L-Phe was directly used to link with benzene via catalytic reactions to synthesize aromatic yet flexible polymeric membranes. c. Chiral symmetric molecules can be used to react to COF-type monomers to prepared 2-D chiral COF membranes. 60

Figure 17. a. Example of conventional in situ interfacial polymerization of amines and acyl chlorides on supporting membranes. b. Schematic example of interfacial polymerization performed at free liquid-liquid interface. c. SEM surface image of MPD-TMC film formed from conventional interfacial polymerization, showing crumpled texture which was caused by convection. d. SEM surface image of MPD-TMC film formed from interfacial polymerization at free liquid-liquid interface. 65

Table 3. Reported polyamide thin film composites and monomer structures. Permeances and rejections were reported based on specific supporting substrates in pressurized filtration. 68

Figure 18. Typical thin film nanocomposite membranes with nanoparticle doping. TiO_2 was used as the doping agent into polyamide matrix leading to dendrimers forming and particle aggregation on film surface. 71

Figure 19. Rejections and methanol permeances of TFN and TFC membranes. 72

Figure 20. Co-solvent effects on membrane physical properties. a and b. Addition of acetone co-solvent in oil phase decreased membrane surface roughness. Addition of diethyl ether in oil phase increased membrane surface roughness. c. Addition of regulating agents in aqueous phase can affect film formation in interfacial polymerization. Glycerol increased viscosity of aqueous phase which caused amine diffusion rate towards liquid-liquid interface to be slower. This has led to less convention happening hence synthesized polyamide film was much smoother compared with films synthesized from same conditions but with less viscous water as co-solvent. 74

Figure 21. Schematic showing of thin film composites with and without gutter layer between selective layer and supporting membranes. TFC membranes with gutter layers had higher water permeances under same operation conditions. 76

Figure 22. Green: selective layer. Yellow: gutter layer. Grey: support layer. Conventional two-layer composite membranes can suffer from pore penetration into porous supports. In addition, permeance of

selective layer is significantly lower than supporting membranes. Fabrication of an intermediate gutter layer, which can be less porous than support layer but is more permeable than selective layer, can mitigate pore penetration and enhance permeation efficiency. 77

Table. 4 Example cross-sectional SEM images presenting existing polymer thin film structures. 82

Figure 23. Schematic showing of one-step IP reaction followed by direct capturing on support membranes. Polymer thin films were synthesized from IP at free liquid-liquid interfaces. Amine monomers were dissolved in alcohol-water phase, acyl chloride monomers were dissolved in hexane phase. 10 s, 1 minute, 2 minute, 5 minute polymer films were formed directly using above-mentioned technique in a fumehood environment. 30 minute polymer thin films were formed with reactor covered with a big water bath tank... 85

Figure 24. HPLC assay analysis of different solutes intended for chiral separation using chiral SPA membranes. 88

Figure 25. Sub-pilot scale cross-flow filtration RIG used for nanofiltration performance testing. And stainless steel cross-flow filtration unit cell stream structure. 90

Figure 26. Chemical structures of SPA-1 and SPA-2. DBMPA was used to react with TPC and TMC separately via free-interface interfacial polymerization. 96

Figure 27. Self-standing polyamide (SPA-1) thin films were formed from free interface interfacial polymerization. A novel type of contorted DBMP amine was first dissolved in MeOH-water then used to react with commercially available acyl chloride TPC dissolved in hexane. a. Schematic showing of free-interface interfacial polymerization of DBMP amine and TPC, and formation of self-standing heterogeneous film comprising of a skin layer and porous layer. b. UV adsorption of opposite phase representing monomer concentration development in the opposite phase due to monomer crossover through liquid-liquid interface. c. UV adsorption representing TPC concentration development in opposite aqueous phase due to monomer crossover through formed SPA-1-150nm film. 97

Figure 28. a. N_2 gas adsorption isotherms of SPA-1 and SPA-2. b. CO2 gas adsorption isotherms of SPA-1 and SPA-2. c. DFT pore size distribution of SPA-1 and SPA-2 polymer films derived from N_2 gas adsorption. d. DFT micropore size distributions of SPA-1 polymer films derived from CO_2 gas adsorption. e. FTIR-ATR spectrums of SPA-1, SPA-2 and MPD-TMC films. 98

Figure 29. TGA thermal analysis of SPA-1, SPA-2 and MPD-TMC films. b. DSC thermal analysis of SPA-1, SPA-2 and MPD-TMC films. 99

Figure 30. Sputtered and unsputtered SPA-1 film cross-sections and top-view AFM imaging. a. SEM imaging of polymer films on AAO. (i) Cross-sectional SEM images of $DBMPA_{0.06}$-$TPC_{0.01}$-1min film captured on AAO supporting substrates. 0.06 wt% of DBMPA was dissolved in aqueous phase and 0.01 wt% TPC was dissolved in hexane phase. (ii) Cross-sectional SEM image of $DBMPA_{0.06}$-$TPC_{0.1}$-1min membrane captured on AAO supporting substrates. (iii) Zoomed-in cross-sectional FIB SEM image of $DBMPA_{0.06}$-$TPC_{0.1}$-5min membrane captured on AAO supports. Cross-sections were not sputtered. (iv) Cross-sectional SEM image of $DBMPA_{0.06}$-$TPC_{0.1}$-30min membrane captured on supporting substrates. b. Top-view AFM image of $DBMPA_{0.06}$-$TPC_{0.01}$-1min membrane captured on silicon wafer with partial skin layer peeled off. Height profile from AFM analysis suggests skin layer is smoother than porous layer. 100

Figure 31. Top-view AFM images of SPA-1 and SPA-2 films synthesized under different reaction time. Overall film thicknesses were evaluated from surface height profile histograms. 101

Figure 32. Microscopy images of SPA-1 films synthesized using ethanol and isopropanol as co-solvents in aqueous phase separately. 102

Table 5. SPA membranes samples with synthesis conditions including monomer concentrations, film thicknesses and acetone permeability. a. In standard sample labelling such as DBMPA0.06-TPC0.1-2min, 0.06 stands for 0.06 wt% of DBMPA was dissolved in aqueous phase solvent, 0.1 stands for 0.1 wt% of TPC was dissolved in hexane phase, 2min means reaction was allowed to progress for 2 minutes. b. Solvent

permeability was calculated based on standard deviations from parallel solvent permeance measurements and averaged membrane thickness. 103

Figure 33. XPS depth profiling and elipsometry techniques were further used to analyze properties of skin layers and porous layers. a. Appearance of self-standing SPA-1 film formed from 0.06 wt% DBMPA and 0.1 wt% TPC over 1 minute floating on water bath. b. Top-view SEM surface image of SPA-1film synthesized over 30 minutes. c. XPS depth profiling of SPA-1 film synthesized over 1 minute, 5 minutes and 30 minutes. And skin/porous layer thickness measurements from elemental analysis. d. Light refractive indices throughout entire SPA-1 IP film. e. Schematic showing of different layers of SPA-1 film deposited on silicon wafer. 105

Figure 34. XPS elemental etching analysis of SPA-1 membranes synthesized with 1min, 5min, 30min reaction time. 106

Table 6. Element counts and molecular weights of monomers. 107

Figure 35. UV adsorption of opposite phase. a. Diffusion of TPC from hexane phase into methanol-water phase through pristine PAN support. b. TMC diffusion from hexane phase into water aqueous phase through 20 nm MPD-TMC nanofilm on PAN support. 107

Figure 36. Top-view AFM height profiles of DBMPA-TPC films formed under different monomer concentrations and reaction time. a. DBMPA-TPC films formed using low DBMPA concentration (0.01 wt%) in aqueous methanol-water phase. b. DBMPA-TPC films synthesized under low TPC concentration (0.01 wt%) in hexane. 109

Figure 37. AFM peak force error imaging of DBMPA-TPC films synthesized under 1 minute reaction time using different monomer concentrations. With ultra low DBMPA concentration and high TPC concentration only porous layer structure was formed. With intermediate DBMPA concentration and low TPC concentration only skin layer dense structure was formed. With intermediate DBMPA concentration and high TPC concentration distinguishable asymmetric structures was formed. 109

Figure 38. Cross-sectional SEM images of DBMPA-TPC films synthesized over 30 minutes, but with different monomer concentrations. a. SEM cross-sectional image of DBMPA-TPC film synthesized with 0.06 wt% amines in aqueous phase and 0.01 wt% TPC dissolved in hexane phase. b. SEM cross-sectional image of DBMPA-TPC film synthesized with 0.06 wt% amines dissolved in aqueous phase and 0.1 wt% TPC dissolved in hexane phase. c. SEM cross-sectional image of DBMPA-TPC film synthesized with 0.25 wt% amines dissolved in aqueous phase and 0.1 wt% TPC dissolved in hexane phase. 110

Figure 39. SEM cross-sectional image of convex structures that created small ‘bumps’ on the film. 111

Figure 40. TPC solids were directly added into 0.06 wt% DBMPA solution in methanol and water. Vial reactor was gently shaken for about 1 minute then left for ~ 10 minutes. Powder-like suspension formed as a result. SEM surface imaging suggests the powder like clusters had close resemblance with porous layer structures in SPA films..... 111

Figure 41. Film layer growth profile and separation performances using dye as markers. a. SPA IP film layer thickness development against reaction time measured from AFM, MPD-TMC nanofilm thicknesses against reaction time measured from AFM. b. Dried self-standing SPA-1 film synthesized over 120 minutes using 0.06 wt% DBMPA and 0.1 wt% TPC. SPA-1 film can now be directly picked up by mechanical force after drying. c. SPA-1 membrane synthesized over 1 minute reaction time deposited on PAN supporting substrate. d. Acetone permeances vs SPA-1 IP layer thicknesses. Pure acetone permeance was tested under 10 bar and 80 L hr-1 flow rate in a continuous cross-flow filtration RIG. e. Escalating acetone solvent permeability vs thicknesses of SPA-1 IP layers. f. Dye marker rejections of SPA-1-150nm, SPA-1-2400nm and MPD-TMC-16nm membranes in acetone solvent under continuous cross-flow filtration..... 112

Figure 42. Dye marker rejections of SPA-1 TFC membranes with thicknesses in acetone solvent, in cross-flow filtration under 10 bar 80 L hr^{-1} flow rate..... 113

Figure 43. Contact angles of water and organic solvents on SPA-1, SPA-2 and MPD-TMC films captured in quartz crystals. 114

Figure 44. SPA-1-PAN TFC membrane appearances after consecutive dye rejections in acetone over ~ 1 week. 115

Table 7. Dye adsorption of SPA-2 TFC membranes compared with pristine supports. 116

Figure 45. UV spectrums of Acid Fushin solutions with different membranes immersed separately. 116

Figure 46. UV spectrums of Azobenzene solutions with SPA-PBI membranes and PBI support immersed separately. 117

Figure 47. Dye rejections of SPA-1 membranes with different thicknesses in methanol solvent in cross-flow filtration under 10 bar and 80 L hr^{-1} flow rate. 117

Figure 48. Dye rejections of SPA-2 membranes with different thicknesses in acetone solvent in cross-flow filtration under 10 bar and 80 L hr^{-1} flow rate. 118

Figure 49. Dye rejections of SPA-1-150nm membranes in acetone, methanol and acetonitrile solvents. 118

Figure 50. Parallel cross-flow filtration processes using SPA-1-2min membranes. Filtration was performed under 6 bar and 80 L hr^{-1} in acetone solvent using high concentration dye marker. a. UV absorbance of filtration permeate and feed solutions using 100 ppm Azobenzene solution in acetone. b. UV absorbance of filtration permeate and feed solutions using 100 ppm Acid Fushin solution in acetone. c. UV absorbance of filtration permeate and feed solutions using a mixture of 100 ppm Azobenzene and 100 ppm Acid Fushin solution in acetone. 119

Figure 51. Chemical structure of chiral RBA-DBMPA-TPC (RBA-SPA-1). 122

Figure 52. Top-view AFM image and height profile of synthesized chiral RBA-DBMPA-TPC film, with a manual cut in the middle of the film. 123

Figure 53. Circular dichroism of RBA-DBMPA-TPC film before methanl washing, methanol used for film washing and RBA-DBMPA-TPC film after washing. 124

Figure 54. RBA-SPA-1 self-standing film synthesized and captured on PTFE and PAN supports. 125

Figure 55. Water contact angle at initial state and after 120 seconds of RBA-SPA-1 film captured on quartz substrates. 125

Figure 56. a. HPLC spectrums of permeate side in static chiral diffusion using RBA-SPA-1 film collected after ~ 3 days. Over the first few days peaks were too weak to analyse, samples were collected each day. b. Enantiomeric excess in both feed side and permeate side in static chiral diffusion, and separation factor in permeate side through membrane. c. Feed concentration HPLC spectrum profiles. d. Enantiomer concentrations in permeate side through membranes. 126

Figure 57. TAPA-TFP thin film preparation using liquid-solid templated growth method in vial reactor followed by etching in alkaline solution. 129

Figure 58. a. Chemical structures of TAPA-TFP polymer. b. Top-view AFM image of TAPA-$TFP_{0.05}$ self-standing film synthesized over 48 hours. c. Schematic of liquid-solid templated growth method for film synthesis in a glass vial reactor. d. TAPA-TFP films synthesized with 0.05 mmol TAPA and 0.05 mmol TFP dissolved in 100 g of DCM over different reaction time. e. Cross-sectional SEM image of TAPA-$TFP_{0.05}$ film reacted for 5 minutes on PAN substrate. 130

Figure 59. Microscopic image of synthesized TAPA-TFP film and 3-D AFM analysis of TAPA-$TFP_{0.05}$-48hr film. 131

Figure 60. a. Top-view AFM imaging analysis of 2 μm × 2μm scan of TAPA-$TFP_{0.05}$-48hr film. b. 200 nm × 200 nm scan AFM images of TAPA-$TFP_{0.05}$-48hr film. 132

Figure 62. a. Schematic of simplified redox flow battery set-up. b. Ionic conductivity dependence of TAPA-TFP membranes captured on PAN support synthesized with different reaction time against temperature. c. TAPA-$TFP_{0.05}$-48hr-PAN TFC membrane performances in neutral flow battery using viologen (SPr)2V and potassium ferrocynide as redox couples..... 134

Figure 63. a. TAPA-$TFP_{0.05}$-48hr membrane resistance under different temperatures. b. TAPA-$TFP_{0.05}$-96hr membrane resistance under different temperatures..... 135

Figure S1. a. FTIR spectrums of DBMPA monomer in dry air. b. DFT pore size distributions of SPA-2 shattered films derived from CO2 gas adsorption isotherms..... 158

Figure S2. UV adsorption spectrums of 0.0003wt% DBMPA dissolved in MeOH. 159

Figure S3. UV adsorption spectrums of 0.001wt% TPC dissolved in MeOH-water mixture with 1:1 weight ratio. 159

Figure S4. Top row: 5 mg of MPD and DBMPA was dissolved in 20 g of hexane separately. Bottom row: After sonication at 35 °C MPD completely dissolved in hexane while DBMPA had poor solubility in hexane. 160

Figure S5. Storage modulus of SPA-1-5min film measured from AFM nanoindentation method..... 160

Figure S6. AFM top-view image of $DBMPA_{0.06}$-$TPC_{0.1}$ film formed from isopropanol-water as sub-phase solvents reacted for 5 minutes. 161

Figure S7. Surface current mapping using AFM PF-TUNA measurements of SPA-1-5min film. 161

Figure S8. AFM top-view image of MPD-TMC-30min membrane. 162

Figure S9. Zoomed-in cross-sectional SEM images of DBMPA-TPC films synthesized with different monomer concentrations and captured on AAO supports..... 162

Figure S10. Zeta-potential measurements of SPA-1, SPA-2 and DBMPA-TripC membrane at pH > 7..... 163

Figure S11. Salt rejections of SPA-1 and SPA-2 TFC membrane using PAN support in water. 164

Table. S1 Properties of dye markers used in OSN. 165

Table. S2 Properties of acyl chloride reagent used in polyamide film synthesis..... 166

Figure S12. Reproduced chiral separation performances of NEA in static diffusion using chiral RBA-DBMPA-TPC membrane with PTFE support. 167

Table S3. In situ TAPA-TFP film growth directly on supports. PAN, PAN-COOH and PBI supports were directly immersed in COF precursor solutions in DCM. 168

Figure S13. Chemical structures of PPD-TFP polymer synthesized from liquid-solid templated growth.... 168

Figure S14. Top-view AFM image, 3-D AFM height profile analysis and height profile of PPD-TFP self-standing film captured on silicon wafer. 169

Figure S15. Ionic concentration development in permeate sides using TAPA-TFP-PAN TFC membranes, PAN support membranes and PPD-TFP-PAN membranes..... 170

Figure S16. PPD0.1-TFP0.1-72hr-PAN-COOH RFB cycling performances in neutral pH RFB. 171

Figure S17. PPD0.1-TFP0.1-72hr-PAN-COOH TFC membrane appearance before and after running > 80 cycles in neutral pH RFB. 171

Figure S18. Self-standing MPD-TMC nanofilm synthesis was performed in a petri-dish reactor, synthesized films were transferred to water bath and captured using supporting substrates. 172

Figure S19. a. Neutral pH RFB battery performances using MPD-TMC-PAN-COOH membranes as separator. b. MPD-TMC nanofilm composite membrane appearance after battery cycling. c. Discharge capacities of RFB from 5th, 50th, 100th and 200th charge-discharge cycle. d. Resistance measurement of MPD-TMC-PAN-COOH membrane. 173

Figure S20. Alkaline redox flow battery performances using SPA-2 membrane synthesized for 1 minute with DHAQ and $K_4Fe(CN)_6$ as redox couples. 174

Figure S21. Ion permeation through MPD-TMC-PAN-COOH membrane in static dialysis using salt solutions as feed sides. a. Development of permeate side conductivity through PAN-COOH membrane. b. Development of permeate side conductivity through dip-coated MPD-TMC-PAN-COOH membrane. c. Development of permeate side conductivity through MPD-TMC-PAN-COOH membrane synthesized from IP at free interface. 175

Figure S22. Chemical structures of BHPF and TMC monomers used in polyester thin film synthesis. 176

Figure S23. Top-view AFM images of BHPF-TMC membranes synthesized with different reaction time. 176

Table S5. Film properties of BHPF-TMC membranes synthesized with different reaction time. 177

Figure S24. Film thicknesses of BHPF-TMC membranes synthesized with different reaction time. 177

Figure S25. Acetonitrile permeance of BHPF-TMC-2min membrane on PAN support under 10 bar, and Rose Bengal rejections in same solvent. 178

Figure S26. Charging-discharging performances in Li-S coin cell batteries using BHPF-TMC membranes and commercial Celgard membranes as separators. 178

Figures S27. Current-voltage curves of Li-S coin cell batteries using BHPF-TMC as membrane separators. 179

Chapter 1. Introduction

1.1 Background

High energy input of separation processes is the primary concern regarding net-costs and applicability. Chemical separations and purifications take up > 10% of world total energy input.[1] The majority of separation processes is performed in liquids and gases.[2, 3] Industrial waste stream treatment has a cost expectancy of 1 ~ 6 USD per cubic meter, through applications of membrane separation technology this value can be further reduced, Carbon emissions, mainly from burning fossil fuels releasing CO_2, is of great concern in terms of global climate change. Measures have been taken by many countries to reduce carbon emissions through carbon taxes, CO_2 capture technologies and measures as such. All separation processes are based on differentiating mass transport of guest molecules, among which liquid phase separation accounts for most purification and resource recovery. Conventional liquid separation process, distillation given as an example, is based on thermal-induced phase change of liquids with different boiling points. [4]The process is complicated and necessitates multiple primary phase change stages, energy consumption can not be easily reduced or recovered. [5, 6] Single-phase separation techniques such as chromatography would often require regeneration of separation units, extra steps to restore column unit capacity yet consume more energy and resources.[7, 8]

As a green, non-hazardous, low-cost next-generation separation process, membrane-based technology does not necessitate phase change or unit restoration. Application-wise, membrane devices have been broadly implemented in desalination, water purification and battery separators. Nonetheless, despite the many benefits brought by membrane technologies, the separation performances are not yet satisfactory.[9] State-of-art membranes are either limited by low permeability or low selectivity towards guest solutes, this trade-off has become the bottleneck of developing up-scalable high-efficiency membrane technologies.[10-12]

1.2 Motivation of research

To tackle this global challenge in membrane research and innovation, thorough understanding of solute/solvent properties, molecular transport through membrane materials, structure-performance relationships of membrane materials must be fulfilled. Polyamides are robust, solvent-resistant polymers renowned for preparing membranes, plastics and textile products. [13-19] Polyamide membrane backbones are resilient, and usually self-assemble into densely-packed matrix thus providing impressive mechanical strength and performances.[18, 20, 21] Conventional condensed polyamide architecture results in very low fractional free volumes (FFV), when fabricated into membranes the intrinsic liquid permeability of materials is very low.[22, 23] It would require very

high operation pressure (>15.5bar) to increase the liquid flux through the membranes. However, polyamide membranes have high and stable rejections towards salt ions as well as organic molecules.[23, 24] To improve the permeation performances, research efforts have been mainly committed into tuning membrane physical properties, functionalization of materials and exploring new monomeric species for material synthesis. [25-27]

Polymers of intrinsic microporosity (PIMs) is an exceptionally interesting class of amorphous porous polymers, kinked building-block structures prevent chain packing as well as crystalline domain formation.[28-30] Intrinsic interconnected micropores can greatly enhance molecular transport with more open, continuous passages for selective permeation. PIMs have been mostly prepared via phase-inversion process which is benefitted from good solubility of linear PIMs in organic solvents. However, this property makes PIMs membranes unsuitable for separation in certain organic solvents.

Thin-film composite (TFC) membranes are classes of high-performance multi-layered membranes already dominating filtration membrane market.[31, 32] An ultra-permeable backing substrate is used to support a thin selective layer, which primarily contributes to selective permeation with low resistance. The selective layer can be manufactured to be as thin as possible to provide superior permeance and selectivity as long as it is defect-free. TFC membranes are mostly prepared by interfacial polymerization (IP).

In my PhD research I have postulated that break-through separation performances can be achieved by synthesizing ultra-thin crosslinked microporous membranes. Reported ultra-thin membranes are difficult to scale up which is primarily due to poor mechanical properties of thin films. To resolve this issue my PhD research will investigate how micropores in PIM-type thin films can affect membrane preparation in interfacial polymerization, and preparation of microporous thin films with scalable structures by manipulating advanced membrane hierarchical structures. Within the scope of my post-graduate research, I aim to synthesize and functionalize scalable, crosslinked, intrinsically microporous membranes with high permeability and selectivity in solvent-based molecular separations.

1.3 Outline of thesis and post-graduate research

Chapter 2

Literature review up to calender year 2022 with respect to organic solvent nanofiltration, energy storage devices, fabrications and applications of thin-film composite membranes. Most notably, this literature review discusses about importance of microporosity in membranes and how to take advantage of it to innovate new technologies and high performances.

Chapter 3

Details of polymer film synthesis, membrane performance testing and characterization methods.

Chapter 4

IP reaction is a facile and efficient technique used in TFC membrane preparation. Moreover, during recent years IP reaction can be applied in preparing a variety of ultra-performance membranes in gas and liquid phase separation. Increasing membrane permeance have been exceptionally challenging in gas separation membranes due to preparation difficulty in ultra-thin thins. After maturing of lab-scale thin film preparation routes via interfacial polymerization at free liquid-liquid interface and spin-coating, unprecedented performances of thin film membranes have been uncovered. But ultra-thin films are difficult to scale up and can very easily have defects, this is now becoming most challenging for liquid phase separation due to high pressure required in pressurized filtration system in organic solvents and water.

In this chapter crosslinked microporous polyamide networks with unprecedented heterogenous structures were successfully prepared using IP reaction at free interface. Compared with all existing IP membranes we report a new film formation mechanism, that can help prepare high permeance, high rejection 'thick' membranes from singular IP reaction at free interface. An asymmetric structure was achieved in thin film membranes with an autonomous supporting porous layer. By reacting bulky high molecular weight contorted amine monomers and smallest di-functional aromatic acyl chloride, well-defined bi-layer structure with clear boundaries was achieved from interfacial polymerization. We allow top low MW acyl chloride reagent(s) to rapidly crossover formed nanoporous polyamide film to react with amines underneath, this has led to automatic self-supported polyamide structure being formed featuring a skin layer and porous layer. Top dense skin layer can be synthesized to be < 50 nm thick to provide good selectivity and permeance. Micropores in synthesized thin films allowed reagents to diffuse through formed thin films, robust asymmetric structures were achieved which are beneficial to preserving performances.

This mechanism was revealed to achieve crosslinked asymmetric structure through one-step membrane synthesis.

This chapter includes experimental methods and result discussions.

Chapter 5

Membrane-based chiral separation is considered as most difficult separation process. This is mainly due to unique separation mechanisms which usually do not apply to any other separation processes. High chiral separation selectivity through membranes can usually be achieved by adsorption from

docking at surfaces or inside bulk of membranes. But chiral adsorption membranes will inevitably lose selectivity over time after saturation. To reduce net-costs of chiral separation processes, membranes with stable performances over time are more ideal.

In this chapter chiral microporous thin film membranes were synthesized from contorted reagents and chiral additives. Chiral polyamide networks based on contorted monomer geometry were successfully prepared with incorporation of axially chiral bi-naphthalene structures. In this project spatial chirality in crosslinked rigid polymer networks was successfully introduced. Chiral rigid thin films synthesized with (R)-bi-naphthal diamine showed stable chiral selectivity in static diffusion. Stable chiral selectivity of $\sim 16\%$ was achieved and this performance did not further decrease over time.

This chapter includes experimental methods and result discussions.

Chapter 6

Redox flow batteries are promising energy storage devices. A RFB device features a membrane separator to isolate cathode and anode materials, this separator forces electrons to transport via outer circuit to provide currents and electric energy. However, existing membrane separator performances are not satisfactory.

In this chapter semi-crystalline COF-type self-standing thin films were successfully prepared from liquid-solid templated growth. Synthesized COF-type polyimide film was stable in electrolyte solutions and had good performances in neutral pH redox flow batteries.

This chapter includes experimental methods and result discussions.

Chapter 7

Conclusion and future research directions following this PhD research.

Chapter 2. Literature review and objectives

2.1 Introduction to membrane separation processes

Membranes are semi-permeable filter materials that selectively transport or retain different solute species. Depending on applications in different phases, separation mechanism differs based on established models and mass transport theory. (Fig. 1) Liquid-phase separation membrane technologies have been widely applied in desalination, filtration, battery separators.[33-38] By driving forces membrane separation can be divided into two types, static diffusion and pressurized filtration (PF). In static diffusion concentration gradient is the only driving force, thus permeation rates of solutes or solvents are low. In PF process an extra pressure gradient is imposed across the membranes, thus dramatically improving mass transport rate.[39] Desalination of seawater is a typical PF process, sea water or brackish water are pushed under pressure through membrane units to obtain drinkable water. Salt ions are retained in the saline stream while only pure water comes through.[40] In energy storage devices such as flow batteries or fuel cells, membranes are core components to separate anode and cathode materials to maintain charge-discharge capacity for longer life span. Conductive membranes can be prepared to help with charge carrier transfer. Both permeability and selectivity of membranes are important indexes to evaluate separation performances.

PF processes can be divided into reverse osmosis (RO), nanofiltration (NF), ultrafiltration (UF) and microfiltration (MF) sequenced with increasing molecular weight cut-offs of membranes.[41] NF processes can be applied in both aqueous and solvent systems, which account for most of the existing effluent purification, peptide separations and food ingredient separations.[42-44] Over the past decades novel membrane materials have been reported for chiral separations, active pharmaceutical ingredient (API) separations, oil-water separation and crude oil separation which raised great interests in membrane nanofiltration in organic solvents.[3, 45-47] Applying membranes in organic solvent nanofiltration (OSN) processes is challenging due to swelling and instability of existing polymeric membranes in organic solvents, while inorganic membrane fabrication processes are overall energy-consuming and complicated.[48-50] Inorganic membrane preparation usually requires expensive raw materials while polymeric membranes can be based on abundant organic matters.[51] Hence, developing solvent-durable high-performance polymeric membranes for OSN is important to the research community and future sustainable industries.[52]

Here all separation processes have been classified as one or more of the following, i) Molecule to molecule separation, ii) Molecule to ion separation, iii) Ion to ion separation. Typical molecule to molecule separation can be nanofiltration (NF). In a NF solvent purification process, solute molecules are first dispersed in solvent molecules, the mixture is then permeated through a membrane barrier.

Under ideal scenario only solvent molecules can pass through the membranes and all solute molecules are retained in the feed tank.[53, 54] In an alkaline redox flow battery device, membrane separators need to transport charge carriers, which are usually monovalent ions such as K^+. But membrane separators need to reject organic redox active molecules such as DHAQ, potassium ferrocyanides, azobenzene etc.[55] In redox flow battery devices membrane separators are responsible for separating molecules from charge carriers. In Li-ion batteries membranes need to permeate Li^+ but reject other ionic species such as Mg^{2+}.[56, 57] In Li+ recovery process membranes need to separate Li+ from other monovalent or multivalent ions. In desalination processes membranes need to be permeable to water but reject Na^+, K^+, Mg^{2+} etc.

Based on sizes, charges and solute stereochemical properties, selective permeation/rejection mechanisms in membranes can be largely summarized as the follows, i) size-exclusion or molecular sieving effects, ii) Donnan exclusion effects, iii) selective stereo-binding effects.[58-60] This thesis will specifically focus on liquid-phase separations using solid membranes.

Two different types of mass transport models are dominant in describing molecular mass transport behaviours in membranes focusing on liquid phase separations, the solution-diffusion model and pore flow model.[61] The solution-diffusion model is generally used for non-porous membranes while pore flow model is used for porous membranes. Classic recognition of porous materials refers to materials with porosity ranging from 0.1 μm to 100 μm, where non-porous materials can still have sub-nanopores to allow transport of much smaller molecules. Latest researches have further extended the concepts, where microporous materials (pore dimensions < 2 nm) and mesoporous materials (pore dimensions > 2 nm) have been categorized.[62] Microporous nanostructures especially in membranes are more appealing for NF and RO applications for faster molecular transport.[63] Sub-2nm scale pore sizes are comparable to those of non-porous membranes, thus providing almost equivalent selectivity to small molecule separation for higher molecule weights. [64] Gas molecules typically have smallest dimensions thus requires tight membranes with smaller pores, organic molecules have intermediate dimensions which usually require NF or UF membranes to separate.[65]

That is to say, so-called pore properties in semi-permeable membranes are vital regarding controlling and achieving separation in different phases. Precise control of nanometer pores in membranes is challenging to achieve, especially in disordered amorphous materials. Highly distinctive separation mechanisms and pore property requirements for separation in different phases enforced comprehensive understanding of materials structure-performance correlations. (Fig. 1)

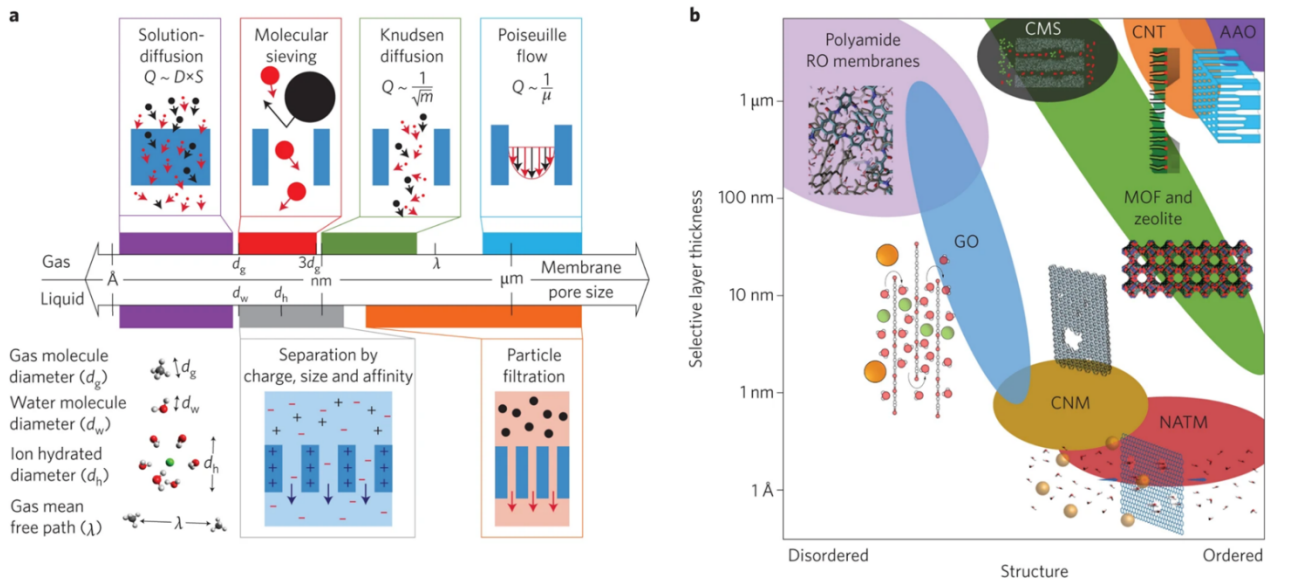


Figure .1 Distinct separation mechanisms in liquid-phase separation and gas separations. And existing representative thicknesses of membranes with disordered or ordered structures. (reprinted from reference 65)

Non-porous membranes are existing dominant materials applied in RO and NF with high rejections towards salt ions and organic molecules, but permeances are usually low.[22] This is due to limitation of their low free volumes and poor pore interconnectivity which led to low intrinsic permeability. Reducing membrane thickness is a universal approach to reduce resistance and increase permeance to compensate for low permeability. Most common polyamide RO membrane synthesized from MPD-TMC has sub-nano pore sizes on the scale of less than 4 angstroms according to CO_2 gas adsorption, and very low pore volume density which primarily lead to low water permeance.[66] Despite polyamides generally have hydrophilic surfaces, sub-10nm MPD-TMC nanofilm membranes with smooth surfaces only have < 3 L m^{-2} hr^{-1} bar^{-1} water permeance.[67] The permea-selectivity is determined by both surface interactions (solution) and mass transport (diffusion) in the bulk of membranes.

$$Q = D \times S \quad \text{(Equation - 1)}$$

Where Q stands for permeation of certified species, D stands for diffusion of that species and S stands for solution of that species. RO and NF membranes have limited fractional free volumes and less open pores on the surface, this has led to unsatisfactory dissolution of guest molecules from the surface and low permeation rates inside membranes. Pore properties and molecular interactions heavily affect membrane performances. Specifically pore size, pore density and pore interconnectivity are important properties to evaluate. Pore interconnectivity is difficult to evaluate,

but it is generally considered higher pore volumes and density can lead to better pore interconnectivity. Existing studies on amorphous porous polymers have shown contorted monomer structure does not significantly change micropore sizes, but increases pore volumes and interconnectivity. Precise control of pore sizes in amorphous polymers is challenging, as structural disordered packing thermodynamically disrupts formation of fine pores with consistent geometry.

2.2 Porous polymeric membranes

Membranes are distinctive units featuring semi-permeability, the definition suggests each membrane unit ought to be designed to selectively transport or reject targets with maximized efficiency. Enhancing intrinsic porosity in membranes is a key strategy to enhance permeability of membranes as well as selectivity.[68, 69] This is based on pores with well-defined dimensions that deny mass transport of undesired species. Porosity introduction can be realized by bombarding on atomic level to create atomic defects such as in GO membranes and carbon nanotube (CBN), but technique as such is complicated and not applicable to all materials.[70, 71] In addition, physical or chemical modification of existing membrane materials is limited by their architecture and chemical reactivity. Other approaches such as templating involves multiple steps that ncrease preparation net-costs and may cause technical issues. Hence novel materials, that can be intrinsically microporous or nanoporous, should be developed to cater to uprising demands.

Fractional free volumes (FFV) exist in all polymeric materials due to electron repelling forces between segments.[72] FFVs are usually dynamic and can be temperature-dependent.[73] FFVs decrease as temperature decreases. (Fig. 2) Mitchell and others reported studies on free volume development down to cryogenic conditions using PALS. Interestingly average positron life time eventually reached almost constant value meaning free volumes stopped collapsing with decreasing temperatures while probing thiol-ene networks synthesized from PETT with lowest molecule weight. For a range of thiol-ene networks, with constantly decreasing temperatures from 80 °C to -230 °C free volumes collapsed more slowly under Tg. This suggests FFVs are more stable in glassy state. Membrane technology features low costs and is preferably operated under near room temperature, this is sometimes also determined by low boiling points of solvents or thermal stability of guest solutes. From this perspective, membrane materials should preferably be in glassy state under operation temperature. This suggests polymers with high Tg are desirable to protect pore structure integrity. Pores in polymeric materials are intrinsic FFVs that have become large enough for guest molecules to access. To create pores and consistently control pore structures in membrane materials under practical conditions are key challenges to resolve practical challenges.

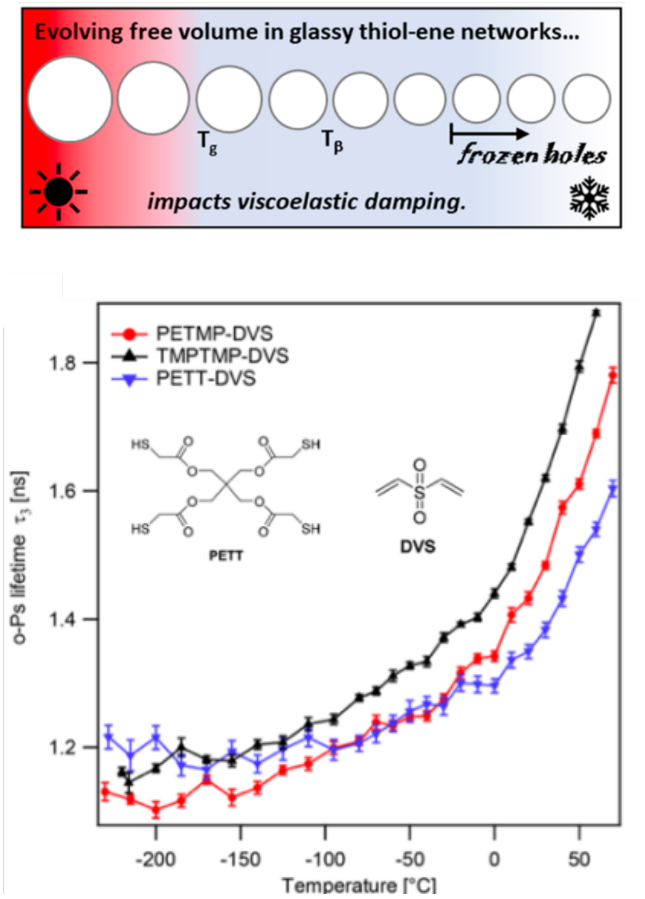


Figure 2. Fractional free volume dependence against temperatures in crosslinked polymers. Under decreasing temperature free volumes in crosslinked polymers shrink, while with increasing temperatures fractional free volumes increase. (reprinted from reference 73)

However, these membrane pores must be interconnected throughout front-side of membranes to rear-side of membranes to form continuous passages enabling mass transport.[74] Porosity contributes to reinforce membrane semi-permeability. Controlling FFVs, or pore properties, in membrane materials is key to controlling and designing membrane performances. Pores in membranes should be large enough to maximize permeability towards small molecules, but at the same time should be small enough to reject molecules that require separation or enrichment in the feed stream. Hence, controlling pore size properties is necessary to maximize selectivity and permeability. And of course, pores can be functionalized towards different separation mechanism. Most of reported microporous membranes have hierarchical pore size, these results already demonstrated progress in controlling porosity in membranes.[75-77] Yet it is still difficult to construct uni-pores in disordered amorphous polymer membranes, apart from other semi-crystalline materials with ordered cavities and pore alignment. While hierarchical pore size distributions may benefit mass transport, uniform pore size distributions can benefit precise molecular screening for enhanced selectivity.[78]

Total pore volume is another key characteristic in microporous material design. Higher pore volume density usually leads to better pore interconnectivity, lower membrane resistance and higher permeance.[79] However, mere improvement of membrane permeability is not enough to address energy issues in membrane industry due to trade-off effects.[80] Understand pore formation, controlling pore sizes and enhancement of pore volume density are thus all important steps to prepare ultra-performance membranes.[81] Moving towards that objective, a few most notable strategies have been adopted to prepare porous membranes, i) control monomer geometry to enhance repelling forces between backbone segments, ii) Crosslink well-defined macrocycles or small oligomers with permanent intrinsic cavities. iii) Apply porous filler materials in membranes to enhance both permeability and selectivity. In addition, by far ultra-thin membranes have shown greatest potentials to improve membrane permeance. Assuming that pore size and pore volume density are constant, infinitely thin membranes are expected to maintain high sieving selectivity and lowest resistance.

2.2.1 Polymers of intrinsic microporosity (PIMs)

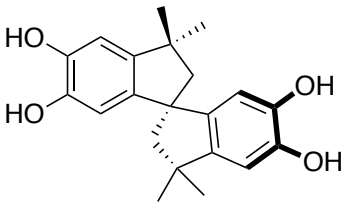
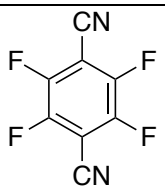
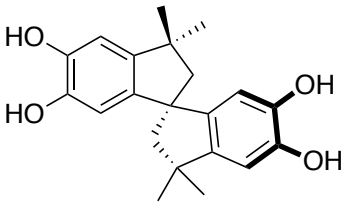
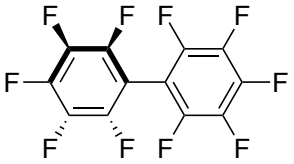
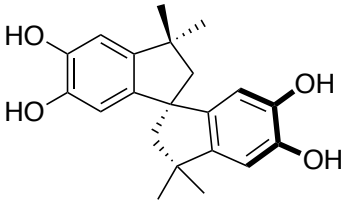
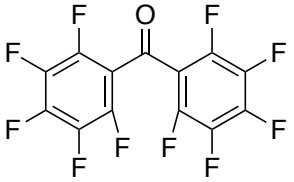
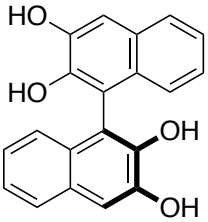
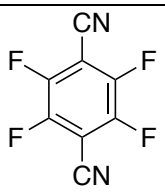
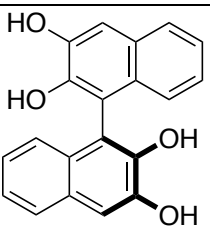
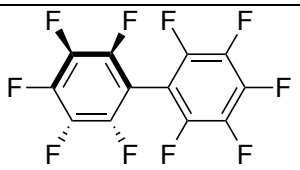
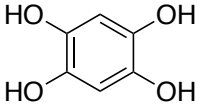
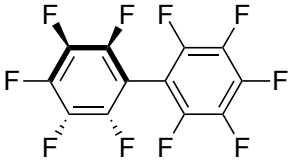
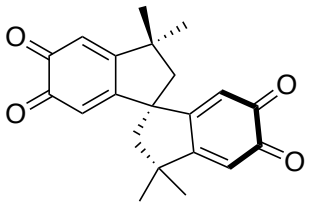
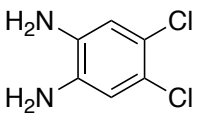
All polymers have, to some extent, certain amount of unoccupied free volumes. Yet not all polymers have free volumes that are highly interconnected and large enough for mass transport. PIMs are constructed from monomers with rigid contorted geometry, they are linear ladder-like polymers that can stack into disoriented amorphous states.[82] PIMs can be spin-coated or phase-inverted into membranes ranging from ~35nm to 30um. After solvent removal PIMs collapse into semi-condensed structures with intrinsic microporosity and high surface area[83]. PIMs have high glass transition temperatures > 200°C and are thermally stable under room temperature. Tg of PIMs is even higher than some crosslinked materials.[84] Young's modulus of PIMs ranges from 1.7 to 3 GPa, due to kinked structures and lack of crosslinkages PIMs only have moderate elasticity and can easily experience permanent deformation under tensile stress. PIMs polymer chains have higher inter-chain friction and higher extent of chain entanglement owing to unique chain geometry. Reported PIMs especially AO-PIMs have high gas permeability especially high solubility coefficient for CO_2, but it is difficult to be processed into sub-10nm defect-free membranes unlike crosslinked polymers.[85, 86] Hence increasing PIMs permeance is a key challenge despite their intrinsic microporosity and high permeability. Linear PIMs are bottlenecked by further reducing resistance maintaining homogeneous microporosity. It has been difficult to make ultra-thin PIMs, where studies have also shown ultra-thin PIMs membranes actually have reduced permeability.

In liquid phase separation PIMs have decent solvent permeance for alcohols, but broad MWCO which is primarily due to swelling in organic solvents. Porosity of PIMs is not stable especially in organic solvents. When casting down to sub-100nm scale solvent permeability of PIM-1 increases then quickly decreases. This is due to activated chain relaxation in liquids which eliminated local

micropore regions.[87] Ultra-thin 35nm PIMs membranes have lower solvent permeability than 140nm membranes, meaning porosity in PIMs is not homogenous and can change with thicknesses of films. Interestingly, 35nm PIMs membranes also had lower permeance than 140nm membranes. By far linear PIMs membranes for OSN applications have not been reported in harsh solvents like DMF or DMSO etc.[88] Membrane micropores of PIMs can slowly collapse over time under dry conditions.[89, 90] Aging effect of PIMs was reflected by increasing selectivity, decreasing permeability in gas separation and increase in Young's modulus. [91, 92] Methanol vapor permeance also decreased after aging of PIMs, suggesting decreased permeability is related to structural changes.[93] These results imply PIMs micropore collapsing not only effects pore volumes inside bulk of membranes but possibly average pore sizes as well. Nanoparticles can be embedded into PIMs to mitigate physical aging nonetheless.[94] This is due to rigid solid fillers that helped prevent structural collapse.

Linear PIMs have been reported synthesized from different monomers with various types of contortion.[95] (Table. 1) All PIMs show high BET surface area mostly benefited from inefficient packing of polymer chains which leads to large pore volumes.[96] PIMs backbone synthesis usually features reaction between contorted non-planar monomer A and planar monomer B in -A-B-A-B- format. Resulted ladder-like polymer backbone repeating units are in kinked orientations thus creating non-accessible cavities to adjacent backbone segments. Microporosity of PIMs is more like preserved than fabricated from unique monomer geometry applied in polymer synthesis. TTSBI-OH is a common PIM reagent, two reactive -OH groups of TTSBI are close to each other which may sterically hinder reactions. PIMs synthesis generally takes long reaction time to obtain high-molecular-weight polymers. Controlling molecular weight of PIMs could be an issue due to spatial hindrance of reactive groups. Adding fluoride ion could increase polymer product yield and obtain PIMs with high molecular weights.[97] PIMs membranes prepared from low molecular weight polymers can easily have defects and poor selectivity. Polydispersity is an important index to evaluate dope solution properties before membrane casting. To existing experimental knowledge, membrane casting of low molecular weight PIMs dope solutions can lead to defected membrane areas and high variations in separation performances. When processing non-crosslinked PIMs into membranes, poor polydispersity can also lead to high variations in performances as polymers were randomly dispersed without crosslinking causing pore properties to be inconsistent.

Table. 1 Examples of reported linear pristine PIMs and contorted monomer structures used in synthesis.

Monomer A	Monomer B	Reference name
		PIM-1
		PIM-2
		PIM-3
		PIM-4
		PIM-5
		PIM-6
		PIM-7

Side -CN groups on PIM-1 backbone can be functionalized into -COOH or amidoxime etc.[98]. Bulkiness of side groups/chains may also affect microporosity in PIM-type structures. Apart from TTSBI, triptycene derivatives have more conjugated planar contortion. Extremely contorted and rigid tri-planar structures can be modified with functional groups such as amines, hydroxyl groups, acyl chlorides, halides etc.[99] Triptycenes have been applied in linear PIMs synthesis, resulted Trip-PIM has higher surface area than conventional PIMs.[100] (Fig. 3) In linear PIMs synthesis using triptycene structures, only two planes of triptycenes are functionalized. The residue aromatic plane is bulky and helps increase overall BET surface area, by further preventing efficient 2-D packing. Adding molecular weights to bulky aromatic segments onto the side groups can improve BET surface area of resulted polymers.[101] (Fig. 4) Triptycene polyimides (TPI) synthesized from pristine triptycene structures had 39 to 68 $m^2 g^{-1}$ BET surface area, while from bulkier triptycene monomers with naphthalene structures showed 360 to 430 $m^2 g^{-1}$ BET surface area. More importantly, triptycene polyimides are still soluble in a variety of solvents allowing solution processing.

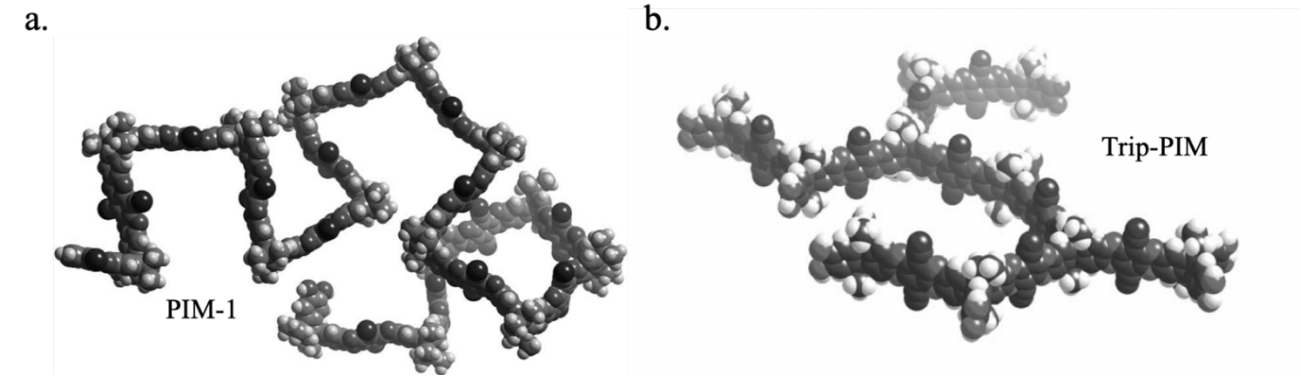


Figure 3. 3-D structures of most popular PIM-1 and novel type of Trip-PIM synthesized from tri-planar triptycene structures. (referred from Neil et al)

Tri-functional triptycene derivatives can also be used to synthesize crosslinked microporous polymers.[102] (Fig. 4) Due to high surface area triptycene-based networks have high gas adsorption capacity. This property is desirable in gas storage, gas separation, catalysis and liquid separation. Triptycenes have three rigid symmetric planes with dihedral angles of 120 °C each, meaning three separate polymer chains can potentially be extended from one single crosslinking node. This geometry promotes further inefficient chain packing by purposefully separating each plane.

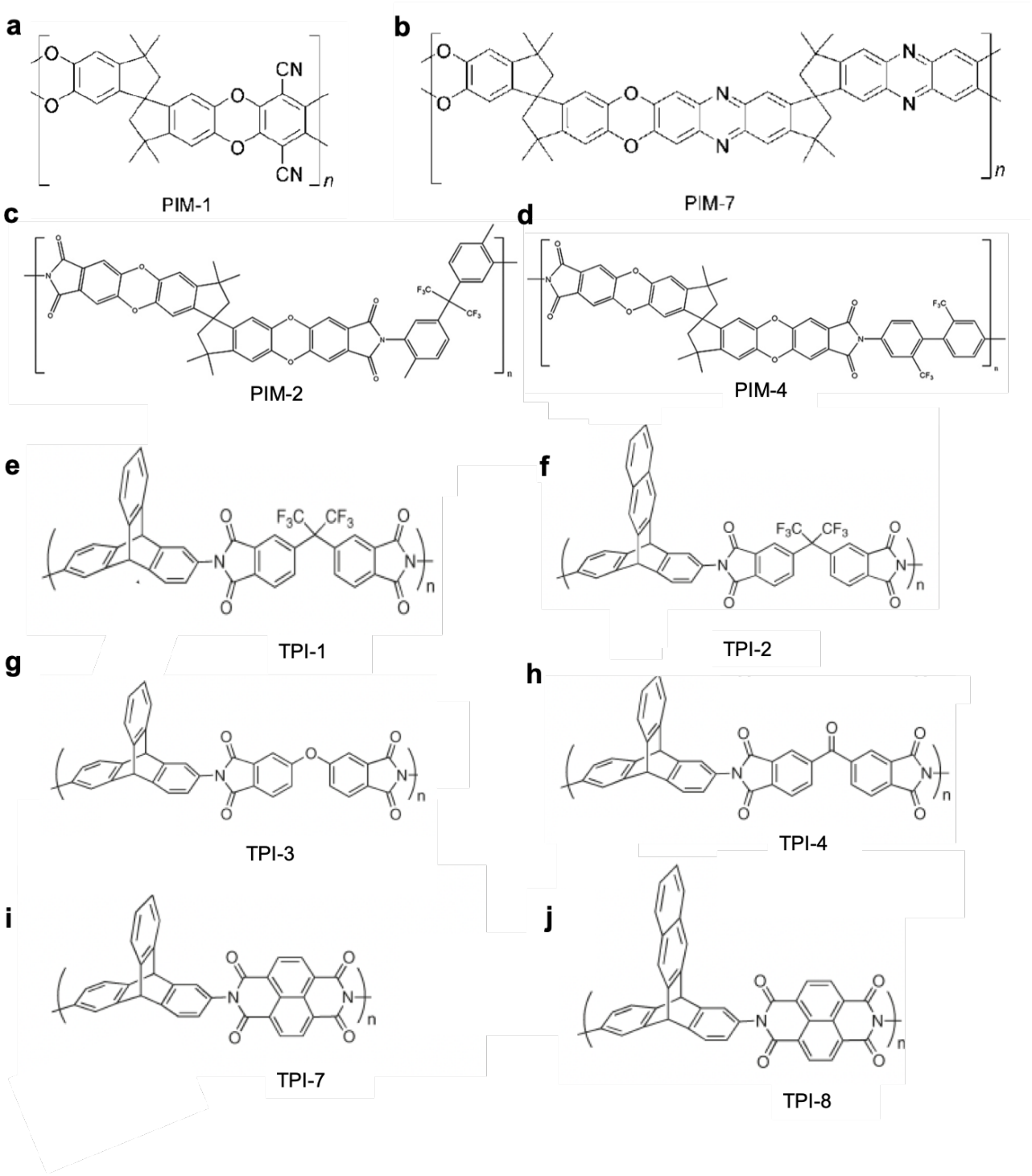


Figure 4. Chemical structures of chosen linear PIMs, and novel polyimide PIMs using triptycene structures as part of polymer backbones. TPI-1 through TPI-8 were designed and prepared using di-functional triptycene with one inert plane, increasing the bulkiness of inert side chain segments increased BET surface area which was concluded to be due to enhanced inefficient packing.

PIMs can be chemically crosslinked to improve selectivity and maintain gas permeability.[103] However, due to backbone rigidity it is difficult to increase crosslinking degree of PIMs by crosslinking agents. Crosslinking of PIMs enhanced pore stability and restricted pore collapsing,

membranes are more stable and have lower swelling in nanofiltration.[104] PIM synthesized from branched TB-OH showed quite significant swelling in water, reflected by increasing water flux under longer water exposure time. PIM-TB-OH membranes soaked in water for 5 days showed decreased PEG oligomer rejections from initial ~ 80% down to ~ 0%, decreased $CuSO_4$ rejections from initial 82.6±8.6% to 5.9±2.0%. Tris(4-hydroxyphenyl)methane triglycidyl ether (TGE) was used as a crosslinking agent to connect -OH groups. With 6 wt% TGE crosslinking agent content, crosslinked PIM-TB membranes showed 44% CuSO4 rejection even after 5 days of water exposure, increasing TGE loading increased CuSO4 rejection up to 87%. Alas higher crosslinking agent content decreased water permeance from 41.6 to 0.3. Apart from crosslinking PIMs can be carbonized under high temperature to behave like carbon molecular sieves in gas separation.[105] In 2020 Joen and others reported carbonization of PIMs membranes via pyrolysis crosslinking improved water flux in aqueous filtration, carbonization removed fluorine groups and improved hydrophilicity.[106]

2.2.2 Covalent organic frameworks (COF)

Amorphous polymers are disordered by nature, controlling pore sizes is challenging due to random thermodynamic behaviours of segments and disoriented polymer chain configurations. Semi-crystalline COFs are usually synthesized from reversible condensation reactions between amines and aldehydes forming crystalline regions from aligned honeycomb structures.[107]

Polymerized imide polymers can reshuffle into ordered structures due to reversibility of aldehyde-amine condensation reactions. COFs are synthesized from highly symmetric monomers. Instead of forming 3-D crosslinked materials COFs are considered as 2-D crosslinked materials with well-defined pore structures due to symmetry and stacking of crystals.[108] Over the decades COFs have been mainly synthesized as nanoparticles for catalysis, gas storage, or chromatography stationary phases due to ultra-high surface area up to ~ 2000 $m^2 g^{-1}$.[109-111] Previously reported COFs have high surface area but poor processability. However, self-standing COF thin films were successfully prepared by a few groups using interfacial polymerization. Interfacial synthesis confined assembly of monomers at liquid-liquid interface. (Fig. 5)

Processing COF structures into independent membranes is challenging, COFs have been mainly reported to be incorporated into polymer matrix to form Mixed Matrix Membranes (MMM) as fillers.[112, 113] Covalently-bonded structures is highly compatible with polymeric backbones, COF-MMMs have enhanced surface area and permeability without significant phase separation or defects.[114]

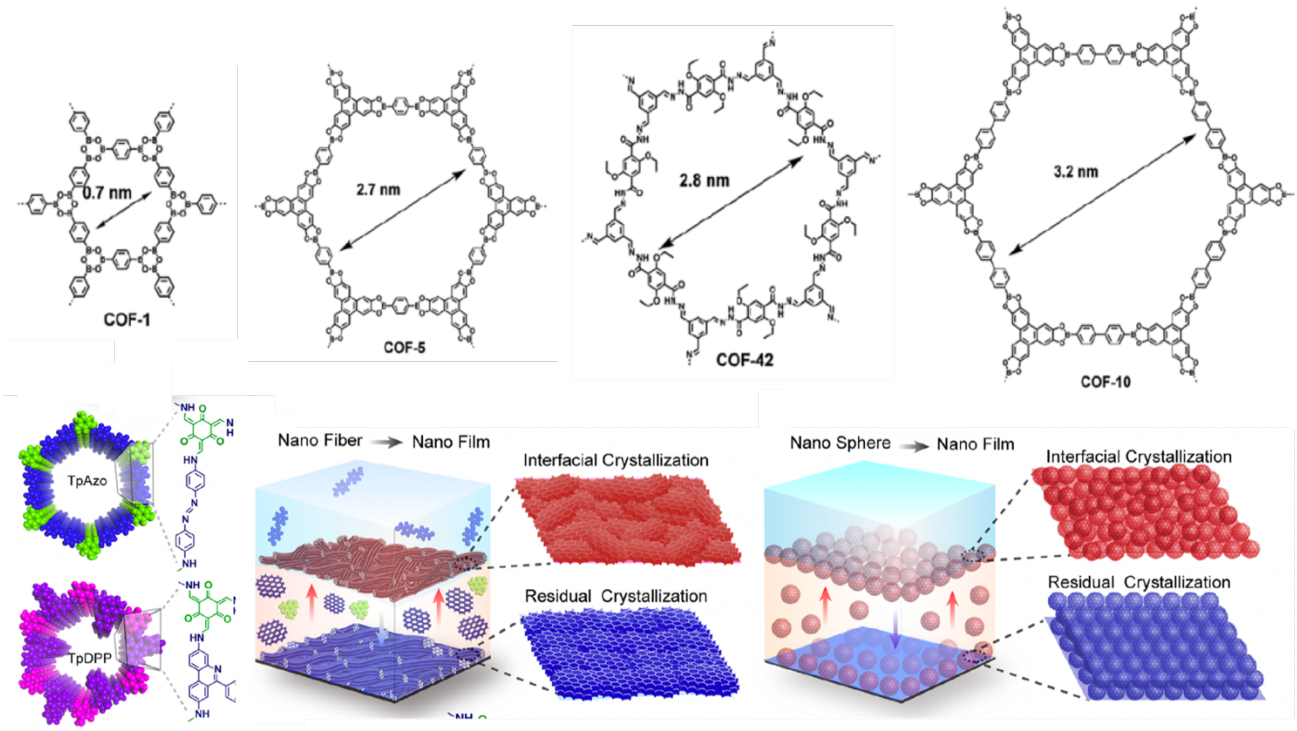


Figure 5. Well-defined and ideal COF ordered structures can be prepared from reacting symmetric monomers under controlled conditions. Recently Banerjee and others revealed COF thin film formation via fibre-to-film or sphere-to-film mechanism. 2-D polymeric materials with uniform micropores or even mesopores can now prepared into thin films via interfacial polymerization.

2.2.3 Porous organic cages (POC)

Porous organic cages are symmetric small oligomers with intrinsic cavities preserved by covalent bonds.[115] Cage crystals are soluble small molecules with outstanding processability and high surface area. Preparation of conventional cage crystals features symmetry of monomers and cycloimination for local reaction termination. Synthesis of cage molecules is challenging due to delicate requirement of reagent geometry, removal of side products and temperatures. POCs have attracted particular interests towards gas storage and sorbent media such as porous liquids.[116, 117] POCs can be easily dispersed in liquids. In 2011 Michael and others studied fundamental cavity determination and pore properties in CC9 and CC10, highlighting pores in cage assembly can be both intrinsic and extrinsic instead of only one configuration. [118] This property is singular as conventional microporous polymeric materials can only have pore formed either intrinsically or extrinsically. Polymer chains and side groups will take up free volumes, while the unoccupied free volumes in bulk of polymer material can thus only be extrinsic. Pores from cage assembly assume binary properties due to strengthened inefficient packing, pores in cage single molecules are protected by covalent bonds and do not collapse. These properties highlight their potential for commercialization and scale-up.

POCs can be spin-coated into membrane layers on top of support, which showed promising gas separation performances.[119] In addition, cage molecules can be incorporated into polymer matrix to improve separation performances. [120]

2.2.4 Interfacially-polymerized microporous polymers

Contorted monomers can be co-polymerized with conventional planar monomers such as PIP-TMC. [121] SBI or TB were directly mixed with PIP in aqueous phase to co-polymerize with TMC at water-hexane interface. Resulted membrane had >99% rejections of Na_2SO_4 and $MgSO_4$. Water flux of SBI5-PIP5 was 18.1L m^{-2} hr^{-1} bar^{-1}. Despite low rejections for monovalent salt ions both SBI-PIP and TB-PIP membranes showed enhanced nanofiltration performances. Rigid contorted monomers can also be doped with MPD in aqueous phase to copolymerize with TMC. Resulted membranes showed > 99% rejection of RDB (479 g mol^{-1}) and 11.3 Lm^{-2} hr^{-1} bar^{-1} methanol permeance due to enhanced microporosity. Membranes were quite stable in DMF.[122] These results imply contortion of building blocks adds to rigidity of polymer network and prevents structure swelling in harsh solvents. (Fig. 6)

PIM-type contorted monomers can also be directly used as independent reagents to synthesize crosslinked microporous polymers via interfacial polymerization. In 2016 Maria and others reported the first polyester nanofilms synthesized from TTSBI/BHPF and TMC. It was discovered that application of contorted PIM-type monomers in crosslinked polymer synthesis enhanced polyester intrinsic microporosity.[123] Microporous polyester nanofilms showed higher methanol and acetone permeances than flat MPD-TMC nanofilms, and > 90% rejections towards most organic dye molecules, polystyrene oligomers and polyethylene glycols (PEGs). (Fig. 6a) Polymer nanofilms were robust enough to withstand transfer-deposition and high pressure. Molecular weight cut-offs measured from organic dyes, polystyrene oligomers and PEG solutions were different. This is associated with linear solute molecular configurations such as coiled or stretched in solvents, which could change dimension properties when entering or leaving membranes. To further enhance network backbone rigidity, contorted triptycene structures have been applied as reagents in one-step polyamide synthesis.

In 2020 Ali and others reported TFC membranes with microporous skin layers via *in situ* interfacial polymerization of planar m-phenylene diamine and tetra-functional triptycene acyl chloride. [66] (Fig. 6b) Resulted MPD-Trip polymers have enhanced micropore volumes compared with MPD-TMC, but similar sub-nano pore sizes. MPD-Trip membranes have higher solvent permeances and almost identical rejections and MWCOs (~210g/mol) compared with MPD-TMC membranes. These results suggested contorted monomer geometry of triptycene improves micropore volumes of resulted

polymers, which enhanced only small solvent molecule permeability. According to CO2 gas adsorption experiments both MPD-Trip and MPD-TMC polymers have < 4 Å pore sizes derived from DFT model, while MPD-Trip had higher gas uptake than MPD-TMC. MPD-Trip membranes have ~9 L m^{-2} h^{-1} bar^{-1} water permeance, ~25 L m^{-2} h^{-1} bar^{-1} acetone solvent permeance and are stable in most mild solvents including hexane and acetonitrile.

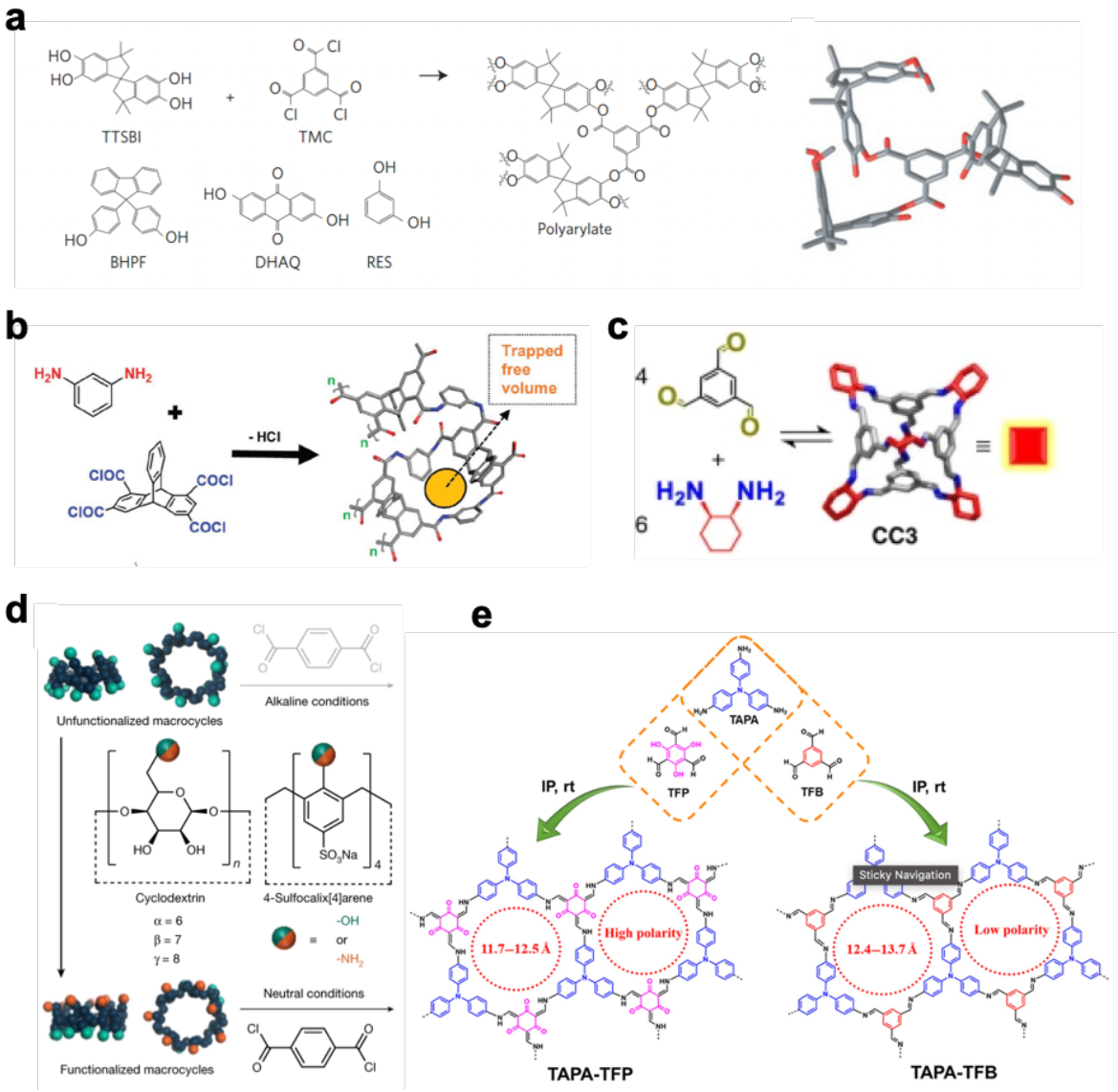


Figure 6. Microporous polymer thin films prepared from interfacial polymerization by applying, a. contorted monomers such as TTSBI and BHPF, b. commercial MPD and triptycene acyl chloride, c. connected cage molecules, d. cyclodextrins with asymmetric hydrophilicity, e. commercial COF precursors synthesized into 2-D ordered COF structures.

Conventional MPD-TMC polyamide nanofilm membranes synthesized from IP only had ~2.7 L m^{-2} h^{-1} bar^{-1} water permeance. MPD-Trip has slightly lower NaCl ~ 96% of rejections than MPD-TMC membranes with ~ 99% and identical cut-off with MPD-TMC. (Fig. 7a, 7b, 7c) It was discovered that

conventional in situ interfacial polymerization of MPD-Trip polymer gives crumpled surface texture which improved active membrane areas for permeation, which is consistent with MPD-TMC film morphology behaviours. This result suggests crumpled morphology is more correlated with amines rather than acyl chlorides.

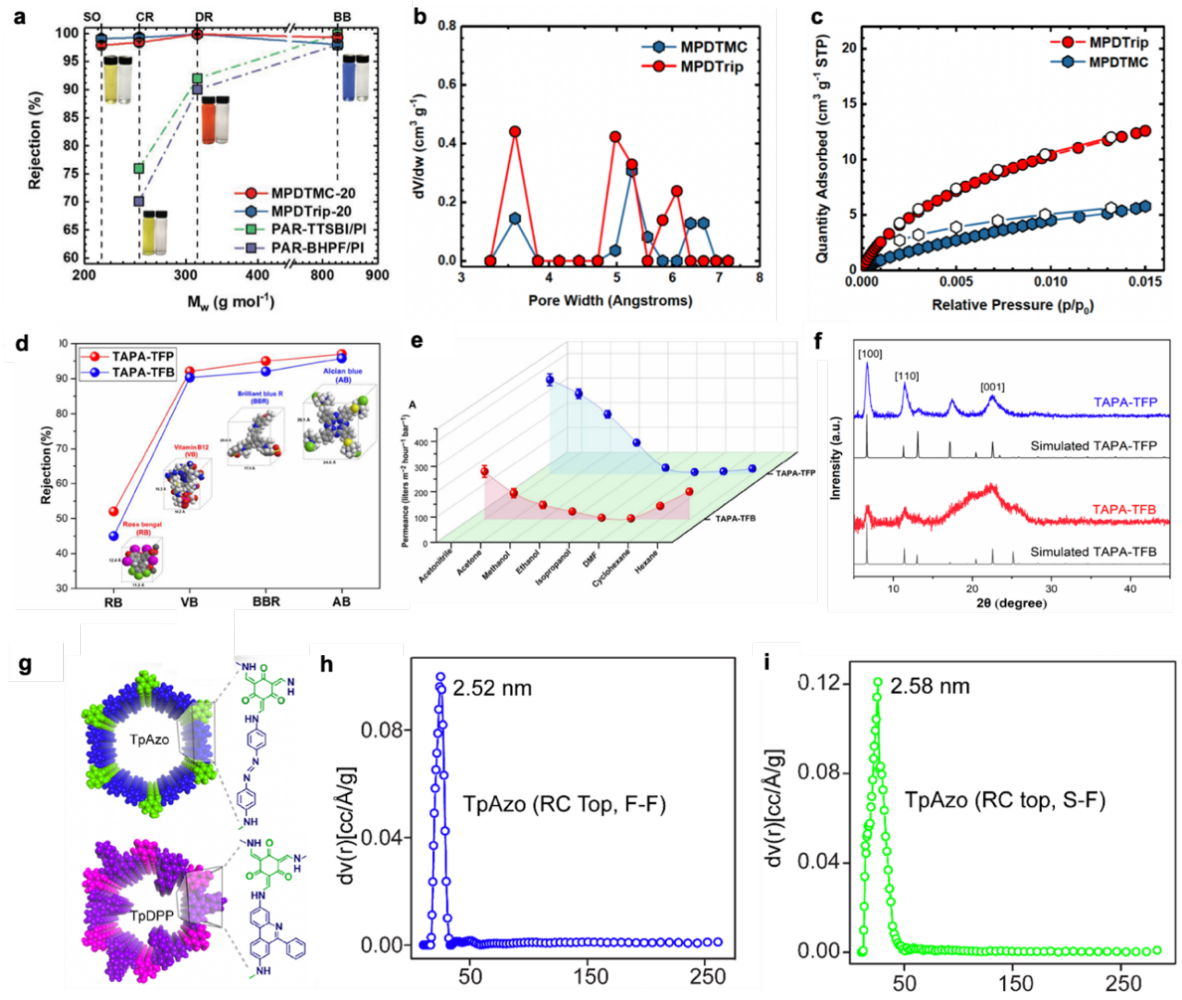


Figure 7. Separation performances and pore sizes of 2-D thin films and 3-D networked PIM membranes. a. Dye rejections in MeOH solvent using MPD-TMC, MPD-Triptycene, TTSBI-TMC polyester, BHPF-TMC polyester membranes in nanofiltration. b. BET pore size distributions derived from CO2 adsorption isotherms of MPD-TMC and contorted MPD-Triptycene polymers. c. CO2 gas adsorption isotherms. d. Dye rejections of 2-D TAPA-TFP and TAPA-TFB self-standing COF films in acetonitrile solvent in dead-end filtration. e. Solvent permeances of 2-D TAPA-TFP and TAPA-TFB COF films in nanofiltration. f. XRD spectrums of reported TAPA-TFP and TAPA-TFB COF thin films. g. Molecular structures 2-D COF membranes reported by Banerjee group. h and i, Pore size distributions of Tp-Azo COF films synthesized from fibre-to-film and sphere-to-film methods.

Apart from amorphous polymers IP reaction can also be applied in semi-crystalline polymer nanofilm synthesis. In 2020 Jiantao Liu and others reported a one-step synthesis of self-standing COF nanofilms.[124] Unlike previously reported IP reactions of amines and acyl chlorides dissolved in separate phases, aldehydes and amines can be dissolved in single DCM phase. An aqueous phase

containing acids was deposited on top of the heavy oil phase to promote interfacial reaction and construction of COF structures. Due to slow reaction rate and reversibility of amine-aldehyde condensation, reaction time scale can go up to several days. It was reported that self-standing COF films are still highly crystalline meaning lamellae stacking and alignment of ordered macrocycles are key to achieving high permeance. Obtained COF films formed from acid-mediated interfacial polymerization were smooth. In pressurized filtration tests, both TAPA-TFP and TAPA-TFB self-standing COF nanofilms achieved up to 300 L $m^{-2}hr^{-1}bar^{-1}$ permeances for acetonitrile, with > 90% rejections of Vitamin B12 and ~50% rejections for Rose Bengal. (Fig. 6e and Fig. 7d, 7e, 7f)

Self-standing COF thin films have also been reported to have promising molecular sieving effects in gas separation with well-defined sub-nano pores.[125] Self-standing COF film formation mechanism was studied from interfacial residue crystallization by Banerjee and others, showing controllable pathways to grow continuous COF films with comparable BET surface area to that of COF nanoparticles ~2093 m^2g^{-1}.[126] (Fig. 7g, 7h, 7i)Self-standing COF film growth was credited to both fibre-to-film and sphere-to-film mechanisms. Both COF particles and thin films had identical peak positions in XRD spectrums, meaning synthesized COF films are highly crystalline preserving geometrical configuration and stacking. Reported self-standing COF films are considered as benchmark 2-D polymeric membrane materials due to macrocycle alignment and stacking. More importantly, unlike most polymer materials with multiple observable peaks in pore size distributions from DFT models COF thin films surprisingly exhibited very uniform pore sizes and single peaks. Despite the full width half maximum (FWHM) of COF pore size distribution peaks are large, this is already significant progress in promoting uni-pore formation in polymeric materials.

In 2021 Xiaolei Cui and others reported MOF-type membranes synthesized from interfacial polymerization with commercial acyl chloride, which was the first report of interfacial reactions of MOF-type precursors. Resulted membranes have ultra-fast water permeance up to 55.9 L m^{-2} hr^{-1} bar^{-1} and high dye rejection of 99.8%.[127]

Instead of creating pores by inefficiently packing of contorted linear polymer chains or construction of 2-D marcocycles. Porous polymers can also be prepared by directly crosslinking symmetrical monomers but forming 3-D structures. Ai and Zhiwei reported successful preparation of porous organic cage membranes from interfacial polymerization by preparing and crosslinking CC3 cage reagents.[128] Self-standing CC3 thin films were synthesized from IP by dissolving cage reagents CHDA and TFB in water and DCM separately. (Fig. 6c) Resulted membranes succeeded intrinsic cavities of cage structures, and can assume two different phases in different solvents. CC3α-PAN support showed 43.0 L m^{-2} hr^{-1} bar^{-1} water permeance and 55.9 L m^{-2} hr^{-1} bar^{-1} toluene permeance

indicating amphiphilic property. CC3α-PAN membranes showed stable water permeances under different pressures. Cage membranes has rather sharp MWCO around 700 g mol^{-1} which is benefitted from well-defined pore properties of cage molecules. In 2022 Zhiwei and others reported alignment and crosslinking of CD macrocycles at free-interfaces from IP. CD molecules were functionalized with both hydrophobic and hydrophilic groups to control film growth at solvent interfaces. (Fig. 6d) This is the pioneering work that shows aligned pores in amorphous polymers enhance performances. Meanwhile, crosslinked CD membranes with aligned pores also showed increasing crystallinity thus shifting out of complete amorphousness. This work implies that uni-pores in polymer matrix can be benefited from ordered structural packing. Resulted CD membranes have good solvent permeances and sharp MWCOs towards dyes. Moreover, CD membranes with well-defined porosity can be applied into continuous CBD separations in continuous cross-flow filtration with high yield.[129]

2.3 Organic solvent filtration membranes

OSN is an emerging process that targets separations of molecules in organic solvents. It has been mainly used to separate molecules < 1000 g mol^{-1}. Previous membranes used in aqueous phase separations can be easily swollen in organic solvents which can cause dramatic loss in selectivity or permanently damage membrane structures. Rising demands of membrane separation in organic solvents call for novel membrane materials with stable performances in solvents.[130] All OSN processes can be divided into three types of separation based on applications, i) Solute to solute separation, ii)Solute to solvent separation, iii)Solvent to solvent separation. Solvent permeances and MWCOs are two most important standards to evaluate OSN membrane performances.

Evaluation of rejections and MWCOs can be dependent on the solutes used during measurements. Over the past decade or so dye molecules are popular solutes for MWCO measurements as they are 3-D molecules with fixed dimensions in solvents. Yet some of the dyes carry negative or positive charges which may interact with membrane surfaces, thus making it inaccurate to measure the intrinsic selectivity of OSN membranes. Other linear solutes such as PEGs and polystyrene have also been used as marker molecules for rejection measurements, but molecular transport through membrane pores is difficult to understand due to coiled or stretched conformation of polymer chains in different solvents. Most recently, separation of active pharmaceutical ingredients (API) and crude oil have attracted significant amount of interests due to rising demands. To design membrane materials for advanced solvent-based separations, structure-performance relationship in membranes urgently demands more insights. To date popular categories of OSN membrane materials include, poly ether ether ketone (PEEK), polyimide (PI), polyvinylidene fluoride (PVDF), polybenzimidazole (PBI), polyamide (PA) and polymers of intrinsic microporosity (PIMs).

2.3.1 Molecular mass transport in organic solvents

Size-exclusions account for most known membrane separations. Molecular species with larger dynamic dimensions could not enter the bulk of membranes thus will be fully rejected, those with smaller dimensions will be transported.[131] Membranes may have different swelling ratios in different solvents which alter membrane pore properties, thus membranes may have different rejections of identical solutes in different solvents. In most organic solvent dispersion systems solutes are rarely associated with solvent molecules, as most common organic solvents have much lower polarity and dielectric constants than water. Only few organic solvents have larger dipole moments than water.

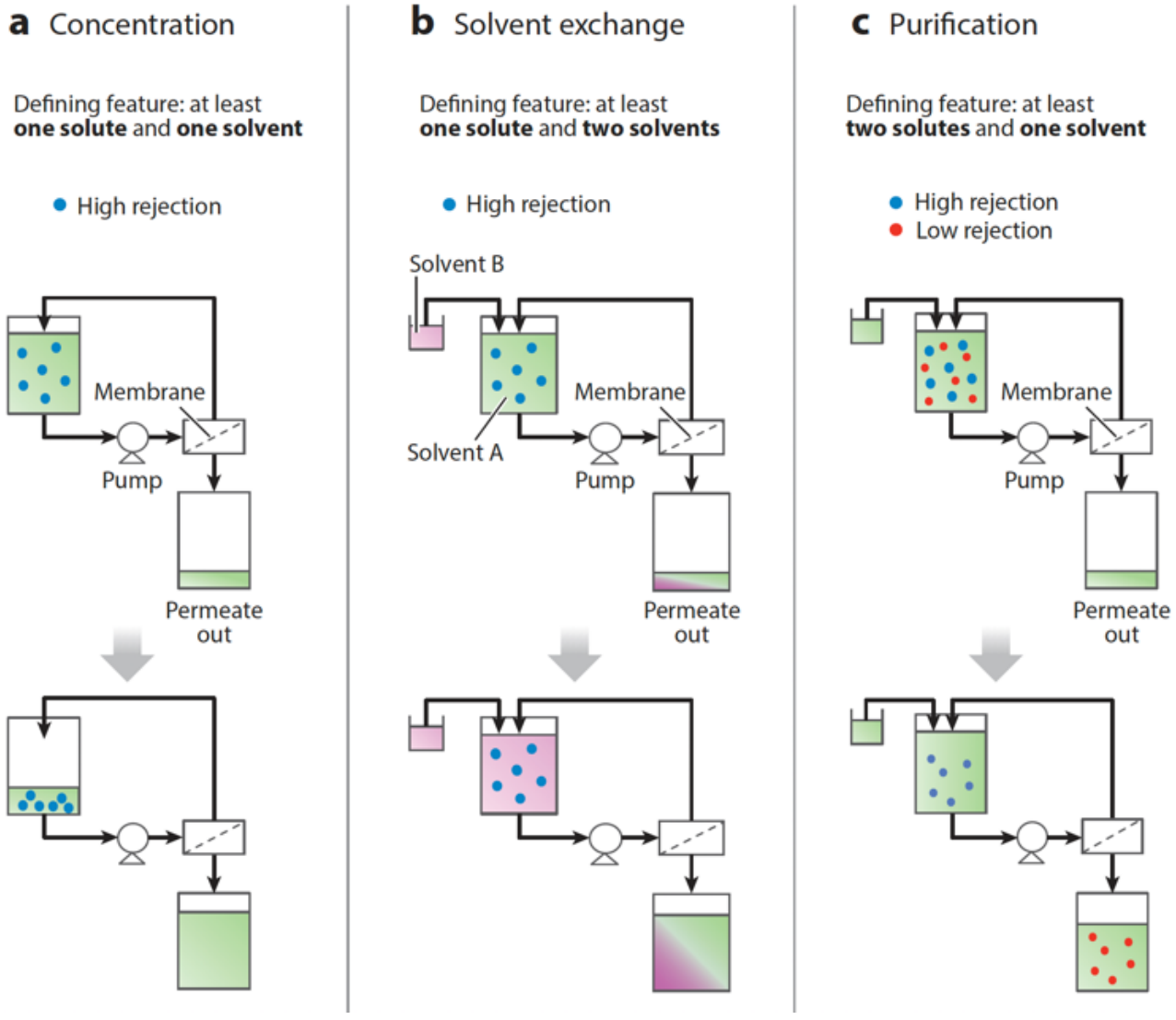


Figure 8. Organic solvent filtration can be divided into a few categories including concentration, solvent exchange and purification applications.

Dynamic radius of solutes dispersed in organic solvents do not have significant changes. All existing OSN processes can be largely categorized as three types, i)solute concentration, ii) solvent exchange, iii) solute purification.[132] (Fig. 8) All currently summarized OSN processes require membranes to be either super permeable to solvents or tight enough to give 100% rejections towards solutes, and ideally both of course. In which case solute to solute separation and solute to solvent separation must be both maximized to achieve highest yields and product purity.

Solvents used in OSN usually refer to small molecules below 100 g/mol, most OSN membranes are permeable to molecules with molecular weights on this scale. Rejections of molecules are primarily measured from abstracting ratios of solute permeate concentrations over feed concentrations. Surface open pore properties are of vital importance regarding size-exclusion effects. Species with large dynamic radius than surface pores could not even enter bulk of membranes, thus will always be given 100% rejections. This value should best represent the lower bound of one membrane overall rejection performance, meaning any molecules larger than this dimension should as well be fully rejected. Dimensionally smaller molecules will enter surface pores then subsequently traverse through interconnected free volumes in the bulk. Meanwhile measured rejections are also affected by adsorption.[133] Adsorptive membranes usually have high solute/solvent uptake and require regeneration treatment.[134] Mass loss due to adsorption can also yield 100% membrane 'rejection' selectivity, but these measured rejections are not associated with molecular dimensions and do not represent membrane intrinsic pore selectivity. It is worth noting here ideally size-excluded molecules should always be given 100% rejections from membranes, those not excluded should always have 0% rejections. According to empirical measurements reported for most membranes, this is not true as bulk resistance from membranes also provided rejections. Patricia and others proposed a figure of merit to mathematically visualize solute to solute selectivity, where maximum solute A to solute B selectivity is no more than 100% based on the assumption that membrane has 0% rejection for solute A and 100% rejection for solute B. This implies that selectivity of all existing membranes have not yet been maximized.

Membrane swelling is an important factor in filtration in organic solvents. As extensively swollen membranes in solvents have much larger pores which influence size-exclusion effects in separation. Polymer chains are more dynamic due to solvation. Both linear polymers and crosslinked polymers have tendency to dissolve in solvents. Linear polymers do not have crosslinkages between polymer chains to obstruct chain relaxation and solvation.[135] Crosslinked polymers do not dissolve in solvents due to existence of crosslinking sites to form macromolecules with ultra-high molecular weights. Covalently bonded networked polymers do not have specific molecular weight per chain unit and will not be dispersed in solvents. Hansen solubility parameter has been used to model solvent

transport and extent of membrane swelling in solvents.[136, 137] Swelling of networks can remove residue oligomers that are trapped in the matrix and re-orient matrix for improved performances. Polyamides have severe swelling in DMF, but low swelling in other aprotic solvents such as acetone or acetonitrile. Conventional MPD-TMC membranes have low rejections in DMF and high DMF solvent permeance, but high rejections in water and low permeance. (Fig. 9) Swelling of OSN membranes is not preferred due to shifts in membrane free volumes and hence selectivity. But membrane swelling in certain solvents can be used to activate membranes for performance enhancement.[138, 139]

Since most amorphous polymeric membranes do not have uniformly distributed pores or free volumes for mass transport, thus reported MWCOs of polymeric membranes are usually broad due to non-uniform pore size distributions. This is notably true for amorphous membranes where disordered structures do not lead to uniform pore size distributions as a result of thermodynamic molecular motions. Non-uniform pore size distributions are not desirable for maximizing selectivity. It is difficult to design such amorphous membranes to separate specific molecules with similar dimensions. Instead of porosity manipulation other methods have been reported to enhance selectivity.

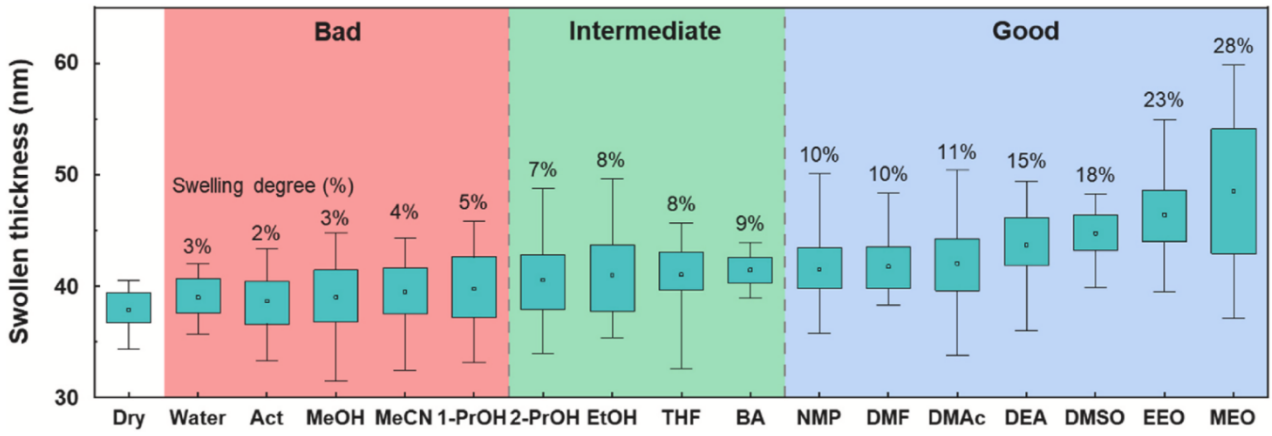


Figure 9. Swelling degrees of membranes in organic solvents. Swelling of membranes does not necessarily restricted to polar solvents, but is rather dependent on solubility of the membrane materials in solvents. (reprinted from reference 136)

Donnan exclusion effect describes contribution of charges in membranes towards separation. If the membrane surfaces include ionizable functional groups such as -COOH, membrane surfaces can be deprotonated and thus negatively charged giving higher rejections towards negatively charged solutes due to dielectric effects. In these cases, Donnan dielectric effects contribute to hindering mass transport of negatively charged molecules, but have minimal effects towards permeation of neutral molecules.[25] Adopting this strategy there have been a few reports on modifying amorphous membrane surfaces with charges to improve rejections.[140, 141] However, charged surfaces may

result in heavy adsorption of oppositely charged solutes. The adsorbed charged solutes further reduce membrane permeances and increase rejections due to pore-filling effect, which blocks permeation of all molecules. Positively charged membranes surfaces can improve membrane rejections towards monovalent and divalent ions in desalination, but may have heavy adsorption of negatively charged molecules in OSN dye filtration process causing mass loss in solute concentration process.[142] Electrostatically adsorbed molecules can't be easily removed from membrane surfaces. Charging membrane surfaces is not always the best solution especially for charged multi-component resource recovery processes.

Liquid flow dynamics near membrane surfaces also affect mass transport. In dead-end filtration processes rejected molecules accumulate and deposit near membrane surfaces leading to concentration polarization, which decreases membrane rejections as well as permeances.[143, 144] Under medium flow rate in cross-flow filtration processes, tangential or angular stream flow patterns are created near membrane surfaces thus can efficiently remove filter cakes and mitigate concentration polarization.[145, 146] However, under high flow rate liquid streams bypass membrane surfaces quickly thus could not create effective tangential flow on site. Under low flow rate liquid streams could not create strong enough tangential flow for filter cake removal. Crossflow can be coupled with rotations or be operated under high temperature to process viscous or suspensions such as mud slurry.[147]

2.3.2 Phase inverted membranes

Phase-inversion is a popular scalable technique to cast large area of membranes.[148] The process features dissolution of polymers in a good solvent, followed by membrane casting and solvent exchange in a bad solvent. Selected polymers are not soluble in the exchange solvents, polymer chain relaxation is quickly stopped in the exchange solvent environment leaving unoccupied free volumes in precipitated condensed solids. Most polymers based on hydrocarbon backbones have poor solubility in water, water has been mostly used as the exchange solvent to precipitate polymer solids on substrates. Solvents used during phase inversion can affect membrane porosity and morphology. Addition of acetone solvent in PVDF dope solution in phase inversion decreased PVDF membrane porosity and increased crystallinity.[149] Concentrations of casting dope solutions have the greatest effects on membrane separation performances, which directly affects porosity and density of membranes. [150] Lower dope solution polymer concentrations caused membranes to have lower rejections and higher permeances. Most importantly, phase inversion process for membrane casting require the polymers to be solution processable. Hence crosslinked polymers, which are usually not

solution processable, would not fit in such process. Crosslinking of PIMs enhance consistent separation performances in solvents and water. (Fig. 10)

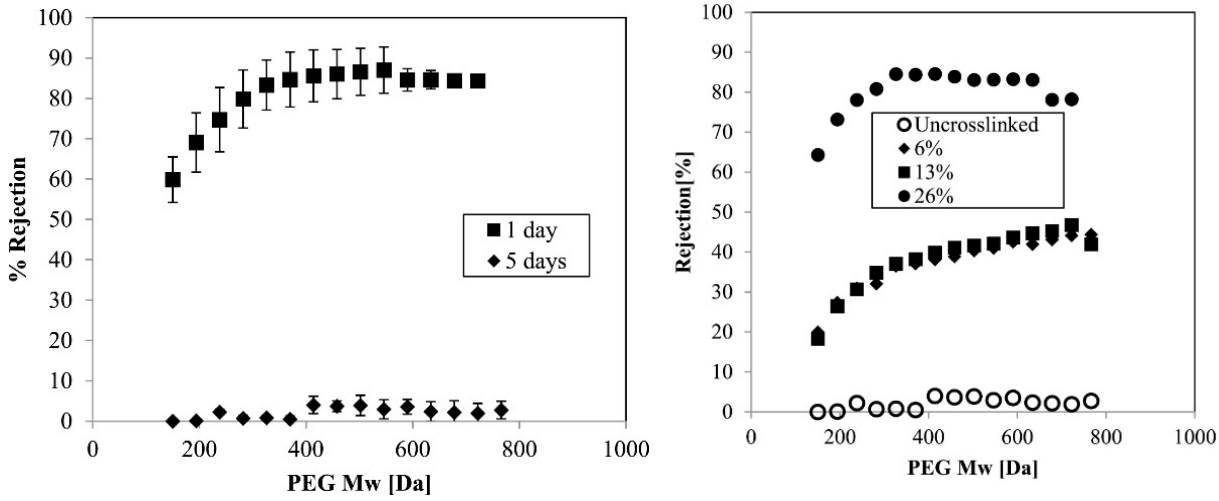


Figure. 10 Left: PEG rejections of TB-OH PIM membrane in water and PEG rejections of same membrane after 5 days of water treatment. Right: PEG rejection comparison of crosslinked TB-OH membranes with different crosslinker weight percentage and uncrosslinked TB-PH membranes. (reprinted from reference 104)

PIMs are promising microporous materials in terms of scalable casting and separations. Over the past decade there have been increasing reports of PIM polymers in liquid separation.[151] Jin and others successfully obtained MWCO of AO-PIMs-1 in EtOH solvent, AO-PIM-1 TFC membrane has 15.5 L m^{-2} hr^{-1} bar^{-1} ethanol permeance with MWCO around 600 g mol-1 and comparable Rose Bengal rejection with commercial Starmem240.[152] AO-PIM-1 dope solution was spin-coated on water-saturated PAN support, thus local phase inversion helped PIMs solids quickly condense. Over a few weeks of filtration AO-PIMs-PAN TFC membranes had stable solvent permeances, meaning linear AO-PIM-1 membrane swelling in solvents and compaction under pressure can eventually reach equilibrium. PIM TFC membranes can also be prepared directly from dip-coating. A type of PIM-PAN TFC membrane was reported from dip-coating and solvent vapor annealing approach. Resulted membrane has 93.7% rejections of Methyl Orange (327 g mol^{-1}) and 4.3 L m^{-2} hr^{-1} bar^{-1} ethanol permeance.[153] These results are consistent with sub-nano level porosity of PIMs. Degree of swelling can dramatically influence membrane performances, yet there have been few reports of applying PIMs in organic solvent filtration in other solvents. To restrain PIMs membrane swelling, crosslinking is effective in preparing solvent-resistant PIMs. Praveen and others reported crosslinking of PIM-TB-OH and performances of crosslinked PIM-TFC membranes in water. Uncrosslinked PIM-TB-OH lost PEG rejections after swelling for 5 days in water, where crosslinked PIM-TB-OH

maintained > 70% rejections of PEG-200 after 5 days of swelling in water. Gao and others reported crosslinked PIMs with thioamide groups using TMC as crosslinker.[154] Thioamide PIMs had > 90% rejection of Brilliant Blue R with MW of 627 g mol^{-1} and 3 L m^{-2} hr^{-1} bar^{-1} ethanol permeance. Impressively, crosslinked PIMs showed 97% rejection of Rose Bengal (974 g mol^{-1}) and permeance of 12.4 L m^{-2} hr^{-1} bar^{-1} in acetone. This indicates crosslinking between PIM polymer chains enhanced solvent endurance and constrained swelling.

PIMs-1 can be functionalized with other functional groups. Nitrile groups on PIM backbone can be converted into -COOH groups using sulfuric acid and acetic acid under ~100 degree. Amidoxime-functionalized PIMs are easier to be chemically modified than PIMs with nitrile groups. AO-PIM-1 can be converted into C-PIMs with -COOH side groups to enhance hydrophilicity and separation performance.[155] PIMs concept were extended regarding backbone chemistry, where ladder-like contorted linear polyamides and polyimides with ~550 m^2 g^{-1} surface area have been successfully synthesized and processed in solvents.[13]

Conventional Poly ether ether ketone (PEEK) was synthesized from 4,4'-difluorobenzophenone and hydroquinone. However, PEEK solvent permeance is generally low due to efficient packing of polymer chains compressing free volumes, existing PEEKs are expensive to process limiting broader use.[156] However, PEEK membranes are durable and mechanically robust even in harsh organic solvents. Yet poor processability of PEEKs is difficult to resolve, as PEEKs are only soluble in strong acids and can form crystallines. [157] Contorted PIM-type building blocks were introduced in PEEK synthesis to enhance porosity and performance. Abdulhamid and others reported applications of spirobisindane, Troger's base and triptycene derivative contorted structures as backbone building blocks to synthesize microporous PEEKs.[158] Resulted contorted PEEKs had surface area of 205-250 m^2 g^{-1}. MWCOs of contorted PEEKs can be tuned from 450 g mol^{-1} to 845 g mol^{-1} with solvent permeance up to 11.1 L m^{-2} hr^{-1} bar^{-1}. Along with introduced chain contortion of PEEKs crystallinity was reduced because of inefficient chain packing, processability was dramatically enhanced. Compared with polyimide and polybenzimidazole PEEKs showed anti-aging property even in DMF at 140°C.[159] Pore structures remained unchanged over DMF treatment.

Asymmetric membranes consist of multiple layers with different structures but formed from same materials. Sponge-like structures induce high rejections and low fluxes, while finger-like pores induce low rejections and high fluxes.[160] Polyimide (PI) asymmetric membranes are durable and highly selective in organic solvents. Asymmetric PI skin layers have low resistance and high rejections for organic molecules. PIs are thermally stable until 500°C according to TGA and can be easily casted via immersion precipitation, also referred to as phase inversion.[161] Reported asymmetric polyimide

membranes have nominal MWCOs from 230 – 700 g mol^{-1} in toluene, and are more permeable to aromatics than non-aromatics.[162] To improve membrane stability in organic solvents, crosslinking has been used to prevent polymer dissolution. Aliphatic diamines were used By See-Toh and others to crosslink integrally skinned Lenzing P84 polyimide membranes.[163] Crosslinked P84 membranes had low MWCO < 400 g mol^{-1} and DMF permeance up to 8 L m^{-2} hr^{-1} bar^{-1}, with outstanding stability in THF, DMF and n-methyl pyrrolidone. Crosslinking agents used such as 1,2-ethylene diamine are cheap and easy to obtain, making amine-crosslinking process more up-scalable. Matrimid membranes were crosslinked using p-xylylenediamine, crosslinked polyimides were stable in DMF and DMSO with ~ 98% dye rejections and 5.4 L m^{-2} hr^{-1} bar^{-1} harsh solvent permeances.[164] Crosslinked PI prepared from diacetylene additive enhanced solvent resistance and had comparable gas separation performances with PI before crosslinking.[165] See-Toh and others reported crosslinked P84 PI membrane with controllable MWCOs which covered broader range of molecular separation, where co-solvent 1,4-dioxane added in dope solution affected membrane structures hence rejections.[166] A brief summary of existing OSN membranes is given. (Table. 2)

Table 2. Popular organic solvent nanofiltration membranes directly prepared on backing support or on ultrafiltration supporting substrates.

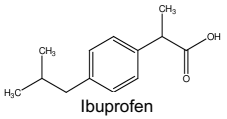
Membrane	Application solvents	Support
PIM	Water, alcohol, non-polar solvents	PAN/non-woven
PEEK	Water, acids, almost all organic solvents including DMF, THF, DMSO	Non-woven
X-PI	Water, almost all organic solvents including DMF, THF, DMSO	Non-woven
PVDF	Non-polar solvents.	Non-woven
X-PBI	Water, organic solvents including DMF	Non-woven
PA	Water, milder solvents such as acetone, acetone, alcohol	PAN, PSF etc.

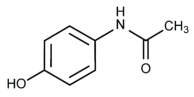
Other popular OSN membranes include Poly(vinylidene fluoride) (PVDF) membranes and PBI membranes also found wide application in solvent filtrations. [167-169] Crosslinking of preformed membranes all showed enhanced solvent durability and selectivity in nanofiltration. Functionalization of filtration membranes with ion-exchange groups also exploited their potentials as ion exchange membranes.[170]

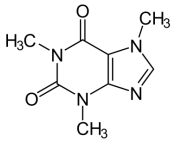
To date application of membranes in organic solvents is demanding due to uprising energy crisis globally. Low-carbon policy throughout Europe, Asia and America greatly invigorated membrane technology research to reduce carbon emissions and reduce energy consumption in separation. A list of commonly used solutes and solvents reported in literatures is given here to help summarize progress of filtration in organic solvents. To date crosslinked polymers are preferable for solvent filtration use, such as crosslinked PBI, crosslinked polyimide and crosslinked polyamides. Chiral species such as active pharmaceutical ingredients and amino acids drew greater interests as solutes. More recently, water-oil separation and hydrocarbon separations using hydrophobic membranes are of significant interests.

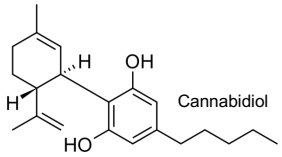
Most of emerging OSN membranes reported especially in academia used dye molecules as markers, this is due to dye molecules have stable 3-D structures. Most dye markers are commercially available and it is easier to visualize and analyze dye solute concentrations directly via UV adsorption. More importantly, it is more sensible to compare different membrane performances towards same category of solutes or solvents. It can be inferred from here that dye molecules will remain standard solutes to compare OSN separation performances for some time before a unified application is raised. However, dye molecules are of less interests to industrial applications right now with constantly emerging new membrane technologies for other solutes. A list of solutes and solvents that have been most reported in membrane separation is given as follows,

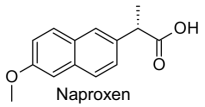
APIs

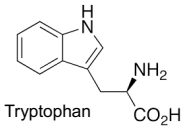

Ibuprofen

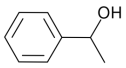

paracetamol

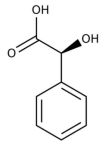

Caffeine

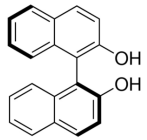

Cannabidiol

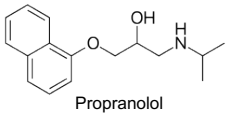

Naproxen

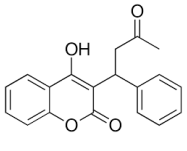

Tryptophan

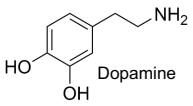

Phenyl ethanol


Mandelic acid

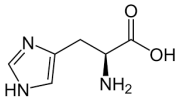

Binol

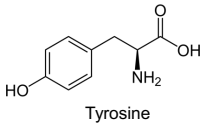

Propranolol

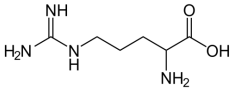

Warfarin

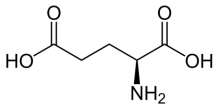

Dopamine

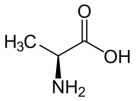
Amino acids

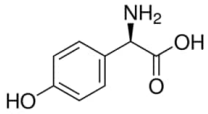

Histidine

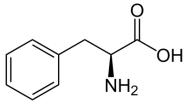

Tyrosine


Arginine


Glutamic acid

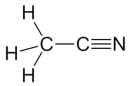

Alanine


P-hydroxylphenyl glycine


Phenyl alanine

Common solvents


Acetone


Acetonitrile

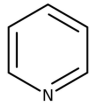

Methanol

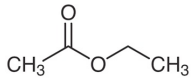

Ethanol


Isopropanol

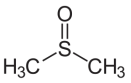

Hexane


Dimethylformamide

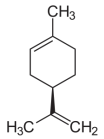

Pyridine

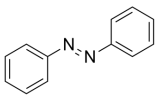

Ethyl Acetate

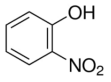

Tetrahydrofuran

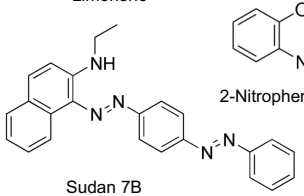

Dimethyl sulfoxide

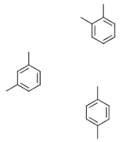
Other organic molecules

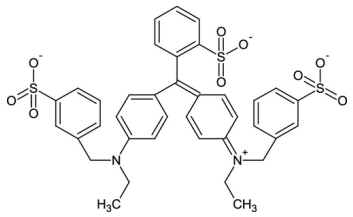

Limonene

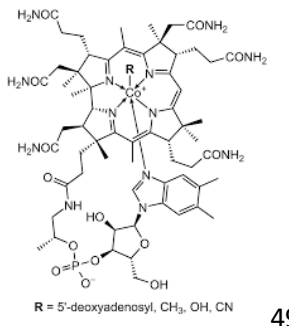

Azobenzene


2-Nitrophenol

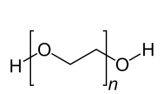

Sudan 7B


Xylene isomers

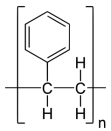

Brilliant Blue


Vitamin B12

R = 5'-deoxyadenosyl, CH_3, OH, CN


Polyethylene glycol


Toluene


Polystyrene

Phenylethylamine

Methyl orange

Acid Fushin

Rose Bengal

2.3.3 Composite membranes

A thin-film composite membrane consists of at least two or more layers. In general, a typical TFC membrane is fabricated by combining a selective layer and support layer. The selective layer accounts for the separation performances and support layer mechanical strength. In NF and RO TFC membranes' support layers are usually based on polyacrylonitrile and polysulfone, which are ultrafiltration membranes themselves. For TFC membranes with ultra-thin skin layers, a gutter layer is usually fabricated between the skin layer and support layer to avoid pore penetration. Selective layers in TFC membranes are usually synthesized via interfacial polymerization. In order to avoid layer delamination, other approaches such as crosslinking skin layers and support surfaces have also been explored. But grafting selective layers onto supporting membrane layers can be challenging as surface of supporting layer needs to be chemically active. It is difficult to control selective layer properties via this approach, which can be heavily influenced by surface modification chemistry and reactivity of functional groups.

PIMs can be hydrolysed to yield PIM-COCl which can subsequently react with amine-functionalized polyacrylonitrile to form composite membranes.[171] PIM-PAN composite membranes showed > 94% rejections of crystal violet (CV) and high ethanol flux. Without functionalization PIM-1 can be directly blended with other polymers such as Matrimid. Matrimid-PIM-1 blend was dip-coated onto P84 support to fabricate TFC membrane, coated blend layer showed enhanced selectivity between riboflavin and isatin.[172] Apart from mixing or coating surfaces with selective layers, interfacial polymerization is the dominating technique to prepare thin film composite membranes both continuously or batch-wise. [173]

MPD and PIP were most commonly used as reagents to react with TMC to form selective layers on top of support substrates from interfacial polymerization. Polyamide TFC membranes generally have high rejections in water and most organic solvents, and are scalable for a variety of applications. MPD-TMC and PIP-TMC TFC membranes are hydrophilic and have > 90% rejections towards almost all organic molecules > 200 g mol^{-1}. Tight membranes with low MWCOs as such do not have satisfactory separation performances in hydrophobic solvents and for precise molecular grading of molecules with 200 – 1000 g mol^{-1}. MPD-TMC membranes even with crumpled surface textures have <1 L m^{-2} hr^{-1} bar^{-1} permeance for hydrophobic solvents such as heptane. Maria and others pioneered the work of directly reacting PIM-type monomers with crosslinker TMC. BHPF -TMC on crosslinked PI support has up to 8 L m^{-2} hr^{-1} bar^{-1} methanol permeance and MWCO of 300 g mol^{-1}, TTSBI-TMC on crosslinked PI support had up to 6 L m^{-2} hr^{-1} bar^{-1} methanol and MWCO of ~ 310 g mol^{-1}. TTSBI-TMC on PI support showed ~ 99% rejection towards Crystal Violet (408 g mol^{-1}) but only ~ 70% rejection for Chrysoidine (249 g mol^{-1}). This work suggests TFC membranes with microporous skin

layers have vast potential for separating solutes of different molecular weights in NF. In addition, it should be noted here existing PIMs membranes can be both casted by phase inversion and spin-coating. Spin-coated PIMs membranes can be readily transferred onto support to prepared TFC membranes as well.

2.4 Chiral separation membranes

Chirality is closely associated with all organic living individuals, both biologically and toxicologically. [174] Chiral separation is crucial especially regarding organic synthesis, biological ingredient separations and pharmaceutical productions.[175-177] It is a resolution process to separate enantiomer pairs in different streams or enrich only one enantiomer in the collecting phase. In pharmaceutical industries, drug enantiomers have different potency when consumed by patients. Yet most of drugs to treat heart diseases or even COVID-19 were sold as racemates.[178] While one drug enantiomer functions as therapeutic agent to treat diseases, the other enantiomer can be harmful to patient's biological systems.[179, 180] Eutomers are considered as the primary active components and distomers are not desirable. Impotent distomers should be preferably removed from products. With same dose of drugs, 100% of eutomer composition can achieve 200% potency compared with racemates. Since enantiomers have almost exactly same properties, separation of racemic mixtures is extremely difficult and costly. Industrial separation of enantiomers often includes multi-stage chromatography operations using different columns and large amount of solvents. (Fig. 11) Thus enantio-pure drugs are very expensive and normally not affordable to majority of population. Instead of chromatography and recrystallization, low-cost green technologies must be developed to reduce chiral separation net-costs.[181]

Separation of enantiomers using membranes have been reported feasible traced back from 20 years ago. Up to 2022 both chiral membranes and achiral membranes have been reported for chiral separation. Yet the specific separation mechanisms in these membranes are still not fully understood. It is difficult to design membranes to separate specific chiral molecules on demands. Due to unstable performances of membranes there are no established chiral membrane separation technologies. Sorbent membranes usually require unit restoration. Most reported diffusion-based membranes do not possess stable selectivity under filtration. Inspired by natural systems where chirality broadly exists, community has focused on preparing chiral membranes for stereoisomeric separations. Chiral membranes can be prepared from both natural chiral molecules and artificial reagents. [182]

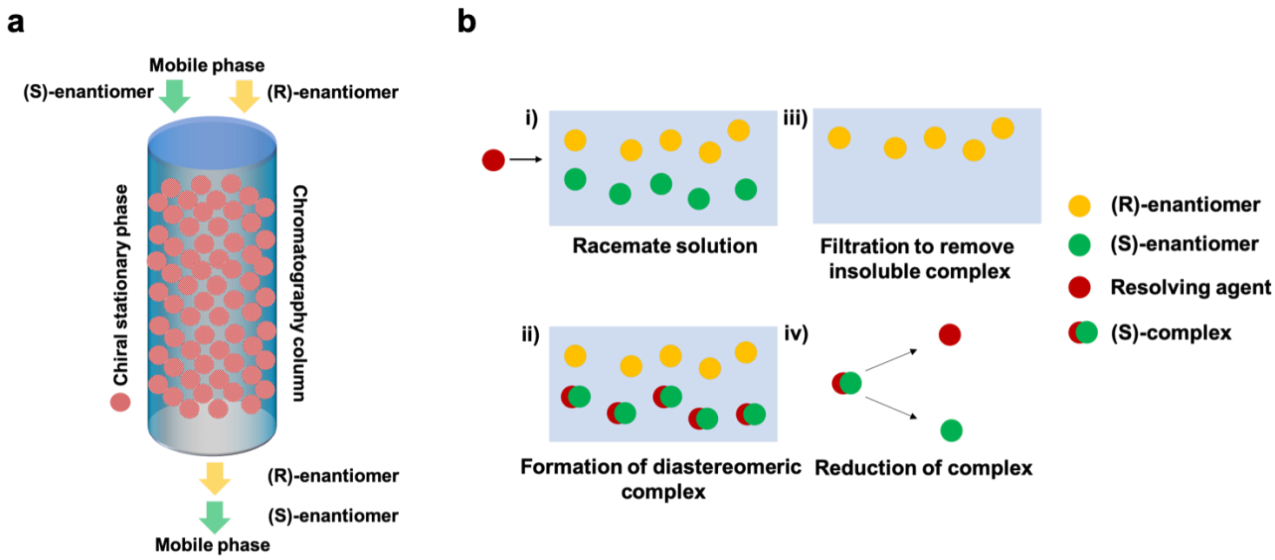


Figure 11. a. Chiral separation using columns and chiral stationary phase. Mobile phase will carry both enantiomers through the chiral column, each enantiomer has different retention time in the column hence high purity enantiomers can be collected from the permeate side of the column. b. Racemates are first dissolved in solvents, a resoling agent is added into the solution which will selectively bind with one enantiomer forming diastereomeric complex. Diastereomeric complex usually have low solubility in the chosen solvents, thus can be removed by filtration or methods alike. Pure counter enantiomer can be obtained dissolved in the solution.

2.4.1 Organic chiral molecule mass transport through membranes

Membrane-based chiral separation requires the membranes to selectively transport only one enantiomer molecule rather than the other, which is an advanced type of molecule to molecule separation. Since enantiomer pairs have identical functional groups, molecular dimensions, boiling points as well as other physical properties, conventional size-based separation mechanism will no longer suffice. The signature difference between enantiomer pairs is atomic orientation in non-superimposable configurations. Separation of organic chiral molecules in organic solvents using membranes are majorly based on steric effects, meaning guest enantiomers interact with membranes differently due to specified functional group orientations.[183] (Fig. 12) To achieve this, membranes need to have surface or bulk structures with special atomic orientations for selective binding. The most straightforward method to achieve such special atomic orientation is to synthesize chiral membranes to separate chiral species.

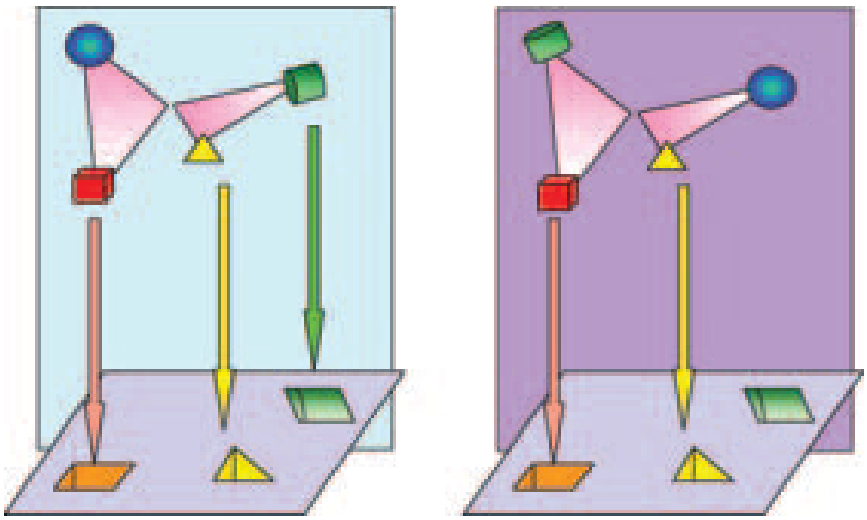


Figure 12. Chiral separation mechanism based on selective binding of guest enantiomers and separation media. Due to different spatial orientation one enantiomer interacts strongly with selector surface while the counter enantiomer interaction is weak. This was interpreted by Berthod resembling a 'LEGO' fitting process.

In general, two different mass transport strategies can be summarized in selective chiral mass transport in membranes, i)retarded transport of counter enantiomer, ii)facilitated transport of desired enantiomer. Membranes can be functionalized with chiral side-chains or adsorption sites to bind with counter enantiomer, allowing the desired enantiomer to diffuse at optimal rate. In the other case membranes can be modified at surfaces to allow faster dissolution of desired enantiomer and diffusion, while counter enantiomer dissolves and diffuses at normal rate. A variety of membranes based on natural chiral molecules and artificial chiral materials have been uncovered. To date chiral separation in membranes are summarized to be based on chiral adsorption and desorption mechanisms. [184, 185] Chiral molecules are considered to have been selectively adsorbed by the membranes or selectively desorbed which will lead to eventual selective permeation through membranes.

In both non-porous and porous membranes chiral permeation selectivity is controlled by two stages, surface adsorption and bulk transport. Non-chiral membranes can be functionalized to only have chiral surfaces, thus selective enantiomer surface interaction is the control step. Enantiomers are adsorbed into chiral surfaces at differentiated rates but will be transported in the bulk with same rate. Non-chiral membranes can also be doped with chiral selectors such as optically active chiral COFs or MOFs fillers, thus selective enantiomeric diffusion through bulk is the control step. Enantiomers are adsorbed into non-chiral surfaces at same rate but will be transported in the bulk with differentiated rates.

2.4.2 Grafting chiral side chains onto backbones

Most biological molecules in natural environments are chiral, such as amino acids, saccharides, nucleic acids. Cyclodextrin (CD) is a class of molecules with exceptional interests from the community, source of cyclodextrins is abundant in nature and comes from bacterial degradation of starch via enzymic metabolism. CD features macrocyclic structures with multiple chiral carbons in all α,β,γ forms. Chiral separation based on polysaccharides has high selectivity in membranes and columns. Each CD macrocycle has multiple -OH groups linked to each chiral carbon. Plural -OH groups linked to chiral carbons in one single CD molecule provide plural H-bonding cites with guest molecules. CD can be first functionalized then directly grafted on membrane surfaces to control dissolution of drugs by forming inclusion complexes, whilst steric hindrance could also play a role under different synthetic or treatment conditions.[186] CDs can be used for surface modification via covalent bonds. In 2007 Xiao and others reported chiral selective cellulose acetate membrane with CD immobilization on surface.[187] Under static dialysis D-tryptophan preferentially permeated through CD-CA membranes than L-tryptophan with permeation separation factor of 1.1. This study revealed selective binding mechanism of CDs towards amino acid enantiomers. Xiong and others reported amine-functionalized (beta)under bar-cyclodextrin membranes crosslinked with TMC, but no chiral separation performance was studied.[188] Diethylamino-beta-cyclodextrin (EDA-beta-CD) was interfacially polymerized with TMC in situ on commercial cellulose acetate support membrane.[189] CD served as chiral selectors grafted to the PA backbone, CD-PA TFC membrane showed 80.7% BSA rejection and 27.2% enantioselectivity for tryptophan. A type of solvent-resistant chiral thin film composite membrane was prepared using (2-hydroxypropyl)-beta-cyclodextrin as doping selector.[190] HP-beta-CD membrane showed 60 - 80% enantioselectivity in hexane under static diffusion. Additionally CDs can be grafted onto artificial nanochannels in membrane matrix to allow faster transport of drug enantiomers such as (S)-naproxen instead of (R)-naproxen.[191] Simple chiral side-chain grafting on backbone could also contribute to chiral recognition. Monofunctional (-)-(S)-acetoxypropionyl with only one chiral carbon was used as a linear chiral selector grafted onto the backbone of MPD-TMC network by Signh and others.[192] Resulted chiral PA membranes showed ~ 90% selectivity for both arginine and alanine racemates. The mechanism was supposedly due to selective H-bonding between enantiomers and side-chain chiral chromophores.

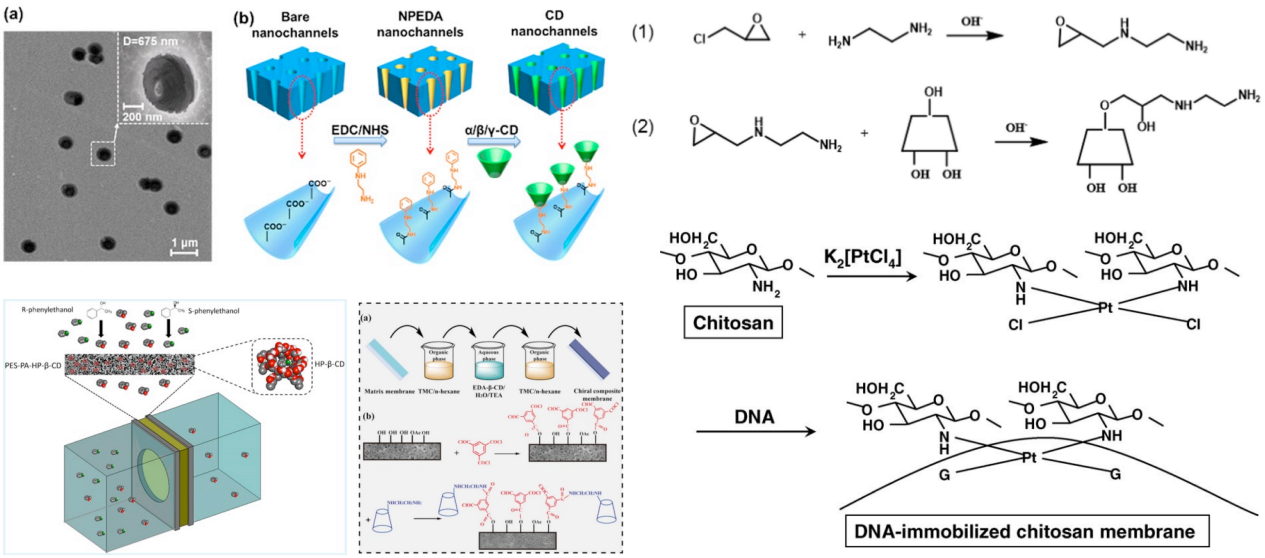


Figure 13. Cyclodextrin-based chiral separation membranes can be designed and prepared via several methods. CD can be grafted onto existing functionalized nanochannels to create chiral nanochannels. CD can also be grafted to functionalized membrane surfaces to create chiral surfaces to promote chiral -selective adsorption. In addition natural chiral polymers such as DNA can also be grafted into bulk of chitosan membranes to create chiral pores due to bulkiness of DNA molecules.

DNA is one vivid example of chiral helical polymers in nature. Yuki and others reported DNA immobilized chitosan membranes for chiral ultrafiltration, as DNA-chitosan membranes had large pores due to bulkiness of immobilized DNA molecules as side groups.[193] (Fig. 13) For DNA-chitosan membranes with > 6.4 nm L-phenylalanine was preferentially adsorbed by the membrane, sorption selectivity disappeared for membranes with pore size <6.4nm. This subsequently indicates chiral side chains can help form chiral pores or channels for selective adsorption of enantiomers into the bulk. Only enantiomers of matching sizes with chiral pores will be preferentially transported.

2.4.3 Direct assembly of optically active building blocks

Instead of grafting chiral side-groups onto the main polymer backbone, chiral building blocks can be directly reacted with other reagents. Chiral segments will thus become repeating blocks in polymer backbones introducing intrinsic chirality. Ingole and others reported polyamide TFC membrane prepared from trans-1,4-diamino cyclohexane and TMC on polysuflone support. Under pressurized filtration chiral polyamide showed >92% enantiomeric enrichment towards arginine in the permeates.[194] Chiral selectivity remained almost constant over permeation time, which implies backbone stereostructure is stable. This work indicates instead of conventional chiral building blocks geometrical stereoisomer can also be used to prepare chiral separation membranes and lead to selective permeation of chiral molecules. Instead of artificial chiral molecules, natural chiral

molecules especially polysaccharides with multiple chiral centres can be used for chiral membrane preparation, as mentioned in the previous section. Kim and others reported crosslinked sodium alginate and crosslinked chitosan membranes in separating tryptophan and tyrosine enantiomers under pressure-driven filtration.[195] Chitosan was crosslinked using glutaraldehyde to form continuous membranes, yielding 98% enantiomer excess in the permeates under low pressure.

Intrinsically chiral long polymer chains can promote unique steric effects such as DNA, where inter-chain and intra-chain interactions can lead to unique structures such as helices. Recently Guo and others reported MOF nanosheets from packing of 1-D chiral helices.[196] A pyridyl group was conjugated D-threonine to form ligand N-(4-pyridylmethyl)-l(d)-threonine-HCl, Zn was used as the metal node to react with conjugated chiral ligand to form 1-D helical metal-organic linear chains. 1-D chains further pack into 2-D lamellar grids via inter-chain H-bonding then into 3-D sheets on nanometer scale thickness. Chiral MOF nanosheets showed as high as 82% enhanced selectivity for $Cr(ox)_3^{3-}$ compared with crystals of 48%. Chiral MOF nanosheets had BET area of 21.3 $m^2 g^{-1}$ which is 5 times higher than MOF crystals only ~ 4.2 m^2 g^{-1}. A type of chiral poly[p-(oligopinanylsiloxanyl)phenylacetylene] polymer have also been reported with unique helical structures due to intrinsic chirality. [197] Yet not all synthesized new chiral materials have not been reported with chiral selectivity in membrane separation.

2.4.4 Filler incorporation and enantiomer templating

Apart from manipulating optical properties in polymers via chemically modifying polymer chains or networks, highly selective chiral fillers can be incorporated into a non-chiral matrix to enhance chirality and performances. Whilst membrane original matrix could be non-chiral, during synthesis or membrane casting filler materials such as chiral COFs or MOF crystals can be incorporated to additionally create chiral centres in membranes.[198]

A type of cellulose acetate mixed matrix membrane using beta-cyclodextrin COF as fillers were reported in 2022. CD-COF MMM showed 100% enantioselectivity towards D,L-tryptophan and enantiomeric excess (ee) of 58.1% for mandelic acid racemates. [199] Homochiral MOF functionalized with CD was used as filler materials in polyethersulfone (PES) matrix.[200] (Fig. 14) With 20wt% loading of CD-MOF fillers CD-MOF-PES membranes showed almost 100% selectivity in hexane of (R)-1-phenylethanol over (S)-1-phenylethanol. Enantioselectivity is stable in hexane rather than in alcohols where selectivity decreased over time, indicating non-polar solvents are more suitable to achieve sustainable chiral separations. Amino acids are among most significant natural chiral species both as reagents and products.

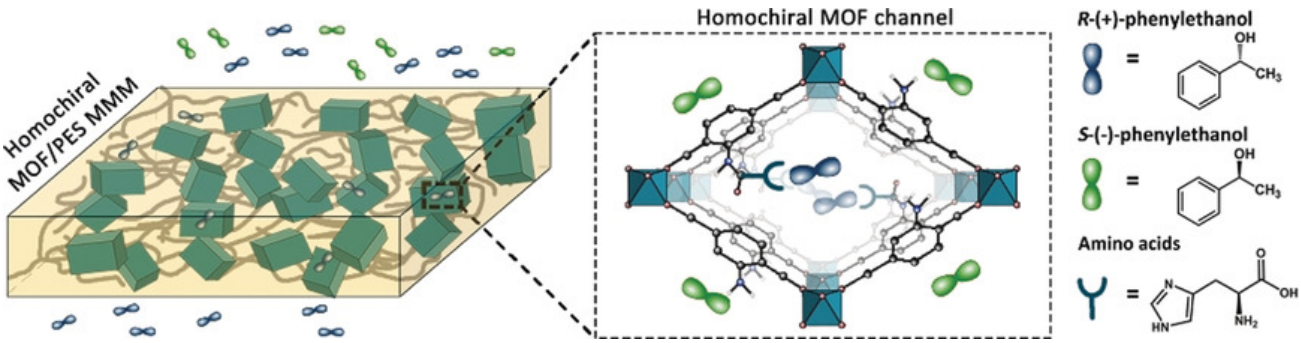


Figure 14. Chiral MOF crystals can be doped into PES membranes to prepare Mixed Matrix Membranes (MMM). (reprinted from reference 201)

In 2019 L-histidine and L-glutamic acids were used to introduce homochirality into MIL-53-NH2 MOF nanocrystals.[201] Chiral MOF crystals were then loaded into PES matrix to fabricate chiral MOF MMM. Chiral MMM showed almost 100% selectivity separating racemic 1-phenylethanol. With 20wt% loading of MIL-53-NH2 MOF into PES matrix, permeation selectivity of MMM decreased very quickly from initial ~100% down to 85% within 8 hrs. (Fig. 15) Interestingly, among three membranes prepared with 10 wt%, 20 wt%, 30 wt% MOF loading 20wt%-MMM showed highest selectivity. This implies permeation selectivity in these MOF MMMs are not completely dependent on sorption selectivity. There should be an optimal point of crystal loading into the matrix to achieve best performances. In 2022 homochiral L-His-ZIF-8 was used as fillers into polyamide(imide) matrix instead of mostly used PES.[202] Up to 25 wt% loading of chiral fillers was incorporated into polyamide(imide) matrix. Chiral separation was achieved in filtration to selectively permeate (R)-phenylethanol over (S)-phenylethanol with a selectivity of ~ 4%. It can be seen from cross-sectional SEM images up to 20 to 25 wt% loading of MOF crystals into polymer matrix that micron-level heterogeneity was introduced. Filler crystals were wrapped by polymers but did not create significant defects in the matrix. It can be deduced that with increased loading of crystals average density of crystal quantities per volume of matrix increased.

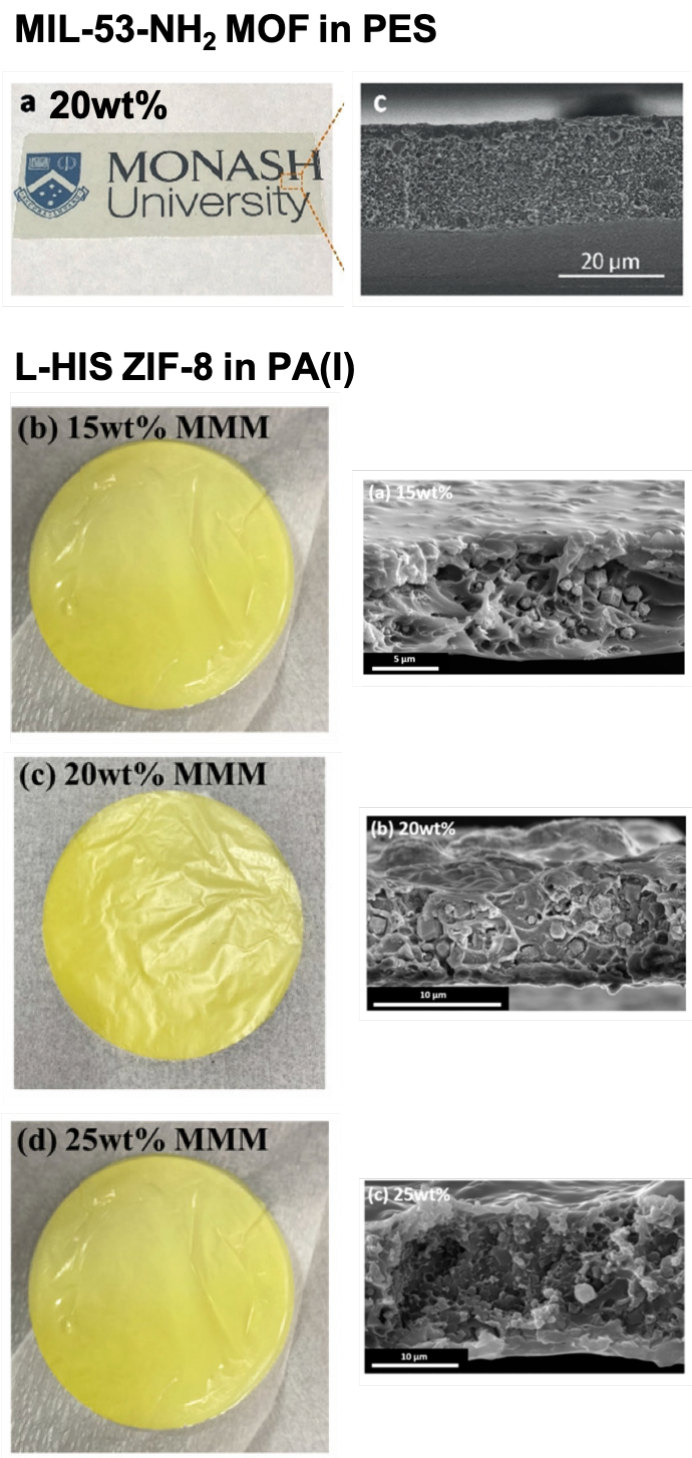


Figure 15. Cross-sectional morphology of chiral MMMs prepared from doping amorphous polymers with chiral MOF or ZIF crystals. As can be seen from cross-sectional SEM images of MMMs doped with different weight percentages of MOF/ZIF crystals, phase separation between amorphous phase and crystal phase is very obvious but within ~ 25 wt% crystal loading membranes were still defect free. Doped crystals were not uniformly distributed in the amorphous polymer matrix.

Molecular templating is one other technique to enhance selective mass transport for different enantiomers. Original polymer was first doped with inert chiral molecule, after membrane casting

inert molecules were rinsed off bulk of membranes leaving templated pores. These templated pores help achieve selective adsorption and/or diffusion for chiral molecules. In 1999 a type glutamic acid molecularly imprinted cellulose acetate membrane was reported by Yoshikawa and others. Z-D-Glu membrane showed preferential transport of D-Glu, while Z-L-Glu membrane showed preferential transport of L-Glu. [203] Separation mechanism was summarized to be selective adsorption from enantioselective electrodialysis. Similarly, D-Glu or L-Glu were also used to template pulysulfone/aldehyde membranes.[204] D-Glu templated PSF-CHO membranes showed preferential adsorption for D-isomers. Instead of templating only membrane bulk to obtain chiral pores with fixed shape, templating can also be performed on surfaces to achieve chiral recognition.[205]

2.4.5 Chiral porous polymers

Despite most reported MMMs showed most promising performances, filler synthesis and loading of fillers can be difficult for scalable preparation regarding costs and manufacturing. Polymeric membranes are cheap in costs, easy to manufacture and simple to process. In order to design high-performance chiral separation membranes, understanding and controlling separation mechanism are important. For chiral non-porous polymeric membranes mass transport is controlled by two stages, thus making materials' chiral structural design more complicated especially on deconvoluting host-guest interactions in each stage. Chiral porous polymers are advantageous within this regard, surface dissolution of solutes is much faster thus bulk transport in chiral porous polymers dominates selectivity. It is easier and more proficient to rationalize chiral separation membranes by simplifying separation mechanism.

Hyper-crosslinked polymers may induce microporosity due to steric effects. A type of chiral hyper-crosslinked polymer was reported in 2020.[206] (Fig. 16) D- or L-phenylalanine was used to react with benzene and FDA, formed polymers had high surface area of 393 m^2 g^{-1} with 1:1 mixing ratio of phenylalanine to benzene. Saturation adsorption selectivity of resulted polymers reached 55.46% towards L-tryptophan and 41.82% towards D-tryptophan.

As PIMs are synthesized from contorted non-planar molecules. Most of PIMs type monomers have non-planar structures with non-superimposable stereoisomers. Instead of one or multiple chiral carbons with orientation chirality, tial chirality is more intriguing especially due to influences on architecture. Spirobisindane and bi-naphthalene structures feature unique axial chirality, and have also been used in PIMs synthesis. (Fig. 16) Simplest chiral molecule from such tial axial chirality can be TTSBI or binaphthol. Rotation of C-C single bond is restricted by bulkiness of naphthalene groups, thus both enantiomers of binaphthol do not racemize easily under room temperature but can still

racemize under high temperature. Similar chirality can be derived from biphenyl structures, phenyl rings on each plane were grafted with bulky functional groups to restrict C-C single bond rotation. This intra-molecule steric effect leads to stereoisomers with unique spatial chirality.[207] Binaphthols are often introduced in intrinsically chiral polymer synthesis as building blocks.[208] Chirality of polymers grafted with chiral side-groups can be quantified by number of chiral carbons per unit, enhancing chirality further using this approach is limited by backbone reactivity. Porous polymers with chiral backbones are thus expected to be more suitable to achieve satisfactory performances.

In 2011 Nicola and others reported a new type of PIM-like chiral polyimide synthesized from binaphthalene enantiomers.[209] (+)-BINAM was used to directly polymerize with PMDA. Despite reaction temperature could go up to 200 °C, resulted helical chiral polyimide based on binaphthalene structures still showed clear and strong Cotton effect in circular dichroism. In addition, contorted PIM-like structures preserved high free volumes giving 230-280 $m^2 g^{-1}$ surface area. Most recent example would be a type of circular polarized luminescence (CPL) polymers of intrinsic microporosity.[210] Novel cyclohexyl-fused spirobindane-based chiral PIM was synthesized via catalytic enantioselective synthesis. Backbone chirality was confirmed by Circular Dichroism indicating twisted backbone homochirality was achieved. Intrinsically chiral polymer has entire main chain fixed with one handedness.

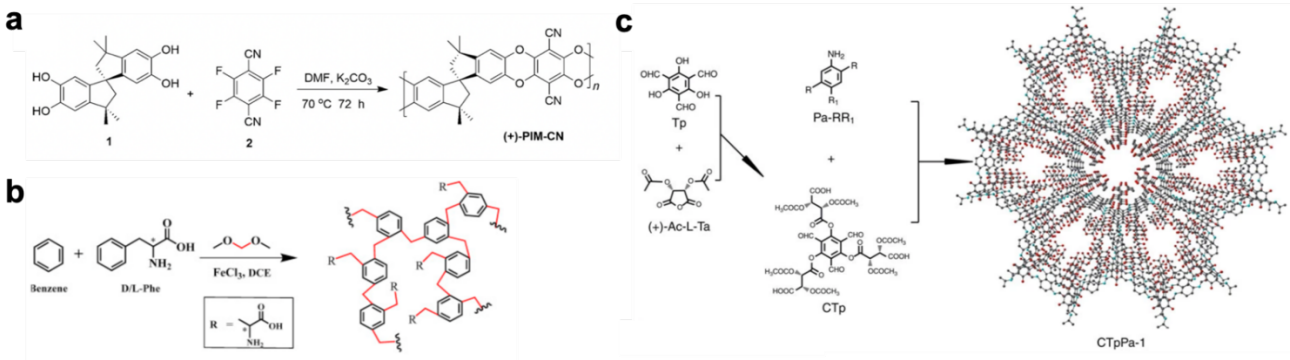


Figure 16. Intrinsically chiral porous polymers synthesized using chiral molecules as direct building blocks. a. Chiral PIMs synthesized from TTSBI enantiomer. b. Amino acids can usually be directly used as reagents due to their natural chirality and abundance in nature. D/L-Phe was directly used to link with benzene via catalytic reactions to synthesize aromatic yet flexible polymeric membranes. c. Chiral symmetric molecules can be used to react to COF-type monomers to prepared 2-D chiral COF membranes.

This means axially chiral building blocks could enhance chirality of entire polymer itself instead of mere local segmental modification. Chiral PIM-1 synthesized from enantio-pure TTSBI monomer exhibited retarded transport mechanism in chiral separation, while (+)-PIM-CN permeated (D)-binol at a slower rate than (L)-binol.[211] Racemic mixtures were directly used as feed solutions, (+)-PIM-

CN showed 32% ee for Mandelic Acid and 87% ee for TTSBI which was used as backbone building blocks. This implies that intrinsically chiral polymeric membranes may have more distinguished selectivity for their chiral building blocks. Chiral (+)-PIM-1 showed strong and clear Cotton effect in circular dichroism (CD) meaning chirality was greatly enhanced. Within 9 hours timeframe (+)-PIM-CN showed quite stable chiral selectivity under static diffusion.

A type of chiral covalent triazine frameworks (CTFs) was reported in 2021.[212] Porous quartz fibre membrane was first immersed in HCl to activate -OH groups. Triazine monomers were first reacted with activated fibre membrane surface, then treated with (S)-methylpiperazine (S-MP) or 2R,5S-2,5-dimethyl-piperazine to grow frameworks in situ. Chiral porous frameworks promoted decent separation performances. Pores in frameworks are much more well-defined than in amorphous networks, pores are easier to become interconnected eventually forming channel-type membranes to engage rapid molecular transport. However, synthetic challenge of such structures is critical. Yuan and others reported among first nanochannel COF membranes for amino acid enantiomer separation.[213] Two types of COFs were prepared by polymerizing C-3-symmetric trialdehyde with diamines with and without divinyl groups. COFs with divinyl groups were further modified with chiral beta-cyclodextrin via thiol-ene click reactions. Both chiral and non-chiral COFs had 1-D mesoporous channels formed by AA or AB stacking. AA stacked COF membrane had higher enantiomeric selectivity towards histidine enantiomers. Chiral COF nanochannel membranes showed retarded transport for L-histidine and selectively transported D-histidine. Zhang and others reported synthesis of L-tyrosine functionalized COFs and formation of COF membranes with chiral nanochannels via one-step reaction without post-modification. [214] Nanochannel COF membranes showed 94.2% enantiomeric excess towards S-NPX. Highest enantiomer permeation flux was 1.33 mmol m^{-2} hr^{-1}. Such high enantio-selectivity was credited to the matching sizes of NPX enantiomers and membrane channel entry dimensions. Intrinsically chiral COFs are faced with synthetic challenges of competing kinetics between symmetry of COF structures and chiral entities. A type of chiral COF c-TpPa-1 was reported from bottom-up synthesis approach in 2016. According to Argon gas adsorption c-TpPa-1 had concentrated micropore regions mainly distributed near ~ 1.5 nm. c-TpPa-1 was applied as stationary phase in capillary column in gas chromatography and showed very good resolution between 1-phenylethanol, phenyl-1-propanol, limonene and methyl lactate enantiomers.[215]

2.5 Flow battery separator membranes

Flow batteries are emerging technologies that provide alternative energy sources for gird-scale power plants or portable power supplies. In a typical flow battery set-up, cathode and anode were stored in separate tanks dissolved in liquid electrolytes with charge carriers. During charging process anode

material is oxidized while cathode is reduced. In a discharging process cathode is oxidized while anode is reduced. Charges are transferred via outer circuit to provide electricity. A membrane separator immersed in the electrolyte solution serves to prevent mixing of cathode and anode. Direct mixing of anode and cathode material will result in no electron transfer via outer circuit thus no discharge capacity.

Membrane separator is key component in a flow battery set-up.[216] A few standards for membrane separators in a flow battery include, i) membranes should be permeable to charged carriers such as monovalent ions K+ or Na+, ii) membranes should reject cathode and anode materials in all cases to prevent capacity loss, iii) membranes should be stable in acidic or alkaline conditions depending on electrolyte conditions, iv) membranes should be robust in between sealing gaskets to avoid physical defects. Flow batteries as alternative power sources that have drawn significant attention both academically and economically.[217] By far all-vanadium flow batteries and bromine-based batteries showed most notable commercial development. Yet power density of all-vanadium battery is difficult to improve. Research efforts devoted into flow battery research include, i) novel cathode and anode material, ii)new electrolytes and new battery systems, iii) membranes with enhanced conductivity and selectivity.

Conductance and selectivity are two most important performance parameters for battery separator membranes. Membrane separator selectivity serves to prevent crossover of cathode and anode materials which usually have large dimensions, high membrane conductivity serves to rapidly transport smaller charge carriers which can also be greatly benefited from material microporosity. Ion exchange membranes are popular candidates, incorporation of ion exchange groups in membranes greatly enhanced conductivity. Yet enhanced hydrophilicity from ion exchange groups may sabotage mechanical stability and cause phase separation. On the basis of that, most reported ion exchange membranes did not have satisfactory selectivity to prevent crossover under electrolyte conditions. Hence preparing conductive, robust, microporous membranes that are stable in electrolytes are most intriguing direction of research. PBI membranes are highly stable in organic solvents and can be prepared massively via phase inversion. But non-porous PBI membranes have low permeability for vanadium ions in VRFBs. A type of porous PBI membrane was reported from water vapour phase inversion to induce porosity.[218] PBI casting solution was doped with H2SO4, resulted PBI membrane had 16.6 mS cm^{-1} proton conductivity and 4.5×10^{-8} cm^2 min^{-1} VO2+ permeability. VRFB with porous PBI separator achieved 10% higher energy efficiency (EE) than Nafion 112 under current densities of 20 – 40 mA cm^{-2}. In 2020 Rui Tan and others reported successful application of AO-PIMs membranes in flow battery based on alkaline systems. [219] 2,6-DHAQ and$K_4Fe(CN)_6$ were used as redox couples, AO-PIM-1 self-standing membranes and PIM-EA-TB TFC membranes were

applied as battery separators. AO-PIM-1 membranes had enhanced microporosity and high conductivity, meanwhile very good selectivity for monovalent and divalent ions in aqueous systems. Self-standing AO-PIM-1 membranes were stable over 300 cycles with 0.5% discharge capacity loss per day, while Nafion 212 had 2.3% capacity loss per day. PIM membranes showed as high as >90% energy efficiency. PIM-based redox active materials have also been reported by Anqi and others as electrodes instead of membranes, showing great potentials of PIMs in energy storage device applications. [220]

Other than amorphous porous membranes, COF-based membranes with well-defined porosity have also been tested in flow batteries. COFs membranes without ion-exchange groups were reported in 2020 for VRFBS.[221] COF membranes showed excellent hydrated proton sieving and no permeation of vanadium. COF VRFB showed 76.4%-93.5% energy efficiency over 500 cycles, >1300hrs of operation at relatively high current density 80 mA cm^{-2}. Within this regard, controlling pore dimensions in membranes to achieve diffusion selectivity between electrode materials and charge carriers are promising approaches to design next-generation battery separators. External porous conductive fillers have been applied to regulate performances of conventional membranes. As recently rationalized by Xu and others in 2023, a type of sulfonated piperazine covalent triazine framework (CTF) incorporated sulfonated poly (ether ether ketone) (SPEEK) membrane was prepared as VRFB separators.[222] Hybrid membranes showed long-term stability for 900 cycles over 400 hours with 85%-87.2% energy efficiency at 120 mA cm^{-2}. SPEEK membranes are stable in solvents and have high conductivity. Another type of SPEEK mixed matrix membrane was prepared from doping with Schiff base network (SSNW-1) COFs. SSNW-1-SPEEK membranes showed much lower vanadium permeability than pristine SPEEK and Nafion 212, comparable voltage efficiency and superior capacity retention over charge-discharge duration.[223]

2.6 Thin film composite membranes

2.6.1 Interfacial polymerization

Cadott and others developed the initial interfacial polymerization technique in 1960s. It is a technique that promotes polymerization not inside single phase, but at the solvent interfaces. It is renowned for massively preparing traditional reverse osmosis (RO) membranes to obtain drinkable water for pilot-scale facilities. Synthesized selective layers are ultra-thin and defect-free, as both monomers will keep diffusing to and reacting at any interfacial pin-whole areas driven by concentration gradients and chemical potentials. Hence, IP technique is considered the dominant technology to prepare scalable defect-free TFC membranes for RO and NF.[224]

In a typical interfacial polymerization process water and hexane are commonly used as aqueous phase and oil phase solvents, as they have most distinguished polarity differences and are immiscible. During conventional interfacial polymerization amine monomers are first dissolved in aqueous phase, an ultrafiltration support substrate is treated with amine aqueous solution to impregnate with amine monomers. Amine-saturated support is then treated with acyl chloride solutions in hexane. Defect-free ultra-thin films are thus formed directly on the support substrate. Processed IP substrate is rinsed with hexane to remove residue acyl chlorides and dried to deplete solvents between support layer and IP layer. Polyamide condensation reaction is an exothermic reaction releasing heat during solid formation. In situ IP reaction is directly performed on the top of and inside solid porous support, generated heat could not dissipate efficiently thus quickening local hexane solvent evaporation. Compared with TMC molecule MPD has lower molecular weight and good partition coefficient in hexane, thus in conventional MPD-TMC polyamide synthesis upward nodule-like structures are usually formed due to MPD crossover and localized hexane evaporation.[27] While IP at free interface would yield rather flat morphology. (Fig. 17c and Fig. 17d))

Top skin layer of a NF TFC membrane is considered to control overall membrane performances, since commonly used support substrates such as PAN has high solvent permeance but usually no rejections towards small molecules below 2000 g mol^{-1}. Most research efforts have been focused on tuning selective skin layer properties. Yet in conventional TFC membrane preparation, support substrate properties directly affect in situ IP kinetics of skin layers. It is difficult to deconvolute skin layer property itself from other influencing factors such as support properties. An ultrafiltration support such as PSF was first treated with amine solutions in water, followed by dip-coating approach by TMC in hexane phase. A polyamide layer is then formed directly on the top of the support. Amine monomer distribution on PSF surface and reaction zones of polyamide condensation is heavily dependent on support properties. (Fig. 17a)

Free-interface interfacial polymerization is an emerging technique to prepare IP layers independently without support substrates.[67] (Fig. 17b) In this case both monomers diffuse towards near the liquid-liquid interface as monomers will be quickly consumed. Formed dense MPD-TMC film is impermeable to reagents hence an ultra-thin MPD-TMC nanofilm can be formed from on-step reaction. IP reaction does not take place on the support, but at interfaces between two liquid phases. It is advantageous in being able to synthesize and modify IP layers separately before casting on support substrates to prepare TFC membranes. Stability of liquid-liquid interface can significantly affect interfacial film formation, if two liquid phases have high miscibility convection flow of liquids may cause film formation process to be discontinuous. Free-interface IP of conventional MPD-TMC nanofilms is self-confined and can be controlled on nanometer scale precision via controlling reaction

conditions. MPD-TMC membranes synthesized from IP at free interfaces showed fewer nodule-like textures on the surface compared with in situ IP on polysulfone.(Fig. 17d) Other than hexane, hydrophobic solvents such as n-dodacane, toluene can also be applied as oil phase solvent. In all cases aqueous phase must have high hydrophilic content to ensure immiscibility with oil phase.

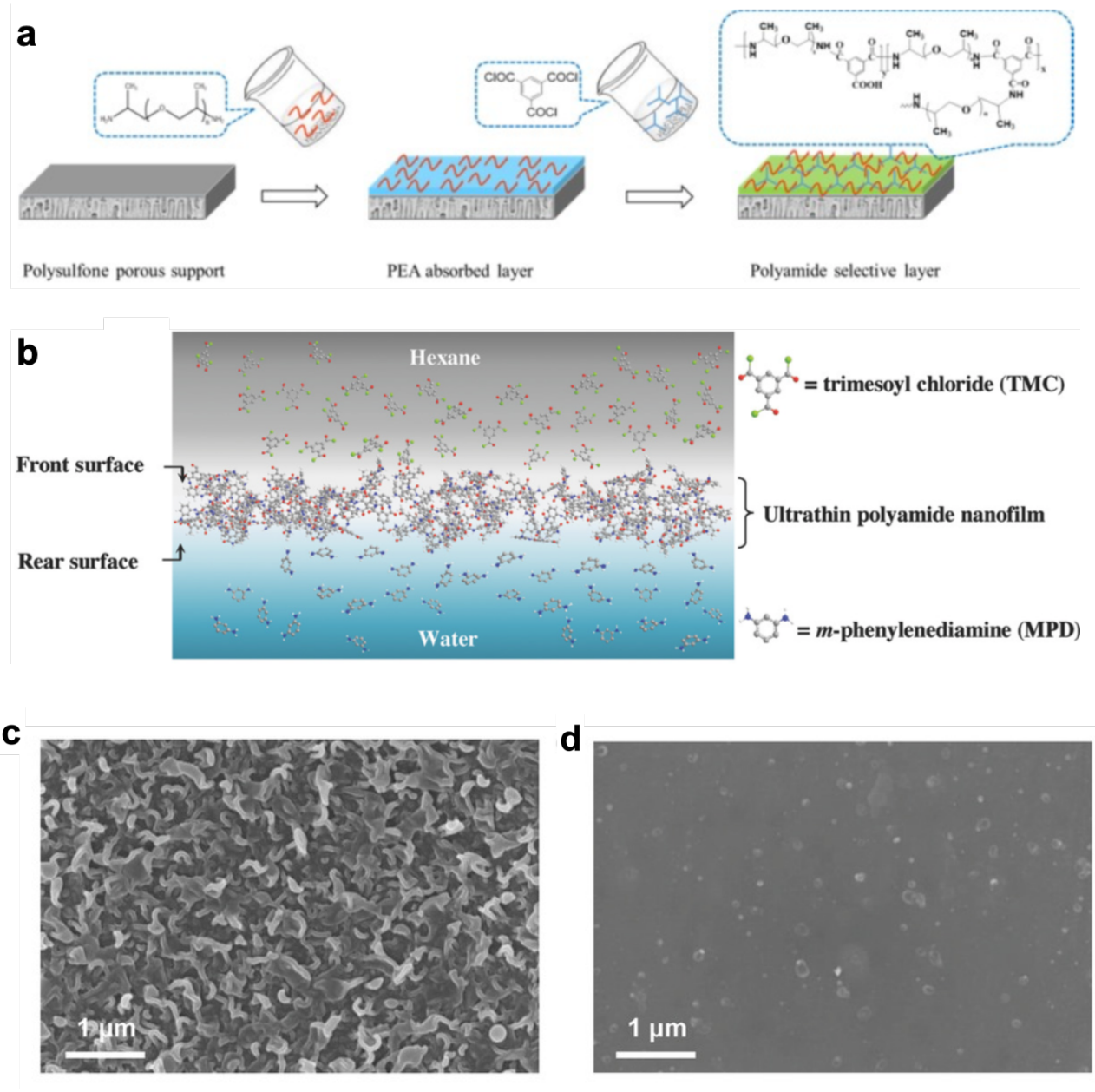


Figure 17. a. Example of conventional in situ interfacial polymerization of amines and acyl chlorides on supporting membranes. b. Schematic example of interfacial polymerization performed at free liquid-liquid interface. c. SEM surface image of MPD-TMC film formed from conventional interfacial polymerization, showing crumpled texture which was caused by convection. d. SEM surface image of MPD-TMC film formed from interfacial polymerization at free liquid-liquid interface.

Solubility of monomers and film robustness are two main challenges to prepare ultra-thin polymer films via free-interface interfacial polymerization. Poor solubility of monomers in each phase will dramatically reduce crosslinking degree of synthesized films, precipitated solute solids may reek severe defects in synthesized films. To resolve monomer solubility issues a co-solvent can be applied to help disperse monomers. Choices of co-solvent are restricted by absolute miscibility with same-phase solvent.

Due to traditional self-confinement characteristics in IP reactions, obtained membranes are usually on the scale of 5 nm – 100 nm thick making them difficult to process. Up to date it is not possible to directly test performances of nanofilms without supports owing to poor mechanical strength. But synthesized nanofilms were at least robust enough to be transferred and processed into TFC membranes for filtration or diffusion applications. Since oil phase solvents have low boiling points and high vapor pressures, IP reactions are usually performed at room temperature. Currently there exists no machinery for the free-interface membrane casting. Up to date, the intrinsic permeability of conventional polyamides prepared from IP is still very low despite efforts to enhance permeance, it is difficult to improve selectivity in non-porous polyamides with such low permeability.

2.6.2 Monomer species used in reactions

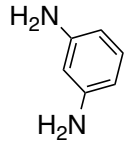
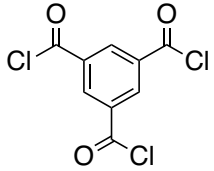
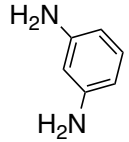
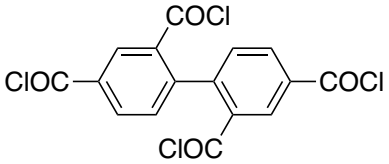
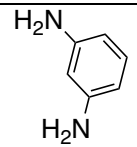
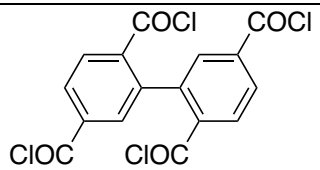
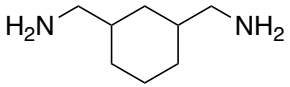
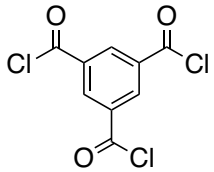
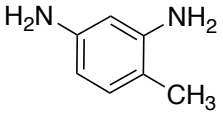
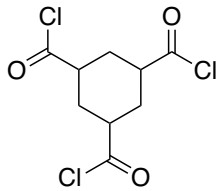
Existing desalination membranes are mostly prepared from MPD and TMC. MPD-TMC is hydrophilic polymer due to existence of amide groups and low hydrophobic aromatics content. PIP is another commercial monomer to be polymerized with TMC to form dense polyamides with high sodium chloride rejections and enhanced hydrophilicity. PIP-TMC membranes have lower MWCO than MPD-TMC membranes thus intrinsic water permeability could not be improved significantly. Alternatively, other amine or acyl chloride species have been used to synthesize RO or NF polyamide membranes.

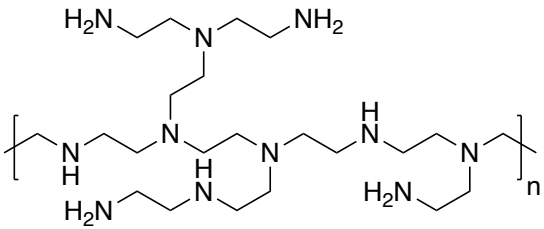
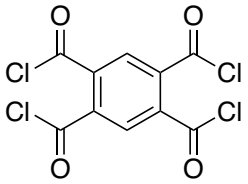
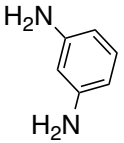
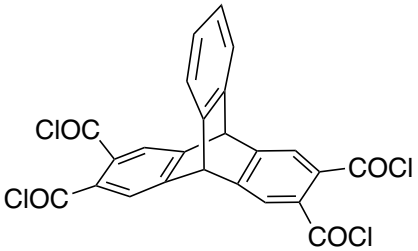
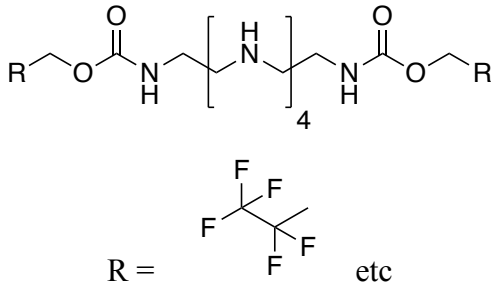
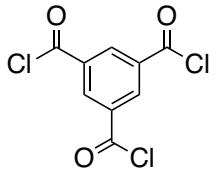
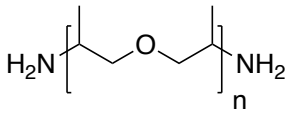
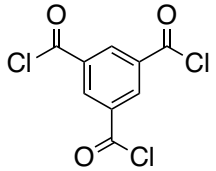
To investigate side-group effects, a chemical modified type of m-phenylenediamine-4-methyl was synthesized and used to react with HTC.[225] Three types of reactive isomeric acyl chlorides were synthesized and reported in novel polyamide preparation by Li and others in 2008.[226] MPD was used as the amine reagent to react with 3,3',5,5'-biphenyl tetraacyl chloride (mm-BTEC), 2,2',4,4'-biphenyl tetraacyl chloride (om-BTEC) and 2,2'-5,5'-biphenyl tetraacyl chloride (op-BTEC). MPD-om-BTEC and MPD-op-BTEC membranes had much higher fluxes but lower rejections than MPD-mm-BTEC. This work specifically compared three isomers with different functional group positions, PA membranes synthesized from chloride isomers showed different separation performances. MPD-op-BTEC showed highest water permeance of ~2.7 L m^{-2} hr^{-1} bar^{-1} and 97.2% rejections for NaCl,

MPD-mm-BTEC showed lowest water permeance of ~1.6 L m^{-2} hr^{-1} bar^{-1} and NaCl rejections of 98.4%. With errors considered three acyl chloride monomers do not have significant influences for performances. A type of novel amine monomer 1,3-cyclohexanebis (methylamine) (CHMA) was used to react with TMC .[227] Resulted CHMA-TMC membrane had ~55 L m^{-2} hr^{-1} bar^{-1} water permeance but < 80% NaCl rejection.

Hai and others reported polyamide synthesized from 1,2,4,5-benzene tetracarbonyl chloride with ethylenediamine and hyperbranched poly(ethyleneimine) on crosslinked poly(ether imide) support.[228] Resulted polyamide TFC membrane showed 100% rejection of Rose Bengal and 1.4 L m^{-2} hr^{-1} bar^{-1} methanol permeance. After DMF/DMSO solvent activation membranes showed 3 Lm^{-2} hr^{-1} bar^{-1} methanol permeance and 90.4% rejection for RB. Branched side groups in PEI can help enhance repelling forces between crosslinking nodes, thus open up more free volumes for solvents to access. Ali and others applied contorted rigid triptycene acyl chloride to react with MPD. Resulted MPD-trip membranes showed identical surface morphology with MPD-TMC, implying similar film formation mechanism. MPD-trip membranes had very comparable selectivity for salts and organic molecules with MPD-TMC, but with enhanced permeability.[66] In 2020, a type of polyether amine (PEA) was used to react with TMC. PEA-TMC showed ~16.6 L m^{-2} hr^{-1} bar^{-1} water permeance under 0.4 MPa, high methyl blue rejection of 95.4% and low NaCl rejection 16.4% in mixture separation. Due to bulkiness of amine monomers, PEA-TMC membranes were loose with larger free volumes.[229] Siyao and others reported a new series of amphiphilic polyamide nanofilm membranes by polymerizing fluorinated multiblock oligomer amines (MOA) with commercial TMC. [46] With increasing fluorine content F_5 to F_{13} grafted onto the side-chains MOA-TMC membranes showed decreased heptane permeance from ~ 43 L m^{-2} hr^{-1} bar^{-1} to ~18 L m^{-2} hr^{-1} bar^{-1}. This is due to bulkiness of side groups that Fluorine and alkane series membranes had MWCOs of ~400 g mol^{-1} but hundreds of folds higher non-polar solvent permeances than conventional hydrophilic polyamides. Branched hydrophobic side groups self-assembled into micelles which created small bumps on membrane surfaces, but overall membrane surfaces were smooth which is preferable to process.

Table 3. Reported polyamide thin film composites and monomer structures. Permeances and rejections were reported based on specific supporting substrates in pressurized filtration.

Amine	Chloride	Permeance ($L\ m^{-2}\ hr^{-1}\ bar^{-1}$)	Rejection (%)	Support	Reference
		Water, 2.7±0.1	NaCl 96.0%±1.9%	PSF	[67]
		Water, 2.5	NaC, 97.6%	PSF	[226]
		Water, 2.7	NaCl 97.1%	PSF	[226]
		Water, 55	NaCl 79%	PES	[227]
		Water, 3.1	NaCl 97.2%	PSF	[225]

		Methanol, 1.3	Tetracycline 76.9%	PEI	[228]
		Methanol, 8.7 Water, 9.2	Dyes MWCO in methanol of ~200g mol^{-1}, Sudan Orange G (216 $gmol^{-1}$) 99.1±0.6%, NaCl ~96%	PAN	[66]
		Hexane, 63.9±5.6 Methanol, 11.2	Polystyrene oligomers MWCO of 395 to 450 $gmol^{-1}$, Rhodamine B (479$gmol^{-1}$) ~90%	PAN	[46]
		Water, 16.6	Methyl Blue (799.8 $gmol^{-1}$) 95.4%, NaCl 16.4%	PSF	[229]

Commercial MPD-TMC and PIP membranes have very low permeances for hydrophobic solvents such as hexane. A novel type of hexafluoroalcohol (HFA) aromatic diamine was applied to react with commercial TMC in 2010.[230] Hydrophobicity was greatly enhanced in HFA-amine-TMC membrane under neutral pH indicated by contact angel measurements ~ 90 °C. Interestingly under basic conditions HFA-PA membranes became more hydrophilic, under pH >8 membranes showed higher water permeance > 3 L m^{-2} hr^{-1} bar^{-1} than MPD-IPC reference. Under pH < 6 HFA-PA membranes showed lower water permeance ~ 1.9 L m^{-2} hr^{-1} bar^{-1} than MPD-IPC of 2.5 L m^{-2} hr^{-1} bar^{-1}. HFA PA had slightly lower salt rejections than MPD-IPC for pH from 4 to 10.

2.6.3 Composite membrane selective layers with fillers

To improve membrane permeability, porous filler incorporation into dense membranes have been extensively reported over a decade. This technique takes advantage of highly permeable filler materials to reduce bulk resistance by artificially implementing cavities into non-porous matrix. To avoid phase separation and defects when applying external filler materials, compatibility of filler materials with membrane matrix is important.

Thin film nanocomposite (TFN) membranes are TFC membranes doped with filler materials to enhance performance. (Fig. 18) This has led to a new category of TFC membranes with varying doping agents, including afore mentioned COF and MOF fillers. In order to loosen tight conventional networked polyamide, crystallite components are usually directly mixed with reagents, during progression of polymerization these functional crystallite filler materials serve to increase hydrophilicity of membranes to boost separation performances.

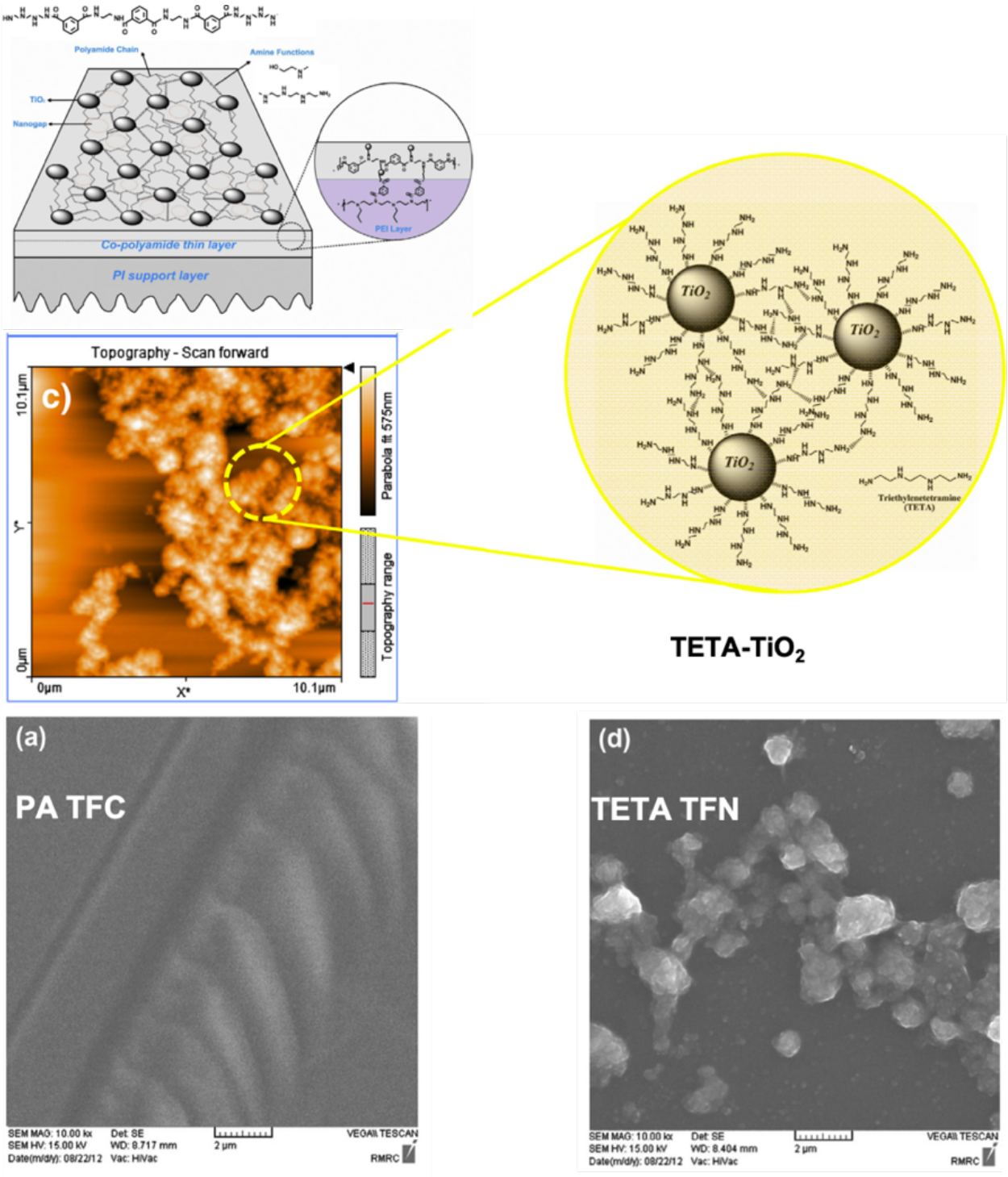


Figure 18. Typical thin film nanocomposite membranes with nanoparticle doping. TiO_2 was used as the doping agent into polyamide matrix leading to dendrimers forming and particle aggregation on film surface.

Lee and others reported one of pioneering type of nanocomposite membranes with amine-modified TiO2 nanoparticles.[231] TiO_2 was first dispersed into oil phase with TMC similar to 5 wt% loading, followed by interfacial polymerization with MPD. Resulted thin film nanocomposite membranes showed > 95% rejection for $MgSO_4$ and water flux of 9.1 L m^{-2} hr^{-1}. Addition of functionalized TiO_2

particles increased surface roughness by ~ 2.4 folds, methanol flux increased from ~ 128 L m^{-2} hr^{-1} of PA TFC to ~ 140 L m^{-2} hr^{-1} of TETA TFN membranes with ~ 20% increase in rejections for crystal violet (408 g mol^{-1}). (Fig. 19) Zeolite crystals have also been used as doping agents in PA matrix.[232] Addition of zeolite nanoparticles with different sizes yielded different impacts on performances and surface properties.

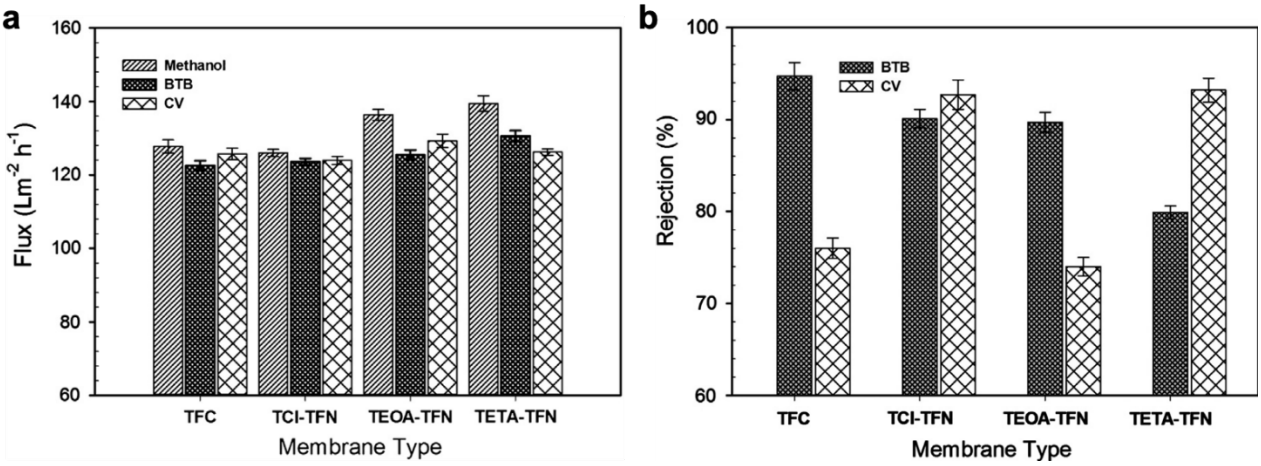


Figure 19. Rejections and methanol permeances of TFN and TFC membranes.

Small zeolite nanoparticles helped form more permeable membrane, while large zeolite nanoparticles changed surface properties more. Channel-type multi-walled carbon nanotubes (MWCNTs) have been doped into polyamide matrix using mixing followed by IP.[233] MWCNTs powder was directly mixed with MPD or TMC for membrane casting. Resulted mixed matrix membranes showed enhanced water flux and comparable salt rejections to pristine MPD-TMC. Hydrophilic MWCNT-COOH doped in MPD-TMC membrane had highest water permeance of ~2.8 L $m^{-2}hr^{-1}bar^{-1}$ than hydrophobic MWCNT doped PA membranes. These research results revealed that hydrophilic fillers should be more desirable to improve IP PA membrane performances. This could be due to relevant hydrophilicity between fillers and matrix. TFN membranes with embedded silicalite nanocrystals were also studied in 2012 by Li and others.[234] With increased loadings of silicalite nanocrystals higher water fluxes were achieved, but salt rejections decreased significantly. With 0.5(w/v) loading of silicalite TFN membranes had only 50% rejection while plain polyamide had 98.1% salt rejection. Water fluxes were increased by 5 times at the cost of selectivity. Graphene oxide (GO) are hydrophilic materials with high water permeability. A type of GO-TFN membrane was reported by Lai and others in 2018. GO nanosheets were embedded into PA matrix. GO nanosheets helped improve PA hydrophilicity. With 0.02gm-2 GO loading TFN membranes showed 97.7% rejections for MgSO4 and 31.4% higher water permeance than pristine PA membranes.[235]

COFs are organic polymers with outstanding compatibility with polymer matrices. COFs can be used to increase pore volumes in dense polymer matrix for improved permeability.[236] MPD was first mixed with COF nanoparticles then used to impregnate PI substrate, followed by crosslinking with TMC. Resulted selective layers had ~80nm thickness compared with pristine PA formed from MPD and TMC estimated to be ~140nm with rough surface. In situ polymerized PA-COF membrane surface was still rough with identical nodule textures as seen in most polyamides. This suggests nanoparticle doping does not change PA film formation mechanism.

2.6.4 Synthesis condition effects

Changing synthesis conditions can subsequently affect membrane performances by changing membrane surface morphology, charges, thicknesses etc. Increasing monomer concentrations usually lead to increase in membrane thicknesses and higher rejections.[237] IP reaction is performed at liquid-liquid interfaces, while polymerization is considered to take place mainly in the organic phase. Role of surfactants added in monomer solutions for PA synthesis was studied but not extensively. Jegal and others applied three types of surfactant triethyl benzyl ammonium bromide (TEBAB), trimethyl benzyl ammonium bromide (TMBAB) and triethyl benzyl ammonium chloride (TEBAC) in PA synthesis. It turned out only TEBAB improved water permeance ~ 40% with 0.2 wt% surfactant additives. This suggests structures and functional groups in surfactants have specific effects for PA film formation.[238] This effect is further coupled with viscosity and solubility, where dispersion force played an important role during polymer film synthesis.

A co-solvent in aqueous or oil phase can be applied to modify membrane properties or help dispersing insoluble monomers.[239] (Fig. 20) According to Lee and others addition of DMSO as co-solvent reduced polyamide membrane crosslinking degree and thickness, by increasing TMC diffusion rate to the interface. Addition of acetone in oil phase increased considerable ratio of water permeance in PA without loss in salt rejections, higher acetone content in oil phase further increased water permeance but decreased salt rejections.[240] In 2016 n-dodecane was used as base oil phase solvent to mix with acetone, diethyl ether, and ethyl acetate separately. Acetone as co-solvent greatly increased membrane pore sizes with lower rejections and highest permeance among three combinations.[241]

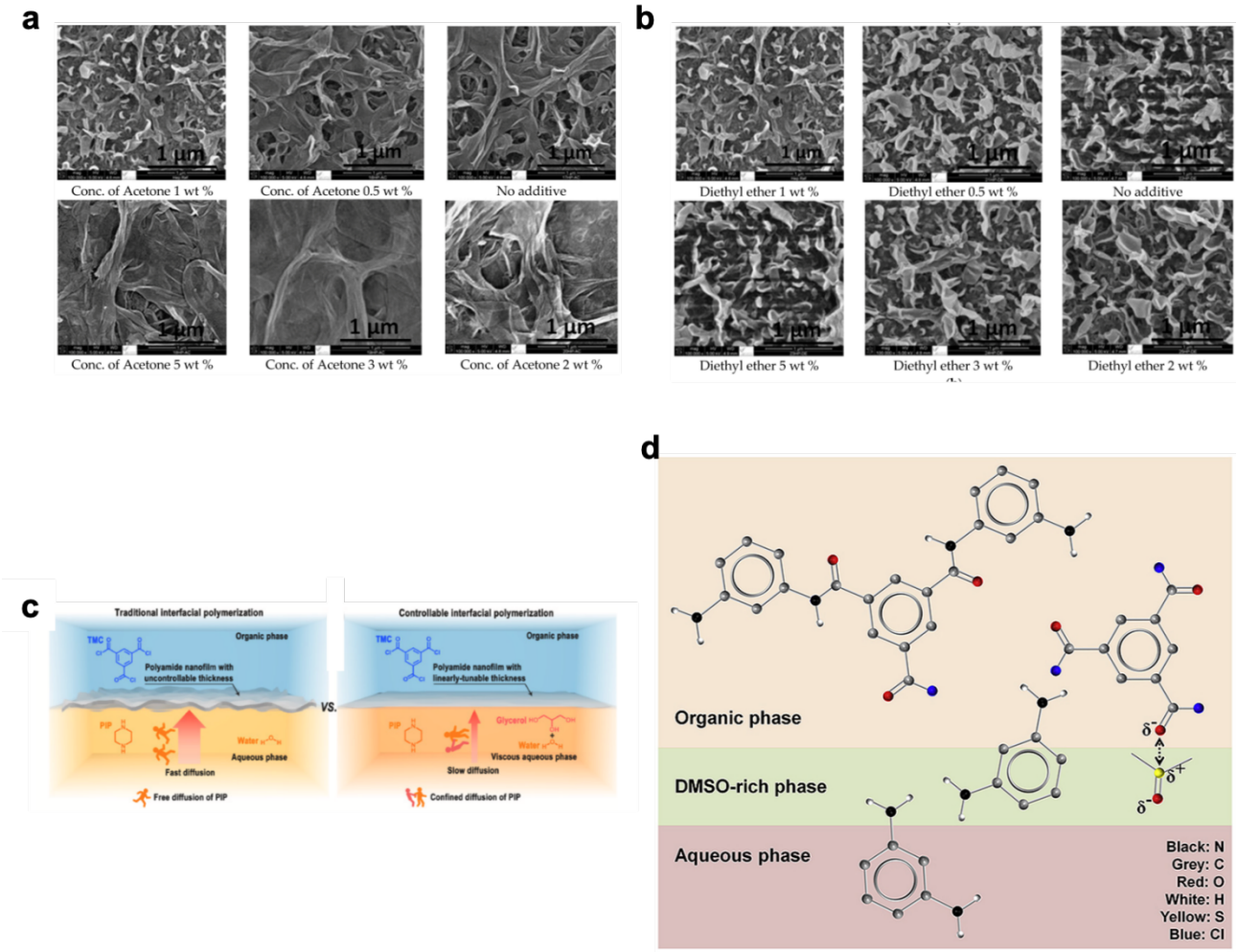


Figure 20. Co-solvent effects on membrane physical properties. a and b. Addition of acetone co-solvent in oil phase decreased membrane surface roughness. Addition of diethyl ether in oil phase increased membrane surface roughness. c. Addition of regulating agents in aqueous phase can affect film formation in interfacial polymerization. Glycerol increased viscosity of aqueous phase which caused amine diffusion rate towards liquid-liquid interface to be slower. This has led to less convention happening hence synthesized polyamide film was much smoother compared with films synthesized from same conditions but with less viscous water as co-solvent.

Addition of acetone in oil phase resulted in fibre-like surface textures instead of nodules. This year Liu and others reported solvent and mechanical force effects on PA synthesis. Dimethyl carbonate (DMC) can be applied as organic co-solvent, while 1-methylimidazole (1-MI) can be applied as aqueous co-solvent. DMC-mediated polyamide had higher roughness than 1-MI-mediated polyamides.[242] Instead of co-solvent additives such as glycerol can be used to regulate polyamide film growth in IP.[243] Glycerol is hydrophilic due to hydroxyl groups and highly miscible with aqueous phase solvents. Addition of glycerol increased aqueous phase solvent viscosity thus creating more frictions for monomeric diffusion in solvents. PA layer thickness can be tuned from 32.3 nm

down to 5.6 nm with addition of glycerol additive resulting >50% increase in water permeances while maintaining Na2SO4 rejections > 94%.

As ultra-thin polyamide selective layers have poor mechanical properties, layer-by-layer deposition of PA materials proved efficient to enhance overall membrane rejections and amend for defects.[244] Wu and others reported layer-by-layer synthesis of PA formed from polyethylenimine(PEI) and TMC on PES support. Single polyimide (TMC-PEI) selective layer formed from 3.5wt% PEI and 0.7wt% TMC showed 94.4% rejection for MgSO4 and 85.1% for NaCl with pure water permeance of ~3.1 L m^{-2} hr^{-1} bar^{-1}. Single PEI-TMC layer only had ~ 40% rejection towards MgSO4. Increasing cycles of reagent deposition increased PEI-TMC salt rejections non-linearly, implying initial PEI-TMC films may not be defect-free upon only one cycle of interfacial polymerization.

Very recently an electrochemical interfacial polymerization technique was reported to assist in preparing thin COF membranes with high rejections up to 99.96%.[245] In addition, interfacial polymerization using ionic liquids, magnetic fields, vapour deposition have been explored over recent years.[246]

2.6.5 Gutter layer effects

A traditional TFC membrane consists of a dense selective layer for separation and a porous support substrate to provide mechanical support. However, existing studies suggest that following molecular permeation through selective layer, liquids need to go through horizontal flow in order to entre pores of the bottom support substrate which is ineffective towards overall direct permeation through TFC membrane. This phenomenon can actually lead to decreased permeation efficiency of molecules through TFC membranes while permeability of selective layer could be much higher. This defective flow behaviour through different layers in TFC membrane is termed as Funnel effect. Funnel effect is not desirable for composite membrane permeation.[247] To decrease horizontal flow rate one approach is to increase surface pore density of support substrates, which can shorten the travel path length of horizontal flow to assist direct vertical permeation. But support substrate pore properties can be difficult to control in some cases. Pore properties of support substrates are heavily dependent on materials. Increasing surface pore density of support substrate can be limited by casting methods and it is complicated to control modification conditions. Moreover, high support pore density can easily lead to pore penetration from selective layer into the support substrate causing TFC membrane performance failure.

A most appreciated approach is gutter layer incorporation. Majority of membrane research only focused on selective layer development, studies on gutter layers are not extensive to date. Pore

properties, materials and thicknesses of gutter layers are considered to be important influencing factors to successfully prepare highly permeable TFC membranes. A gutter layer is an intermediate layer between the selective layer and support substrate, it should have higher permeability than selective layer in order to improve permeation efficiency. A gutter-layered TFC membrane thus has at least tri-layer structures with different permeabilities. Selective layer is still the tightest layer thus controls overall separation performances. Solvents can now more easily transport from gutter layer to support substrate with reduced horizontal flow. An intermediate gutter layer can also help resolve selective layer delamination from surfaces when directly deposited on support substrate with opposite hydrophilicity.

Gutter layers must not delaminate from support substrates, similarly selective layers must not delaminate from gutter layers. Hence surface and rear compatibility of gutter layers with contacting layers is most vital for TFC membrane preparation. In this case, it is ideal that all three layers are prepared from identical materials to avoid any potential delamination problems. However, this is difficult to achieve as tuning the porosity of identical polymer material from sub-nanometer scale to sub-micron scale is not realistic in membranes.

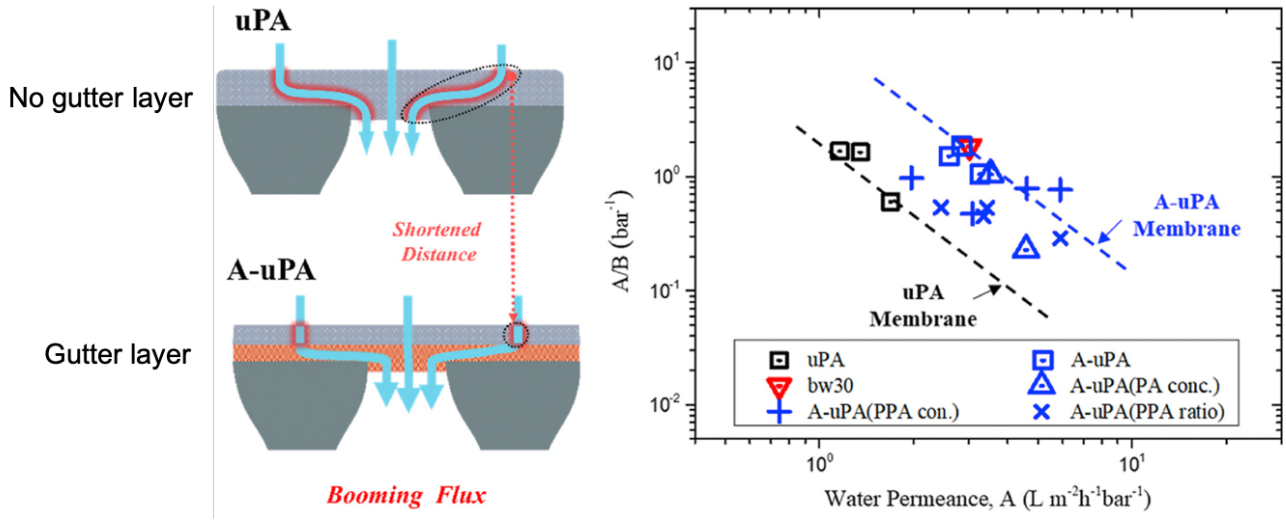


Figure 21. Schematic showing of thin film composites with and without gutter layer between selective layer and supporting membranes. TFC membranes with gutter layers had higher water permeances under same operation conditions.

Conventional polyamide membranes are mainly applied in desalination as RO membranes. Reported polyamide nanofilms are mostly deposited on PSF or PAN supports. Existing supports have low surface porosity thus caused significant transverse diffusion. This problem was addressed in 2020 by applying an intermediated layer of polypiperazinamide between selective PA nanofilms and support.[248] (Fig. 21) The process involved a two-stage interfacial polymerization on the support.

Entire TFC membrane with dual-layer asymmetric polyamide structures as selective layers had ~2.5 folds higher permeability to water and higher salt rejections.

Most common gutter layers materials include PTMSP, PDMS etc. As these materials are elastic and very permeable under room temperature with great compatibility with organic surfaces. PTMSP is a popular gutter layer material for gas separation membranes with high gas permeability. Peter and others implemented poly[1-(trimethylsilyl)-1-propyne] in between poly(acrylonitrile) support and crosslinked Matrimid (R) 5218 selective layer.[249] PTMSP gutter layer significantly reduced pore penetration from selective layer into support layer, and enhanced gas permeances as well as selectivity. For the long-term operation gutter-layered membranes gas permeances decreased. PDMS and PAN were both used as gutter layer substrates for PIM hollow fibre membranes instead of flat sheets in 2018.[250] PTMSP can be used as both support and gutter layers. Borisov and others reported PIM-1 coated directly on self-standing PTSMP support using co-solvents chloroform and trichloroethylene.[251] Resulted membranes showed CO_2/N_2 selectivity of 35.8-55.7, while PIM-1 and crosslinked PTSMP had 18.5 and 3.7 separately. This suggests selectivity is still dominated by PIM-1 layer, gutter layers helped enhance membrane performance. In liquid phase separation Maria and others applied PTSMP as gutter layers in nanofiltration membranes with polyester nanofilms. PE TFC membranes showed high solvent permeances, durability and potentials for long term operations. Recently other materials such as MOF nanosheets have also been applied as gutter layers to enhance performance.[252]

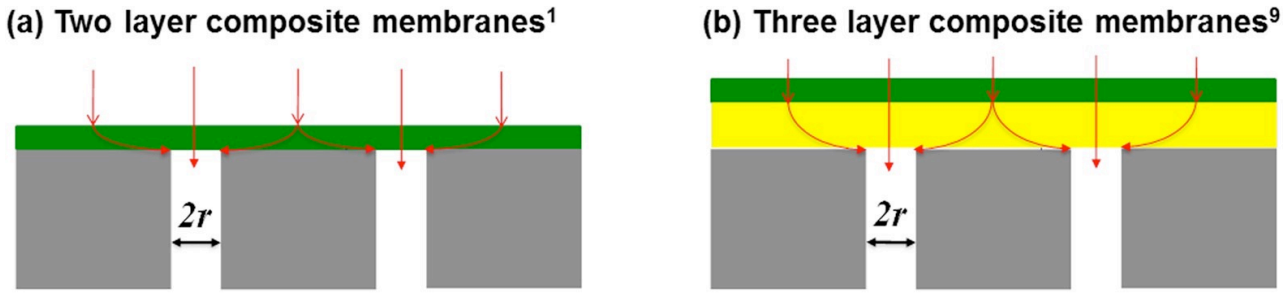


Figure 22. Green: selective layer. Yellow: gutter layer. Grey: support layer. Conventional two-layer composite membranes can suffer from pore penetration into porous supports. In addition, permeance of selective layer is significantly lower than supporting membranes. Fabrication of an intermediate gutter layer, which can be less porous than support layer but is more permeable than selective layer, can mitigate pore penetration and enhance permeation efficiency.

MOF gutter-layered TFC membrane compromised pore penetration of microporous selective layer on the top and showed high H_2 permeance of 8.2×10^{-7} mol m^2 s^{-1} Pa^{-1} and ideal H_2/CO_2 selectivity of 12.3-12.6. In 2016 Maria and others applied PTSMP gutter layer to prepare microporous polyester (PE) TFC membranes. PE nanofilm TFC membranes had stable performances under pressurized

filtration >5 bar indicating pore structures of ultra-thin PE selective layer were well preserved in filtration.

Optimal thicknesses of gutter layers can be determined by simulation and calculation. A comprehensive study was given in 2015 by Moon and others.[253] (Fig. 22) Mathematic transport model of penetrant A through membrane selective layer on a porous support was evaluated using following equations,

$$Per_A = \frac{P_A}{l_{eff}} = \frac{N_A}{S(P_{2A} - P_{1A})} \qquad \text{(Equation - 2)}$$

Where Per_A is the permeance of penetrant A through selective layer (green layers in Fig. 22), P_A is the permeability of penetrant A in selective layer, l_{eff} (red lines in Fig. 22) is the efficient diffusion path length of A through selective layer, N_A is the steady state flux of A through membrane, S is the membrane surface area for permeation, $(P_{2A} - P_{1A})$ is the transmembrane pressure calculated by abstracting downstream pressure from upstream pressure. r shown in the figure represents average pore radius in the porous support, apparently assumed from circular surface pores. It can be seen that actual penetrant diffusion path length l_{eff} is much longer than selective layer thickness l_s in most cases, which is the primary cause for lower permeation efficiency characterized by the following equation,

$$\beta_A = \frac{(Per_A)_{Apparent}}{(Per_A)_{Ideal}} \qquad \text{(Equation - 3)}$$

Where β_A is the permeation efficiency of penetrant A through membranes, $(Per_A)_{Apparent}$ is the entire membrane permeance towards A from models or can be measure values, $(Per_A)_{Ideal}$ is the ideal selective layer permeance towards A without influence from support and gutter layer. β_A was always much lower than 1 meaning in a TFC membrane performance of the selective layer was not maximized. Again unfortunately it is not possible to accurately measure independent performances of nanofilm membranes thus obtaining empirical values is difficult.

Thin gutter layers may not provide enough pore volumes to improve permeation efficiency, thick gutter layers consume more materials and may increase resistance.

2.7 Challenges, scientific question and research objectives

Membrane separation processes can be either single-stage or multi-stage based on number of membrane units. In multi-stage process pressure drops through each separation unit, fouling and requirement of high pump power all account for much higher costs.[254] To minimize net-costs and complexity continuous efficient single-stage separation is ideal. Permeability and selectivity are primary properties to evaluate performances of membranes. General approaches to improve intrinsic permeability of a membrane include, i)Tune surface hydrophilicity and hydrophobicity to increase solute or solvent dissolution at surfaces. ii)Chemical modifications of bulk materials' functional groups to facilitate mass transport. iii)Create artificial permeable channels for faster molecular transport. iv)Increase pore sizes and accessible fractional free volumes (FFV) for faster molecular transport with low resistance. v) Increase active membrane surface area to increase flux. To improve membrane's selectivity of desirable species over the others, following strategies are often adopted, i)Functionalize membrane surface with charges to reject undesirable solutes with same charges. ii)Narrow down materials' pore sizes and accessible FFVs to increase rejections. iii) Functionalize membranes with 'capture' functional groups for retarded transport of undesirable species. The trade-off effect between permeability and selectivity arises from opposite strategies taken in membrane performance design, where selectivity enhancement often involves sacrificing permeability of one or more species. It is extremely challenging to manipulate and breach this trade-off especially in NF and RO applications. The dynamic molecular properties of desired and undesired guest species are even harder to distinguish in these cases.

Controlling polymeric membrane microporosity down to sub-nano scale is the key challenge to achieve maximum selectivity for NF and RO membranes. Ideally membranes with well-defined pores can separate molecules with trivial dimension differences by molecular sieving. By far only a few COF structures have been reported with well-defined sub-nano pores below 2nm. There have been even fewer reports on amorphous polymers with well-defined pores on this scale. Reported application of contorted structures in polyamide synthesis only increased micropore volumes but had minimal impacts on pore sizes. We postulate enhanced contortion of building block geometry in crosslinked polymer synthesis can help tune micropore dimensions. Outstanding knowledge gap is lack of understanding and controlling methodology of porosity formation in amorphous polymers. Additionally, by far two different types of IP film morphology have been reported, i) flat surface with homogeneous IP layer structure. ii) crumpled surface with bent homogeneous films. These architectures are merely results of self-confinement of IP reaction, where formed films were either not permeable to reagents or reagents have low partition coefficients in opposite phase. IP film formation when, i) formed solid film is permeable to reagents, ii) one or more reagents have high

partition coefficients in opposite phase, has not been studied. A list of cross-sectional SEM images are given in table. 4 to present an overview of existing polymer thin film structures.

Phase-inversion, or solid precipitation, is probably the most scalable membrane casting technology that can easily produce membranes on square meters via continuous processes. Integrally Skinned Asymmetric (ISA) membranes can be easily produced from phase inversion processes but can suffer from pore collapsing and poor performances in nanofiltration. Yet casted ISA membrane layers can be prepared to be ~ 100 μm thick in total, but with a very thin selective layer only ~ 2 μm thick. Success of ISA membrane is inspiring in terms of being self-supported on-piece membrane featuring multiple pore structures, while only the top thin skin layer provides selectivity and mass transport resistance in filtration applications.

Reported up to date, synthesis of ultra-thin membranes with superior performances is not novel. Yet existing self-standing ultra-thin films have poor mechanical properties for scale-up. Ultra-thin membranes with superior performances are obtained when tested on thick supports, where intrinsic separation performances of ultra-thin membranes themselves could not be examined. Reported thin membranes synthesized from interfacial polymerization are usually based on self-confined film formation kinetics, this is due to either both monomers could not diffuse through formed films or diffusion of both reagents towards phase interface at stoichiometrically balanced rates.

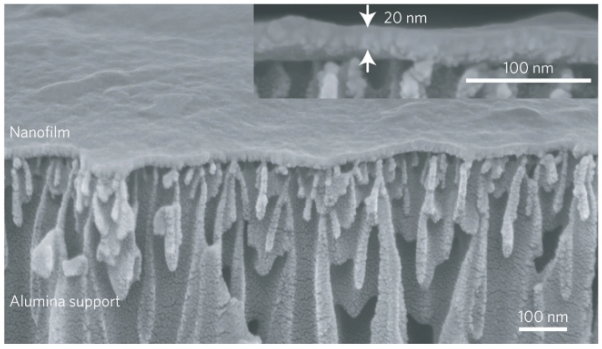
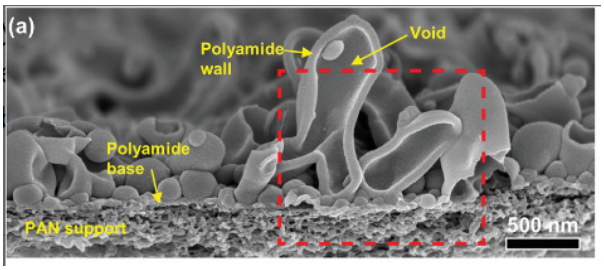
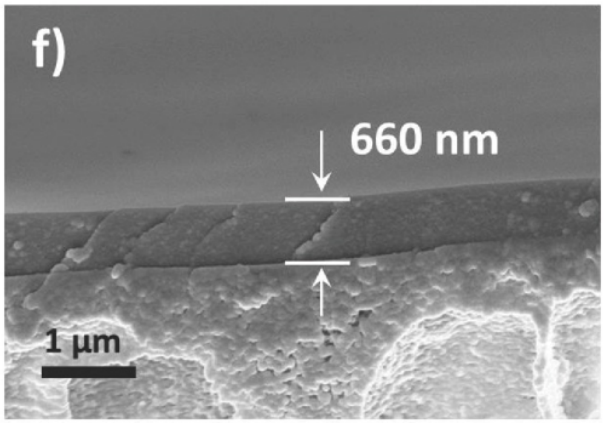
The primary scientific question in my research is to investigate the applicability of controlling crosslinked amorphous polymer microporosity via manipulating monomer geometry. Compared with existing research where there already have been studies on how micropores affect mass transport in solid barriers, this thesis research focuses rather on how micropores can affect thin film formation in IP, as well as in separation. Further I aim to generate in-depth knowledge in understanding membrane structure-performance correlations, and fabricate self-supported ‘ultra-thin’ films with novel structures for scalable casting.

During my post-graduate research program at Imperial College London, main research objectives are listed as follows,

1) Synthesis of robust, crosslinked, microporous, ultra-thin defect-free membranes from reagents with contorted geometry via interfacial polymerization.
    a. Synthesis of self-standing non-porous nanofilms using planar monomers MPD and TMC.
    b. Synthesis of self-standing microporous thin films using contorted monomers DBMPA and TPC/TMC.
    c. Characterize microporosity of materials synthesized from tetra-planar amine reagents and acyl chlorides.

2) Identify best strategy to fabricate up-scalable thin film membranes. Tune reaction conditions to control IP membrane structures.
    a. Evaluate monomer concentration effects on film formation.
    b. Evaluate IP reaction solvent composition on film formation.
    c. Identify molecule geometry effects on solid film formation at liquid interface.
    d. Synthesize novel 3-D membrane structures from IP reaction from free interface.
3) Develop and functionalize microporous membranes for molecular separations.
    a. Apply synthesized microporous thin film membranes in organic solvent nanofiltration.
    b. Functionalize microporous thin film membranes and apply in chiral separation.
    c. Evaluate semi-crystalline thin film membrane performances in aqueous RFBs.
    d. Evaluate microporous thin film membrane performances in Li-S batteries.
    e. Evaluate polymer nanofilm performances in RFBs.

Table. 4 Example cross-sectional SEM images presenting existing polymer thin film structures.

Membrane	Structure	Method	Ref
Polyester		Interfacial polymerization	123
Polyamide		Interfacial polymerization	66
PIM-1		Spin-coating	Ultrathin Polymer Films with Intrinsic Microporosity:Anomalous Solvent Permeation and High Flux membranes, Patricia Gorgojo et al, Adv. Funct. Mater. 2014, 24, 4729-4737

Chapter 3. Methods

3.1 Materials

Dibenzomethanopentacene amine (DBMPA) was synthesized by Dr. Richard Malpass-evans from Prof. Neil B. Mckoewn's group from University of Edinburgh. Trimesoyl chloride (TMC) and teraphthaloyl chloride (TPC), (R)-binaphthalene diamine (RBA), tris(4-aminophenyl)amine (TAPA), 2,4,6-triformylphloroglucinol (TFP), p-phenylene diamine (PPD), m-phenylene diamine (MPD), dye marker molecules, chiral solutes were all purchased from Sigma Aldrich. Polyacrylonitrile support was prepared by Prof. Andrew G. Livingston lab. Solvents were purchased from VWR. PBI membranes were synthesized and provided from Prof. Andrew G. Livingston lab.

3.2 Experimental characterizations

Polyamide film synthesis:

DBMPA monomers were synthesized and kindly provided by Prof. Neil Mckeown group from University of Edinburgh. SPA membranes were prepared by reacting DBMPA and TPC or TMC from free interface interfacial polymerization between MeOH-water phase and hexane phase. SPA-1-50nm. SPA-1-150nm, SPA-1-450nm, SPA-1-1300nm, SPA-1-1400nm, SPA-1-2400nm were prepared from reacting DBMPA 0.06 wt% dissolved in MeOH-water mixture and TPC 0.1wt% dissolved in hexane. SPA-2-350nm, SPA-2-580nm and SPA-2-1100nm were prepared from reacting DBMPA 0.06 wt% dissolved in MeOH-water mixture and TMC 0.1 wt% dissolved in hexane. 0.06 g of DBMPA was first added in 50 g of MeOH followed by sonication of ~ 5 min. 50 g of water was then slowly added into DBMPA-MeOH solution after sonication to prepare DBMPA-MeOH-water phase. 0.1 g of TPC was added into 100 g of hexane, followed by sonication >10min to prepare TPC-hexane phase. 0.1 g TMC was added into 100 g of hexane, followed by sonication >10min to prepare TMC-hexane phase. 80 ml of DBMPA-MeOH-water solution was first added into a circular deep petri-dish, after solution surface was stable > 60 ml of TPC-hexane solution was slowly added onto previous solution. Self-standing SPA-1 membranes SPA-1-50nm membrane was prepared by more quickly adding TPC-hexane phase then allowing reaction to progress for ~ 10 s. SPA-1-2400nm membrane was prepared by performing the polymerization under sealed environment by chambering the reactor for 30 min. Self-standing SPA films were then obtained by allowing the reaction to progress ≥ 10s. Self-standing films were robust enough to be transferred to a water bath and be captured on water surface.

Synthesis of self-standing chiral SPA-1 film:

0.02 g DBMPA and 0.007 g (R)-binaphthalene diamine (RBA) were first dissolved in 8 g of MeOH and sonicated for ~ 10 minutes. 8g of water was then added into the sonicated solution slowly to prepare aqueous phase solution in interfacial polymerization. 0.1 g of TPC was added into 100 g of hexane and sonicated for ~ 30 minutes to prepare oil phase solution. 16 g of aqueous phase solution containing DBMPA and chiral RBA was first added into a small glass petri-dish reactor. After surface of aqueous phase stabilized ~ 20 ml of TPC-hexane solution was added onto the aqueous phase to completely cover aqueous phase surface. Reaction was initiated after oil phase solution deposition and reaction was left to carry on for 2 minutes. RBA-DBMPA-TPC (R-BA-SPA-1) thin film was formed at the interface between aqueous phase and oil phase. Both aqueous phase and oil phase solutions were depleted by using a stainless steel scalpel to create a small cut at edge of the film. Polymer thin film was then transferred onto a water bath to deplete residue solvents, PTFE or PAN support was used to capture the thin film on the surface and left drying overnight in ventilated space before further testing.

Thin film composite membrane preparation:

Prior to reaction a circular stainless steel disc was pre-made by Imperial College London workshop with a stainless steel handle attached. Circular shape of supporting substrates (polyacrylonitrile or polybenzimidazole membranes) were carved from original rolls or sheets with diameters matching the sizes of the circular stainless steel disc. Harvested supports were then tightly taped on the surface of the disc by immoblizing the edges. The SS disc with the support substrates taped on the surface were then placed in the reactor. DBMPA-MeOH-water solution was slowly added from the edge of the reactor to immerse the disc ($\geq$ 80 ml). TPC-hexane solution was then added onto the amine solution. After predetermined reaction time the stainless steel disc with the taped support, with synthesized membrane on top of the support was slowly lifted from the reactor. Hexane was used to very gently rinse surface of the membrane, after which the membrane was placed in a ventilated fumehood to dry overnight. Membranes were ready to use after drying for a variety of purposes.

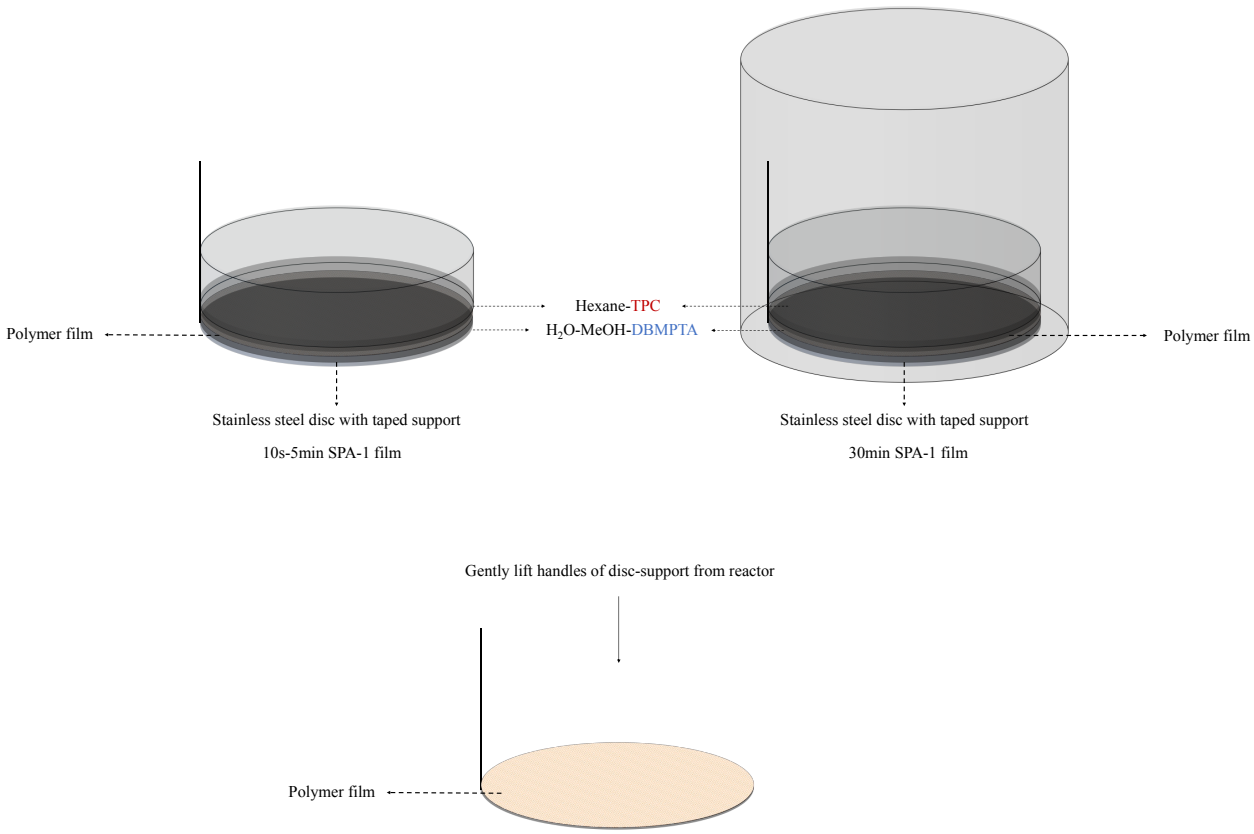


Figure 23. Schematic showing of one-step IP reaction followed by direct capturing on support membranes. Polymer thin films were synthesized from IP at free liquid-liquid interfaces. Amine monomers were dissolved in alcohol-water phase, acyl chloride monomers were dissolved in hexane phase. 10 s, 1 minute, 2 minute, 5 minute polymer films were formed directly using above-mentioned technique in a fumehood environment. 30 minute polymer thin films were formed with reactor covered with a big water bath tank.

SPA film powder preparation:

A stirring bar was first placed in a glass bottle reactor. 100 ml of 0.06 wt% of DBMPA-MeOH-water was then added in the glass bottle reactor, 100 ml of 0.1 wt% TPC-hexane or 0.1 wt% TMC-hexane was added onto the amine aqueous phase. Since this technique enables breaking existing interfaces and reforming new interfaces, it is considered polymer films formed in the reactor mainly to be interfacial polymer skin layer films. Solution(s) in the reactor were kept under stirring overnight > 16 hrs. Shattered polymer films started to form almost instantly under stirring. Solutions in the reactor were taken out to be vacuum filtrated. Obtained polymer solids were first rinsed with MeOH then acetone to remove any unreacted monomers or solvents. Rinsed polymer solids were then freeze-dried at - 50 ºC for > 1 hr to remove any potential residue solvents. Freeze-dried polymer film powders were stored in a small glass vial for further use.

Ultra-violet adsorption: UV adsorption analysis of solutions was performed using a Shimadzu UV-1800 spectrometer. Cuvettes were rinsed thoroughly 3 times with pure solvents before each absorbance measurement. Standard calibration curves were obtained to determine solute adsorption peaks and calculate solute concentrations, rejections were directly calculated from UV absorbance intensity for each solute in same solvent under same conditions. Absorbance of solutions were measured from 200 nm to 800 nm maximum wavelength range.

AFM topological imaging: AFM imaging was used to evaluate film surface roughness and thicknesses, which was performed using a Bruker Dimension Icon facility located at London Centre of Nanotechnology (LCN) in Bloomsbury campus at University College London. Self-standing polymer films were synthesized from free-interface IP reaction and captured directly on top of silicon wafers. A sharp-tip tweezer was used to create several cuts on the films to expose bottom silicon wafer sections. AFM imaging was conducted using a Scanyst Air cantilever made from silicon tip with nitrile coating, with a 0.4N/m spring constant under dry ambient environment. Images were obtained with 0.5Hz to 1Hz scan rate, 256 lines and probing parameter peak force setpoint no more than 0.07V. Images were obtained with aspect ratio of 1:1.

Scanning Electron Microscopy (SEM): SEM analysis were performed at Imperial College London. SEM imaging was performed using a GEMINI facility from Carl Zeiss Ltd with a x-act senor 51-1385-046 and model of 51-ADD0011. Samples were prepared on AAO supporting substrates and dried overnight. Samples were then broken in liquid nitrogen and fixed onto SEM stand using conductive tapes. Gold or chromium sputtering were performed on each sample up to 10 min before testing depending on the day's instrumental availability.

Focused Ion Beam (FIB) SEM: Focused Ion Beam SEM was performed at Imperial College London using Auriga SEM machine. Film samples were captured on top of silicon wafer and dried overnight before testing. Sample surfaces were coated with gold or chromium to stabilize polymer samples under charged beam. 2 nA ion beam was first used to create a pit cut from polymer surface down into wafer section with depth of 2 μm. Under microscopy film cross-section was first located and focused, 50 pA ion beam was then used to polish a clean cross-section for imaging.

Fourier-transform infrared spectroscopy (FT-IR): FT-IR ATR analysis was performed in analytical lab at Imperial College London using Agilent Technologies ATR set-up with a model of Agilent Cary 630. Samples were either dry monomer powders or dried films stirred into small pieces. Sufficient amounts of samples were placed between the stage and diamond tip, spectroscopy was obtained with background scans of 32 and sample scans of 32. Happ-Genzel function was applied for apodization.

Gas adsorption: Gas adsorption uptake and membrane porosity were evaluated using micromeritics 3-flex 5.0 gas adsorption analyzer at Imperial College London analytical lab, and Nova 4200e gas adsorption analyzer at Queen Mary University of London. Brunauer-Emmett-Teller (BET) surface areas were evaluated from both CO_2 adsorption and N_2 adsorption at 273K, pore size distributions were evaluated primarily from DFT model. All samples were degassed at 50 or 80 degree under vaccum overnight before adsorption experiments, this is dependent on sample wet status. Since from TGA and DSC measurements polyamide materials are stable up to 300 °C, this temperature value will not affect sample property during degassing. Up to 57.5 mg of polymer film powder samples were used for measurements, sample densities were not previously measured but assumed to be 1.0 g/cm^3 for convenience of analysis.

Thermal Gravimetric Analysis (TGA): Thermogravimetry (TGA) was conducted using a NZ Simultaneous Thermal Analysis (STA) machine with STA 449 Jupiter model at Imperial College London analytical lab. ~ 5 mg of polymer scattered film samples were used in the pans to take measurements. Measurements were taken up to 900 °C for each sample.

Differential Scanning Calorimetry (DSC): Differential Scanning Calorimetry (DSC) was conducted at Imperial College London analytical lab together with NZ Simultaneous Thermal Analysis (STA) of STA 449 Jupiter model. ~ 5 mg of polymer scattered film samples were used in the pans to take measurements. At least 1 heating and cooling cycle was performed for each polymer sample with a scanning rate of 10 °C/min. Measurements were taken up to 300 °C for each sample.

Contact Angle (CA): Contact Angles (CA) of different solvents on membrane surfaces were measured at Imperial College London analytical lab using a KRUSS Drop Shape Analyzer machine. Sessile drops of 10 µl or 20µl liquid volume were deposited on film surfaces using an injector with motor control. Liquid drops with fixed volume were quickly injected on film surfaces, measurements were immediately taken from 0 s up to 120 s time span. Angular analysis was automatically performed by machinery analysis.

HPLC methods to calculate chiral content in separate streams:

High Performance Liquid Chromatography (HPLC) was primarily used for trace analysis of enantiomers in liquids using a Shimadzu protein HPLC with maximum pressure up to 50 bar. Standard calibration curves were first obtained for several chiral solutes including commercial pharmaceuticals. Retention time for each enantiomer was determined from assay analysis at 220 nm wavelength and 240 nm wavelength depending on solute absorbance. A Daicel ODH column was used for chiral trace analysis and temperature was controlled to be ~ 30 ºC. HPLC spectrums of R enantiomers, S enantiomers and enantiomer mixtures of several notable chiral species are presented

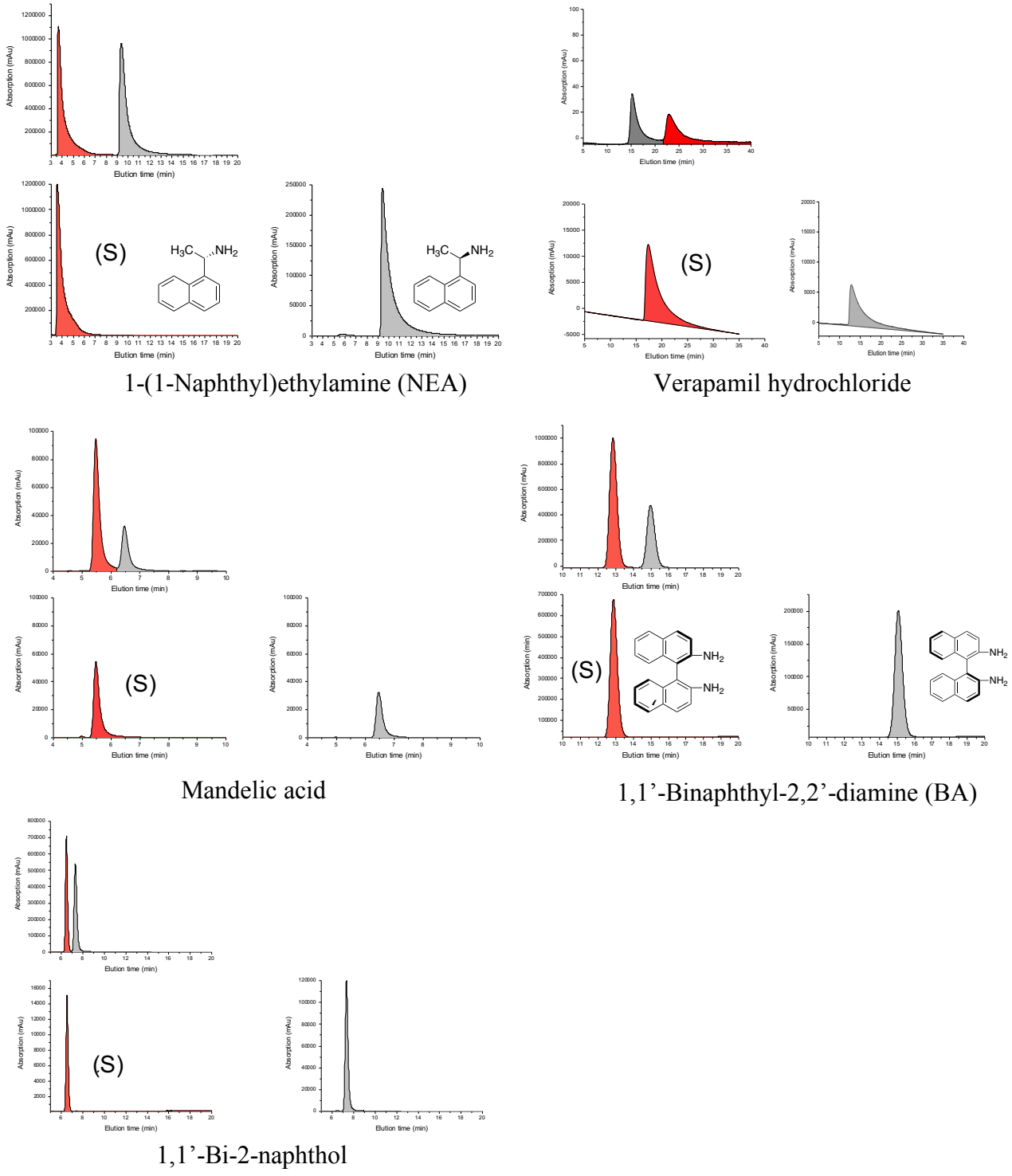


Figure 24. HPLC assay analysis of different solutes intended for chiral separation using chiral SPA membranes.

HPLC trace analysis was performed using a chiral Daicel ODH column under 50 bar pressure. (Fig. 24) 5µl to 20µl injection volumes were applied to each sample analysis. Stationary phase of Daicel column is prepared from cellulose tris(3,5-dimethylphenylcarbamate) coated on silica gel, mobile phase of chromatography consists of hexane and IPA with TFA as acidic buffer. Trace analysis of

Mandelic acid, 1-(1-Naphthyl)ethylamine and 1,1'-Bi-2-naphthol was performed using IPA(15v%), hexane (85v%) plus TFA (0.1v%) as mobile phase solvents. Trace analysis of 1,1'-Binaphthyl-2,2'-diamine was performed using IPA(10v%), hexane (90v%) plus buffer TFA (0.1v%) as mobile phase solvents. Trace analysis of Verapamil hydrochloride hydrate was performed using IPA(20v%), hexane (80v%) plus TFA (0.1v%) as mobile phase solvents. Standard calibration curves of HPLC peak area vs concentrations were plotted by preparing 5 different concentrations of each enantiomers in MeOH, and obtaining their corresponding HPLC spectrums.

Membrane selectivity was primarily evaluated by analysing enantiomeric excess (ee) in the permeate streams which have been calculated as follows,

$$ee(\%) = 100 \times (C_{p(S)} - C_{p(R)})(C_{p(S)} + C_{P(R)}) \quad \text{(Equation – 6)}$$

where $C_{p(s)}$ is the concentration of S-enantiomer, $C_{p(R)}$ is the concentration of R-enantiomer in the permeates. Enantiomer excess (ees%) is defined by the filtered concentration differences between two enantiomers. The results were derived from HPLC analysis via peak integration, further calculated from calibrated standard curves from HPLC enantiomer assay. Separation factor (α) is calculated as,

$$\alpha = \frac{C_{p(S)}/C_{p(R)}}{C_{f(S)}/C_{f(R)}} \quad \text{(Equation – 7)}$$

where $C_{p(S)}$ is the concentration of S-enantiomer in the permeate, $C_{p(R)}$ is the concentration of R-enantiomer in the permeate, $C_{f(S)}$ is the concentration of S-enantiomer in the feed solution, $C_{f(R)}$ is the concentration of R-enantiomer in the feed solution.

Circular dichroism (CD): Circular Dichroism of RBA-SPA-1 film was measured at materials department at Imperial College London at chemistry department. Chiral polymer films were first placed on quartz crystals to prepare testable samples. Samples were then immersed in methanol in a quartz cuvette to be held and measured in the CD instrument.

3.3 Nanofiltration and diffusion testing methods

Dead-end filtration: Dead-end filtration experiments were performed using Sterlitech HP4750 dead-end filtration cell. TFC membrane samples were first submerged in the solvents used for filtration experiments for ~10min, then loaded into cell bottom section sealed by two PTFE encapsulated O-rings and SS gaskets. 150ml to 200ml of feed solution was then added into the cell. The cell was sealed by the set-up and connected to a N_2 gas cylinder pressure regulator. Permeates were collected over certain time intervals to calculate permeances and rejections. Equations used are same to cross-flow filtration testing methods and are specified in the following session.

Cross-flow filtration: Cross-flow filtration experiments were performed in a sub-pilot scale filtration RIG manufactured and fused together by Imperial College London workshop. TFC membrane samples were submerged in the solvents used for the tests for ~10min, then loaded into each cross-flow filtration cell. 2 L of feed solution was used for each filtration test. Diaphragm pump power was set to provide 80L/hr liquid flow rate, a downstream pressure regulator was used to maintain 6 bar or 10 bar of hydraulic pressure in membrane cell units. Dye feed solutions were circulated inside the cell units until reaching equilibrium. All permeances and rejection ratios calculated were from analysing permeates collected after 24 hours of circulation and membrane compaction for each solution. Filtration tests of dye solutions were performed in the sequence of Acid Fushin (ACF) – Sudan 7B (S7B) – Disperse Red (DR) – Azobenzene (Azo) – Rose Bengal (RB). Membrane performances in different solvents were measured in the following sequence acetone-methanol-acetonitrile.

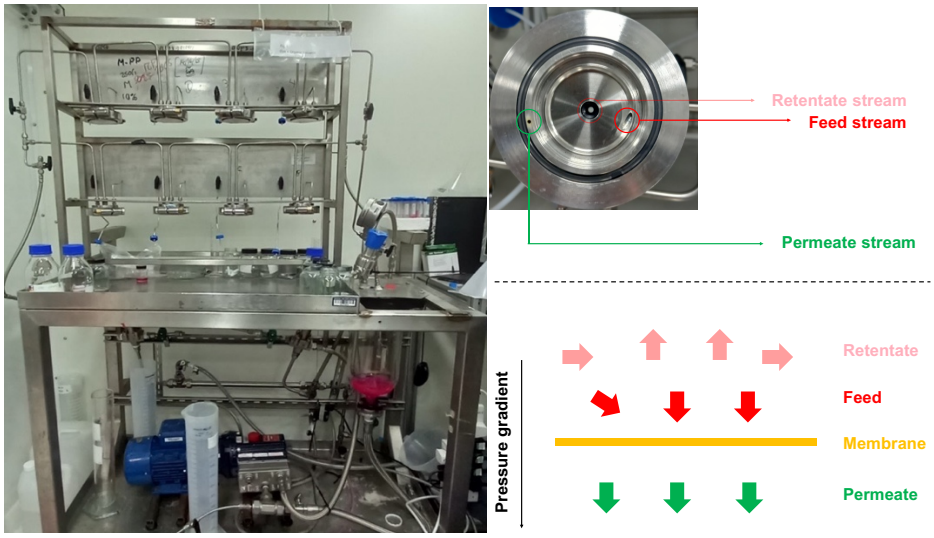


Figure 25. Sub-pilot scale cross-flow filtration RIG used for nanofiltration performance testing. And stainless steel cross-flow filtration unit cell stream structure.

Permeance of membranes to liquids were calculated as follows,

$$P_i = \frac{\Delta V}{(\Delta p \times A \times \Delta t)} \quad \text{(Equation – 4)}$$

Where P_i stands for membrane permeance towards chemical species i. ΔV stands for liquid volume that passes through membranes within Δt. Δp stands for hydraulic transmembrane pressure measured and controlled using downstream pressure regulators. A stands for active membrane area that was in direct contact with liquids in filtration. Δt stands for unit time per permeate sample collection measured from a stopwatch.

Rejections of membranes to solutes were calculated as follows,

$$R_i\% = \left(1 - \frac{C_{pi}}{C_f}\right) \times 100 \quad \text{(Equation – 5)}$$

where R_i stands for percentage rejections from membranes to chemical species i. C_{pi} and C_f stand for marker species concentrations in permeate streams and feed streams separately.

Static diffusion of enantiomers:

A homemade diffusion H-tube set-up was used to evaluate enantiomer permeation through membranes under static diffusion. A small membrane holder was fixed between the tubes to enable mass transport between feed side and permeate side through the membrane sample in the middle. 0.1g of racemic 1-(1-Naphthyl)ethylamine (NEA) was dissolved in 100ml of MeOH to prepare feed solution with 0.05 g of (R)-NEA and 0.05 g of (S)-NEA enantiomers. 25 ml of racemic NEA feed solution was added into the feed side tube, while 25 ml of pure MeOH was added into the permeate side tube. Inside each tube a stirring bar was placed and kept stirring over entire experiment time span. Concentrations of (R)-NEA and (S)-NEA in both feed side solutions and permeate side solutions were monitored over > 1 week to evaluate enantiomeric permeation rates and selectivity of membranes.

Monomer diffusion experiments:

Monomer crossover experiments without membranes were directly performed in a UV cuvette. Pure MeOH-water (with solvent mass ratio 1 : 1) solvents were directly added into the cuvette, 0.1 wt% TPC-hexane solution was then added into the cuvette to be covered by the plastic holder inside the

UV chamber. UV adsorption of substance species in MeOH-water phase was monitored over 30min time directly in the UV chamber, to further determine crossover rates of TPC species. 0.06 wt% DBMPA-MeOH-water solution was directly added into a UV cuvette, followed by addition of pure hexane solvent. A folded foil was used to partially wrap the UV cuvette and meanwhile completely covering DBMPA-MeOH-water phase. UV adsorption of substance species in hexane phase was directly monitored over 30 minutes in the UV chamber.

Monomer crossover experiments with membranes were performed in a H-cell set-up. 50 ml of MeOH-water solvent was added in one flanged bottle, 50 ml of 0.1 wt% TPC-hexane solution was added into the other glass flanged bottle. SPA-1-150nm-PAN or pristine PAN membrane was fixed in between the glass flanges sealed using rubber O-rings encapsulated by PTFE. 2 ml of solution from the solvent phase were collected periodically and added into the UV cuvette to analyze UV adsorption hence concentrations. Samples were then quickly put back into the MeOH-water flanged glass bottle to maintain osmotic pressure.

50 ml of 0.1 wt% TMC-hexane solution was added in one flanged bottle, while 50ml of water was added into the other flanged bottle. MPD-TMC-16nm-PAN membranes were sealed in between the flanges using O-rings and PTFE. Identical sampling procedure was used, which was mentioned above, to analyze substance UV adsorption in water phase.

3.4 Flow battery performance testing methods

Redox flow battery performances were tested using home-made flow battery set-up. Membranes were first treated with electrolyte solutions for ~ 5 minutes, then chopped into samples with dimensions of ~ 3 cm × 3 cm were first loaded in between rubber gaskets. Battery cells were then sealed with 8 bolts tightened around the gaskets. In neutral pH flow battery testing 0.1 M/L cathode or anode materials were dissolved in 1 M/L KCl electrolyte solutions in water. In alkaline flow battery testing 0.1 M/L cathode or anode materials were dissolved in KOH solutions. 20 mA cm^{-2} was set as current density during charge-discharge measurements.

Chapter 4. Self-supported polyamide membranes from interfacial polymerization

4.1 Research motivation

Nanofiltration(NF) refers to membrane-based pressurized filtration processes that specifically aim to reject small organic molecules of 500 ~ 1000 g mol^{-1}. Applying NF in organic solvent systems, namely organic solvent nanofiltration(OSN), is substantially impactful in terms of industrial waste treatment, pharmaceutical separations and solvent resource recovery. The tightest known NF polymeric membranes are prepared from reacting piperazine/m-phenylenediamine with low molecular weight aromatic acyl chlorides. Despite successful preparation of ultra-thin crumpled MPD-TMC polyamide nanofilms with superior solvent permeances, the intrinsic permeability of conventional polyamides is still very low. It is challenging to further improve permeability/permeance of low molecular weight cut-off membranes, as increment of membrane rejections will inevitably sacrifice membrane permeability. Moreover, sub-10nm polyamide nanofilms have poor mechanical strength which could easily lead to local defects when casted on large areas.

Polyamides from interfacial polymerization are renowned for scalable preparation techniques and high rejections. However, conventional non-porous MPD-TMC membranes have low intrinsic permeability limiting further performance improvement.

Polymers of Intrinsic Microporosity (PIMs) is a family of amorphous linear polymers synthesized from kinked building blocks, but with intrinsic microporosity after being solution-processed into membranes. The interconnected micropores enhance differentiated molecular transport in gas separation and recently liquid-phase separation. Interconnectivity and high micropore volumes are primary reasons for nanoporous PIMs to have high gas permeability. Alas, micropore properties in conventional linear PIMs membranes can be easily disrupted due to solvation or aging. Linear uncrosslinked amorphous PIMs membranes inevitably age over time usually coupled with a loss in permeability.

Linear polymers such as PIMs and polyacrylonitrile are advantageous in being solution processable. This property has enabled efficient large-scale casting of these membranes using phase-inversion process even continuously via roll-to-roll casting. Yet solution processable polymers usually have very low crosslinking degree or are uncrosslinked, making them unstable in a variety of organic solvents. PIMs are generally soluble in chloroform, thus it would not be possible to perform membrane filtration in solvents as such, membranes will be dissolved and have no selectivity. Existing reports of PIMs polymers have high micropore volumes and sub-nano pore sizes suitable for

gas separation, yet hydrophilic PIMs with similar micropore properties can easily swell in water and have no rejections for PEGs oligomers after water treatment. There had been indeed reports on crosslinking PIMs or similar categories of linear polymers to enhance solvent endurance while further increasing polymer molecular weights, but it is challenging to control and increase crosslinking degree by applying post-treatment methods after phase-inversion.

Integrally Skinned Asymmetric (ISA) membranes prepared from phase-inversion process have unique hierarchical structure comprising of thin top skin layer and bottom porous layer combined in one piece. This feature very much resembles multi-layered TFC membranes prepared from multiple steps. This 'bi-layer' structure is extremely beneficial in terms of bottom porous layer providing solid mechanical support for the top thin selective layer.[150, 160, 163]

Networked polymers can be considered as macromolecules with infinite molecular weights, a highly crosslinked polymer becomes insoluble in solvents which often give them outstanding stability in solvents and are much more suitable for applications in organic solvents. Due to insolubility in solvents they can not be casted via phase-inversion process, but they can still be synthesized separately or in situ on support substrates to prepare TFC membranes. A type of asymmetric PIP-TMC polyamide thin film composite (TFC) membrane prepared from two-step IP reaction was reported in 2020.[255] The dendrimer porous layer improved PIP-TMC PSF TFC membrane water permeance by ~ 3 folds. To date it has not been possible to prepare crosslinked asymmetric structures directly from one-step IP. IP is hence mostly applied only in thin selective layer synthesis, which is due to the classic self-confinement reaction kinetics. Reagents usually have low partition coefficients in the opposite phase or formed solid thin films were not permeable to reagents.[256]

To maximize separation performances the separation layer should be preferably as thin as possible, and supporting substrate as porous as possible to minimize resistance. But in reality it is difficult to manage this trade-off as high support pore density will lead to defective separation layer deposition, when operated under high pressure skin layer will penetrate into porous support causing performance failure with no selective permeation.

In this work, I adopted new series of multi-functional, highly contorted amine monomer in multi-layered polyamide thin film synthesis, through direct one-step interfacial polymerization with commercially available acyl chloride. Free-standing submicron self-supported polyamide (SPA) films were obtained from interfacial polymerization with autonomously formed supporting porous layers underneath. Heterogeneous polyamide structures were formed at solvent interface and inside aqueous phase simultaneously, revealing a brand new film formation mechanism exactly opposite to conventional IP from MPD and TMC. Thicknesses of obtained SPA polymer films could be tuned

from ~ 50 nm up to ~ 2850 nm by controlling monomeric concentrations and reaction time. Under high acyl chloride concentrations (0.1wt%) heterogeneous structures were formed in polyamide films due to TPC crossover and condensation reactions in aqueous phase, under low TPC concentration (0.01 wt%) in oil phase only homogenous layers were formed instead. 2.4 μm SPA membranes showed highest up to 12 L m^{-2} hr^{-1} bar^{-1} acetone solvent permeance in continuous cross-flow filtration and MWCO of < 350 g mol^{-1}. Novel SPA polymer films showed more than 24 folds increment towards BET surface area compared with MPD-TMC polymers. DFT pore size distributions derived from CO_2 adsorption isotherms suggested enhanced microporosity ranged from 4 ~ 8 Å, suggesting larger micropores compared with reported non-porous MPD-TMC polymers. Intrinsic microporosity on such scale facilitates permeation of small solvent molecules but still rejects marker molecules with higher molecular weights due to molecular sieving effects.

Instead of investigating how micropores can affect mass transport in membrane materials, this work rather focused on how micropores can affect polymer thin film formation. And further, this work presents that these novel self-supported microporous polyamide thin films are suitable for organic solvent nanofiltration applications.

4.2 Self-supported microporous polyamide films from IP

This work postulates micropores in crosslinked PIM-type polymer networks affect thin film formation in IP at free liquid-liquid interface. This research reports the synthesis of self-standing microporous polyamide thin films and show asymmetric crosslinked polyamides can be prepared from singular interfacial polymerization (IP). A type of highly contorted norbornene-based tetra-functional dibenzomethanopentacene amine (DBMPA) monomer was used to react with commercially available terephthaloyl chloride (TPC) to prepare crosslinked DBMPA-TPC (SPA-1). (Fig. 26) Here methanol was used as co-solvent in aqueous phase to boost solubility of DBMPA and TPC. Highly contorted DBMPA was directly used as amine reagent dissolved in methanol-water phase to react with di-functional acyl chloride in hexane oil phase. By applying smallest aromatic di-acyl chloride TPC and bulky contorted DBMPA in IP reaction at free liquid interface, TPC was allowed to diffuse through formed interfacial microporous polymer film to continuously react with amines in bottom aqueous phase. It is proposed IP reaction zone is now mainly located in aqueous phase for SPA-1 synthesis, spontaneous heterogeneity of SPA films originates from hydrolyzed DBMPA-TPC dendrimers aggregating in aqueous phase instead of continuing to grow into dense film. (Fig. 27) Both DBMPA and TPC have strong UV adsorption at < 300 nm wavelength even under low concentrations, this is due to their highly conjugated structures. (Fig. S2 and S3) Heterogeneous polyamide structure was formed under high TPC concentration, while homogeneous structures were formed under low TPC concentration or under high DBMPA concentration. This film formation

mechanism is opposite to conventional MPD-TMC thin film assembly at free solvent interface, DBMPA-TPC film is heterogenous with a top skin layer and bottom porous layer with clear boundaries. (Fig. 30)

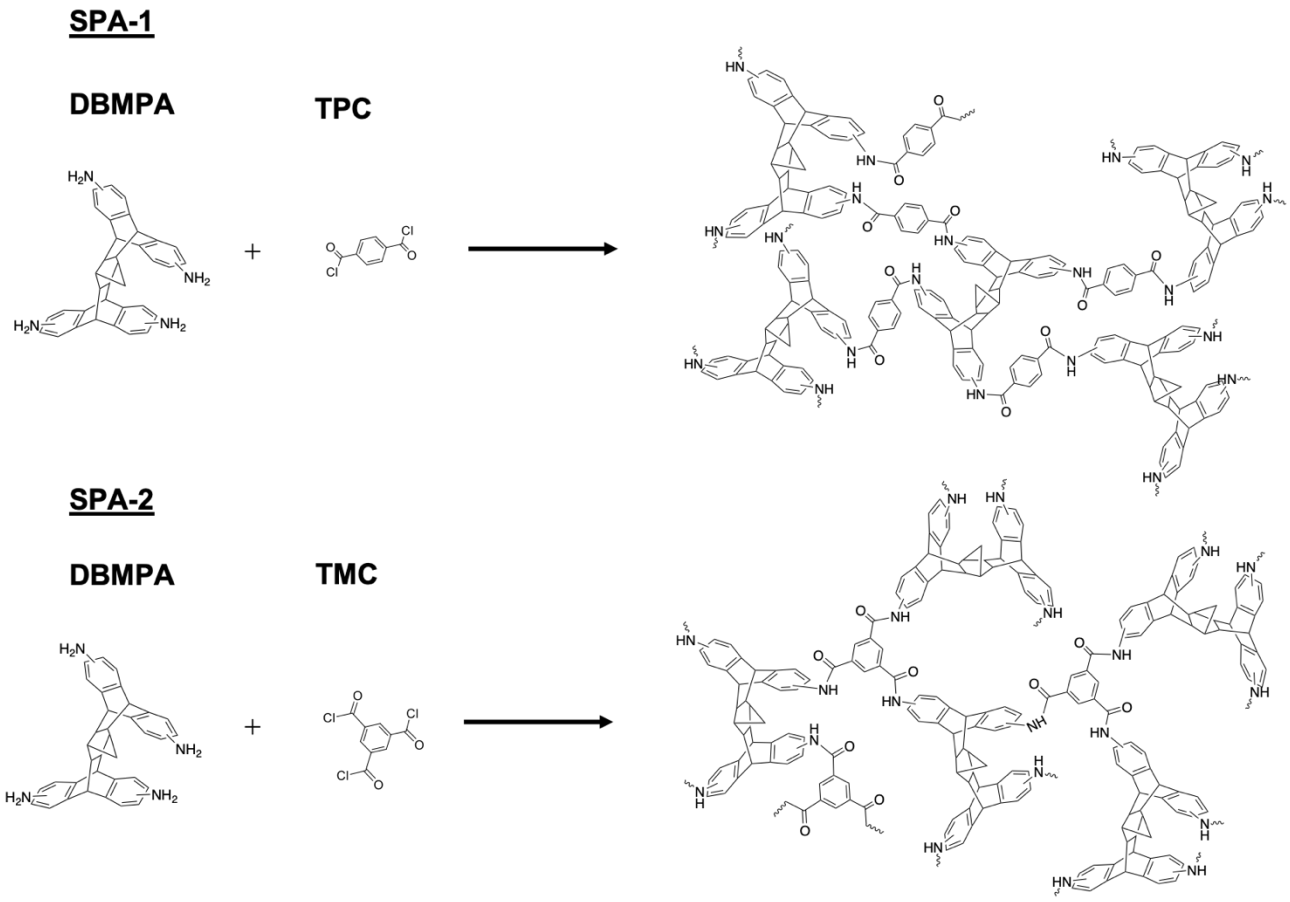


Figure 26. Chemical structures of SPA-1 and SPA-2. DBMPA was used to react with TPC and TMC separately via free-interface interfacial polymerization.

FTIR, BET, AFM, SEM, XPS depth profiling and ellipsometry analysis were conducted on as-synthesized self-standing polyamide films. FTIR of synthesized DBMPA monomer solids indicated successful functionalization with amine groups. (Fig. S1) FTIR spectrums of scattered SPA films confirmed amide bond formation and depletion of primary amines. CO_2 gas adsorption isotherms of SPA-1 and SPA-2 showed high gas uptake under 273K up to 46 $cm^3\ g^{-1}$ STP at 0.03 relative pressure. (Fig. 28b) N_2 gas adsorption isotherms also showed high uptake. DFT Pore size distributions derived from gas adsorption isotherms suggested SPA-1 and SPA-2 polymer films are microporous with sub-1nm pores that are distributed around 4 - 8 Å with similar pore size profiles, meaning number of functional groups in acyl chloride reagent doesn't affect eventual micropore sizes. (Fig. 28d and Fig. S1b)

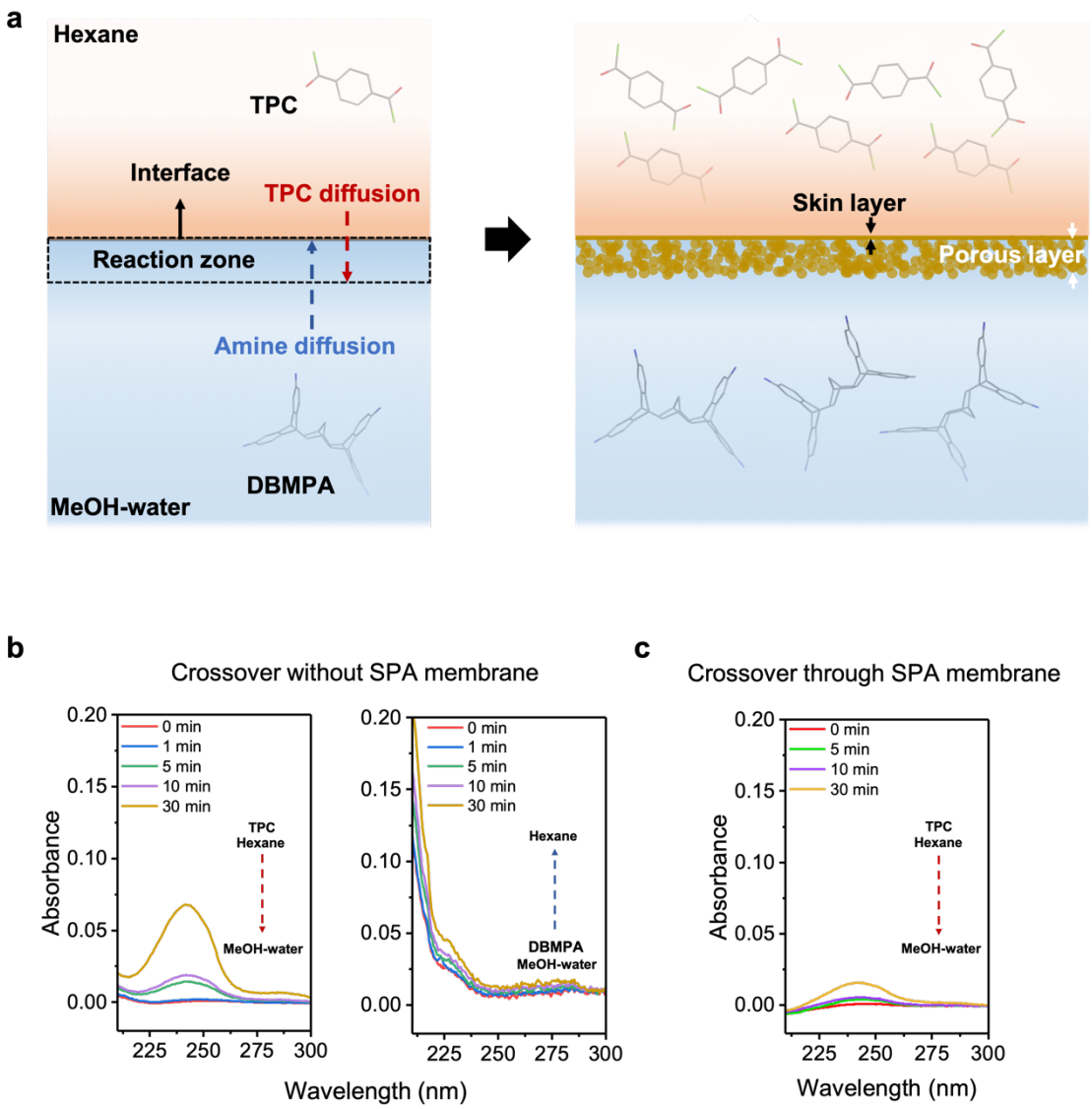


Figure 27. Self-standing polyamide (SPA-1) thin films were formed from free interface interfacial polymerization. A novel type of contorted DBMP amine was first dissolved in MeOH-water then used to react with commercially available acyl chloride TPC dissolved in hexane. a. Schematic showing of free-interface interfacial polymerization of DBMP amine and TPC, and formation of self-standing heterogeneous film comprising of a skin layer and porous layer. b. UV adsorption of opposite phase representing monomer concentration development in the opposite phase due to monomer crossover through liquid-liquid interface. c. UV adsorption representing TPC concentration development in opposite aqueous phase due to monomer crossover through formed SPA-1-150nm film.

SEM samples were captured on AAO supports, no film collapsing or pore penetration into the support were observed. This property suggests DBMPA-TPC self-standing films are robust enough to withstand gravity force on porous supports. TGA and DSC measurements were performed on SPA-1, SPA-2 and MPD-TMC film solids. Both SPA films and MPD-TMC films were stable under 400 ºC with low mass loss. Initial mass loss from MPD-TMC films could be due to incomplete solvent

drying. DSC was particularly used to evaluate glass transition temperatures of SPA polymers, where no transition was observed under 300 °C. These results suggest under room temperature 20 ~ 25 ºC SPA films are in glassy state with stable chemical and physical properties. (Fig. 29) Backbone rigidity of polyamides synthesized from contorted molecular geometry helped constrain segmental movement.

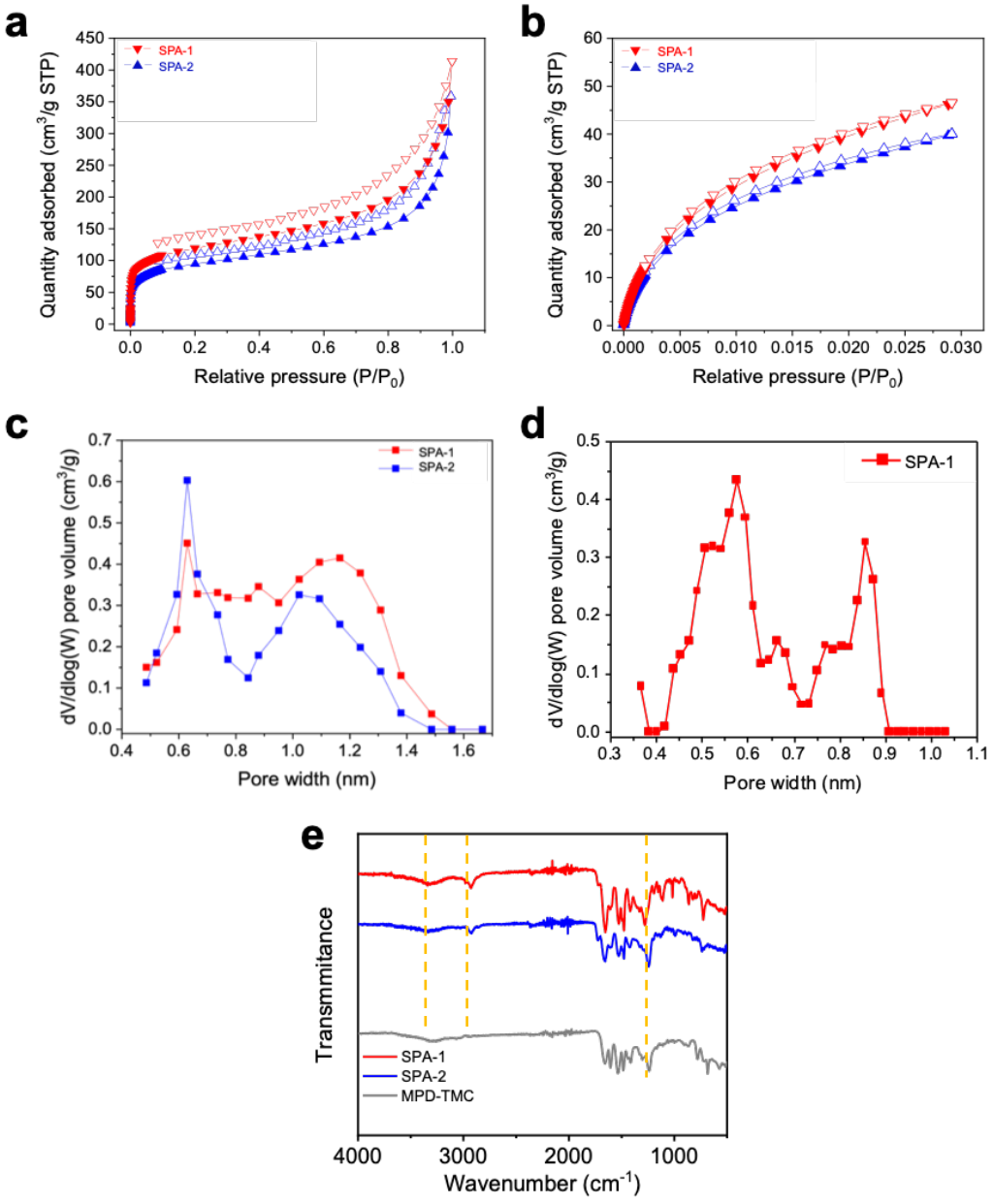


Figure 28. a. N_2 gas adsorption isotherms of SPA-1 and SPA-2. b. CO2 gas adsorption isotherms of SPA-1 and SPA-2. c. DFT pore size distribution of SPA-1 and SPA-2 polymer films derived from N_2 gas adsorption. d. DFT micropore size distributions of SPA-1 polymer films derived from CO_2 gas adsorption. e. FTIR-ATR spectrums of SPA-1, SPA-2 and MPD-TMC films.

Hierarchical microporous gutter-layered polyamide thin film structures formed at free interface were revealed through cross-sectional/surface SEM and ellipsometry. Cross-sectional SEM images

revealed homogeneous structures were formed with 0.06 wt% amine in methanol-water phase and 0.01 wt% TPC concentration in oil phase. (Fig. 30) Heterogeneous structures were formed with 0.06 wt% amine in methanol-water phase and 0.1 wt% TPC monomer concentration in the oil phase. (Fig. 30) Membrane samples were labelled with reagent names, subscripted with weight concentration in each phase solvent.

It was concluded the bottom porous layers were formed from TPC diffusion through microporous SPA films followed by reacting with amines in single aqueous phase. (Fig. 27a) Interfacial SPA film growth should be governed by amide condensation reaction competing with TPC diffusion into aqueous phase. Under high TPC concentration 0.1 wt% most of amide condensation reactions took place in aqueous phase due to high TPC interfacial crossover rate outrunning interfacial reaction rate with amines. (Fig. 27c) Cross-sectional SEM images of SPA films synthesized with 0.01 wt% TPC oil phase concentration revealed almost no bottom porous layer forming. (Fig. 30a) This is due to lower TPC interfacial crossover rate through SPA films under low TPC concentration gradient across the interface into aqueous phase. Hence most of amide condensation reactions took place only near the interface. $DBMPA_{0.06}$-$TPC_{0.01}$ film thickness increased to ~ 200 nm according to SEM imaging maintaining homogeneous structure even after 30 min reaction time span. (Fig. S9b) Interestingly, $DBMPA_{0.25}$-$TPC_{0.1}$ membrane also had homogeneous structure instead of being heterogeneous, with total film thickness up to ~ 300 nm according to SEM. (Fig. S9c) This should be due to increased concentration gradient of DBMPA across the reaction zone forced amines to diffuse to the interface more rapidly, causing majority of condensation reaction now taking place at the interface instead of in aqueous phase.

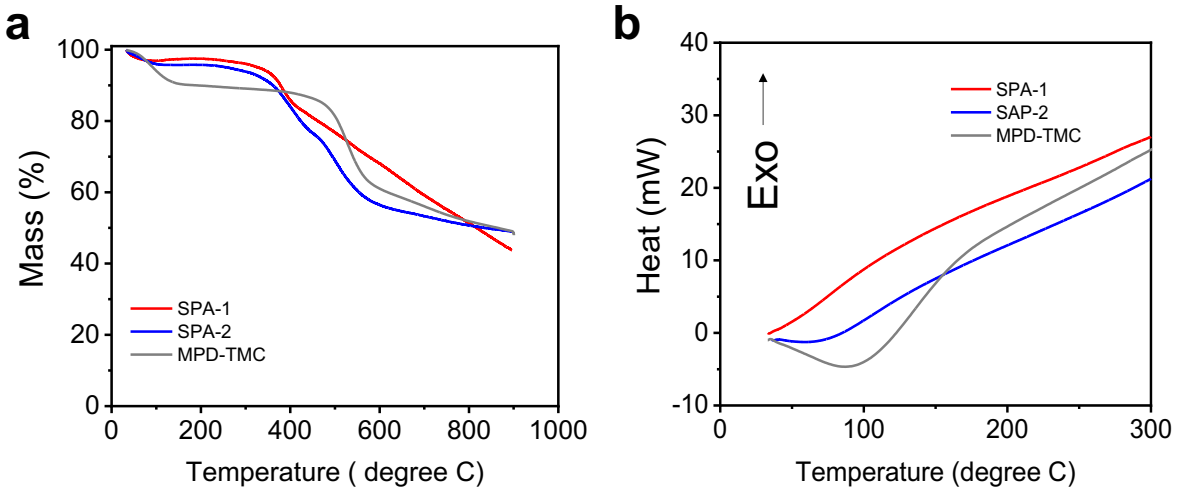


Figure 29. TGA thermal analysis of SPA-1, SPA-2 and MPD-TMC films. b. DSC thermal analysis of SPA-1, SPA-2 and MPD-TMC films.

DFT pore size distributions of SPA-1 membranes showed micropore sizes were around 4 to 8 anstroms. It is due to this particular micropore size distributions that allowed acyl chloride reagent to permeate through formed film that broke traditional self-terminating mechanism. (Fig. 28d and Table. S2) Micropore dimensions of DBMPA-TPC in solvents were not measured due to instrumental limitation. From pore size estimations of porous layer in SPA, it is concluded that only microporous skin layer provides nanofiltration performances. Unsputtered cross-section images of SPA-1 film obtained from FIB SEM revealed genuine porous layer structures, where these intrinsic pores can be on the scale of 50 nm to 150 nm. (Fig. 30a) This result implies porous layer structures should not provide rejections towards dyes < 1000 g mol^{-1} used in nanofiltration.

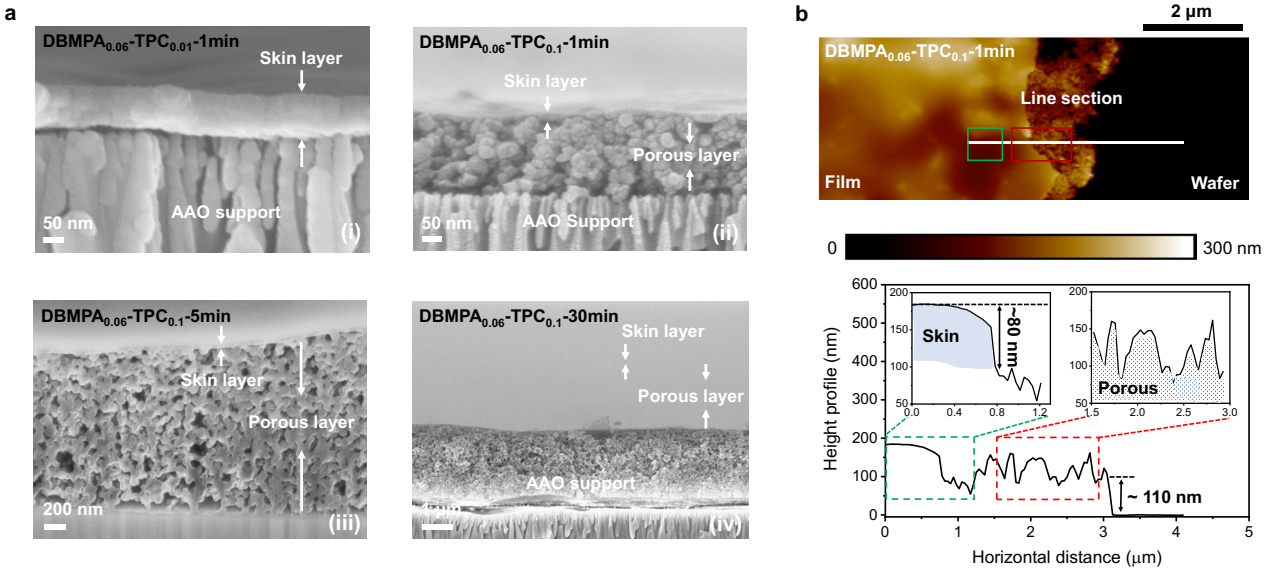


Figure 30. Sputtered and unsputtered SPA-1 film cross-sections and top-view AFM imaging. a. SEM imaging of polymer films on AAO. (i) Cross-sectional SEM images of $DBMPA_{0.06}$-$TPC_{0.01}$-1min film captured on AAO supporting substrates. 0.06 wt% of DBMPA was dissolved in aqueous phase and 0.01 wt% TPC was dissolved in hexane phase. (ii) Cross-sectional SEM image of $DBMPA_{0.06}$-$TPC_{0.1}$-1min membrane captured on AAO supporting substrates. (iii) Zoomed-in cross-sectional FIB SEM image of $DBMPA_{0.06}$-$TPC_{0.1}$-5min membrane captured on AAO supports. Cross-sections were not sputtered. (iv) Cross-sectional SEM image of $DBMPA_{0.06}$-$TPC_{0.1}$-30min membrane captured on supporting substrates. b. Top-view AFM image of $DBMPA_{0.06}$-$TPC_{0.01}$-1min membrane captured on silicon wafer with partial skin layer peeled off. Height profile from AFM analysis suggests skin layer is smoother than porous layer.

Due to heterogeneity of SPA-1 film, thickness of film was not uniform. It can be seen from FIB SEM cross-sectional images that films appeared to be wavy instead of being flat. Cross-sectional FIB SEM image showed porous layer is indeed connected with dense skin layer, surface of porous layer was not smooth and this may cause thickness of whole film layer to vary. This is due to large open pores

in bottom porous layer at the connecting interface with skin layer, that could not provide smooth contact with top skin layer. (Fig. 30b) Thickness of skin layer is rather consistent, but formation of skin layer is heavily dependent on reagent concentrations and amine diffusion through porous layer.

Both SPA-1 and SPA-2 membrane thicknesses increased with increasing reaction time. (Fig. 31) By comparing whole film thicknesses including both skin layer and porous layer structures, overall SPA-2 film grew faster than SPA-1 film under identical reaction conditions. But it is difficult to precisely control porous layer growth underneath the skin layer from existing measures. Growth of each layer with separate pore structures are dependent on each other, and it is postulated that skin layer permeability to reagent TPC can affect porous layer growth underneath. Hence total thickness of one-piece SPA film could have big error ranges measured from top-view AFM. These errors mainly come from porous layer dimensions, as they are not dense films but instead quite spongy and rough rears.

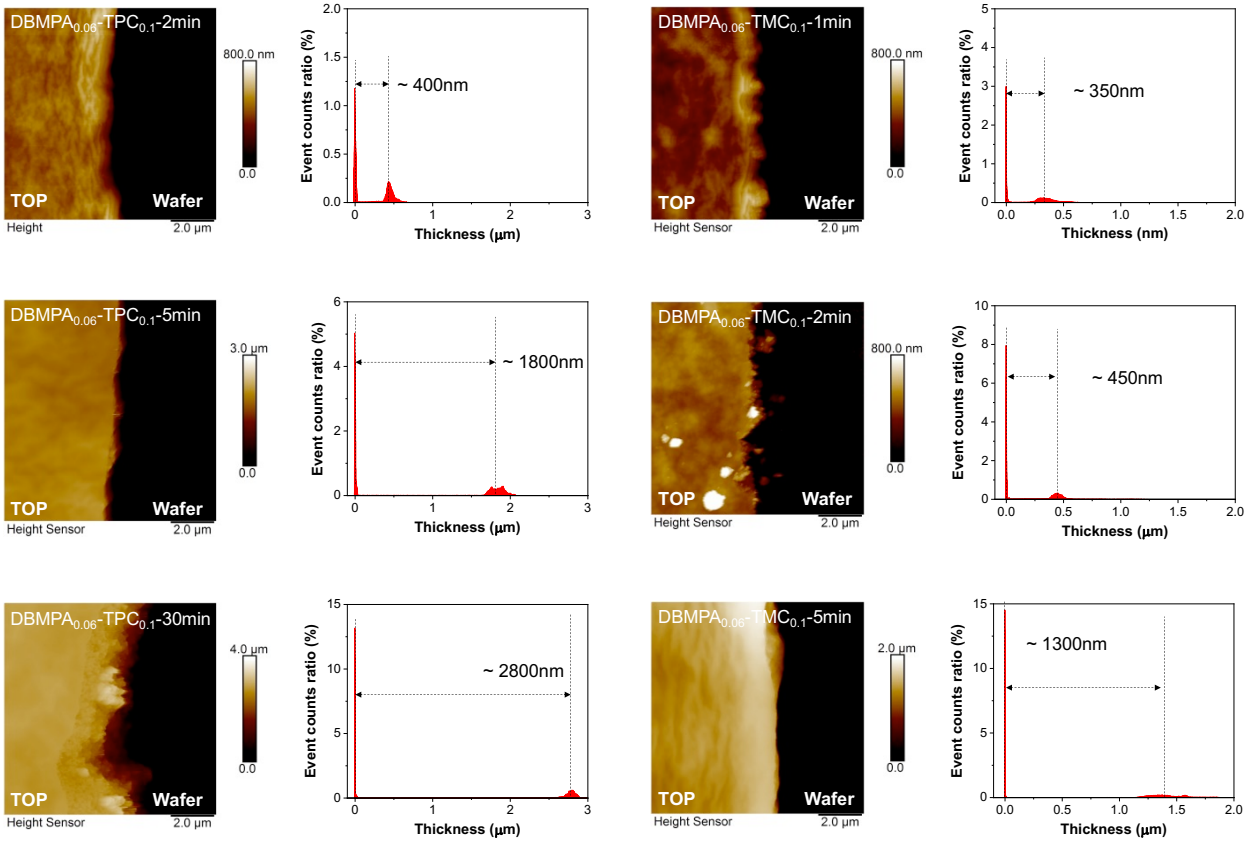


Figure 31. Top-view AFM images of SPA-1 and SPA-2 films synthesized under different reaction time. Overall film thicknesses were evaluated from surface height profile histograms.

To further explicitly investigate film growth of SPA-1, MeOH solvent in the aqueous phase solutions was replaced with alcohols of different viscosities. It was discovered that SPA-1 film growth is much slower with IPA-water as aqueous phase under identical monomer concentrations, reaction time and temperatures. Rough discontinuous films were formed using IPA-water or EtOH-water as aqueous

phase solvents. (Fig. 32 and S6) Films synthesized from EtOH or IPA as aqueous phase co-solvents with 5 minute reaction time did not give rejections in cross-flow filtrations. Films synthesized using IPA as co-solvent can be down to ~ 12 nm thick, but too rough to determine accurate thickness. It can be clearly seen from microscopic images that SPA-1 films synthesized using ethanol-water as sub-phase had isle-like film pieces connected but are defected with visible pin-holes. SPA-1 films formed from IPA-water as sub-phase solvent were also defected with micron scale hole areas. This is due to isopropanol and ethanol have higher viscosity than methanol (2.4 cP, 1.2 cP and 0.6 cP separately under ~ 293 K), hence amine diffusion rate from bulk of sub-phase towards the solvent interface is much slower especially in viscous solvents. Within short reaction time continuous films could not be formed using viscous alcohols. This result implies application of viscous solvent is not desirable for rapid film forming process. It is worth noting here using isopropanol as aqueous phase co-solvent in IP reaction did not yield dense skin layer structure in film synthesis. (Fig. S6) But instead only porous defected layer structure was formed.

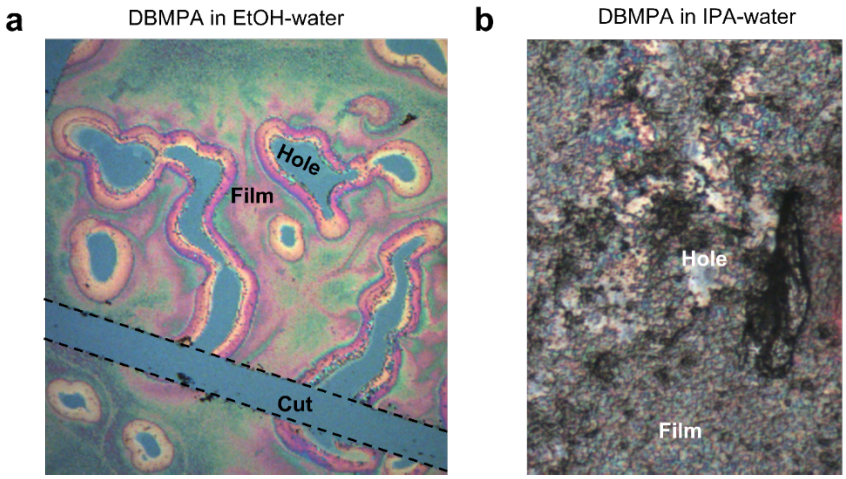


Figure 32. Microscopy images of SPA-1 films synthesized using ethanol and isopropanol as co-solvents in aqueous phase separately.

To conclude, singular free-interface interfacial polymerization of contorted amines and acyl chlorides can form both heterogeneous and homogeneous structures as a result from simply controlling reagent concentrations. Enhanced micropore dimensions in SPA-1 polymer and boosted solubility of acyl chloride are key to achieving this. Under identical concentrations of DBMPA and TPC, changing reaction time does not change overall film structures but rather only thicknesses. During progression of continuous film growth up to micron-level, it was mainly porous layer thicknesses increasing ~ 20 folds from 150 nm SPA membrane to 2400 nm SPA membranes. This suggests film formation of SPA membranes is most relevant to monomer diffusion kinetics.

Table 5. SPA membranes samples with synthesis conditions including monomer concentrations, film thicknesses and acetone permeability. a. In standard sample labelling such as DBMPA0.06-TPC0.1-2min, 0.06 stands for 0.06 wt% of DBMPA was dissolved in aqueous phase solvent, 0.1 stands for 0.1 wt% of TPC was dissolved in hexane phase, 2min means reaction was allowed to progress for 2 minutes. b. Solvent permeability was calculated based on standard deviations from parallel solvent permeance measurements and averaged membrane thickness.

Membrane	Rex conditions	IP layer Thickness (nm)	Acetone permeability ($10^{-10}cm^2s^{-1}bar^{-1}$)
SPA-1-50nm	$DBMPA_{0.06}$-$TPC_{0.1}$-10s	50 ± 31	19 ± 1[b]
SPA-1-150nm	$DBMPA_{0.06}$-$TPC_{0.1}$-1min	150 ± 50	40 ± 10
SPA-1-450nm	$DBMPA_{0.06}$-$TPC_{0.1}$-2min[a]	450 ± 41	56 ± 34
SPA-1-1300nm	$DBMPA_{0.06}$-$TPC_{0.1}$-5min	1300 ± 470	45 ± 26
SPA-1-1400nm	$DBMPA_{0.06}$-$TPC_{0.1}$-17min	1400 ± 310	110
SPA-1-2400nm	$DBMPA_{0.06}$-$TPC_{0.1}$-30min	2400 ± 520	460 ± 210
SPA-2-350nm	$DBMPA_{0.06}$-$TMC_{0.1}$-1min	350 ± 51	18 ± 8
SPA-2-580nm	$DBMPA_{0.06}$-$TMC_{0.1}$-2min	580 ± 120	19 ± 2
SPA-2-1100nm	$DBMPA_{0.06}$-$TMC_{0.1}$-5min	1100 ± 350	200 ± 15
MPD-TMC	$MPD_{0.06}$-$TMC_{0.1}$-1min	16 ± 4	0.09 ± 0.02

4.3 Asymmetry of polyamide and layer properties

Interfacial polymerization is known to be capable of preparing ultra-thin membranes. Both monomers diffuse from each liquid phase to react at the interface under concentration gradient and chemical potential. After polymer solid film formation at the interface, diffusion rates of monomers in solids are dramatically hindered thus terminating the reaction itself.

Free-interface IP of MPD-TMC membranes is most renowned for such mechanism, as MPD-TMC membranes are tight and almost impermeable to most salts and organic molecules alike. Hence both amine and acyl chloride monomers could hardly diffuse through MPD-TMC membranes to promote further reaction. Film growth is rapidly terminated after dense solid MPD-TMC film formation. Albeit due to reaction heat generation and solubility of MPD in hexane, amide polymerization can be extended into oil phase. Monomer diffusion experiments through MPD-TMC membranes suggest TMC could not trespass the solid layer at least within short time frame, which helps validify self-confinement in traditional polyamide thin film formation where reagents were forced to react near liquid interface and then terminated. In addition, MPD is soluble in hexane and has lower molecular weights, while DBMPA appeared to have poor solubility in hexane. (Fig. S4) According to existing knowledge MPD crossover into hexane phase through solid films and exothermic amide condensation are major causes to crumpled texture formation on the top of the nanofilm into oil phase. Reaction zone of know interfacial polymerization of polyamides has been summarized to be at the interface and into the oil phase.

DBMPA-TPC film can be synthesized from IP and transferred to a water bath. (Fig. 33a) Surface of membrane with 30 min reaction still showed no sign of nodules, which were usually caused by interfacial turbulence from classic IP. (Fig. 33b) XPS etching experiment suggested crosslinking degree of polyamides decreased from surface skin layer structure into porous layer structure. This helped explain porous layer chemical structure where they were loosely and less crosslinked with side reactions in water. (Fig. 33c) Ellipsometry suggests one-piece membrane had a shifting refractive index, implying different structures co-exist. (Fig. 33d and 33e) AFM nano-indentation was performed on one-piece SPA film, when probing from top surface modulus of SPA-1 was evaluated to be 2.3 GPa. (Fig. S5) This value is slightly higher than reported PIM-1 membrane with a Young's modulus of 1.9 ± 0.1 GPa. These measurements imply that contorted molecular structure is beneficial towards preparing high modulus polymer materials.

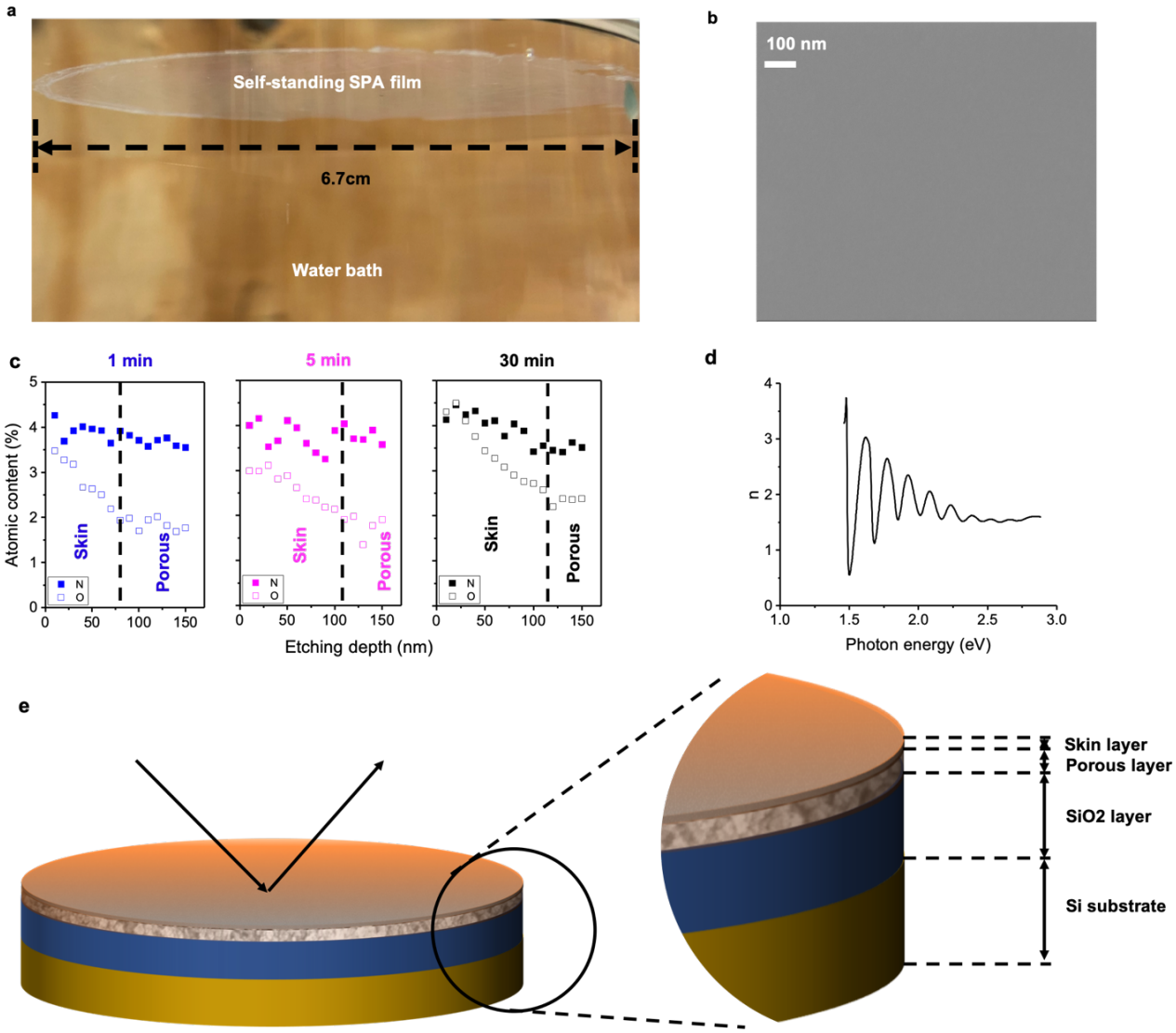


Figure 33. XPS depth profiling and elipsometry techniques were further used to analyze properties of skin layers and porous layers. a. Appearance of self-standing SPA-1 film formed from 0.06 wt% DBMPA and 0.1 wt% TPC over 1 minute floating on water bath. b. Top-view SEM surface image of SPA-1film synthesized over 30 minutes. c. XPS depth profiling of SPA-1 film synthesized over 1 minute, 5 minutes and 30 minutes. And skin/porous layer thickness measurements from elemental analysis. d. Light refractive indices throughout entire SPA-1 IP film. e. Schematic showing of different layers of SPA-1 film deposited on silicon wafer.

XPS elemental composition of SPA suggests almost no Cl elements were present in SPA-1 self-standing films. XPS depth profiling of SPA-1 films indicate Cl element was almost completely depleted through ~ 100 nm out of entire film thickness. Surface Cl element signals may be from residue TPC left on top of the films. (Fig. 34)

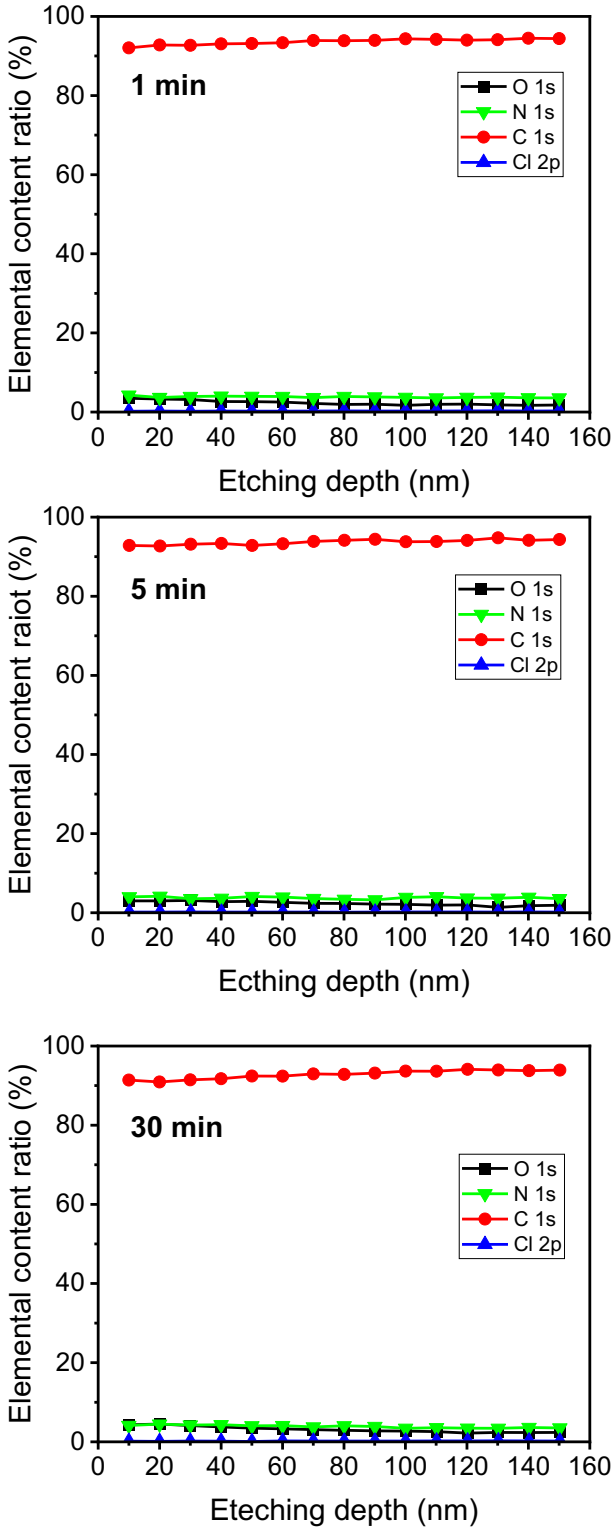


Figure 34. XPS elemental etching analysis of SPA-1 membranes synthesized with 1min, 5min, 30min reaction time.

Compared with reported MPD-TMC polyamide, SPA has exceptionally high carbon element content which took up > 90%. This is due to DBMPA (8.8) has higher C/N elemental ratios than MPD (3.0). (Table. 6)

Table 6. Element counts and molecular weights of monomers.

	C	N	O	Cl	H	MW (g mol^{-1})
DBMPA	35	4	-	-	32	509
MPD	6	2	-	-	8	108
TPC	8	-	2	2	4	203
TMC	9	-	3	3	3	265

IP thin synthesis of SPA-1 no longer terminates at the interface. DBMPA has large molecular weight and is not soluble in hexane with low partition coefficient, thus DBMPA would not diffuse through solid SPA membranes. Over 30 min of time elapse almost no DBMPA diffused from aqueous phase into oil phase through liquid-liquid interface even without membrane, where TPC was able to diffuse through the same interface from oil phase to aqueous phase much more rapidly. (Fig. 27b) In the presence of SPA-1-150nm membrane TPC was still able to diffuse across liquid-liquid interface and the membrane, while in contrast with the presence of pristine PAN support with ~ 20 nm pore size TPC was also able to diffuse into aqueous phase with seemingly faster rate. (Fig. 35a) It should be noted here thickness of PAN could vary from different samples as well as pore properties, it is considered this experiment could not accurately determine quantitative diffusion rates of TPC through PAN membrane. It was not possible to observe valid crossover of TMC from hexane phase into aqueous phase through solid MPD-TMC membrane. (Fig. 35b)

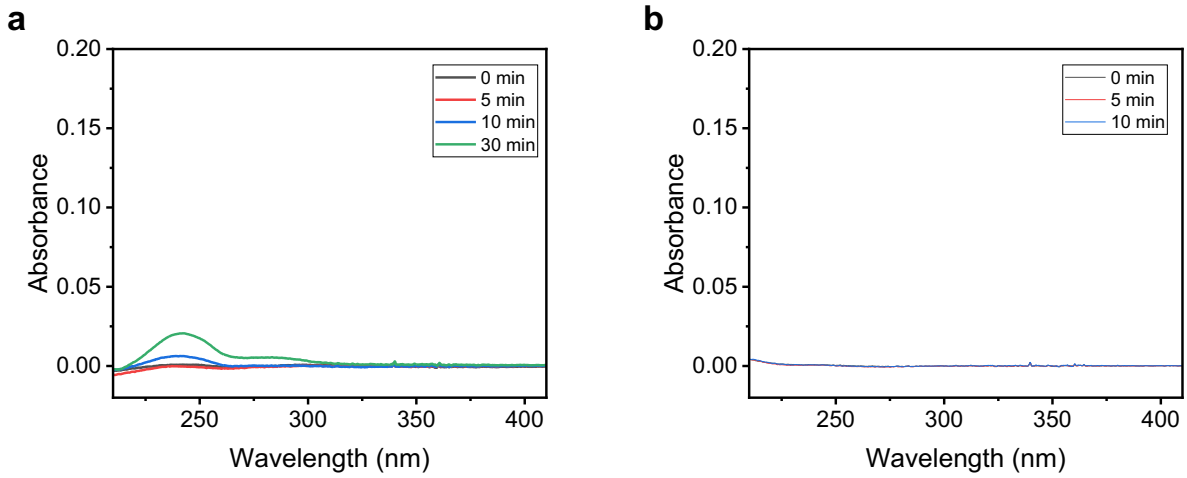


Figure 35. UV adsorption of opposite phase. a. Diffusion of TPC from hexane phase into methanol-water phase through pristine PAN support. b. TMC diffusion from hexane phase into water aqueous phase through 20 nm MPD-TMC nanofilm on PAN support.

Novel thin film formation mechanism of microporous films at free-interface interfacial polymerization is now no longer self-confined, hence self-termination of reaction is no longer valid.

Interfacial skin layer film formation is governed by interfacial reaction rate between DBMPA and TPC, DBMPA diffusion rate from aqueous phase into hexane phase and TPC diffusion rate from hexane phase into aqueous phase. Bottom porous layer formation in aqueous phase is mainly governed by TPC diffusion rate across liquid-liquid interface and solid SPA interfacial film, because the reaction is directly taking place in aqueous phase while solution environment has abundant and excessive amine monomers in presence. It is concluded that, a) Comparable diffusion rates of both -NH_2 and -COCl towards near interface contribute to single dense layer forming, b) Higher diffusion rate of -COCl groups over -NH_2 groups contribute to dense layer plus porous layer forming, since TPC can still permeate through formed SPA-1 film and is very soluble in aqueous phase due to existence of methanol, c) Since DBMPA is poorly soluble in hexane phase, higher -NH_2 groups diffusion rate over -COCl rates contribute to single dense layer forming. While diffusion rates of -COCl groups into aqueous phase is significantly higher than -NH_2 groups diffusion rates to near interface, only porous layer will be formed. (Fig. 36 and Fig. 37) Concentration threshold still awaits experimental determination.

Conventional self-terminating mechanisms in IP is usually due to impermeability of formed solid film to reagents. Only 10 to 30 nm films were formed which does not consume much of reagents. On the contrary, in SPA film synthesis self-termination is no longer valid. This phenomenon suggests reagents kept being consumed during the reaction process. This leads to thick film forming and concentrations of both reagents changing much more rapidly over time. Compared with reported < 20 nm thick MPD-TMC nanofilm from IP at free liquid-liquid interface, SPA-1 film could consume ~ 150 times more reagent mass assuming same densities. Hence heterogeneous SPA film formation is dynamically dependent, during film formation concentrations of amines and acyl chlorides are changing over time. This has made it difficult to control the IP process of asymmetric thin film synthesis, including thickness of separate layers.

AFM surface peak force mapping and height profiling suggests only porous layer structures were formed under low amine concentration. (Fig. 36a) Under low amine concentration $DBMPA_{0.01}$-$TPC_{0.1}$-1min membranes were < 100 nm thick with rough surfaces, surface properties of films synthesized from ultra low DBMPA concentrations resemble only porous layer structures in SPA-1. (Fig. 37a and Fig. 37c) This is due to under low DBMPA concentration 0.01 wt% and high TPC concentration 0.1 wt%, before DBMPA monomers diffused to near interface most of amine reagents already reacted with excessive TPC in aqueous phase.

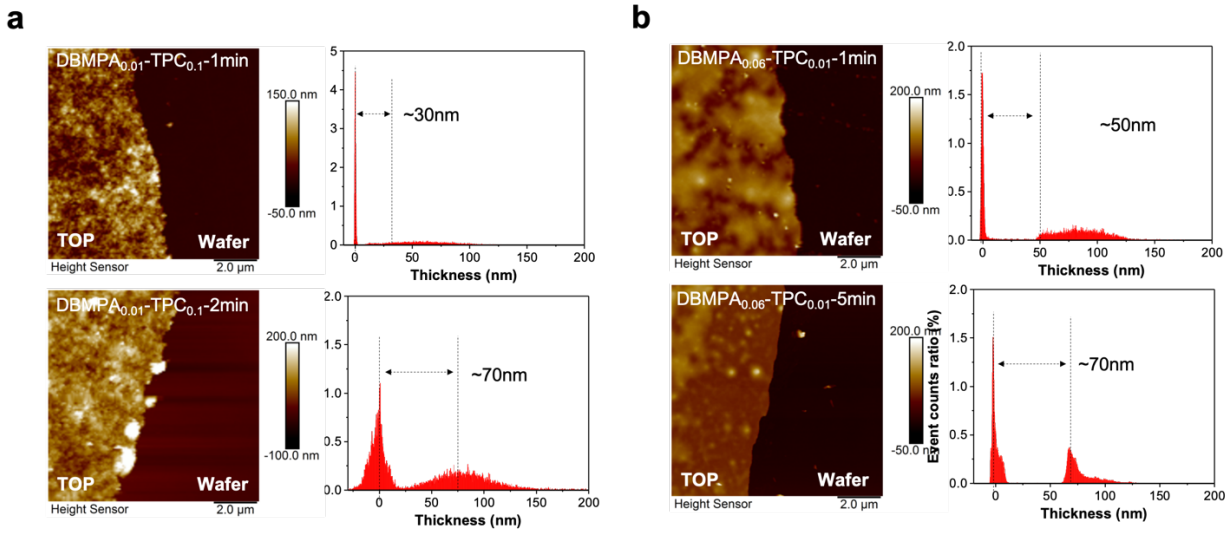


Figure 36. Top-view AFM height profiles of DBMPA-TPC films formed under different monomer concentrations and reaction time. a. DBMPA-TPC films formed using low DBMPA concentration (0.01 wt%) in aqueous methanol-water phase. b. DBMPA-TPC films synthesized under low TPC concentration (0.01 wt%) in hexane.

Deficiency of amines towards near interface did not allow dense skin layer structure to form at interface. Hence majority of amide condensation took place far from the interface but into aqueous phase.

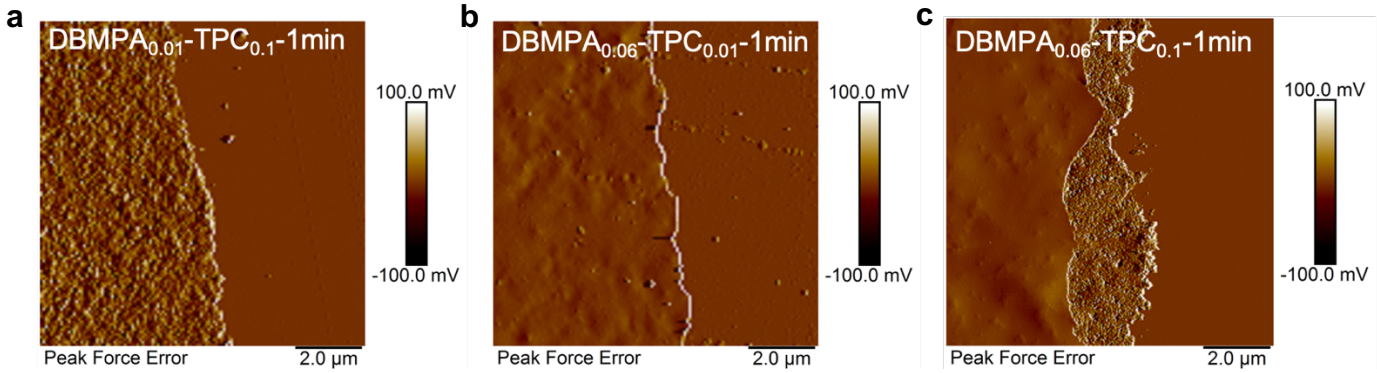


Figure 37. AFM peak force error imaging of DBMPA-TPC films synthesized under 1 minute reaction time using different monomer concentrations. With ultra low DBMPA concentration and high TPC concentration only porous layer structure was formed. With intermediate DBMPA concentration and low TPC concentration only skin layer dense structure was formed. With intermediate DBMPA concentration and high TPC concentration distinguishable asymmetric structures was formed.

Under 0.1 wt % concentration TPC rapidly diffused into aqueous phase, amines were mostly consumed in aqueous phase before reaching near the interface. In contrast, while DBMPA$_{0.06}$-TPC$_{0.01}$-1min had smoother and continuous surfaces, this result is rather consistent with SEM images where under this reaction condition only skin layer structure was formed. (Fig. 37b and Fig. 38a)

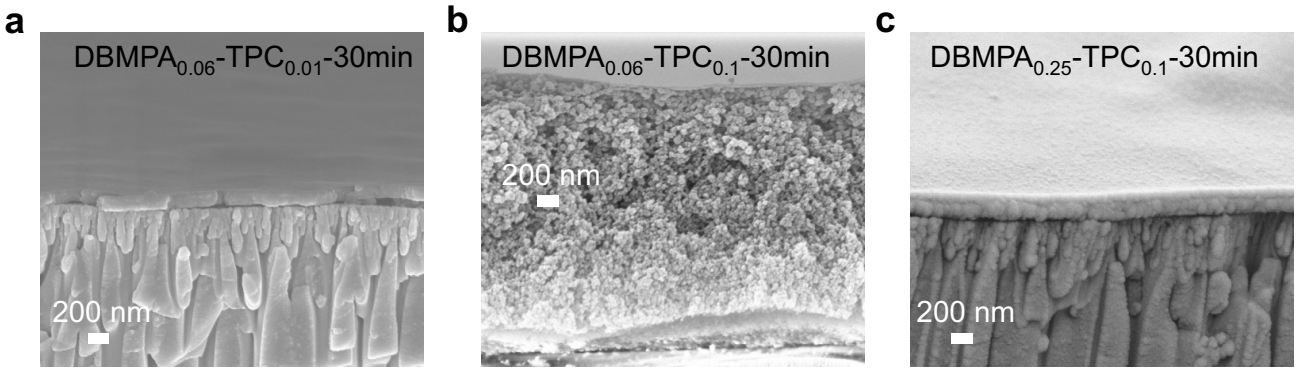


Figure 38. Cross-sectional SEM images of DBMPA-TPC films synthesized over 30 minutes, but with different monomer concentrations. a. SEM cross-sectional image of DBMPA-TPC film synthesized with 0.06 wt% amines in aqueous phase and 0.01 wt% TPC dissolved in hexane phase. b. SEM cross-sectional image of DBMPA-TPC film synthesized with 0.06 wt% amines dissolved in aqueous phase and 0.1 wt% TPC dissolved in hexane phase. c. SEM cross-sectional image of DBMPA-TPC film synthesized with 0.25 wt% amines dissolved in aqueous phase and 0.1 wt% TPC dissolved in hexane phase.

Despite no nodule-like textures were formed on membrane front-side in contact with TPC-hexane phase, surfaces of SPA membranes are not complete smooth but with convex structures on the surface of membranes. A cross-sectional cut of these 'bumps' revealed they are hollow inside, but with loosely connected solid clusters beneath the film. SPA film thickness increased with increasing reaction time. Localized convex structures were formed in both heterogeneous and homogenous SPA films. This is due to tetra-functional DBMPA being more reactive than MPD hence releasing more heat from exothermic amide condensation, causing localized turbulence of solvent interface. Since SPA film growth progresses very rapidly. Much thicker films were formed compared with MPD-TMC nanofilm, hence thick SPA films do not excessively bend or crumple but instead is driven by buoyancy to form these convex structures. Moreover, cross-sectional cut of one convex structure in SPA film on AAO support showed cluster build-up inside the convex structures. Aggregation of unconnected oligomer clusters beneath the SPA film can also lead to these small 'tent' features to form because of random solid build-up. (Fig. 39) It is believed these convex structures can benefit molecular transport as they increase active membrane areas in filtration.

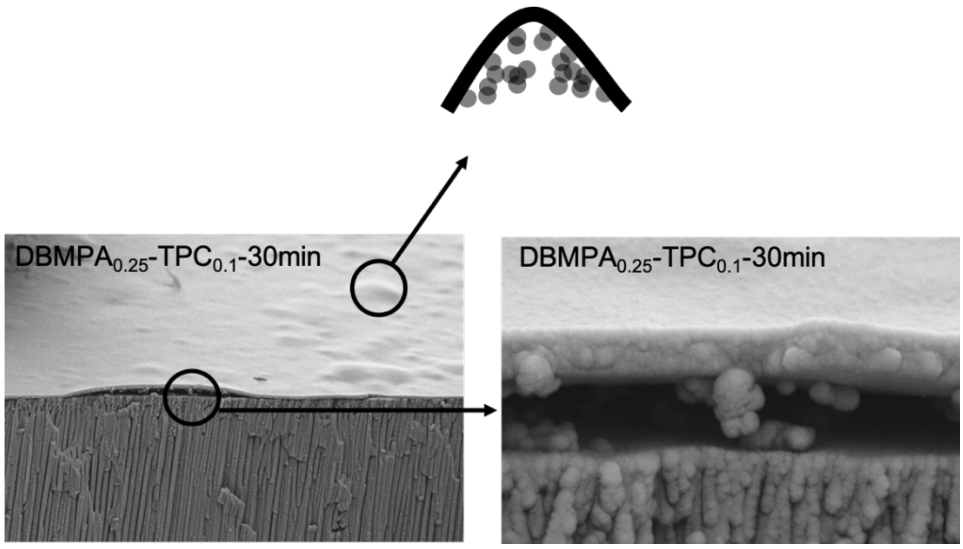


Figure 39. SEM cross-sectional image of convex structures that created small 'bumps' on the film.

Moreover, direct polymerization of TPC and DBMPA dissolved in methanol-water solvents was performed using identical amine concentrations. (Fig. 40) From SEM surface analysis of obtained DBMPA-TPC powder-like solids suspending in the liquids, identical structures with porous layers from films synthesized with 0.1 wt% TPC oil phase concentration were observed.

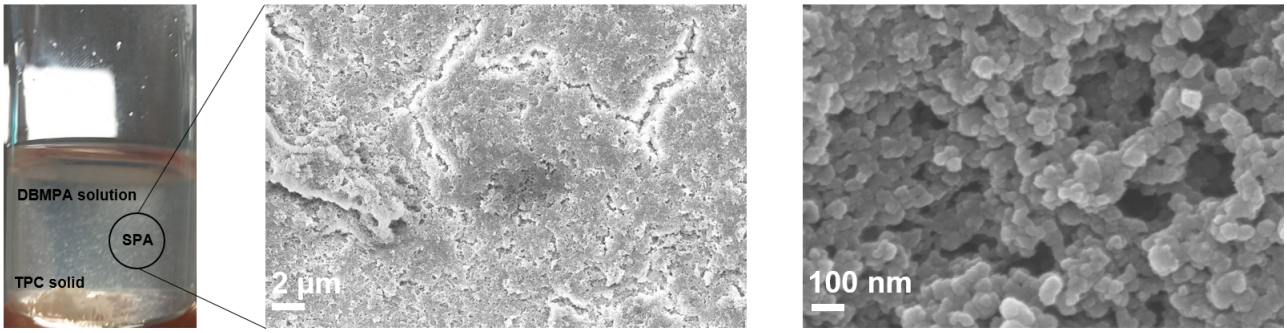


Figure 40. TPC solids were directly added into 0.06 wt% DBMPA solution in methanol and water. Vial reactor was gently shaken for about 1 minute then left for ~ 10 minutes. Powder-like suspension formed as a result. SEM surface imaging suggests the powder like clusters had close resemblance with porous layer structures in SPA films.

4.4 Enhanced solvent permeability from SPAs

Surprisingly, pure acetone solvent permeances do not decrease correspondingly with increasing film thicknesses. Calculated permeability of SPA membranes increased dramatically with increasing film thicknesses, whilst SPA-1-2400nm membranes have highest permeability > 200 10^{-10} cm^2 s^{-1} bar^{-1} than membranes with thinner SPA layers with equivalent rejections. (Table. 5) SPA-1-2400nm PAN

membranes have comparable acetone solvent permeances with thinner SPA-1-450nm membranes. (Fig. 41d) This result indicates growth of films did not increase resistance of SPA membranes. From cross-sectional SEM of SPA-1 films formed from different reaction time, growth of SPA film top skin layer was very slow. Over 1 min to 5 min reaction time film skin layer only grew from ~ 50 nm to ~ 100 nm, whilst entire IP SPA layer grew from specifically 150 ± 50 nm to 1300 ± 470 nm numerically counting in more significant figures from instrumental analysis. This is due to fast-forming porous layers in aqueous phase compromise diffusion of amines from aqueous phase to the interface. As TPC diffusion progresses which leads to thicker porous layers continuously being formed in aqueous phase, fewer amine molecules could traverse the solid porous cluster layer to reach the interface.

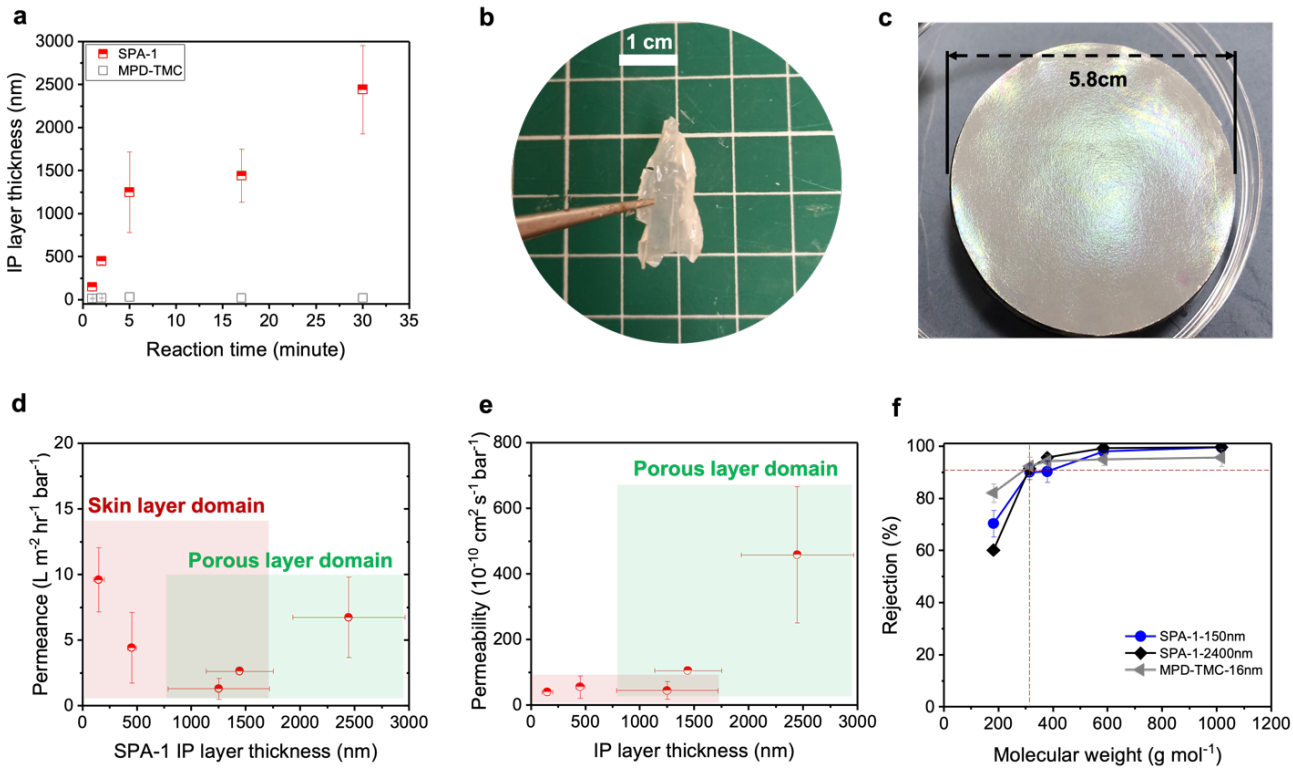


Figure 41. Film layer growth profile and separation performances using dye as markers. a. SPA IP film layer thickness development against reaction time measured from AFM, MPD-TMC nanofilm thicknesses against reaction time measured from AFM. b. Dried self-standing SPA-1 film synthesized over 120 minutes using 0.06 wt% DBMPA and 0.1 wt% TPC. SPA-1 film can now be directly picked up by mechanical force after drying. c. SPA-1 membrane synthesized over 1 minute reaction time deposited on PAN supporting substrate. d. Acetone permeances vs SPA-1 IP layer thicknesses. Pure acetone permeance was tested under 10 bar and 80 L hr-1 flow rate in a continuous cross-flow filtration RIG. e. Escalating acetone solvent permeability vs thicknesses of SPA-1 IP layers. f. Dye marker rejections of SPA-1-150nm, SPA-1-2400nm and MPD-TMC-16nm membranes in acetone solvent under continuous cross-flow filtration.

Cross-sectional images of SPA-1-1300nm and SPA-1-2400nm showed almost identical skin layer thicknesses while SPA-2400nm has doubled overall film thickness mainly due to thicker porous layer. This result further indicates growth of porous layers at rear of films does not provide resistance as much. On the contrary, the porous layers formed at rear of films function as gutter layers to enhance overall film permeation efficiency. (Fig. 41e) This gutter-layer effect contributed to permeability of SPA-1 membranes increasing significantly with membrane thicknesses. Due to overlapping error bars it is considered membrane selectivity in acetone solvent was stable and not significantly influenced by thickness. (Fig. 41f and Fig. 42) SPA-1 had < 20% NaCl rejections in water, while SPA-2 had higher NaCl rejections under same conditions. (Fig. S11) It could be due to residue -COCl groups hydrolysis that increased electrostatic repelling of ions. SPA-1-50 was an instant polymer film formed from IP with 10s reaction time. Instant SPA films may not be defect-free or have lower crosslinking degrees. It is worth noting here SPA-1-50 with 50 nm total film thickness had significant higher MWCO than thicker SPA-1 membranes.

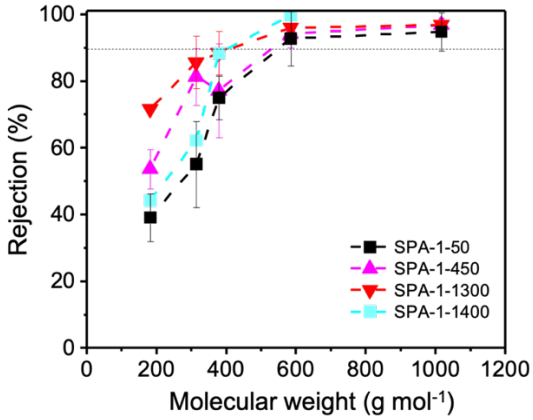


Figure 42. Dye marker rejections of SPA-1 TFC membranes with thicknesses in acetone solvent, in cross-flow filtration under 10 bar 80 L hr^{-1} flow rate.

SPA-1 and SPA-2 self-standing films both showed water contact angles < 90ºC which is comparable with MPD-TMC. Suggesting hydrophilic nature of polyamides. (Fig. 43) Initial 0 second contact angles of acetone, methanol, acetonitrile and hexane liquid drops on membrane surfaces were either < 10 ºC or could not be observed. This result suggests SPA membranes have good surface affinity for organic solvents, both polar and non-polar organic solvents rapidly wetted membrane surfaces followed by fast dissolution into bulk of membranes. On the other hand, solvent evaporation could be another cause since only 20 microliter liquid drops were used.

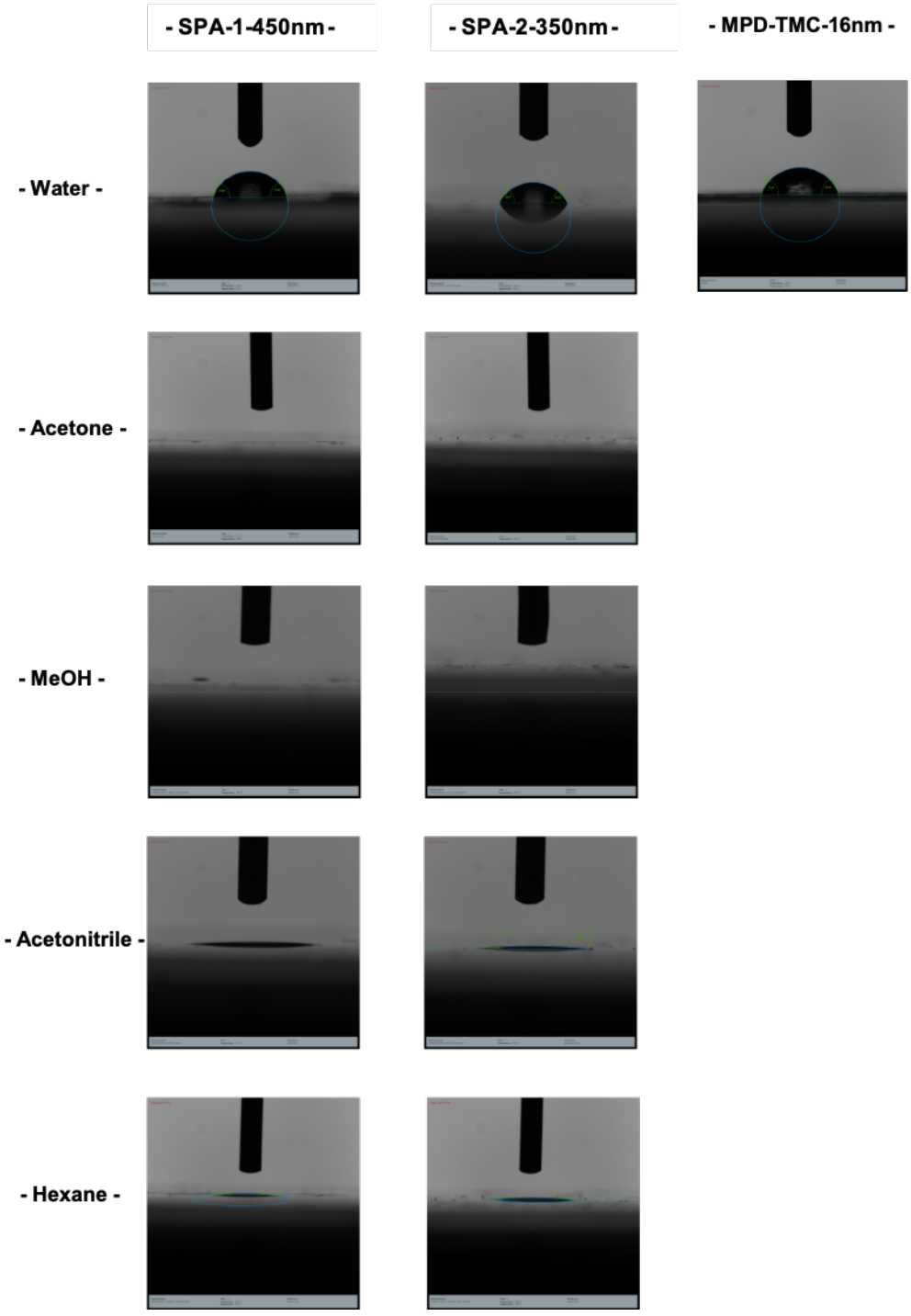


Figure 43. Contact angles of water and organic solvents on SPA-1, SPA-2 and MPD-TMC films captured in quartz crystals.

Despite SPA membranes are thick while controlling polymerization progressing in aqueous phase is difficult, entire membrane from one-step synthesis showed superior acetone permeability. SPA-1-2400nm membranes have more than 100 folds higher solvent permeability than our previously reported sub-20nm polyester nanofilm membranes, and almost doubled acetone permeances with comparable MWCOs. Compared with MPD-TMC-PAN membranes synthesized from free-interface

interfacial polymerization, SPA-1-2400nm membranes have hundreds of times higher acetone permeability than MPD-TMC membranes, despite they are > 100 times thicker.

4.5 Clean rejections for charged solutes in organic solvents

To mitigate concentration polarization near membrane surfaces, nanofiltration experiments were performed in sub-pilot-scale cross-flow filtration using readily prepared SPA-PAN flat-sheet TFC membranes. Self-standing SPA films were captured on top of solution casted PAN supports. No delamination of IP layers was observed after drying under ventilated conditions. After > 1 week of continuous cross-flow filtration of different dye markers, SPA-1 membrane surface was still clean without severe solute adsorption. Pinkish colours near the edge of membrane was credited to cross-flow fluid patterns near dead-zone in the filtration cell.

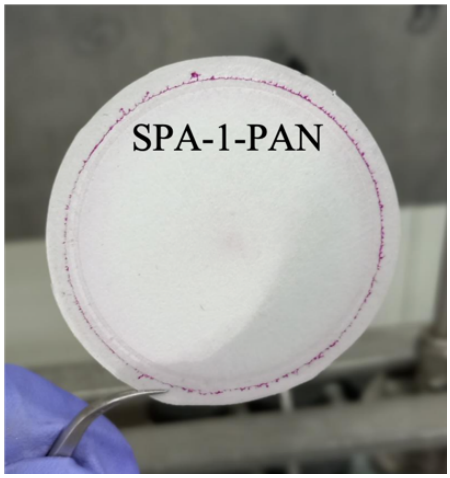


Figure 44. SPA-1-PAN TFC membrane appearances after consecutive dye rejections in acetone over ~ 1 week.

Several neutral and negatively charged dye molecules were chosen as solutes in acetone solvent to determine MWCOs. MPD-TMC nanofilm membranes with flat morphology have low permeances as well as permeability (< 0.1 10^{-10} cm^2 s^{-1} bar^{-1}) as shown in table 5, but high rejections for solutes with a MWCO ~ 320 g mol^{-1}. SPA-1 membranes have MWCOs of ~ 320 g mol^{-1}. Both SPA and MPD-TMC membranes have > 96% rejections towards Rose Bengal (1018g mol^{-1}) and Acid Fushin (585 g mol^{-1}). (Fig. 44) Polyamide membranes were directly deposited on both PAN and PBI supports and immersed in negatively charged dye Acid Fushin in acetone solvent with 25 ppm concentration. After > 2 days of dye solution treatment both PA-PAN and PA-PBI membranes showed negatively charged dye adsorption. However, it can be seen that pristine PAN membranes and PBI membranes also had dye solute uptake compared with TFC membranes. This implies that TFC membrane dye solute uptake during solution immersion is mainly due to support membranes. (Table. 7)

Interestingly, PA-PAN membrane had slightly lower dye solute uptake than pristine PAN membrane, similarly PA-PBI membrane had lower dye solute uptake than pristine PBI membrane. This could be due to the front surfaces of PAN and PBI support membranes were coated with polyamide IP layers, IP polyamide layer did not have adsorption for negatively charged dyes thus decreased contact area between support membranes and dye solutions.

Table 7. Dye adsorption of SPA-2 TFC membranes compared with pristine supports.

	Concentration	Days in solutions	Dye content adsorbed
ACF feed	25.05 ppm	-	-
PA-PAN	17.93 ppm	6	28.4%
PA-PBI	1.84 ppm	2	92.7%
PAN	16.15 ppm	6	35.5%
PBI	0.65 ppm	2	97.4%

Pristine PBI surfaces can be protonated hence had 97.4% adsorption for negatively charged ACF solute, compared with PAN membrane PBI membrane had significantly higher dye solute uptake. (Fig. 45) PA-PBI membranes still adsorbed 92.7% of dye markers in acetone, which is due to porous structures in PBI that allowed diffusion of dyes from solutions into membranes likely from rear of PA-PBI membrane.

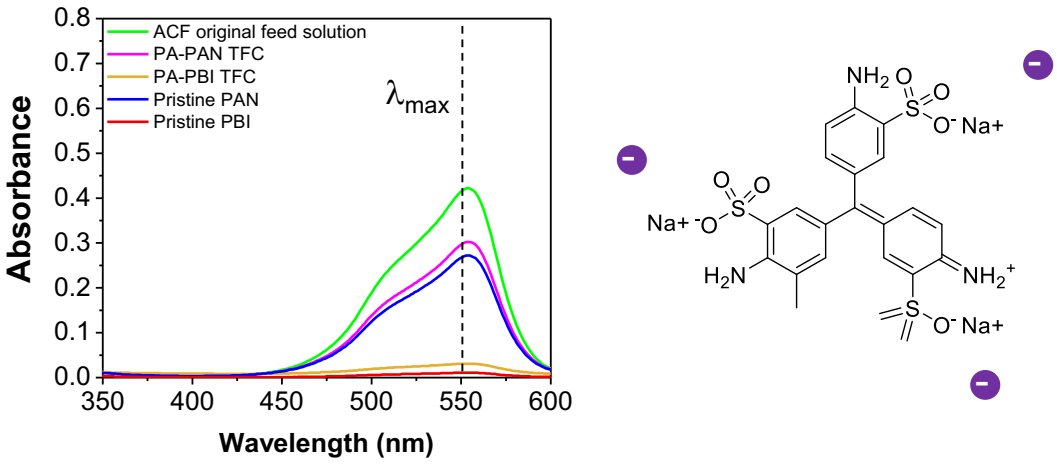


Figure 45. UV spectrums of Acid Fushin solutions with different membranes immersed separately.

Neutral dye Azobenzene adsorption was also evaluated particularly for pristine PBI membranes and PA-PBI membranes. Both PBI and PA-PBI membranes were immersed in 25 ppm Azobenzene solution in acetone for > 3 days, no Azobenzene dye adsorption was observed for both PBI membranes and PA-PBI TFC membranes. (Fig. 46)

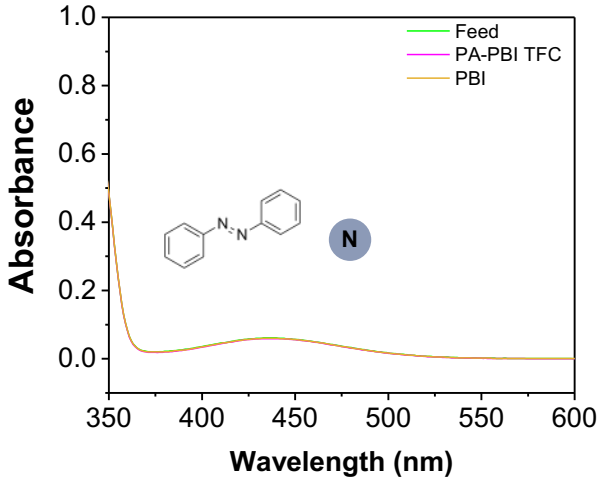


Figure 46. UV spectrums of Azobenzene solutions with SPA-PBI membranes and PBI support immersed separately.

Under neutral pH conditions SPA and MPD-TMC membrane surfaces are barely negatively charged even in water solvent according to zeta-potential measurements, this result suggests the rejection of solutes in neutral pH organic solvent is mainly due to size-exclusions or electrostatic repelling rather than electrostatic adsorption. (Fig. S10)

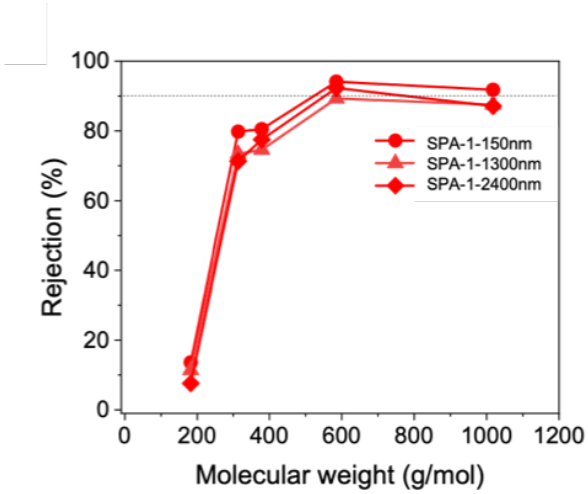


Figure 47. Dye rejections of SPA-1 membranes with different thicknesses in methanol solvent in cross-flow filtration under 10 bar and 80 L hr^{-1} flow rate.

To further understand heterogenous film formation in IP reaction, separation performances in methanol solvent were evaluated in cross-flow filtration. (Fig. 47) In methanol solvent SPA-1 films became very permeable to Azobenzene (182 g mol^{-1}). This result suggests during film synthesis while methanol was co-solvent in aqueous phase SPA-1 film was swollen and permeable to molecules with MW similar to this range. In addition, these results also prove that SPA-1 polymer was indeed

crosslinked and insoluble in methanol solvent while both DBMPA and TPC reagents were soluble in methanol.

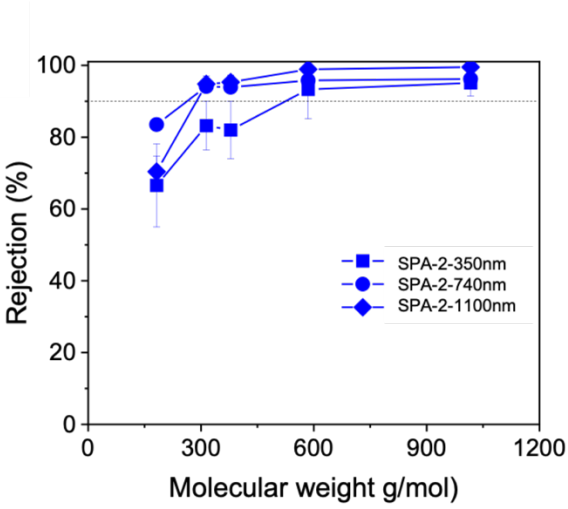


Figure 48. Dye rejections of SPA-2 membranes with different thicknesses in acetone solvent in cross-flow filtration under 10 bar and 80 L hr^{-1} flow rate.

SPA-2 membranes had slightly lower MWCOs with SPA-1 membranes in acetone solvent. (Fig. 48) This could be due to SPA-2 membranes had lower pore volumes and, suggesting potentially less interconnected nanopore channels for mass transport. (Fig. 28c and Fig. S1b)

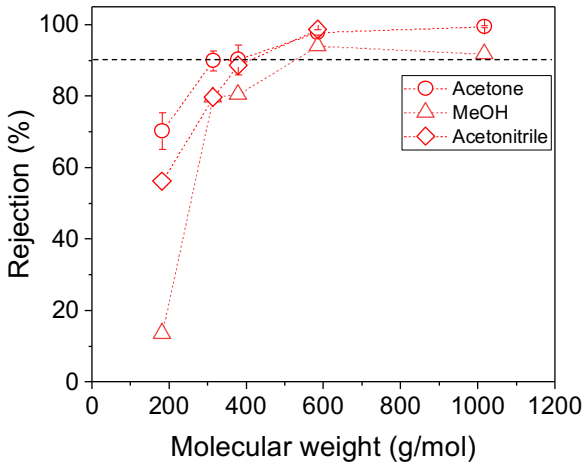


Figure 49. Dye rejections of SPA-1-150nm membranes in acetone, methanol and acetonitrile solvents.

In aprotic solvents acetone and acetonitrile SPA-1 film had comparable rejection behaviours. (Fig. 49) Rejection values were slightly lower in acetonitrile than in acetone. This could be due to higher solvent polarity of acetonitrile than acetone which caused more swelling of membranes in acetonitrile. Polarity of acetonitrile and methanol were similar but in methanol solvent membranes had

significantly lower rejections of Azobenzene neutral dye molecule, this result implies SPA-1 membranes may have different rejection behaviors in protic solvents and aprotic solvents. It has been reasonably considered that methanol solvent can swell the micropores in membranes so small molecules can more easily pass through.

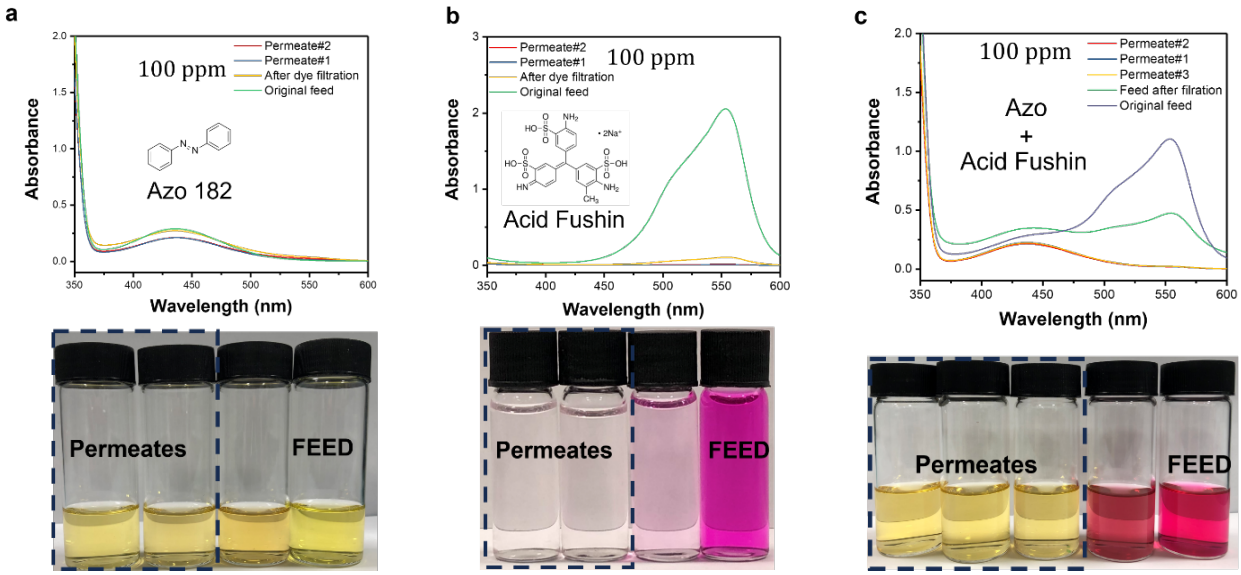


Figure 50. Parallel cross-flow filtration processes using SPA-1-2min membranes. Filtration was performed under 6 bar and 80 L hr^{-1} in acetone solvent using high concentration dye marker. a. UV absorbance of filtration permeate and feed solutions using 100 ppm Azobenzene solution in acetone. b. UV absorbance of filtration permeate and feed solutions using 100 ppm Acid Fushin solution in acetone. c. UV absorbance of filtration permeate and feed solutions using a mixture of 100 ppm Azobenzene and 100 ppm Acid Fushin solution in acetone.

Two dye molecules were mixed in same acetone solvent to prepare high concentration binary complex mixture, and used as feed stream solutions in filtration. (Fig. 49) Single dye marker rejection for Azobenzene (182 g mol^{-1}) was much lower compared with Acid Fushin (585 g mol^{-1}). (Fig. 50a and 50b) Binary mixture was permeated through SPA-1 membrane unit. In the permeate stream Acid Fushin was almost fully retained in the retentate, while Azobenzene permeated through SPA-1 membrane. (Fig. 50c) It could be obviously observed that permeates almost solely consisted of Azobenzene instead of Acid Fushin. Acid Fushin did not have good solubility in aprotic solvents, rejected Acid Fushin crystals precipitated in the retentate which caused loss in Acid Fushin concentration in feed solution from post-filtration rejection.

To summarize, in this work heterogeneous, nanoporous, crosslinked polyamide thin film membranes have been successfully prepared via singular IP reaction. Unlike previously reported thin film membranes with thicknesses down to sub-10nm level synthesized from IP, SPA-1 film formation followed a new mechanism where solid layer can grow up to > 2000 nm. SPA-1 membranes have

stable organic solvent permeances and good selectivity under 10 bar pressure in pilot-scale continuous cross-flow filtration RIGs. Nanoporous crosslinked polyamide composite membranes with thin selective layers can now be synthesized via one-step. This work rationalizes unique structural design for new generation of microporous membranes with enhanced mass transport properties. Proposed preparation mechanism of crosslinked asymmetric membrane structure is important to both academic and industry, and is impactful to next-gen IP membrane manufacturing.

Chapter 5. Functionalized SPA membranes for chiral separation

5.1 Research motivation

Chiral separation is the crown jewel of all separations. Membrane-based chiral separation is challenging due to complicated resolution mechanism, it is difficult to improve both enantiomeric flux and selectivity. Reported chiral MOF membranes, chiral MOF MMMs and chiral porous polymeric membranes showed decent selectivity but under static diffusion the enantiomeric flux is low. Chiral microporous MOF membranes still do not have stable permeation selectivity for enantiomers with decreasing enantiomeric excess over time. This has mainly been accredited to sorption mechanism dominates enantiomeric permeation, saturation of sorption/docking sites caused membranes to no longer provide selectivity for enantiomeric permeation. Selective sorption of enantiomers in current chiral membranes are mostly due to stereo-specific H-bonding or electrostatic binding. Hydrogen atom attached to a chiral carbon can only selectively associate with another electronegative donor attached to another chiral carbon. Likewise temporary complexes between hosts and guests due to strong electrostatic attraction can also lead to selective mass transport. This mechanism is not ideal for long-term chiral separation using membranes. As regeneration of membrane units have to be designed for continuous processes that costs extra energy. In an ideal scenario, membranes should have stable chiral permeation selectivity throughout entire lifespan.

Natural molecules such as DNA, saccharides, polysaccharides and CDs have drawn great interests in chiral separation, especially regarding separation in chromatography. This is primarily due to abundance of natural chiral molecules which exist broadly in organisms. In human bodies only L-amino acids exist meaning unit cell biological activities are mostly based on enantiomers instead of racemates, natural polymers can only selectively interact with specific enantiomers for biological activities. This further implies polymers synthesized from natural chiral molecules can selectively recognize enantiomers. Liposomes in cell membranes can efficiently transport L-amino acids while D-amino acids could not be recognized.

Chiral porous polymers have drawn great interests over recent years, followed by uncovering selective chiral recognition mechanisms from natural chiral selectors. Apart from reported membranes prepared from natural chiral molecules, synthetic polymeric membranes can also have good selectivity in chiral separation. Based on enhanced mass transport through micropores in PIMs, it was postulated and has been demonstrated that chiral PIMs can selectively transport enantiomers with ee up to 87%. This has led to more extensive researches on preparing chiral membranes with micropores to enhance performances.

Spatial chirality in PIMs was introduced by rigid contorted chiral PIM monomers. Traditional PIMs monomers such as TTSBI, BHPF, bi-naphthol have unique spatial chirality that are usually stable at low temperatures. Chiral PIMs could not be easily racemized due to backbone rigidity. Bi-naphthalene structures are particularly interesting due to rotation of single bonds that enhance polymer flexibility. Bi-naphthalene structures can have trans or cis conformation, with each conformation separately has S- and R- enantiomers. This has led to bi-naphthalene structures owning 4 different isomers as well as optical activity. Two naphthalene planes in bi-naphthalene structures rotate out of phase due to electrostatic repelling from phenyl ring conjugations, 1,8 position functionalization with bulky functional groups will improve stability of chirality due to spatial hindrance. Optically active bi-naphthalene structures have been reported in kinked PIMs synthesis and helical polymer configurations. Here in this work I postulate by applying bi-naphthalene structures into networked PIMs will as well introduce chirality and chiral selectivity in membrane permeation.

5.2 Chiral SPAs with bi-naphthalene structures (RBA-SPA-1)

Chiral SPA-1 nanofilms were synthesized using (R)-binaphthalene diamine (RBA), DBMPA and TPC from free-interface interfacial polymerization. RBA molecules were used as building blocks incorporated into SPA-1 network. Amine groups in RBA are also expected to react with TPC to form chiral centres with optically active properties. (Fig. 51) Since amine groups in DBMPA are distant from each other thus it is believed both DBMPA and RBA should be very reactive with TPC to form crosslinked networks. Polymerization was allowed to progress over 2 minutes under room temperature where racemization of RBA is highly unlikely.

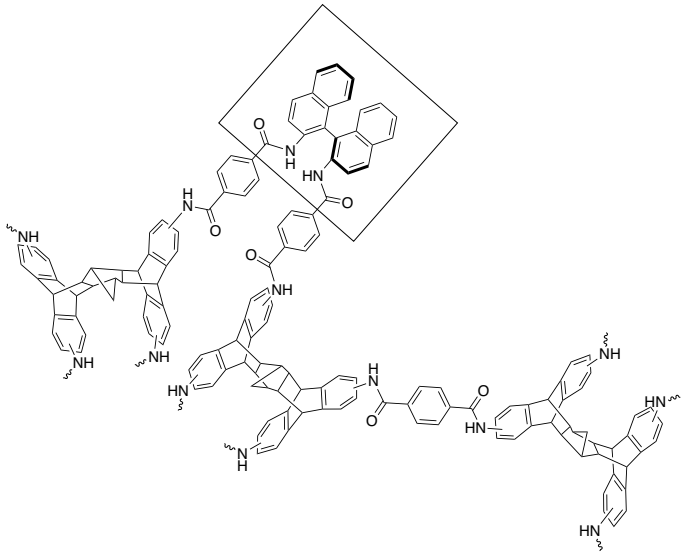


Figure 51. Chemical structure of chiral RBA-DBMPA-TPC (RBA-SPA-1).

AFM top-view images of self-standing chiral RBA-SPA-1 suggested RBA-SPA-1 film thicknesses were significantly lower than all pristine SPA-1 synthesized without chiral building blocks. (Fig. 29h) Chiral RBA-SPA-1 had ~ 40 nm film thickness and did not have nodule textures on the surface of the film. Chiral SPA-1 film was continuous without pin wholes. (Fig. 52)

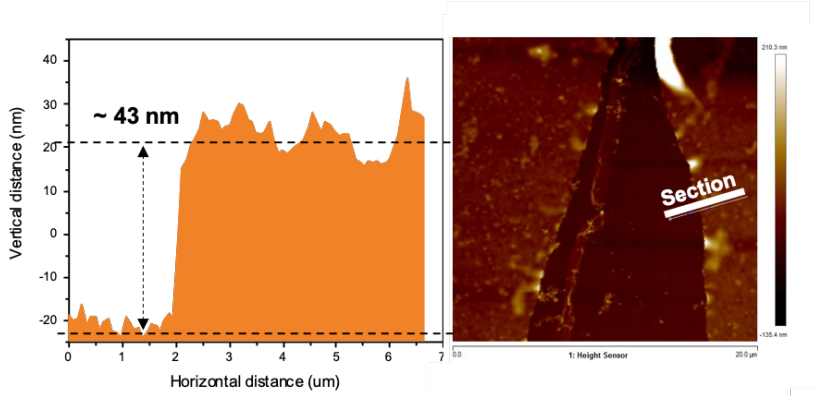


Figure 52. Top-view AFM image and height profile of synthesized chiral RBA-DBMPA-TPC film, with a manual cut in the middle of the film.

Cotton effects from circular dicroism of RBA-SPA-1 membranes confirmed self-standing films are chiral. Obtained RBA-SPA-1 films showed single-handedness and rotated polarized light in one diection. Due to steric hindrances of chiral bi-naphthalene monomers where two amine groups are very close to each other, it is possible that not all chiral building blocks are co-polymerized into the network. After rinsing RBA-SPA-1 membrane with pure MeOH solvent, MeOH-washed RBA-SPA-1 membranes still had same Cotton effects at identical wavelength with unwashed RBA-SPA-1 film. But dichroism intensity was lower, this suggests small amount of optically active contents were removed from the film solids. MeOH solvent that was used to wash RBA-SPA-1 membranes started showing identical light polarization at same wavelength with the film, meaning chiral building blocks were not completely grafted onto the networks but were instead trasnferred into MeOH. (Fig. 53a and 53c) Chiral film lost ~ 5 milidegree of circular dichroism after being rinsed with pure methanol solvent. CD of methanol solvent that was used for chiral film rinsing started showing same Cotton effect from bi-naphthal structures, this is consistent with previous deduction that unreacted bi-naphthal molecules were removed into solvents. (Fig. 53b)

This can lead to actual chiral content in synthesized films lower than expected. Unreacted chiral centres were removed from the film and dissolved into MeOH solvent instead. Since amount of chiral RBA used in sub-100 nm thin film synthesis is very low. Films obtained from IP reaction were less than 50 nm, it is considered unreacted residue RBA moleucles were very little in terms of mass and molarity that it did not affect HPLC trace analysis of chiral solutes.

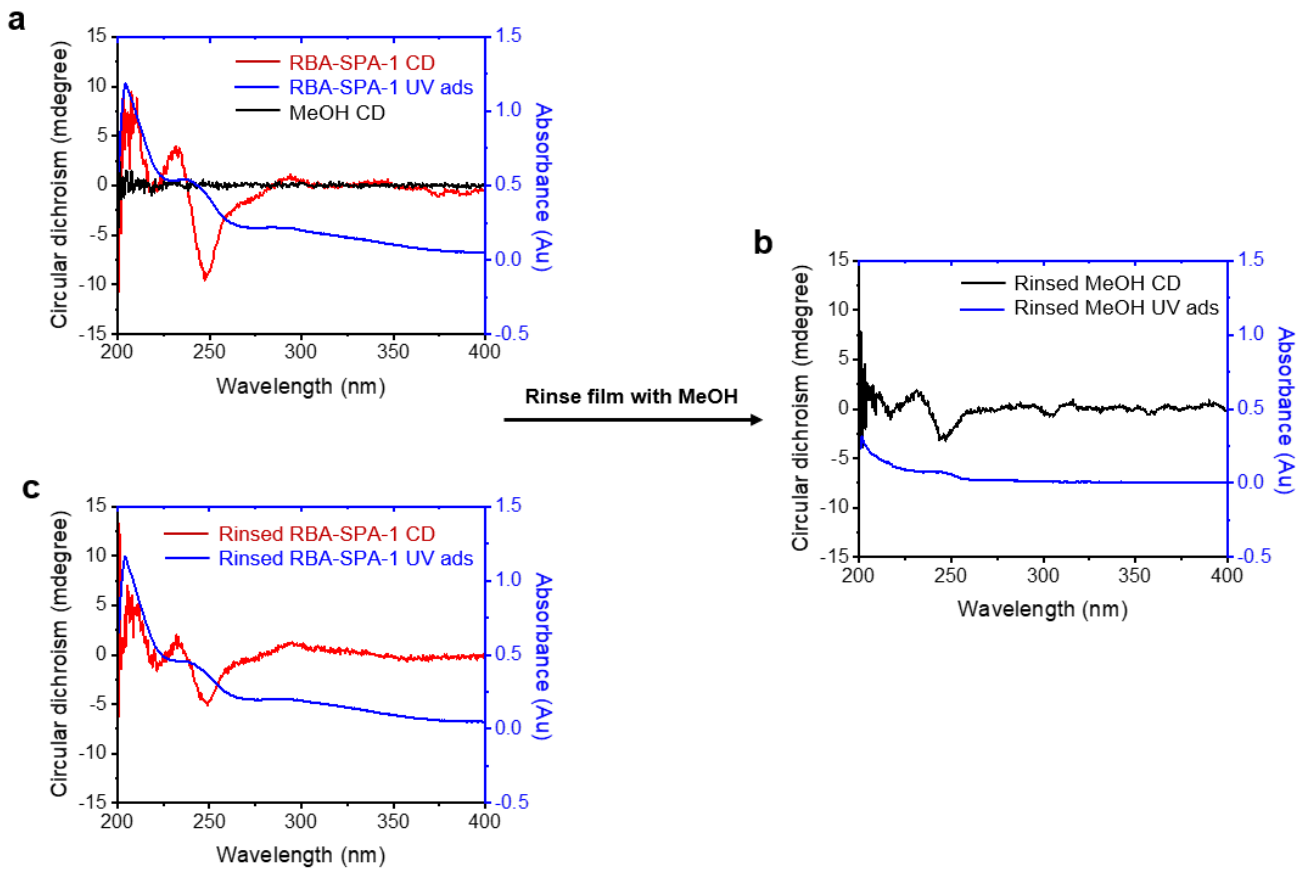


Figure 53. Circular dichroism of RBA-DBMPA-TPC film before methanol washing, methanol used for film washing and RBA-DBMPA-TPC film after washing.

At this stage it can be difficult to exactly quantify chiral content in chiral SPA-1 films, as CD could only evaluate partial film.

5.3 Stable permeate enantiomer excess under static diffusion

Chiral RBA-SPA-1 self-standing films were successfully deposited on PAN and PTFE supports to prepare chiral SPA-1 TFC membranes. After drying for 24 hrs no film delamination from supports was observed, meaning chiral SPA-1 thin films are compatible with both hydrophilic and hydrophobic surfaces. RBA-SPA-1 composite membranes were quite flexible after overnight drying. (Fig. 54) It is worth noting here that RBA-SPA-1 membranes were completely transparent but quite brittle, this is associated by rigidity of contorted backbones and low thicknesses verified by later discussion sections. During water bath transfer chiral SPA-1 films broke easily, only sufficient areas of thin film membranes were captured on supports which were enough for chiral separation tests.

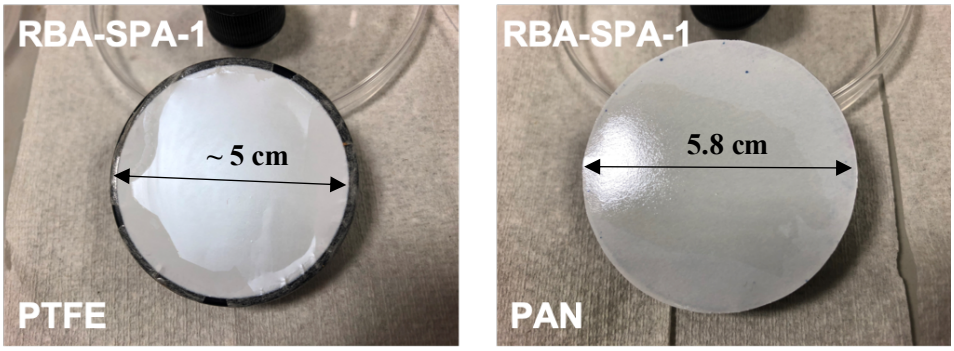


Figure 54. RBA-SPA-1 self-standing film synthesized and captured on PTFE and PAN supports.

Water contact angle of RBA-SPA-1 film was < 90 degree suggesting chiral SPA-1 film have hydrophilic surface. Water droplets stayed in Hemiwicking state over 120 seconds but with very slow rate of film surface wetting. (Fig. 55) Water contact angle decreased only ~ 1 degree after 120 seconds. This result suggests despite chiral polyamide film is hydrophilic with amide bonds, water still can not easily dissolve onto membrane surfaces. It has been credited to highly hydrophobic backbone of DBMPA monomer where C/N ratio is very high. In addition, chiral RBA molecule also has hydrophobic backbones from naphthalene structures. Chiral SPA-1 film surface is only slightly hydrophilic with contact angle measured to be 81.0 ± 0.8 degrees.

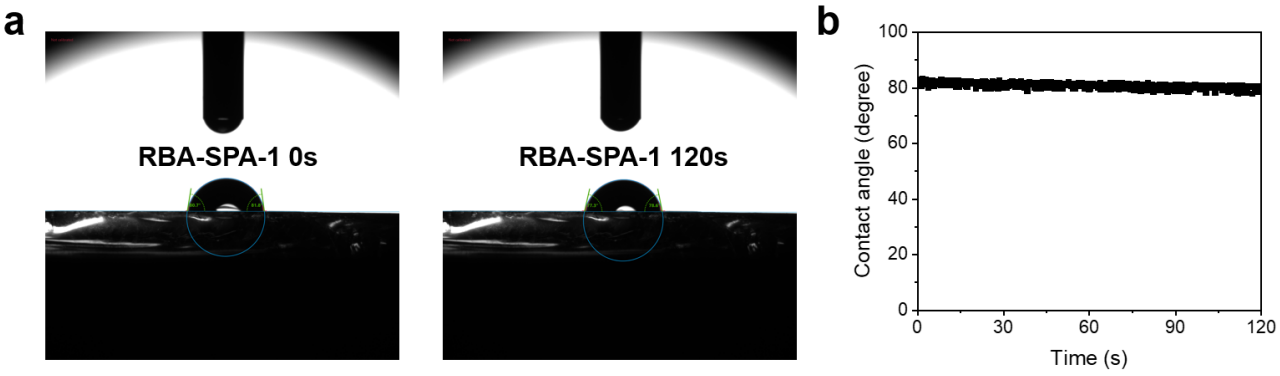


Figure 55. Water contact angle at initial state and after 120 seconds of RBA-SPA-1 film captured on quartz substrates.

Static diffusion experiments using NEA racemates as 1 g L^{-1} feed solutions were performed using RBA-SPA-1-PTFE TFC membranes. During the first ~ 3 days concentrations of NEA in permeate side could not be determined properly due to small peak areas. (Fig. 56a) Calculated enantiomeric excess (ee) in permeate side first decreased then stabilized after ~ 4 days of permeation. ee stabilized at ~ 15% in the permeate side over > 1 week permeation time. (Fig. 56b) It was difficult to detect

concentration change in feed stream solutions via HPLC analysis, this was due to loss of enantiomers in feed stream was very little as enantiomeric permeation through membrane was slow. (Fig. 56c) Enantiomer concentration profiles in the permeate side calibrated from HPLC suggested S-NEA permeated through RBA-SPA-1-PTFE membrane more rapidly than R-NEA. (Fig. 56d)

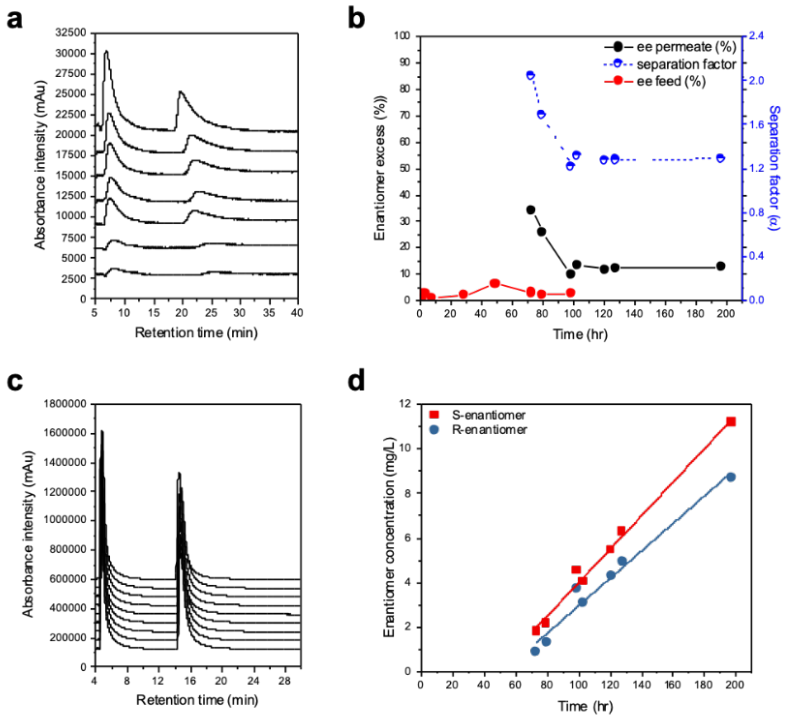


Figure 56. a. HPLC spectrums of permeate side in static chiral diffusion using RBA-SPA-1 film collected after ~ 3 days. Over the first few days peaks were too weak to analyse, samples were collected each day. b. Enantiomeric excess in both feed side and permeate side in static chiral diffusion, and separation factor in permeate side through membrane. c. Feed concentration HPLC spectrum profiles. d. Enantiomer concentrations in permeate side through membranes.

Permeation rates of enantiomers through RBA-SPA-1-PTFE membrane could be evaluated from linear-fitting of concentration vs time plot,

$$\text{S: } Y = -3.55 + 0.08X \quad \text{(Equation - 8)}$$

$$\text{R: } Y = -3.22 + 0.06X \quad \text{(Equation - 9)}$$

where permeation rate of S-NEA through membrane is 0.08 mg L^{-1} hr^{-1} which is higher than R-NEA of 0.06 mg L^{-1} hr^{-1} through membrane. (Equation - 8 and Equation - 9) It is interpreted that chiral selectivity from RBA-SPA-1 membrane permeation in static diffusion originates from both

adsorption and diffusion. Over the first ~ 72 hr it was difficult to detect enantiomer permeation in permeate streams. As indicated by existing literature, it is suggested that enantiomers are still being adsorbed into membranes near feed side streams. Adsorption selectivity slowly decreased starting from when both NEA enantiomers permeated through RBA-SPA-1 then almost disappeared after ~ 4 days. Intrinsic permeation selectivity from RBA-SPA-1 membrane towards NEA enantiomers persisted over entire operation span despite the value is quite low ~ 16 %. NEA racemic diffusion experiment was reproduced under exactly same conditions using separately prepared samples, stabilized ee values in permeate phase were very comparable. (Fig. S12) But rates of enantiomeric permeation were quite different. This could be due to change in film thickness or interconnectivity of micropores.

To summarize, self-standing chiral polyamide thin films were successfully prepared using free-interface interfacial polymerization. Chiral SPA-1 film has < 50 nm thickness and can be readily transferred onto both hydrophobic and hydrophobic surfaces without significant delamination. Intrinsically chiral SPA-1 membranes have stable chiral selectivity ~ 16% ee towards NEA over 196 hour operation time, this is considered only as diffusion selectivity.

Chapter 6. Semi-crystalline thin-film composite membranes for energy storage devices

6.1 Research motivation

Shortage of fossil fuels and expanding demands for environmentally friendly energy-storage devices have greatly stimulated innovation of alternative, renewable energy technologies. As next-generation energy-storage devices, redox flow batteries showed impressive potential towards grid-scale operations with stable charge-discharge performances. Electro-chemical devices as such would require a solvent-stable membrane separator to suppress crossover of anode/cathode species but transport charge carriers. Proton-conductive sulfonated Nafion membranes have yet dominated the commercialization of ion-conductive polymeric membranes, due to microphase separation Nafion membranes still suffer from aqua-swelling resulting in unsatisfactory selectivity. Nafion membranes have low selectivity in RFBs especially using low MW redox couples. Porous, rigid polymers such as PIMs and COFs are classes of materials that exhibited outstanding selectivity in gas separation/storage and liquid-phase separations. COFs themselves have drawn particular interests in gas storage, such as hydrogen and methane due to high internal surface area. Yaghi reported 2-D COF-6 and COF-10 (surface area 1760 $m^2\ g^{-1}$) that showed H_2 uptake of 22.6 mg g^{-1} and 39.2 mg g^{-1} separately, while 3-D COFs such as COF-102 showed much higher hydrogen uptake of 72.4 mg g^{-1}.

Existing COFs reported in rechargeable battery applications are rather limited as electrode materials, such as in lithium-ion, lithium-sulfur and zinc batteries. Overlooking the past decades COFs were mainly prepared as particles or nanospheres, rarely self-standing membranes with decent processability. Recently Liu and others have reported successful preparation of free-standing COF thin films via interfacial polymerization, such films can be readily captured on support substrates to fabricate TFC membranes. Self-standing COF films showed homogeneous structures according to cross-sectional SEM imaging, thicknesses of films can be tuned from 5 ± 1 nm to ~ 300 nm. Moreover, self-standing COF membranes have been successfully applied in pressurized filtration giving ~127.3 $\pm$ 12.5 L $m^{-2}\ hr^{-1}\ bar^{-1}$ ethanol permeance and > 90% rejections for Vitamin B12, brilliant blue R and Alcian blue. These results suggest that COF films are robust enough to withstand hydraulic pressure and can serve as selective barriers for molecular-level separations in liquid phase. Hence it is postulated that self-standing semi-crystalline thin films can also be applied as flow battery separators, where high hydraulic pressure is not even necessarily required for ion transfer and redox couple rejections.

Here in this work self-standing semi-crystalline thin films synthesized from TAPA/PPD and TFP were successfully prepared from templated interfacial polymerization. Synthesized TAPA-TFP thin films had corresponding XRD sharp peaks compared with existing literature, suggesting existence of crystalline structures. Self-standing semi-crystalline films can be readily transferred onto PAN supports to prepare TFC membranes. COF-PAN TFC membranes showed stable high rejections towards Rose Bengal in acetonitrile, high selectivity for ion diffusion in water and decent discharge capacity retention in neutral pH flow batteries.

6.2 Free-standing polyimide film formation

0.05 mmol/0.1 mmol/0.3 mmol of TAPA and 0.05 mmol/0.1 mmol/0.3 mmol of TFP (TAPA-$TFP_{0.05}$/$TFP_{0.1}$/$TFP_{0.3}$) were dissolved in 100 g of DCM solvent. The solution was sonicated over 2 minutes then quickly allocated to 4 vial reactors. In each vial reaction was allowed to continue for 24 hours to 96 hours, a yellowish solid film layer was formed on the inner wall of the vial. Residue solution was drained from vial reactor after reaching certain reaction time, 1M/L KOH solution was used to etch films off inner walls for ~ 10 minutes. A small razor knife was used to gently peel off the films, after which synthesized films were transferred to alcohol bath and captured using different supporting substrates. (Fig. 57)

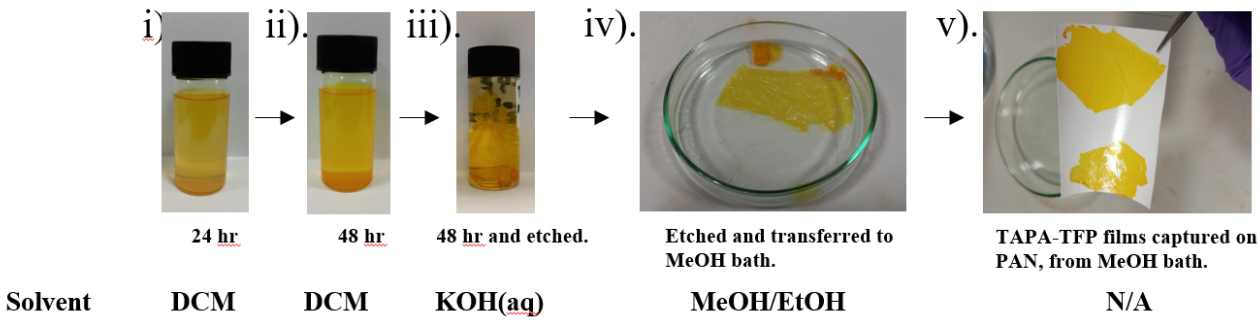


Figure 57. TAPA-TFP thin film preparation using liquid-solid templated growth method in vial reactor followed by etching in alkaline solution.

Semi-crystalline COF films from 24 hours of reaction were not robust enough to be captured in alcohol bath on PAN support. COF films formed after 48, 72, 96 hours of reaction could be easily stretched in alcohol solvents and captured.

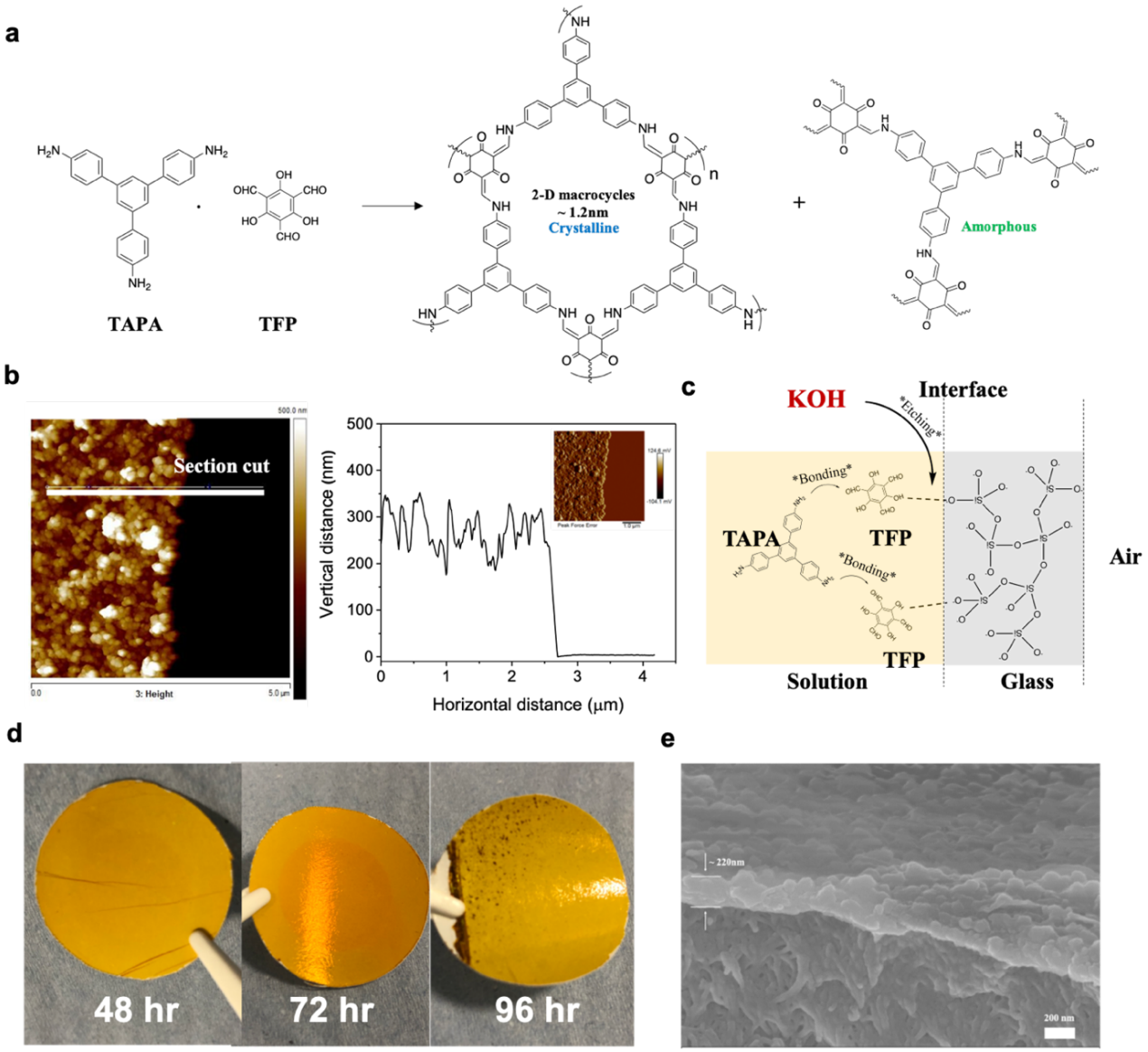


Figure 58. a. Chemical structures of TAPA-TFP polymer. b. Top-view AFM image of TAPA-TFP$_{0.05}$ self-standing film synthesized over 48 hours. c. Schematic of liquid-solid templated growth method for film synthesis in a glass vial reactor. d. TAPA-TFP films synthesized with 0.05 mmol TAPA and 0.05 mmol TFP dissolved in 100 g of DCM over different reaction time. e. Cross-sectional SEM image of TAPA-TFP$_{0.05}$ film reacted for 5 minutes on PAN substrate.

Symmetric TAPA and TFP molecules were chosen as building blocks. (Fig. 58a) Continuous polymer films with dotted surfaces were obtained. (Fig. 58b) Films can also be transferred to water bath followed by support capturing, but films suffered severely from delamination on PAN support surfaces. With increasing reaction time solid COF particles started to accumulate on surfaces of films, which was most obvious for 96 hour COF films. (Fig. 58d) TAPA-TFP$_{0.05}$-48hr film had ~ 200 nm thickness according to top-view AFM imaging with rough surface, implying assembly of COF nanoparticles was not uniform. Cross-sectional SEM image of TAPA-TFP$_{0.05}$-48hr film on PAN

support revealed identical film thickness ~ 220 nm, as well as nanoparticle structures on film surfaces. (Fig. 58e)

Highest measured vertical distance of TAPA-$TFP_{0.05}$-48hr film AFM height profile reached ~ 350 nm while bottom base film was only ~ 200 nm thick. SEM analysis showed independent nanoparticles distributed on film surface, sizes of which were ~ 70 nm but highly variated. These results suggest single-phase liquid-solid templated film growth was not well confined. However, synthesized films were highly continuous without apparent pin-wholes. (Fig. 59)

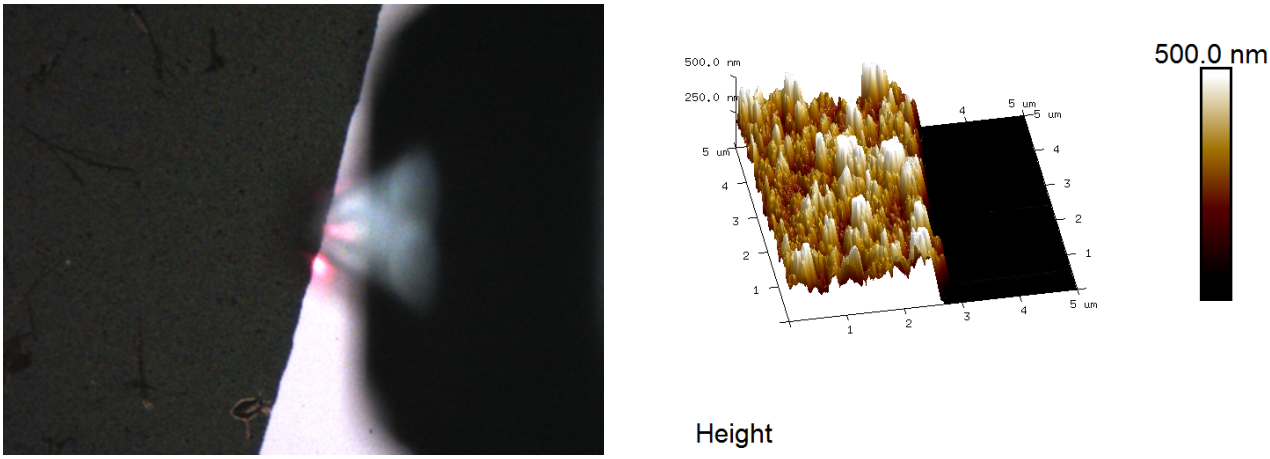


Figure 59. Microscopic image of synthesized TAPA-TFP film and 3-D AFM analysis of TAPA-$TFP_{0.05}$-48hr film.

Amine-aldehyde condensation was allowed to progress freely into DCM phase, leading to rough surface morphology. In addition, side product H_2O was produced along condensation reactions which could not escape the solid surface where polymerization initially started. This can also lead to concentration changes near the reaction zone. As reported from Banerjee's group self-standing semi-crystalline COF films could assume fibre-to-film and sphere-to-film mechanisms. In this study surface of prepared TAPA-TFP thin film membranes showed assembly of smaller particle solids, these solids had spherical dimensions on the scale of 50 nm to 100 nm. (Fig. 60a) It is suggested these TAPA-TFP films formed via sphere-to-film mechanism, graded concentration distributions across film solid formed on reactor inner walls created randomly packed particle structures.

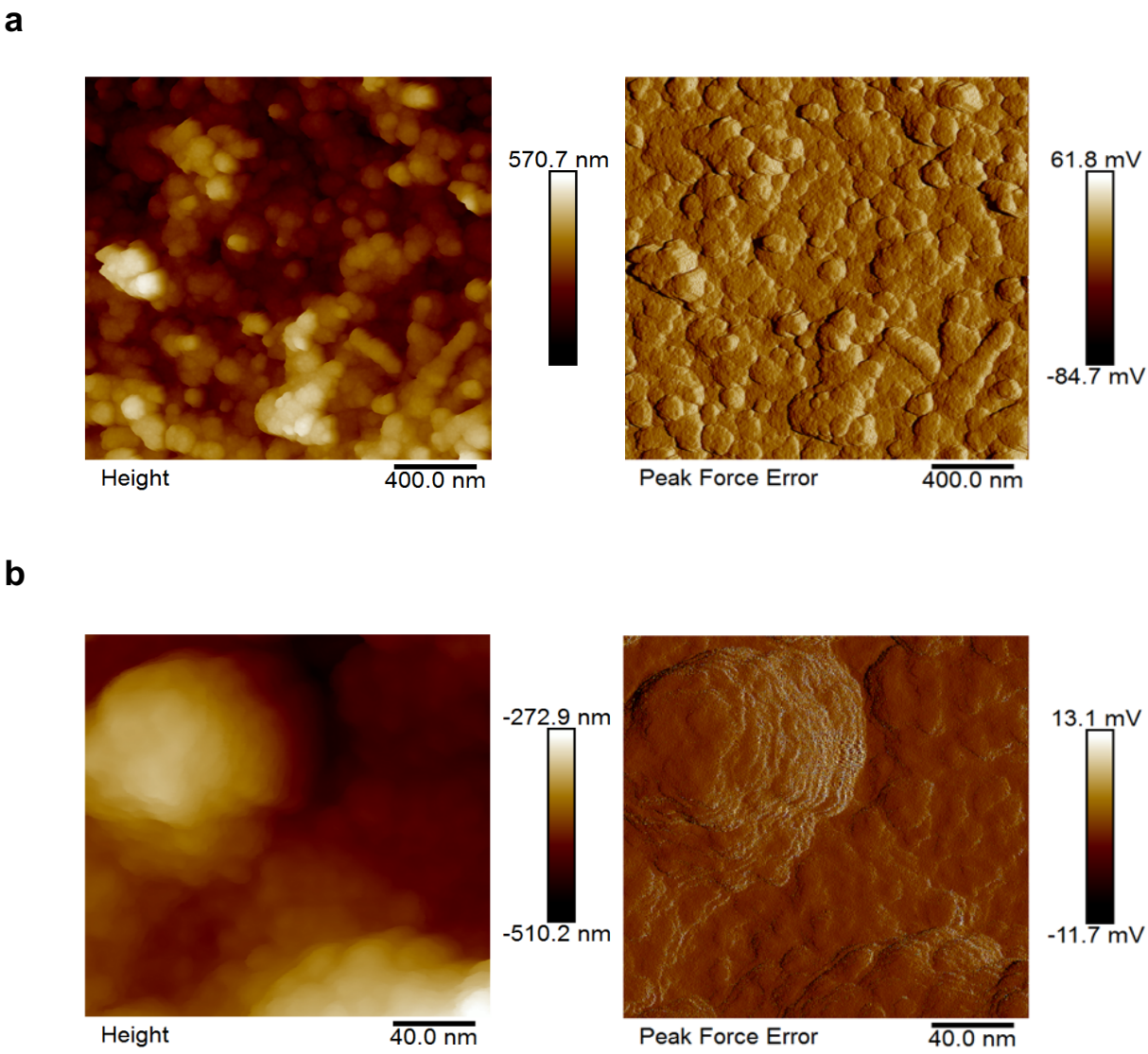


Figure 60. a. Top-view AFM imaging analysis of 2 μm × 2μm scan of TAPA-$TFP_{0.05}$-48hr film. b. 200 nm × 200 nm scan AFM images of TAPA-$TFP_{0.05}$-48hr film.

Compared with amine-acyl chloride condensation reaction, amine-aldehyde condensation reaction is slower hence giving polymer network more freedom for chain relaxation. Zoomed-in AFM surface analysis was performed for TAPA-$TFP_{0.05}$-48hr film. Across 200 nm scan size it can be seen large nanoparticles were formed from smaller ones with 10 to 20 nm in dimensions. (Fig. 60b) 96hr TAPA-TFP film thickness was not evaluated using AFM.

Resulted polymer network was not soluble in DCM and did not drift freely into DCM solvent even under mechanical force. This suggests rear side of TAPA-TFP film towards vial inner wall should be rather flat, but due to uncontrolled reaction into DCM phase polymerization incurred random solid build-up. Under high TAPA and TFP concentrations outstanding solids quickly accumulated on film

surfaces. TAPA-TFP polymer solids had high nitrogen gas uptake and derived BET surface area of 154.6 m^2 g^{-1}.

6.3 Semi-crystalline TFC membrane for neutral pH RFB

To examine crystallinity of as-synthesized self-standing COF films, XRD scattering was performed on TAPA monomer solids, TFP monomer solids, and TAPA-TFP films. Mass of thin film was very small it was difficult to collect enough samples for XRD characterization using TAPA-$TFP_{0.05}$-48hr or TAPA-$TFP_{0.05}$-24hr films. TAPA-$TFP_{0.05}$-96hr films showed sharp crystalline peaks below $2\theta <$ 40 degrees, which is rather consistent with reported TAPA-TFP COF crystalline structures reported from literatures. But crystalline packing peaks were very weak suggesting synthesized polymer film may not have well-defined 2-D structures, but instead have large portion of amorphous regions in the bulk. As can be seen from XRD spectrums, all synthesized TAPA-TFP films showed broadband intensity from 2θ from 20 to 40 degrees. (Fig. 61a) TAPA and TFP monomers showed multiple sharp peaks, most of which were not present in TAPA-TFP polymer films. FTIR results suggest polymer films synthesized with different reaction time did not have chemical composition differences, this means rection time time did not affect chemical structures of synthesized films. (Fig. 61b)

1M/L KCl, NaCl, $CaCl_2$ and $MgCl_2$ were used as feed solutions to evaluate ion permeation through synthesized TAPA-TFP TFC membranes. TAPA-$TFP_{0.05}$-48hr membranes deposited on PAN or PAN-COOH supporting membranes did not show significant differences in terms of ionic permeation rates. Under static diffusion permeation TAPA-$TFP_{0.05}$-48-PAN membrane ionic selectivity of K^+/Mg^{2+} reached 20 while TAPA-$TFP_{0.05}$-48hr-PANCOOH TFC membrane showed almost 36 for same ion pair.(Fig. 61d and 61e) This result means carboxylic acid groups on PAN supports may improve ionic permeation selectivity.

Hence mostly amorphous TAPA-TFP films do not have well-defined pores as conventional 2-D materials. It can be compared with existing literature data that obtained XRD peaks were not as sharp. Packed crystalline regions in polymer film may preserve higher free volumes and larger pores which can enable fast ion transport. So far it had been difficult to de-couple mass transport resistance of crystalline and amorphous regions in synthesized TAPA-TFP membranes, as it is suggested that amorphous reginos and crystalline regions in films contribute to different ion permeation selectivity. (Fig. 61f)

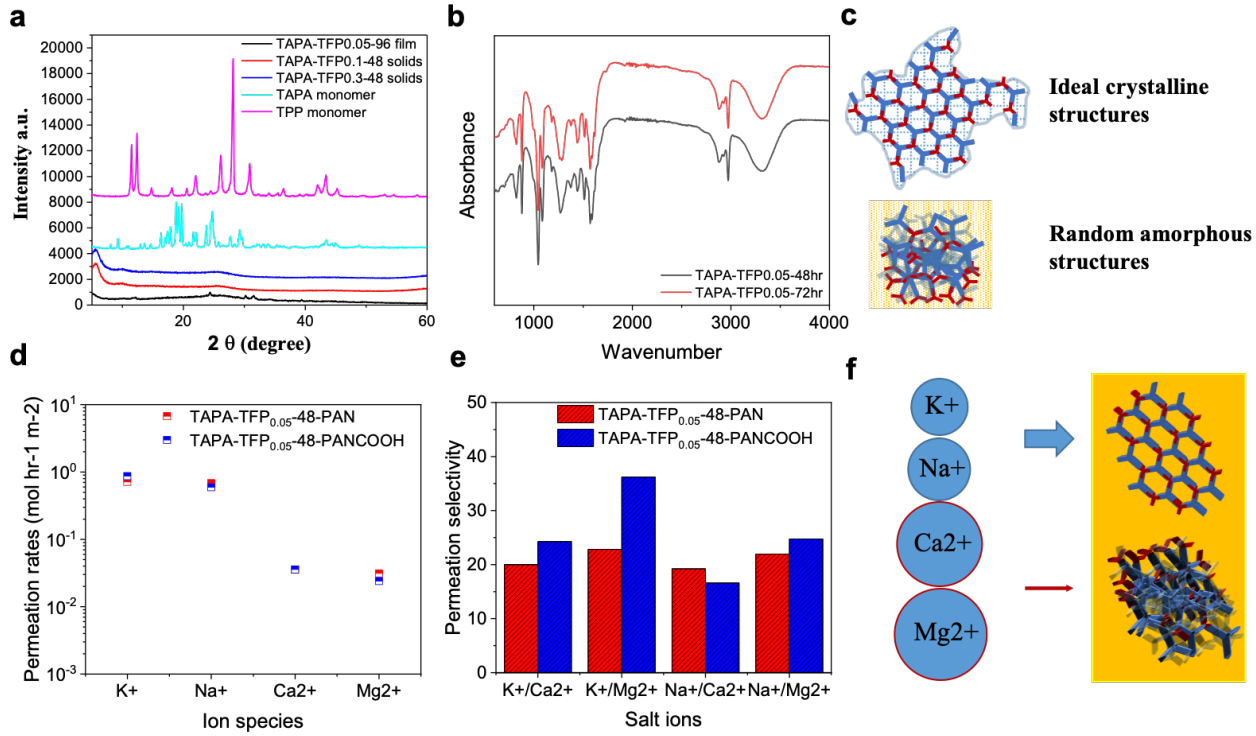


Figure 61. a. XRD spectrums of TAPA monomer, TFP monomer and synthesized TAPA-TFP films under different conditions. b. FTIR spectrums of TAPA-TFP films synthesized with different reaction time. c. Schematics of ordered crystalline regions and amorphous structures co-existing in TAPA-TFP polymer. d. Permeation rates of monovalent and divalent ions through TAPA-TFP$_{0.05}$-48hr on different supporting substrates. e. Ionic permeation selectivity of TAPA-TFP TFC membranes. f. Ordered crystalline regions are supposed to have COF packing hence will increasing ion permeation rates.

RFB performances were tested in a lab-scale set-up. Ionic condcutivity of TAPA-TFP thin films synthesized over different reation time were measured against temperature. (Fig. 62)

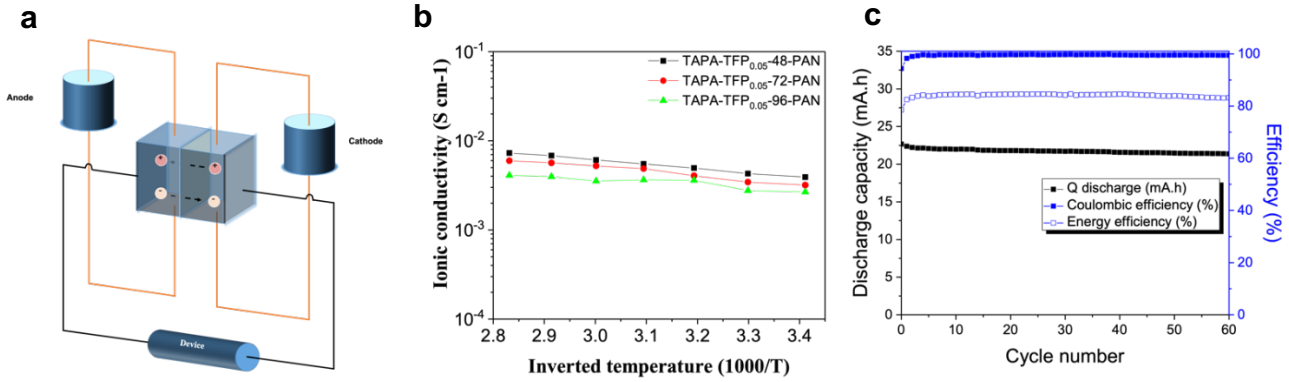


Figure 62. a. Schematic of simplified redox flow battery set-up. b. Ionic conductivity dependence of TAPA-TFP membranes captured on PAN support synthesized with different reaction time against temperature. c. TAPA-TFP$_{0.05}$-48hr-PAN TFC membrane performances in neutral flow battery using viologen (SPr)2V and potassium ferrocynide as redox couples.

Among all COF-type films synthesized with different reaction time, polymer films with longest reaction time showed highest resistance and lowest conductivity. (Fig. 62b) TAPA-TFP-PAN TFC membrane was successfully applied as membrane separator in neutral pH RFB using $(SPr)_2V$ as anode materials and $K_4Fe(CN)_6$ as cathode materials with 0.1M/L concentrations dissolved in 1M/L KCl electrolyte solutions. Over 60 charge-discharge cycles RFB maintained decent capacity with a loss of 0.08% per cycle. The loss of discharge capacity is usually due to redox side reactions or low selectivity of membranes that did not provide full rejections of redox couples. In other cases, this is could also be due to adsorption of redox couples as solutes into the membranes. Low current density was used during charge-dischagre cycling experiments, discharge capacity retention was rather stable suggesting thin film membrane separator did not break during cycling. (Fig. 62c) Energy efficiency was consistent at near 100%, while energy efficiency reached as high as 82% and was stable at this value over 60 charge-dischagre cycles.

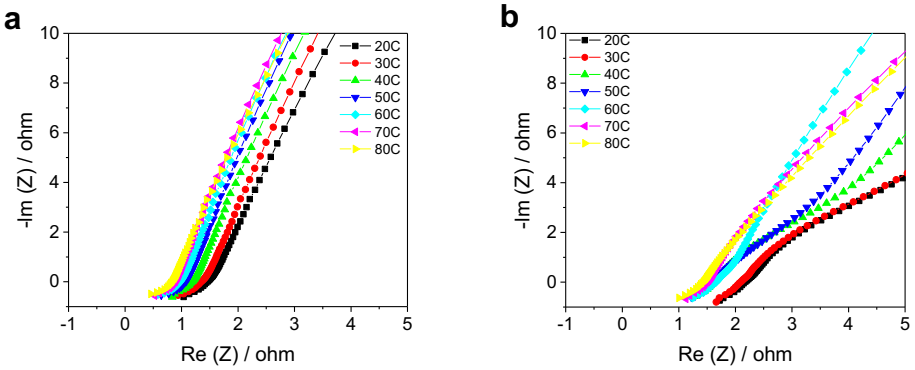


Figure 63. a. TAPA-$TFP_{0.05}$-48hr membrane resistance under different temperatures. b. TAPA-$TFP_{0.05}$-96hr membrane resistance under different temperatures.

Membranes were treated with 1M/L KCl electrolyte solutions for ~ 10 minutes before each conductivity measurement. TAPA-$TFP_{0.05}$ films formed with longer reaction time had higher resistance while TAPA-$TFP_{0.05}$-48hr membrane had lower resistance under same temperatures. (Fig. 63) This is usually due to longer reaction time helped form thicker membranes with higher mass transport resistance.

To conclude, in this project self-standing semi-crystalline TAPA-TFP films were successfully synthesized. Synthesized self-standing semi-crystalline films can be readily transferred onto PAN or PAN-COOH supporting substrates to prepare TFC membranes. Compared with existing literature where water was used as assisting solvent to stretch semi-crystalline films, in this work alcohols were used in the process with fast evaporation to help film deposition. TFC membranes with semi-crystalline selective layers have been successfully applied in neutral pH RFBs with decent charge-discharge performances.

Chapter 7. Conclusion and future perspectives

7.1 Summary of project conclusions

Existing membrane research heavily focused on novel materials preparation. But among most researches done to nudge the cutting-edge boundaries in membrane community, design and construction of new membranes structures have rarely been reported. We believe novel structural design is now more vital, as it is very much related to membrane product manufacturing for practical uses. This is especially true to thin film composite membranes, as existing composite-type membranes necessitate multiple casting processes which are complicated.

Over the last two decades PIMs membranes have become exceptionally interesting. Academically speaking the most notable discovery is the successful formation of nanopores in amorphous polymers. Despite these nanopores are relatively stable and have been shown to greatly enhance membrane permeability, but linear architectures could not prevent collapsing of these nanopores. Pore structure collapsing is undesirable fore practical uses, as continuous filtration or battery charge-discharge performances must be consistent throughout product life span.

Within this thesis work, I show successful preparation of nanoporous, crosslinked, multi-layered polyamide thin film membranes which have good selectivity and permeability in separation processes using polar organic solvents. Defect-free asymmetric microporous polyamide membranes could be prepared via singular IP reaction, which has great promises for scale-up.

Further I have investigated chiral separation performances using crosslinked chiral SPA network under static diffusion. When functionalized with chiral RBA reagent thicknesses of chiral RBA-DBMPA-TPC membranes were only ~ 40 nm, this suggests chiral RBA-DBMPA-TPC polymer film formation could be different from original SPA-1 thin film membranes.

Meanwhile I explored novel synthesis routes of self-standing semi-crystalline thin film membranes and their applications in redox flow batteries. I have also explored application of contorted microporous polyester membranes in Li-S batteries.

SynFabFun:

In this project synthesis of self-standing polyamide nanofilms using contorted PIM monomers via interfacial polymerization for organic solvent nanofiltration and chiral separation was initiated and successfully achieved. Self-standing PIM-type crosslinked polymer nanofilms can be prepared via liquid-liquid interfacial polymerization and liquid-solid interfacial polymerization. ~ 40 nm self-

standing networked chiral DBMPA-TPC polymer films were synthesized and applied in enantiomeric resolution under static pressure. Albeit during initial stage RBA-DBMPA-TPC membrane's chiral selectivity decreased from ~ 30% to ~ 16%, over 1 week of continuous enantiomer permeation enantiomeric excess (ee) in the permeates was stable at ~ 16%. This result suggests chiral selectivity from RBA-DBMPA-TPC membrane is determined by both selective adsorption and selective diffusion. Initial selectivity loss was due to saturation of selective enantiomer adsorption from surface, diffusion selectivity then stabilized given long enough interaction time between solutes and membranes.

SynHiSel:

In this project self-standing, microporous, heterogeneous crosslinked polyamide thin films via one-step free-interface interfacial polymerization were successfully prepared, with enhanced separation performances. To our knowledge, this work reports the first discovery of such asymmetric structures being formed in free-interface interfacial polymerization to date. Rather well-defined dual-layer membrane structure has been achieved from singular reaction. Unlike ISA membranes with hierarchical structures, SPA membranes have distinguishable boundaries between skin layer and porous layer suggesting well-defined bi-layer structure was successfully obtained. Skin layer can be tuned up to ~ 120 nm while supporting porous layer can be tuned from < 100 nm up to 2800 nm thick. This outcome is of high academic values in terms of understanding reaction kinetics in formation of interfacially polymerized PIM-type films. This work could also be of high industrial values as it presents a very promising approach to prepare thin selective skin layer automatically supported by bottom porous layer, which provides great insights to envision scalable thin films prepared from free-interface interfacial polymerization.

Unlike previously established knowledge in MPD-TMC film formation, where amines tend to diffuse into hexane phase to form upward nodule textures. This work has established new knowledge and revealed inverse film formation mechanism by interfacially polymerizing bulky PIM-type amine and commercial acyl chlorides that only have high solubility in one reagent solvent phase. Moreover, microporous SPA membranes with gutter layers showed enhanced solvent permeances and have low MWCOs. Acetone solvent permeability is dramatically enhanced in SPA membranes with increasing gutter layer thicknesses.

As an efficient facile membrane casting technique, interfacial polymerization has drawn tremendous interests from the community. Yet up to date there have been no successful reports of intrinsic performances of pristine self-standing polymer thin films, which is due to their poor mechanical strength. Self-standing films usually only serve as selective layers deposited on top of a thick support

layer, such as PAN, then on top of another layer of backing materials. In our case, thick self-supported microporous polyamides are mechanically robust and more appealing for large-scale preparation. It is believed this research could be a revolutionary game changer of TFC membrane preparations for OSN applications.

ERC:

In this project a variety of self-standing thin films were successfully prepared and their performances in redox flow batteries and Li-S batteries evaluated. Primary objective was to investigate applicability of ultra-thin nanofilms as redox flow battery separators. ~ 20 nm MPD-TMC nanofilm was successfully synthesized and deposited on PAN supports to prepare thin film composite membranes. MPD-TMC-PAN TFC membranes have ~ 100% current efficiency and ~ 80% energy efficiency. Over > 200 cycles of charge-discharge cycling MPD-TMC-PAN TFC membrane showed > 80% capacity retention over 500 cycles. Under static concentration gradient without pressure MPD-TMC-PAN membranes showed good diffusion selectivity between monovalent and divalent ions.

Self-standing semi-crystalline COF-type thin films were also synthesized using TAPA and p-phenylenediamine (PPD) with tri-functional aldehydes separately. TAPA-TFP-PAN TFC membranes had energy efficiency ~ 83% and nearly 100% current efficiency. Over 60 charge-discharge battery cycles COF-type TAPA-TFP TFC membrane showed high capacity retention and was stable in neutral electrolyte. Flow battery charge-discharge performances were also evaluated using SPA-2 membranes. Li-S battery charge-discharge performances were also evaluated using BHPF-TMC membranes and commercial membranes. (S13 to S27)

7.2 Future research directions

In this PhD research a novel crosslinked PIM structure was successfully constructed from interfacial polymerization at free liquid-liquid interfaces. Asymmetric structures can now be directly prepared from one-step interfacial polymerization, prepared self-standing micron level microporous films have high solvent permeances and good selectivity for dye markers in organic solvents. A thin selective layer and a thick supporting layer can now be formed at the same time, and are already crosslinked.

Ideally the selective layer should be as thin as possible to reduce resistance. In thin film composite membranes an additional supporting substrate is required. Future works of this thesis can include,

1. Further adjust concentrations of amines and acyl chlorides to reduce skin layer thicknesses while maintaining asymmetric structure. This might be achieved by applying high TPC concentration 0.1 wt% in hexane, and amine concentrations between 0.01wt % and 0.06 wt% in aqueous methanol-water phase.

2. We postulate a thick enough porous layer can function as both gutter layer and supporting substrate. Reaction time can be further increased > 30 minutes to synthesize much thicker films. In the previous research we observed increasing reaction time > 5 minutes didn't increase skin layer thicknesses. Thick SPA films, with thin selective layers, can potentially be directly captured on backing materials instead of porous supports, which will dramatically reduce IP membrane fabrication technical requirements and costs.
3. Unlike conventional phase-inverted membranes, SPA membranes are intrinsically crosslinked and do not dissolve in organic solvents. Organic solvents such as DMF which usually swell polyamide membranes, can be used to tune MWCOs of SPA membranes towards different applications.
4. This work has opened up new research directions in terms of IP film formation kinetics study. Other porous materials that are permeable to reagents used in interfacial synthesis can be explored regarding film structure formation.
5. Chiral RBA-SPA-1 has stable selectivity under static diffusion. Chiral filtration selectivity still needs to be examined. Separation performances of membranes towards other chiral solutes such as amino acids and pharmaceuticals need to be further examined.
6. COF-type self-standing thin films can be functionalized with ion exchange groups to further increase conductivity.

References:

1. Sholl, D.S. and R.P. Lively, *Seven chemical separations to change the world.* Nature, 2016. **532**(7600): p. 435-7.
2. Brunetti, A., et al., *Membrane technologies for CO2 separation.* Journal of Membrane Science, 2010. **359**(1-2): p. 115-125.
3. Ren, D., et al., *Recent developments of organic solvent resistant materials for membrane separations.* Chemosphere, 2021. **271**: p. 129425.
4. Hinchliffe, A.B. and K.E. Porter, *A Comparison of Membrane Separation and Distillation.* Chemical Engineering Research and Design, 2000. **78**(2): p. 255-268.
5. Halvorsen, I.J. and S. Skogestad, *Energy efficient distillation.* Journal of Natural Gas Science and Engineering, 2011. **3**(4): p. 571-580.
6. Fang, J., et al., *A review of internally heat integrated distillation column.* Chinese Journal of Chemical Engineering, 2019. **27**(6): p. 1272-1281.
7. Getaz, D., et al., *Effect of high pH column regeneration on the separation performances in reversed phase chromatography of peptides.* J Chromatogr A, 2010. **1217**(21): p. 3531-7.
8. Plachka, K., et al., *The effect of column history in supercritical fluid chromatography: Practical implications.* J Chromatogr A, 2021. **1651**: p. 462272.
9. Marchetti, P., et al., *Molecular separation with organic solvent nanofiltration: a critical review.* Chem Rev, 2014. **114**(21): p. 10735-806.
10. Khoonsap, S., et al., *Promoting permeability-selectivity anti-trade-off behavior in polyvinyl alcohol (PVA) nanocomposite membranes.* Journal of Membrane Science, 2017. **544**: p. 287-296.
11. Zhang, Y., et al., *Novel conductive membranes breaking through the selectivity-permeability trade-off for Congo red removal.* Separation and Purification Technology, 2019. **211**: p. 368-376.
12. Park, H.B., et al., *Maximizing the right stuff: The trade-off between membrane permeability and selectivity.* Science, 2017. **356**(6343).
13. Weber, J., et al., *Exploring Polymers of Intrinsic Microporosity – Microporous, Soluble Polyamide and Polyimide.* Macromolecular Rapid Communications, 2007. **28**(18–19): p. 1871-1876.
14. Abe, Y., et al., *[Survey of Primary Aromatic Amines and Colorants in Polyurethane, Nylon and Textile Toys].* Shokuhin Eiseigaku Zasshi, 2016. **57**(2): p. 23-31.
15. de Rezende, C.A., U.F. Schuchardt, and M.d.C. Gonçalves, *Use of nylon 6/polyethylene blends in the preparation of textile yarns.* Journal of Applied Polymer Science, 2006. **102**(3): p. 2142-2148.

16. Jun, B.-M., et al., *Acid stability of polyamide membranes.* Polymer, 2022. **241**.
17. Zimmerman, J. and M.I. Kohan, *Nylon-selected topics.* Journal of Polymer Science Part A: Polymer Chemistry, 2001. **39**(15): p. 2565-2570.
18. García, J.M., et al., *High-performance aromatic polyamides.* Progress in Polymer Science, 2010. **35**(5): p. 623-686.
19. Chen, S.-H., et al., *Preparation and separation properties of polyamide nanofiltration membrane.* Journal of Applied Polymer Science, 2002. **83**(5): p. 1112-1118.
20. El-Gendi, A., *A critical review of the preparation, characterization and applications of polyamide membranes.* Desalination and Water Treatment, 2022. **255**: p. 120-135.
21. Marchildon, K., *Polyamides - Still Strong After Seventy Years.* Macromolecular Reaction Engineering, 2011. **5**(1): p. 22-54.
22. Bera, D., R. Chatterjee, and S. Banerjee, *Aromatic polyamide nonporous membranes for gas separation application.* e-Polymers, 2021. **21**(1): p. 108-130.
23. Lee, K.P., T.C. Arnot, and D. Mattia, *A review of reverse osmosis membrane materials for desalination—Development to date and future potential.* Journal of Membrane Science, 2011. **370**(1-2): p. 1-22.
24. Elimelech, M. and W.A. Phillip, *The future of seawater desalination: energy, technology, and the environment.* Science, 2011. **333**(6043): p. 712-7.
25. Ma, Z., et al., *Investigation on overall charged behavior of polyamide nanofiltration membranes by electrokinetic method.* Desalination and Water Treatment, 2012. **12**(1-3): p. 284-291.
26. Wang, Z., et al., *Ultrathin polyamide nanofiltration membranes with tunable chargeability for multivalent cation removal.* Journal of Membrane Science, 2022. **642**.
27. Karan, S., Z. Jiang, and A.G. Livingston, *MEMBRANE FILTRATION. Sub-10 nm polyamide nanofilms with ultrafast solvent transport for molecular separation.* Science, 2015. **348**(6241): p. 1347-51.
28. Budd, P.M., et al., *Polymers of intrinsic microporosity (PIMs): robust, solution-processable, organic nanoporous materials.* Chem Commun (Camb), 2004(2): p. 230-1.
29. McKeown, N.B. and P.M. Budd, *Polymers of intrinsic microporosity (PIMs): organic materials for membrane separations, heterogeneous catalysis and hydrogen storage.* Chem Soc Rev, 2006. **35**(8): p. 675-83.
30. McKeown, N.B., *The synthesis of polymers of intrinsic microporosity (PIMs).* Science China Chemistry, 2017. **60**(8): p. 1023-1032.
31. Petersen, R.J., *Composite reverse osmosis and nanofiltration membranes.* Journal of Membrane Science, 1993. **83**(1): p. 81-150.

32. Werber, J.R., C.O. Osuji, and M. Elimelech, *Materials for next-generation desalination and water purification membranes.* Nature Reviews Materials, 2016. **1**(5).
33. Kukucka, M., N. Kukucka, and M. Habuda-Stanic, *Water reclamation during drinking water treatments using polyamide nanofiltration membranes on a pilot scale.* Environ Sci Pollut Res Int, 2016. **23**(18): p. 17919-27.
34. Fu, F. and Q. Wang, *Removal of heavy metal ions from wastewaters: a review.* J Environ Manage, 2011. **92**(3): p. 407-18.
35. Goodenough, J.B. and K.S. Park, *The Li-ion rechargeable battery: a perspective.* J Am Chem Soc, 2013. **135**(4): p. 1167-76.
36. Arora, P. and Z.J. Zhang, *Battery separators.* Chem Rev, 2004. **104**(10): p. 4419-62.
37. Shannon, M.A., et al., *Science and technology for water purification in the coming decades.* Nature, 2008. **452**(7185): p. 301-10.
38. Greenlee, L.F., et al., *Reverse osmosis desalination: water sources, technology, and today's challenges.* Water Res, 2009. **43**(9): p. 2317-48.
39. Krauth, K. and K.F. Staab, *Pressurized bioreactor with membrane filtration for wastewater treatment.* Water Research, 1993. **27**(3): p. 405-411.
40. Gohil, J.M. and P. Ray, *A review on semi-aromatic polyamide TFC membranes prepared by interfacial polymerization: Potential for water treatment and desalination.* Separation and Purification Technology, 2017. **181**: p. 159-182.
41. Ulbricht, M., *Advanced functional polymer membranes.* Polymer, 2006. **47**(7): p. 2217-2262.
42. Luo, Y., et al., *A review on the occurrence of micropollutants in the aquatic environment and their fate and removal during wastewater treatment.* Sci Total Environ, 2014. **473-474**: p. 619-41.
43. Korhonen, H. and A. Pihlanto, *Bioactive peptides: Production and functionality.* International Dairy Journal, 2006. **16**(9): p. 945-960.
44. Atra, R., et al., *Investigation of ultra- and nanofiltration for utilization of whey protein and lactose.* Journal of Food Engineering, 2005. **67**(3): p. 325-332.
45. Dmitrieva, E.S., et al., *Polymeric Membranes for Oil-Water Separation: A Review.* Polymers (Basel), 2022. **14**(5).
46. Li, S., et al., *Hydrophobic polyamide nanofilms provide rapid transport for crude oil separation.* Science, 2022. **377**(6614): p. 1555-1561.
47. Anjum, F., M. Wessner, and G. Sadowski, *Membrane-Based Solvent Exchange Process for Purification of API Crystal Suspensions.* Membranes (Basel), 2023. **13**(3).

48. Ouinten, M.L., A. Szymczyk, and A. Ghoufi, *Molecular Dynamics Simulation Study of Organic Solvents Confined in PIM-1 and P84 Polyimide Membranes.* J Phys Chem B, 2023. **127**(5): p. 1237-1243.
49. Simiyu, M.T., et al., *Application of molasses in improving water purification efficiency of diatomaceous earth waste ceramic membranes.* MRS Advances, 2023.
50. Kappert, E.J., et al., *Swelling of 9 polymers commonly employed for solvent-resistant nanofiltration membranes: A comprehensive dataset.* Journal of Membrane Science, 2019. **569**: p. 177-199.
51. Ren, G., et al., *Recent advance in biomass membranes: Fabrication, functional regulation, and antimicrobial applications.* Carbohydr Polym, 2023. **305**: p. 120537.
52. Lee, S. and J. Cho, *Comparison of ceramic and polymeric membranes for natural organic matter (NOM) removal.* Desalination, 2004. **160**(3): p. 223-232.
53. Ignacz, G., A.K. Beke, and G. Szekely, *Data-driven investigation of process solvent and membrane material on organic solvent nanofiltration.* Journal of Membrane Science, 2023. **674**.
54. Zhang, B., et al., *A High-Permeance Organic Solvent Nanofiltration Membrane via Polymerization of Ether Oxide-Based Polymeric Chains for Sustainable Dye Separation.* Sustainability, 2023. **15**(4).
55. Dunn, B., H. Kamath, and J.M. Tarascon, *Electrical energy storage for the grid: a battery of choices.* Science, 2011. **334**(6058): p. 928-35.
56. Xu, R., et al., *Oriented UiO-67 Metal-Organic Framework Membrane with Fast and Selective Lithium-Ion Transport.* Angew Chem Int Ed Engl, 2022. **61**(3): p. e202115443.
57. Huang, J., et al., *Recent Progress of Rechargeable Batteries Using Mild Aqueous Electrolytes.* Small Methods, 2019. **3**(1).
58. Koenig, S.P., et al., *Selective molecular sieving through porous graphene.* Nat Nanotechnol, 2012. **7**(11): p. 728-32.
59. Schaep, J., et al., *Influence of ion size and charge in nanofiltration.* Separation and Purification Technology, 1998. **14**(1-3): p. 155-162.
60. Shen, J. and Y. Okamoto, *Efficient Separation of Enantiomers Using Stereoregular Chiral Polymers.* Chem Rev, 2016. **116**(3): p. 1094-138.
61. Wijmans, J.G. and R.W. Baker, *The solution-diffusion model: a review.* Journal of Membrane Science, 1995. **107**(1-2): p. 1-21.
62. Slater, A.G. and A.I. Cooper, *Porous materials. Function-led design of new porous materials.* Science, 2015. **348**(6238): p. aaa8075.

63. Sarkar, P., S. Modak, and S. Karan, *Effect of Porous and Nonporous Nanostructures on the Permeance of Positively Charged Nanofilm Composite Membranes.* Advanced Materials Interfaces, 2020. **7**(19).
64. Wang, S., et al., *Highly porous ultrathin polyamide membranes for fast separation of small molecules from organic solvents.* Journal of Membrane Science, 2023. **675**.
65. Wang, L.D., et al., *Fundamental transport mechanisms, fabrication and potential applications of nanoporous atomically thin membranes.* Nature Nanotechnology, 2017. **12**(6): p. 509-522.
66. Ali, Z., et al., *Finely Tuned Submicroporous Thin-Film Molecular Sieve Membranes for Highly Efficient Fluid Separations.* Adv Mater, 2020. **32**(22): p. e2001132.
67. Jiang, Z., S. Karan, and A.G. Livingston, *Water Transport through Ultrathin Polyamide Nanofilms Used for Reverse Osmosis.* Adv Mater, 2018. **30**(15): p. e1705973.
68. Davis, M.E., *Ordered porous materials for emerging applications.* Nature, 2002. **417**(6891): p. 813-21.
69. McKeown, N.B. and P.M. Budd, *Exploitation of Intrinsic Microporosity in Polymer-Based Materials.* Macromolecules, 2010. **43**(12): p. 5163-5176.
70. Bai, Z., L. Zhang, and L. Liu, *Bombarding Graphene with Oxygen Ions: Combining Effects of Incident Angle and Ion Energy To Control Defect Generation.* The Journal of Physical Chemistry C, 2015. **119**(47): p. 26793-26802.
71. D'Acunto, G., et al., *Channelling and induced defects at ion-bombarded aligned multiwall carbon nanotubes.* Carbon, 2018. **139**: p. 768-775.
72. Horn, N.R., *A critical review of free volume and occupied volume calculation methods.* Journal of Membrane Science, 2016. **518**: p. 289-294.
73. Anthamatten, M., et al., *Tunability of Free Volume and Viscoelastic Damping of Thiol–Ene Networks Deep in the Glassy State.* Macromolecules, 2018. **51**(7): p. 2564-2571.
74. Hu, C., *Effect of free volume and sorption on membrane gas transport.* Journal of Membrane Science, 2003. **226**(1-2): p. 51-61.
75. Kim, D., et al., *Functional Hierarchical Pores in Polymer Monoliths: Macromolecular Synthesis and Selective Removal of Dyes.* ACS Applied Polymer Materials, 2021. **3**(3): p. 1385-1394.
76. Cao, X., et al., *Effect of pore structure on the adsorption capacities to different sizes of adsorbates by ferrocene-based conjugated microporous polymers.* Polymer, 2021. **233**.
77. Kim, S. and M. Seo, *Control of porosity in hierarchically porous polymers derived from hyper-crosslinked block polymer precursors.* Journal of Polymer Science Part A: Polymer Chemistry, 2018. **56**(8): p. 900-913.

78. Liu, Z., et al., *Theoretical Investigation into Suitable Pore Sizes of Membranes for Vanadium Redox Flow Batteries.* ChemElectroChem, 2017. **4**(9): p. 2184-2189.
79. Sakai, M., et al., *Contribution of Pore-Connectivity to Permeation Performance of Silicalite-1 Membrane; Part I, Pore Volume and Effective Pore Size.* Membranes (Basel), 2021. **11**(6).
80. Shi, B., et al., *Will ultra-high permeance membranes lead to ultra-efficient processes? Challenges for molecular separations in liquid systems.* Journal of Membrane Science, 2017. **525**: p. 35-47.
81. Lee, M.T., et al., *Mechanism and kinetics of pore formation in membranes by water-soluble amphipathic peptides.* Proc Natl Acad Sci U S A, 2008. **105**(13): p. 5087-92.
82. Rose, I., et al., *Polymer ultrapermeability from the inefficient packing of 2D chains.* Nat Mater, 2017. **16**(9): p. 932-937.
83. Ramimoghadam, D., E.M. Gray, and C.J. Webb, *Review of polymers of intrinsic microporosity for hydrogen storage applications.* International Journal of Hydrogen Energy, 2016. **41**(38): p. 16944-16965.
84. Yamato, M., A. Imai, and H. Kawakami, *Thermal properties of polymer with intrinsic microporosity membranes.* Polymer, 2022. **259**.
85. Fang, W., L. Zhang, and J. Jiang, *Polymers of intrinsic microporosity for gas permeation: a molecular simulation study.* Molecular Simulation, 2010. **36**(12): p. 992-1003.
86. Cai, Z., et al., *Ladder polymers of intrinsic microporosity from superacid-catalyzed Friedel-Crafts polymerization for membrane gas separation.* Journal of Membrane Science, 2022. **644**.
87. Gorgojo, P., et al., *Ultrathin Polymer Films with Intrinsic Microporosity: Anomalous Solvent Permeation and High Flux Membranes.* Advanced Functional Materials, 2014. **24**(30): p. 4729-4737.
88. Abdulhamid, M.A. and G. Szekely, *Organic solvent nanofiltration membranes based on polymers of intrinsic microporosity.* Current Opinion in Chemical Engineering, 2022. **36**.
89. Harms, S., et al., *Aging and Free Volume in a Polymer of Intrinsic Microporosity (PIM-1).* The Journal of Adhesion, 2012. **88**(7): p. 608-619.
90. Bandehali, S., et al., *Polymers of intrinsic microporosity and thermally rearranged polymer membranes for highly efficient gas separation.* Separation and Purification Technology, 2021. **278**.
91. Tiwari, R.R., et al., *Physical aging, CO 2 sorption and plasticization in thin films of polymer with intrinsic microporosity (PIM-1).* Journal of Membrane Science, 2017. **537**: p. 362-371.

92. Longo, M., et al., *Correlating Gas Permeability and Young's Modulus during the Physical Aging of Polymers of Intrinsic Microporosity Using Atomic Force Microscopy.* Industrial & Engineering Chemistry Research, 2019. **59**(12): p. 5381-5391.
93. Pilnáček, K., et al., *Aging of polymers of intrinsic microporosity tracked by methanol vapour permeation.* Journal of Membrane Science, 2016. **520**: p. 895-906.
94. Yong, W.F., et al., *Suppression of aging and plasticization in highly permeable polymers.* Polymer, 2015. **77**: p. 377-386.
95. Wang, Y., et al., *Polymers of intrinsic microporosity for energy-intensive membrane-based gas separations.* Materials Today Nano, 2018. **3**: p. 69-95.
96. Budd, P., et al., *Gas separation membranes from polymers of intrinsic microporosity.* Journal of Membrane Science, 2005. **251**(1-2): p. 263-269.
97. Zhang, J., et al., *Fluoride-mediated polycondensation for the synthesis of polymers of intrinsic microporosity.* Polymer, 2015. **76**: p. 168-172.
98. Swaidan, R., et al., *Pure- and mixed-gas CO2/CH4 separation properties of PIM-1 and an amidoxime-functionalized PIM-1.* Journal of Membrane Science, 2014. **457**: p. 95-102.
99. Chen, C.F., *Novel triptycene-derived hosts: synthesis and their applications in supramolecular chemistry.* Chem Commun (Camb), 2011. **47**(6): p. 1674-88.
100. Ghanem, B.S., et al., *A triptycene-based polymer of intrinsic microposity that displays enhanced surface area and hydrogen adsorption.* Chem Commun (Camb), 2007(1): p. 67-9.
101. Sydlik, S.A., Z. Chen, and T.M. Swager, *Triptycene Polyimides: Soluble Polymers with High Thermal Stability and Low Refractive Indices.* Macromolecules, 2011. **44**(4): p. 976-980.
102. Taylor, R.G., et al., *Triptycene-based Organic Molecules of Intrinsic Microporosity.* Org Lett, 2014. **16**(7): p. 1848-51.
103. Ling, H. and J. Jin, *Improved synthesis route and performance of azide modified polymers of intrinsic microporosity after thermal self-crosslinking.* Polymer, 2021. **230**.
104. Agarwal, P., et al., *Nanofiltration membranes from crosslinked Troger's base Polymers of Intrinsic Microporosity (PIMs).* Journal of Membrane Science, 2020. **595**.
105. Song, Q., et al., *Controlled thermal oxidative crosslinking of polymers of intrinsic microporosity towards tunable molecular sieve membranes.* Nat Commun, 2014. **5**: p. 4813.
106. Jeon, J.W., et al., *Carbonization of Carboxylate-Functionalized Polymers of Intrinsic Microporosity for Water Treatment.* Macromolecular Chemistry and Physics, 2020. **221**(5).
107. Cote, A.P., et al., *Porous, crystalline, covalent organic frameworks.* Science, 2005. **310**(5751): p. 1166-70.

108. Diercks, C.S., M.J. Kalmutzki, and O.M. Yaghi, *Covalent Organic Frameworks-Organic Chemistry Beyond the Molecule.* Molecules, 2017. **22**(9).
109. Yusran, Y., et al., *Covalent Organic Frameworks for Catalysis.* EnergyChem, 2020. **2**(3).
110. Zhu, L. and Y.B. Zhang, *Crystallization of Covalent Organic Frameworks for Gas Storage Applications.* Molecules, 2017. **22**(7).
111. Qian, H.L., et al., *Advances in covalent organic frameworks in separation science.* J Chromatogr A, 2018. **1542**: p. 1-18.
112. Wu, G., et al., *Two-dimensional covalent organic frameworks (COF-LZU1) based mixed matrix membranes for pervaporation.* Separation and Purification Technology, 2020. **241**.
113. Liu, Y., et al., *Multifunctional covalent organic framework (COF)-Based mixed matrix membranes for enhanced CO2 separation.* Journal of Membrane Science, 2021. **618**.
114. Lin, X., et al., *Sulfonated covalent organic frameworks (COFs) incorporated cellulose triacetate/cellulose acetate (CTA/CA)-based mixed matrix membranes for forward osmosis.* Journal of Membrane Science, 2021. **638**.
115. Hasell, T. and A.I. Cooper, *Porous organic cages: soluble, modular and molecular pores.* Nature Reviews Materials, 2016. **1**(9).
116. Zhang, F., et al., *Multicomponent Gas Storage in Organic Cage Molecules.* The Journal of Physical Chemistry C, 2017. **121**(22): p. 12426-12433.
117. Charles, C.D. and E.D. Bloch, *High-pressure methane storage and selective gas adsorption in a cyclohexane-functionalised porous organic cage.* Supramolecular Chemistry, 2019. **31**(8): p. 508-513.
118. Bojdys, M.J., et al., *Supramolecular engineering of intrinsic and extrinsic porosity in covalent organic cages.* J Am Chem Soc, 2011. **133**(41): p. 16566-71.
119. Song, Q., et al., *Porous Organic Cage Thin Films and Molecular-Sieving Membranes.* Adv Mater, 2016. **28**(13): p. 2629-37.
120. Mao, H. and S. Zhang, *Mixed-matrix membranes incorporated with porous shape-persistent organic cages for gas separation.* J Colloid Interface Sci, 2017. **490**: p. 29-36.
121. Jiang, C., et al., *Nanofiltration membranes with enhanced microporosity and inner-pore interconnectivity for water treatment: Excellent balance between permeability and selectivity.* Journal of Membrane Science, 2019. **586**: p. 192-201.
122. Li, S., et al., *High flux thin film composite (TFC) membrane with non-planar rigid twisted structures for organic solvent nanofiltration (OSN).* Separation and Purification Technology, 2022. **286**.
123. Jimenez-Solomon, M.F., et al., *Polymer nanofilms with enhanced microporosity by interfacial polymerization.* Nat Mater, 2016. **15**(7): p. 760-7.

124. Liu, J., et al., *Self-standing and flexible covalent organic framework (COF) membranes for molecular separation.* Sci Adv, 2020. **6**(41).
125. Kandambeth, S., et al., *Selective Molecular Sieving in Self-Standing Porous Covalent-Organic-Framework Membranes.* Adv Mater, 2017. **29**(2).
126. Kumar Mahato, A., et al., *Crystallizing Sub 10 nm Covalent Organic Framework Thin Films via Interfacial-Residual Concomitance.* J Am Chem Soc, 2021. **143**(49): p. 20916-20926.
127. Cui, X., et al., *Interfacial polymerization of MOF "monomers" to fabricate flexible and thin membranes for molecular separation with ultrafast water transport.* Journal of Materials Chemistry A, 2021. **9**(32): p. 17528-17537.
128. He, A., et al., *A smart and responsive crystalline porous organic cage membrane with switchable pore apertures for graded molecular sieving.* Nat Mater, 2022. **21**(4): p. 463-470.
129. Jiang, Z., et al., *Aligned macrocycle pores in ultrathin films for accurate molecular sieving.* Nature, 2022. **609**(7925): p. 58-64.
130. Priske, M., et al., *Recent Applications of Organic Solvent Nanofiltration.* Chemie Ingenieur Technik, 2016. **88**(1-2): p. 39-49.
131. Xu, M., et al., *The recent advance of precisely designed membranes for sieving.* Nanotechnology, 2023. **34**(23).
132. Marchetti, P., L. Peeva, and A. Livingston, *The Selectivity Challenge in Organic Solvent Nanofiltration: Membrane and Process Solutions*, in *Annual Review of Chemical and Biomolecular Engineering, Vol 8*, J.M. Prausnitz, Editor. 2017, Annual Reviews: Palo Alto. p. 473-497.
133. Hang, S., *Oil adsorption measurements during membrane filtration.* Journal of Membrane Science, 2003. **214**(1): p. 93-99.
134. Su-Hua, W., D. Bing-zhi, and H. Yu, *Adsorption of bisphenol A by polysulphone membrane.* Desalination, 2010. **253**(1-3): p. 22-29.
135. Termonia, Y., *Polymer solubility in mixed solvents.* Journal of Polymer Science Part B: Polymer Physics, 1999. **37**(19): p. 2782-2787.
136. Shin, M.G., et al., *Solvent transport model for polyamide nanofilm membranes based on accurate Hansen solubility parameters.* Journal of Membrane Science, 2023. **674**.
137. Gharagheizi, F. and M. Torabi Angaji, *A New Improved Method for Estimating Hansen Solubility Parameters of Polymers.* Journal of Macromolecular Science, Part B, 2007. **45**(2): p. 285-290.

138. Sarkar, P., et al., *Precise separation of small neutral solutes with mixed-diamine-based nanofiltration membranes and the impact of solvent activation.* Separation and Purification Technology, 2021. **279**.
139. Jimenez Solomon, M.F., Y. Bhole, and A.G. Livingston, *High flux membranes for organic solvent nanofiltration (OSN)—Interfacial polymerization with solvent activation.* Journal of Membrane Science, 2012. **423-424**: p. 371-382.
140. Meng, B., et al., *Fabrication of surface-charged MXene membrane and its application for water desalination.* Journal of Membrane Science, 2021. **623**.
141. Nguyen, C.T. and A. Beskok, *Water desalination performance of h-BN and optimized charged graphene membranes.* Microfluidics and Nanofluidics, 2020. **24**(5).
142. Peydayesh, M., T. Mohammadi, and O. Bakhtiari, *Water desalination via novel positively charged hybrid nanofiltration membranes filled with hyperbranched polyethyleneimine modified MWCNT.* Journal of Industrial and Engineering Chemistry, 2019. **69**: p. 127-140.
143. Wang, Z., J. Chu, and X. Zhang, *Study of a cake model during stirred dead-end microfiltration.* Desalination, 2007. **217**(1-3): p. 127-138.
144. Balannec, B., et al., *Comparative study of different nanofiltration and reverse osmosis membranes for dairy effluent treatment by dead-end filtration.* Separation and Purification Technology, 2005. **42**(2): p. 195-200.
145. Di, H., G.J.O. Martin, and D.E. Dunstan, *Characterization of particle deposition during crossflow filtration as influenced by permeate flux and crossflow velocity using a microfluidic filtration system.* Frontiers of Chemical Science and Engineering, 2020. **15**(3): p. 552-561.
146. Elimelech, M. and S. Bhattacharjee, *A novel approach for modeling concentration polarization in crossflow membrane filtration based on the equivalence of osmotic pressure model and filtration theory.* Journal of Membrane Science, 1998. **145**(2): p. 223-241.
147. Balavi, H. and Y. Boluk, *Dynamic filtration of drilling fluids and fluid loss under axially rotating crossflow filtration.* Journal of Petroleum Science and Engineering, 2018. **163**: p. 611-615.
148. Hołda, A.K. and I.F.J. Vankelecom, *Understanding and guiding the phase inversion process for synthesis of solvent resistant nanofiltration membranes.* Journal of Applied Polymer Science, 2015. **132**(27): p. n/a-n/a.
149. Kurada, K.V., A. Agarwal, and S. De, *Effect of mixed solvents on phase inversion of polymeric membranes.* Polymer International, 2020. **69**(10): p. 920-932.

150. See-Toh, Y.H., F.C. Ferreira, and A.G. Livingston, *The influence of membrane formation parameters on the functional performance of organic solvent nanofiltration membranes.* Journal of Membrane Science, 2007. **299**(1-2): p. 236-250.
151. Ye, H., et al., *Advances in the Application of Polymers of Intrinsic Microporosity in Liquid Separation and Purification: Membrane Separation and Adsorption Separation.* Polymer Reviews, 2020. **61**(2): p. 239-279.
152. Jin, Y., et al., *Amidoxime-functionalized polymer of intrinsic microporosity (AOPIM-1)-based thin film composite membranes with ultrahigh permeance for organic solvent nanofiltration.* Journal of Membrane Science, 2021. **632**.
153. Li, J., et al., *PIM-1 pore-filled thin film composite membranes for tunable organic solvent nanofiltration.* Journal of Membrane Science, 2020. **601**.
154. Gao, J., S. Japip, and T.-S. Chung, *Organic solvent resistant membranes made from a cross-linked functionalized polymer with intrinsic microporosity (PIM) containing thioamide groups.* Chemical Engineering Journal, 2018. **353**: p. 689-698.
155. Wu, W.H., et al., *Effective Conversion of Amide to Carboxylic Acid on Polymers of Intrinsic Microporosity (PIM-1) with Nitrous Acid.* Membranes (Basel), 2018. **8**(2).
156. McLauchlin, A.R., O.R. Ghita, and L. Savage, *Studies on the reprocessability of poly(ether ether ketone) (PEEK).* Journal of Materials Processing Technology, 2014. **214**(1): p. 75-80.
157. Hendrix, K., G. Koeckelberghs, and I.F.J. Vankelecom, *Study of phase inversion parameters for PEEK-based nanofiltration membranes.* Journal of Membrane Science, 2014. **452**: p. 241-252.
158. Abdulhamid, M.A., et al., *Molecular engineering of high-performance nanofiltration membranes from intrinsically microporous poly(ether-ether-ketone).* Journal of Materials Chemistry A, 2020. **8**(46): p. 24445-24454.
159. da Silva Burgal, J., L. Peeva, and A. Livingston, *Negligible ageing in poly(ether-ether-ketone) membranes widens application range for solvent processing.* Journal of Membrane Science, 2017. **525**: p. 48-56.
160. Strathmann, H., et al., *The formation mechanism of asymmetric membranes.* Desalination, 1975. **16**(2): p. 179-203.
161. Shi, D., et al., *Separation performance of polyimide nanofiltration membranes for concentrating spiramycin extract.* Desalination, 2006. **191**(1-3): p. 309-317.
162. White, L., *Transport properties of a polyimide solvent resistant nanofiltration membrane.* Journal of Membrane Science, 2002. **205**(1-2): p. 191-202.
163. See Toh, Y.H., F.W. Lim, and A.G. Livingston, *Polymeric membranes for nanofiltration in polar aprotic solvents.* Journal of Membrane Science, 2007. **301**(1-2): p. 3-10.

164. Vanherck, K., et al., *Cross-linked polyimide membranes for solvent resistant nanofiltration in aprotic solvents.* Journal of Membrane Science, 2008. **320**(1-2): p. 468-476.
165. Rezac, M.E., E. Todd Sorensen, and H.W. Beckham, *Transport properties of crosslinkable polyimide blends.* Journal of Membrane Science, 1997. **136**(1-2): p. 249-259.
166. See-Toh, Y.H., M. Silva, and A. Livingston, *Controlling molecular weight cut-off curves for highly solvent stable organic solvent nanofiltration (OSN) membranes.* Journal of Membrane Science, 2008. **324**(1-2): p. 220-232.
167. Kang, G.-d. and Y.-m. Cao, *Application and modification of poly(vinylidene fluoride) (PVDF) membranes – A review.* Journal of Membrane Science, 2014. **463**: p. 145-165.
168. Munirasu, S., et al., *Intrinsically superhydrophobic PVDF membrane by phase inversion for membrane distillation.* Desalination, 2017. **417**: p. 77-86.
169. Davood Abadi Farahani, M.H. and T.-S. Chung, *A novel crosslinking technique towards the fabrication of high-flux polybenzimidazole (PBI) membranes for organic solvent nanofiltration (OSN).* Separation and Purification Technology, 2019. **209**: p. 182-192.
170. Rozière, J., et al., *On the doping of sulfonated polybenzimidazole with strong bases.* Solid State Ionics, 2001. **145**(1-4): p. 61-68.
171. Zhou, S., et al., *High-performance functionalized polymer of intrinsic microporosity (PIM) composite membranes with thin and stable interconnected layer for organic solvent nanofiltration.* Journal of Membrane Science, 2019. **591**.
172. Li, J., et al., *Microporous Matrimid/PIM-1 Thin Film Composite Membranes with Narrow Pore Size Distribution used for Molecular Separation in Organic Solvents.* Macromol Rapid Commun, 2023. **44**(6): p. e2200826.
173. Aburabie, J. and K.-V. Peinemann, *Crosslinked poly(ether block amide) composite membranes for organic solvent nanofiltration applications.* Journal of Membrane Science, 2017. **523**: p. 264-272.
174. Burke, D. and D.J. Henderson, *Chirality: a blueprint for the future.* Br J Anaesth, 2002. **88**(4): p. 563-76.
175. Salgin, S., U. Salgin, and N. Tuzlali, *Enantiomeric separation of antidepressant drug fluoxetine based on chiral membranes.* Desalination and Water Treatment, 2018. **105**: p. 245-249.
176. Fernandes, C., M. Tiritan, and M. Pinto, *Chiral Separation in Preparative Scale: A Brief Overview of Membranes as Tools for Enantiomeric Separation.* Symmetry, 2017. **9**(10).
177. Seyhan, S., et al., *Chiral separation of amino acids using a chiral crown ether by impregnation on a polymeric support and monoamine modified silica gel.* Tetrahedron: Asymmetry, 2006. **17**(11): p. 1700-1704.

178. Hendaus, M.A., *Remdesivir in the treatment of coronavirus disease 2019 (COVID-19): a simplified summary.* J Biomol Struct Dyn, 2020: p. 1-6.
179. Ian M. Leck, E.L.M.M., *Incidence of Malformations Since the Introduction of Thalidomide.* British Medical Journal, 1962. **2**(5296): p. 16-20.
180. Vargesson, N., *Thalidomide-induced teratogenesis: history and mechanisms.* Birth Defects Res C Embryo Today, 2015. **105**(2): p. 140-56.
181. Zhao, Y., et al., *Chiral Recognition for Chromatography and Membrane-Based Separations: Recent Developments and Future Prospects.* Molecules, 2021. **26**(4).
182. Higuchi, A., et al., *Polymeric Membranes for Chiral Separation of Pharmaceuticals and Chemicals.* Polymer Reviews, 2010. **50**(2): p. 113-143.
183. Berthod, A., *Chiral Recognition Mechanisms.* Analytical Chemistry, 2006. **78**(7): p. 2093-2099.
184. Cheng, Q., et al., *Chiral membranes for enantiomer separation: A comprehensive review.* Separation and Purification Technology, 2022. **292**.
185. Zhu, Q., et al., *Recent progress of membrane technology for chiral separation: A comprehensive review.* Separation and Purification Technology, 2023. **309**.
186. Hammoud, Z., et al., *Cyclodextrin-membrane interaction in drug delivery and membrane structure maintenance.* Int J Pharm, 2019. **564**: p. 59-76.
187. Xiao, Y. and T.-S. Chung, *Functionalization of cellulose dialysis membranes for chiral separation using beta-cyclodextrin immobilization.* Journal of Membrane Science, 2007. **290**(1-2): p. 78-85.
188. Xiong, S., et al., *Thin film composite membranes containing intrinsic CD cavities in the selective layer.* Journal of Membrane Science, 2018. **551**: p. 294-304.
189. Ke, J., et al., *Novel chiral composite membrane prepared via the interfacial polymerization of diethylamino-beta-cyclodextrin for the enantioseparation of chiral drugs.* Journal of Membrane Science, 2020. **597**.
190. Ong, C.S., et al., *Enantiomeric Separation of Racemic Mixtures Using Chiral-Selective and Organic-Solvent-Resistant Thin-Film Composite Membranes.* ACS Appl Mater Interfaces, 2022. **14**(8): p. 10875-10885.
191. Zhang, S., et al., *β-Cyclodextrin-Self-Assembled Nanochannel Membrane for the Separation of Chiral Drugs.* ACS Applied Nano Materials, 2020. **3**(5): p. 4351-4356.
192. Singh, K., et al., *Optical Resolution of Racemic Mixtures of Amino Acids through Nanofiltration Membrane Process.* Separation Science and Technology, 2014. **49**(17): p. 2630-2641.

193. Matsuoka, Y., et al., *Chiral separation of phenylalanine in ultrafiltration through DNA-immobilized chitosan membranes.* Journal of Membrane Science, 2006. **280**(1-2): p. 116-123.
194. Ingole, P.G., et al., *Preparation of Thin Film Polymer Composite Membranes for Optical Resolution of Racemic Mixture of α-Amino Acids.* Separation Science and Technology, 2013. **48**(12): p. 1777-1787.
195. Kim, J.H., et al., *Optical resolution of α-amino acids through enantioselective polymeric membranes based on polysaccharides.* Journal of Membrane Science, 2003. **213**(1-2): p. 273-283.
196. Guo, J., et al., *Ultrathin Chiral Metal-Organic-Framework Nanosheets for Efficient Enantioselective Separation.* Angew Chem Int Ed Engl, 2018. **57**(23): p. 6873-6877.
197. Aoki, T., et al., *Synthesis of chiral helical poly[p-(oligopinanylsiloxanyl)phenylacetylene]s and enantioselective permeability of their membranes.* Journal of Polymer Science Part A: Polymer Chemistry, 2004. **42**(18): p. 4502-4517.
198. Das, S., et al., *Chiral Recognition and Separation by Chirality-Enriched Metal-Organic Frameworks.* Angew Chem Int Ed Engl, 2018. **57**(28): p. 8629-8633.
199. Wang, Y., et al., *Construction of beta-Cyclodextrin Covalent Organic Framework-Modified Chiral Stationary Phase for Chiral Separation.* ACS Appl Mater Interfaces, 2019. **11**(51): p. 48363-48369.
200. Lu, Y., et al., *Cyclodextrin metal-organic framework-polymer composite membranes towards ultimate and stable enantioselectivity.* Journal of Membrane Science, 2021. **620**.
201. Lu, Y., et al., *Homochiral MOF-Polymer Mixed Matrix Membranes for Efficient Separation of Chiral Molecules.* Angew Chem Int Ed Engl, 2019. **58**(47): p. 16928-16935.
202. Choi, H.J. and D.Y. Koh, *Homochiral Metal-Organic Framework Based Mixed Matrix Membrane for Chiral Resolution.* Membranes (Basel), 2022. **12**(4).
203. Yoshikawa, M., T. Ooi, and J.-I. Izumi, *Alternative molecularly imprinted membranes from a derivative of natural polymer, cellulose acetate.* Journal of Applied Polymer Science, 1999. **72**(4): p. 493-499.
204. Sueyoshi, Y., et al., *Chiral separation with molecularly imprinted polysulfone-aldehyde derivatized nanofiber membranes☆.* Journal of Membrane Science, 2012. **401-402**: p. 89-96.
205. Gao, B., Y. Li, and K. Cui, *Molecularly imprinted membrane with innovative structure and high performance for chiral separation of amino acids.* International Journal of Polymeric Materials and Polymeric Biomaterials, 2017. **67**(8): p. 517-527.

206. Bai, J., et al., *Synthesis of novel hyper-cross-linked chiral porous polymers and their applications in enantioselective adsorption of amino acids.* Microporous and Mesoporous Materials, 2020. **294**.
207. Holy, P., et al., *Self-assembly of chiral hydrogen-bonded grid layers from terephthalic Siamese twins.* Tetrahedron-Asymmetry, 2003. **14**(2): p. 245-253.
208. Valverde-Gonzalez, A., et al., *BINOL-Containing Chiral Porous Polymers as Platforms for Enantiorecognition.* ACS Appl Mater Interfaces, 2022. **14**(48): p. 53936-53946.
209. Ritter, N., et al., *Towards chiral microporous soluble polymers--binaphthalene-based polyimides.* Macromol Rapid Commun, 2011. **32**(5): p. 438-43.
210. Wang, X., et al., *Practical Enantioselective Synthesis of Chiroptical Polymers of Intrinsic Microporosity with Circular Polarized Luminescence.* Macromolecules, 2021. **54**(23): p. 11180-11186.
211. Weng, X., et al., *Chiral polymers of intrinsic microporosity: selective membrane permeation of enantiomers.* Angew Chem Int Ed Engl, 2015. **54**(38): p. 11214-8.
212. Chen, Y., et al., *In situ fabrication of chiral covalent triazine frameworks membranes for enantiomer separation.* J Chromatogr A, 2021. **1654**: p. 462475.
213. Yuan, C., et al., *Nanochannels of Covalent Organic Frameworks for Chiral Selective Transmembrane Transport of Amino Acids.* J Am Chem Soc, 2019. **141**(51): p. 20187-20197.
214. Zhang, S., J. Zhou, and H. Li, *Chiral Covalent Organic Framework Packed Nanochannel Membrane for Enantioseparation.* Angew Chem Int Ed Engl, 2022. **61**(27): p. e202204012.
215. Qian, H.L., C.X. Yang, and X.P. Yan, *Bottom-up synthesis of chiral covalent organic frameworks and their bound capillaries for chiral separation.* Nat Commun, 2016. **7**: p. 12104.
216. Gubler, L., *Membranes and separators for redox flow batteries.* Current Opinion in Electrochemistry, 2019. **18**: p. 31-36.
217. Chakrabarti, M.H., et al., *Redox Flow Battery for Energy Storage.* Arabian Journal for Science and Engineering, 2012. **38**(4): p. 723-739.
218. Luo, T., et al., *Porous poly(benzimidazole) membrane for all vanadium redox flow battery.* Journal of Power Sources, 2016. **312**: p. 45-54.
219. Tan, R., et al., *Hydrophilic microporous membranes for selective ion separation and flow-battery energy storage.* Nat Mater, 2020. **19**(2): p. 195-202.
220. Wang, A., et al., *Solution-Processable Redox-Active Polymers of Intrinsic Microporosity for Electrochemical Energy Storage.* J Am Chem Soc, 2022. **144**(37): p. 17198-17208.

221. Di, M., et al., *Covalent organic framework (COF) constructed proton permselective membranes for acid supporting redox flow batteries.* Chemical Engineering Journal, 2020. **399**.

222. Xu, W., et al., *Sub-2-nm Channels within Covalent Triazine Framework Enable Fast Proton-Selective Transport in Flow Battery Membrane.* Advanced Functional Materials, 2023.

223. Li, J., et al., *Sulfonated Poly(ether Ether Ketone)/Sulfonated Covalent Organic Framework Composite Membranes with Enhanced Performance for Application in Vanadium Redox Flow Batteries.* ACS Applied Energy Materials, 2022. **5**(12): p. 15856-15863.

224. Zhang, F., J.B. Fan, and S. Wang, *Interfacial Polymerization: From Chemistry to Functional Materials.* Angew Chem Int Ed Engl, 2020. **59**(49): p. 21840-21856.

225. Yu, S.C., et al., *Aromatic-cycloaliphatic polyamide thin-film composite membrane with improved chlorine resistance prepared from m-phenylenediamine-4-methyl and cyclohexane-1,3,5-tricarbonyl chloride.* Journal of Membrane Science, 2009. **344**(1-2): p. 155-164.

226. Li, L., et al., *Polyamide thin film composite membranes prepared from isomeric biphenyl tetraacyl chloride and m-phenylenediamine.* Journal of Membrane Science, 2008. **315**(1-2): p. 20-27.

227. Buch, P.R., D. Jagan Mohan, and A.V.R. Reddy, *Preparation, characterization and chlorine stability of aromatic–cycloaliphatic polyamide thin film composite membranes.* Journal of Membrane Science, 2008. **309**(1-2): p. 36-44.

228. Hai, Y., et al., *Thin film composite nanofiltration membrane prepared by the interfacial polymerization of 1,2,4,5-benzene tetracarbonyl chloride on the mixed amines cross-linked poly(ether imide) support.* Journal of Membrane Science, 2016. **520**: p. 19-28.

229. Mi, Y.F., et al., *A loose polyamide nanofiltration membrane prepared by polyether amine interfacial polymerization for dye desalination.* Separation and Purification Technology, 2020. **248**.

230. La, Y.-H., et al., *Novel thin film composite membrane containing ionizable hydrophobes: pH-dependent reverse osmosis behavior and improved chlorine resistance.* Journal of Materials Chemistry, 2010. **20**(22).

231. Lee, H.S., et al., *Polyamide thin-film nanofiltration membranes containing TiO2 nanoparticles.* Desalination, 2008. **219**(1-3): p. 48-56.

232. Lind, M.L., et al., *Influence of zeolite crystal size on zeolite-polyamide thin film nanocomposite membranes.* Langmuir, 2009. **25**(17): p. 10139-45.

233. Al-Hobaib, A.S., et al., *Modification of thin-film polyamide membrane with multi-walled carbon nanotubes by interfacial polymerization.* Applied Water Science, 2017. **7**(8): p. 4341-4350.
234. Li, D., et al., *Preparation of silicalite-polyamide composite membranes for desalination.* Asia-Pacific Journal of Chemical Engineering, 2012. **7**(3): p. 434-441.
235. Lai, G.S., et al., *Tailor-made thin film nanocomposite membrane incorporated with graphene oxide using novel interfacial polymerization technique for enhanced water separation.* Chemical Engineering Journal, 2018. **344**: p. 524-534.
236. Li, C., et al., *Covalent organic frameworks (COFs)-incorporated thin film nanocomposite (TFN) membranes for high-flux organic solvent nanofiltration (OSN).* Journal of Membrane Science, 2019. **572**: p. 520-531.
237. Lau, W.J., et al., *A recent progress in thin film composite membrane: A review.* Desalination, 2012. **287**: p. 190-199.
238. Jegal, J., S.G. Min, and K.-H. Lee, *Factors affecting the interfacial polymerization of polyamide active layers for the formation of polyamide composite membranes.* Journal of Applied Polymer Science, 2002. **86**(11): p. 2781-2787.
239. Lee, J., R. Wang, and T.-H. Bae, *A comprehensive understanding of co-solvent effects on interfacial polymerization: Interaction with trimesoyl chloride.* Journal of Membrane Science, 2019. **583**: p. 70-80.
240. Kong, C., et al., *Controlled synthesis of high performance polyamide membrane with thin dense layer for water desalination.* Journal of Membrane Science, 2010. **362**(1-2): p. 76-80.
241. Al-Hobaib, A.S., et al., *New RO TFC Membranes by Interfacial Polymerization in n-Dodecane with Various co-Solvents.* Membranes (Basel), 2016. **6**(2).
242. Liu, Y., et al., *Is the solvent activation strategy before heat treatment applicable to all reverse osmosis membranes?* Journal of Membrane Science, 2023. **665**.
243. Zhu, C.-Y., et al., *Polyamide nanofilms with linearly-tunable thickness for high performance nanofiltration.* Journal of Membrane Science, 2021. **627**.
244. Wu, D., et al., *Thin film composite nanofiltration membranes assembled layer-by-layer via interfacial polymerization from polyethylenimine and trimesoyl chloride.* Journal of Membrane Science, 2014. **472**: p. 141-153.
245. Wang, M., et al., *Electrochemical Interfacial Polymerization toward Ultrathin COF Membranes for Brine Desalination.* Angew Chem Int Ed Engl, 2023. **62**(13): p. e202219084.
246. Shen, Q., *Advances in unusual interfacial polymerization techniques.* Polymer, 2023. **270**.

247. Wang, F., Z. Yang, and C.Y. Tang, *Modeling Water Transport in Interlayered Thin-Film Nanocomposite Membranes: Gutter Effect vs Funnel Effect.* Acs Es&T Engineering, 2022. **2**(11): p. 2023-2033.
248. Gan, B.W., et al., *Ultrathin polyamide nanofilm with an asymmetrical structure: A novel strategy to boost the permeance of reverse osmosis membranes.* Journal of Membrane Science, 2020. **612**: p. 11.
249. Peter, J. and K.V. Peinemann, *Multilayer composite membranes for gas separation based on crosslinked PTMSP gutter layer and partially crosslinked Matrimid® 5218 selective layer.* Journal of Membrane Science, 2009. **340**(1-2): p. 62-72.
250. Liang, C.Z., et al., *High-performance multiple-layer PIM composite hollow fiber membranes for gas separation.* Journal of Membrane Science, 2018. **563**: p. 93-106.
251. Borisov, I., et al., *Synergistic enhancement of gas selectivity in thin film composite membranes of PIM-1.* Journal of Materials Chemistry A, 2019. **7**(11): p. 6417-6430.
252. Ma, Y., et al., *A microporous polymer TFC membrane with 2-D MOF nanosheets gutter layer for efficient H2 separation.* Separation and Purification Technology, 2021. **261**.
253. Kattula, M., et al., *Designing ultrathin film composite membranes: the impact of a gutter layer.* Sci Rep, 2015. **5**: p. 15016.
254. Blais, H.N., K. Schroen, and J.T. Tobin, *A review of multistage membrane filtration approaches for enhanced efficiency during concentration and fractionation of milk and whey.* International Journal of Dairy Technology, 2022. **75**(4): p. 749-760.
255. Yuan, B., et al., *Asymmetric polyamide nanofilms with highly ordered nanovoids for water purification.* Nat Commun, 2020. **11**(1): p. 6102.
256. Freger, V., *Nanoscale Heterogeneity of Polyamide Membranes Formed by Interfacial Polymerization.* Langmuir, 2003. **19**(11): p. 4791-4797.

Appendix.

Self-supported polyamide membranes from interfacial polymerization:

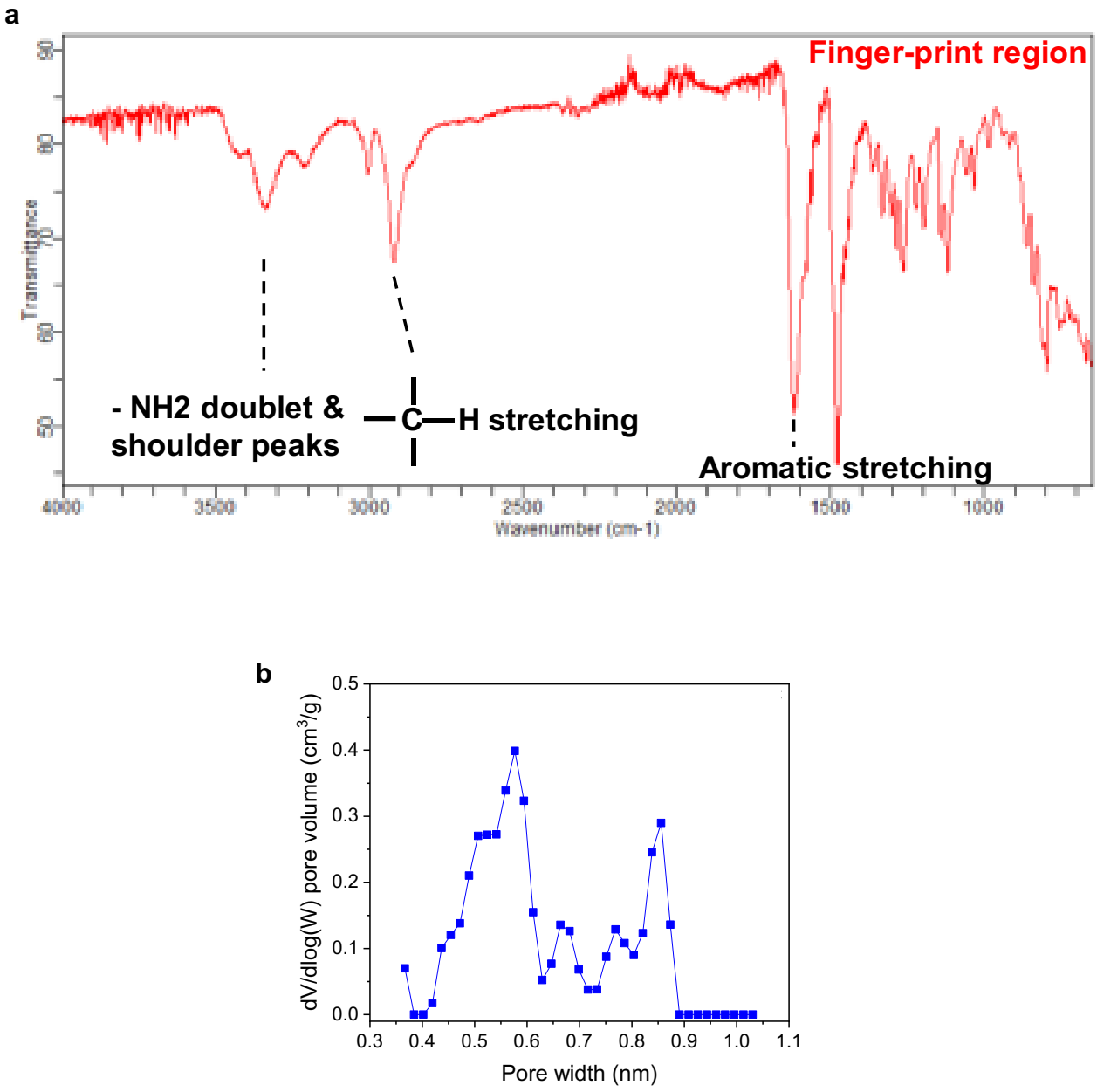


Figure S1. a. FTIR spectrums of DBMPA monomer in dry air. b. DFT pore size distributions of SPA-2 shattered films derived from CO2 gas adsorption isotherms.

Solubility test was performed by dissolving 5mg of MPD into 20g of hexane and 5mg of DBMPA into 20g of hexane separately. Both solutions were sonicated under 35°C for 30 minutes. MPD almost completely dissolved in hexane while almost no DBMPA dissolved in hexane. DBMPA-hexane was a suspension instead of solution.

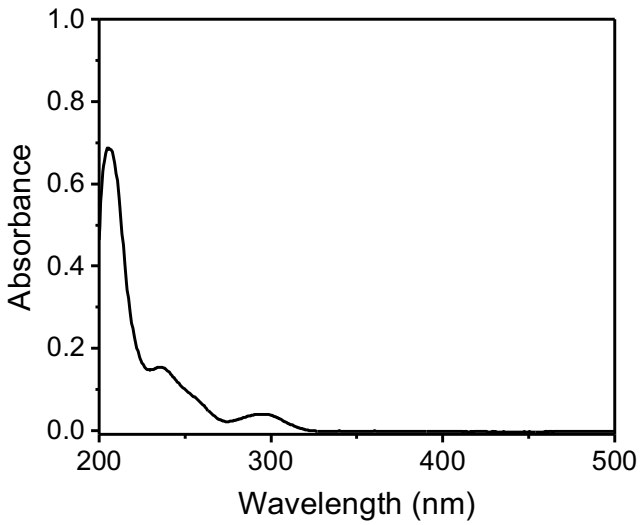


Figure S2. UV adsorption spectrums of 0.0003wt% DBMPA dissolved in MeOH.

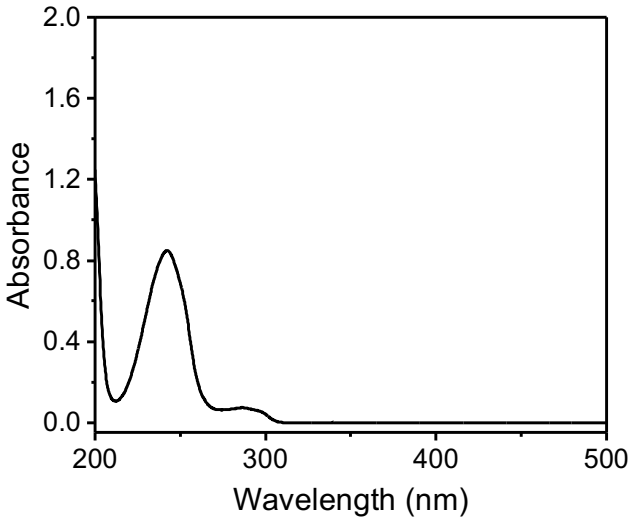


Figure S3. UV adsorption spectrums of 0.001wt% TPC dissolved in MeOH-water mixture with 1:1 weight ratio.

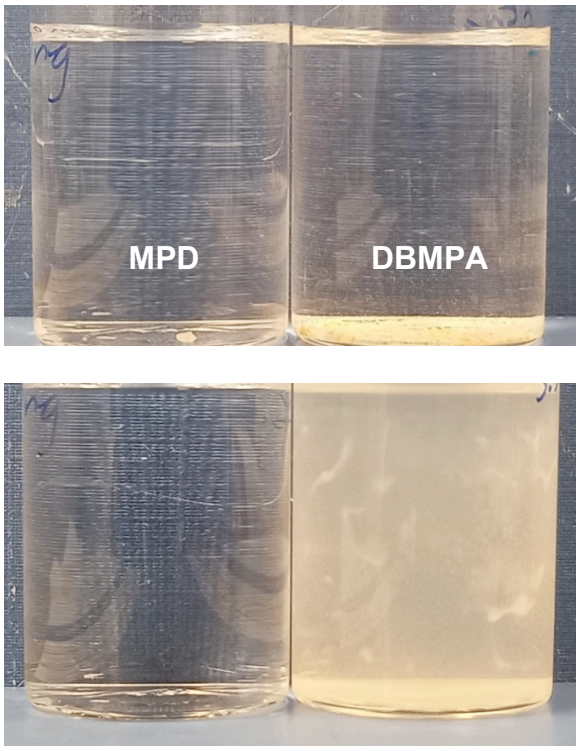


Figure S4. Top row: 5 mg of MPD and DBMPA was dissolved in 20 g of hexane separately. Bottom row: After sonication at 35 °C MPD completely dissolved in hexane while DBMPA had poor solubility in hexane.

DBMPA could hardly be dispersed in hexane suggesting poor solubility, while MPD could be more easily dispersed suggesting moderate solubility.

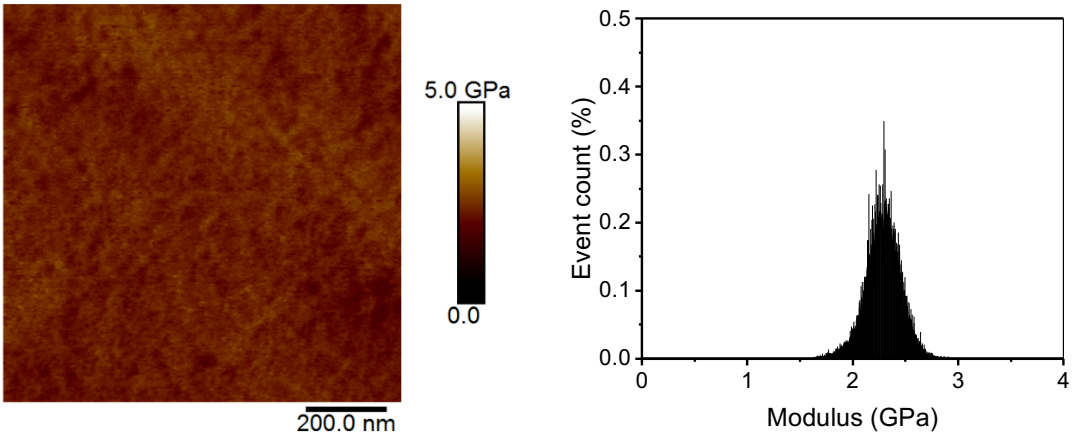


Figure S5. Storage modulus of SPA-1-5min film measured from AFM nanoindentation method.

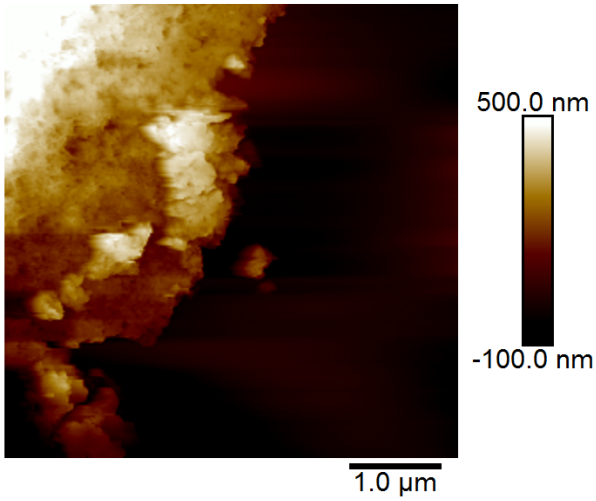


Figure S6. AFM top-view image of $DBMPA_{0.06}$-$TPC_{0.1}$ film formed from isopropanol-water as sub-phase solvents reacted for 5 minutes.

Formed DBMPA film had storage modulus of ~ 2.3 GPa. This value was measured by indenting skin layer surface. (Fig. S5) Since beneath the skin layer it is the porous layer that is supporting the indented surface, actual modulus of dense DBMPA-TPC film could be higher than this value. Isopropanol is more viscous than methanol, amine diffusion rate is slower in this case in aqueous phase. Majority of amide condensation reaction now takes place only in aqueous phase, resulting in only porous layer structure forming without skin layer.

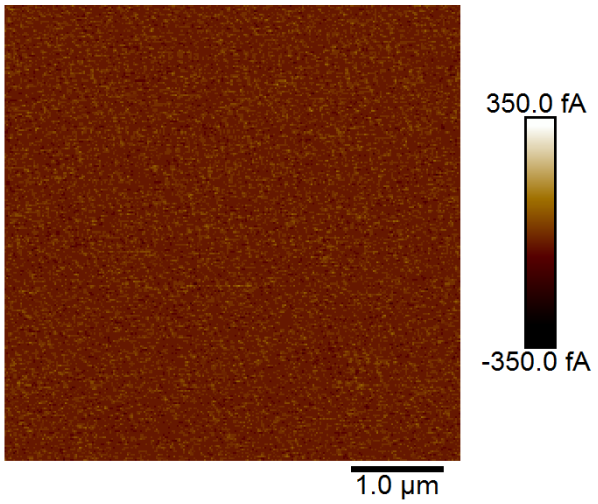


Figure S7. Surface current mapping using AFM PF-TUNA measurements of SPA-1-5min film.

SPA-1 film does not have ion exchange groups and current measurements were taken in dry conditions. Silver paint was applied near edge of entire film to form closed circuit to help take

measurements. This result does suggest top skin layer surface of SPA-1 film is uniform. (Fig. S7) But surface was not very conductive.

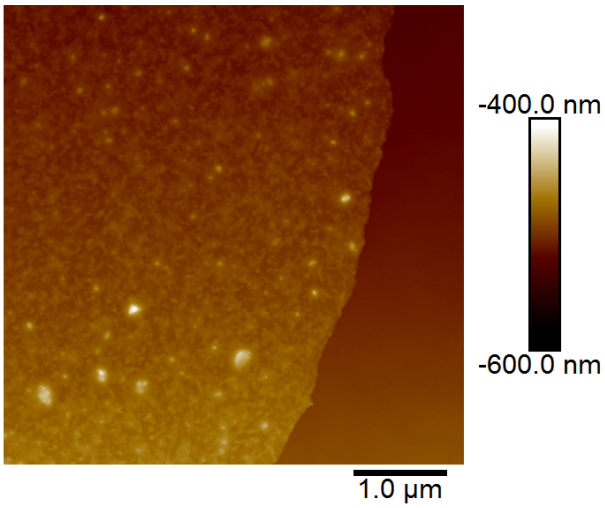


Figure S8. AFM top-view image of MPD-TMC-30min membrane.

MPD-TMC film synthesized over 30 minutes still do not have nodule textures. But according to height profile of surface it is not very smooth. It is worth noting here even after 30 minutes of reaction time MPD-TMC film was still ~ 30 nm thick. This result is consistent with existing self-confinement theory in IP. Formed MPD-TMC is not permeable to reagents under static conditions, hence film growth terminated itself within short time.

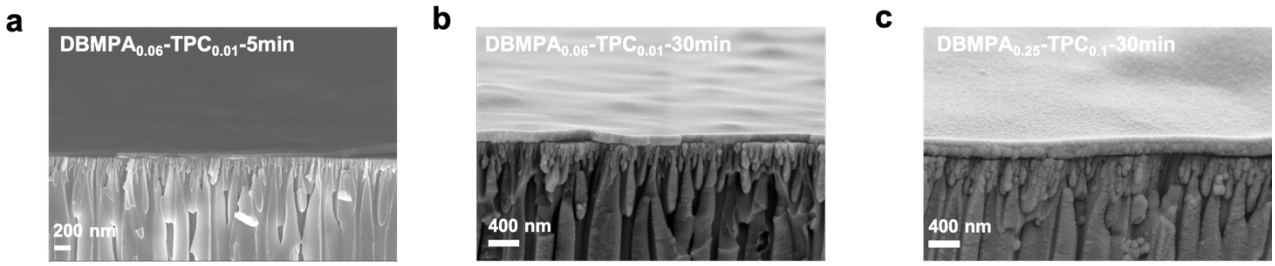


Figure S9. Zoomed-in cross-sectional SEM images of DBMPA-TPC films synthesized with different monomer concentrations and captured on AAO supports.

All SPA-1 films showed exceptionally high carbon content, which is primarily due to DBMPA monomer structure. Synthesized SPA-1 films had low chlorine content suggesting polymerization was rather complete. Cl content in 1 minute SPA-1 film and 30 minute SPA-1 film did not show significant differences suggesting amide condensation indeed happened very quickly. Reaction time does not affect consumption of functional groups very much.

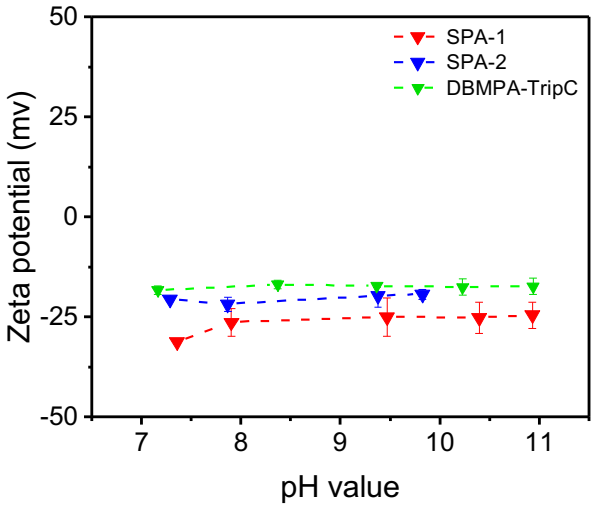


Figure S10. Zeta-potential measurements of SPA-1, SPA-2 and DBMPA-TripC membrane at pH > 7.

Salt rejections of SPA membranes in water were measured in dead-end filtration. Conductivity of permeate side was constantly measured using conductivity meter to calculate rejections of ions.

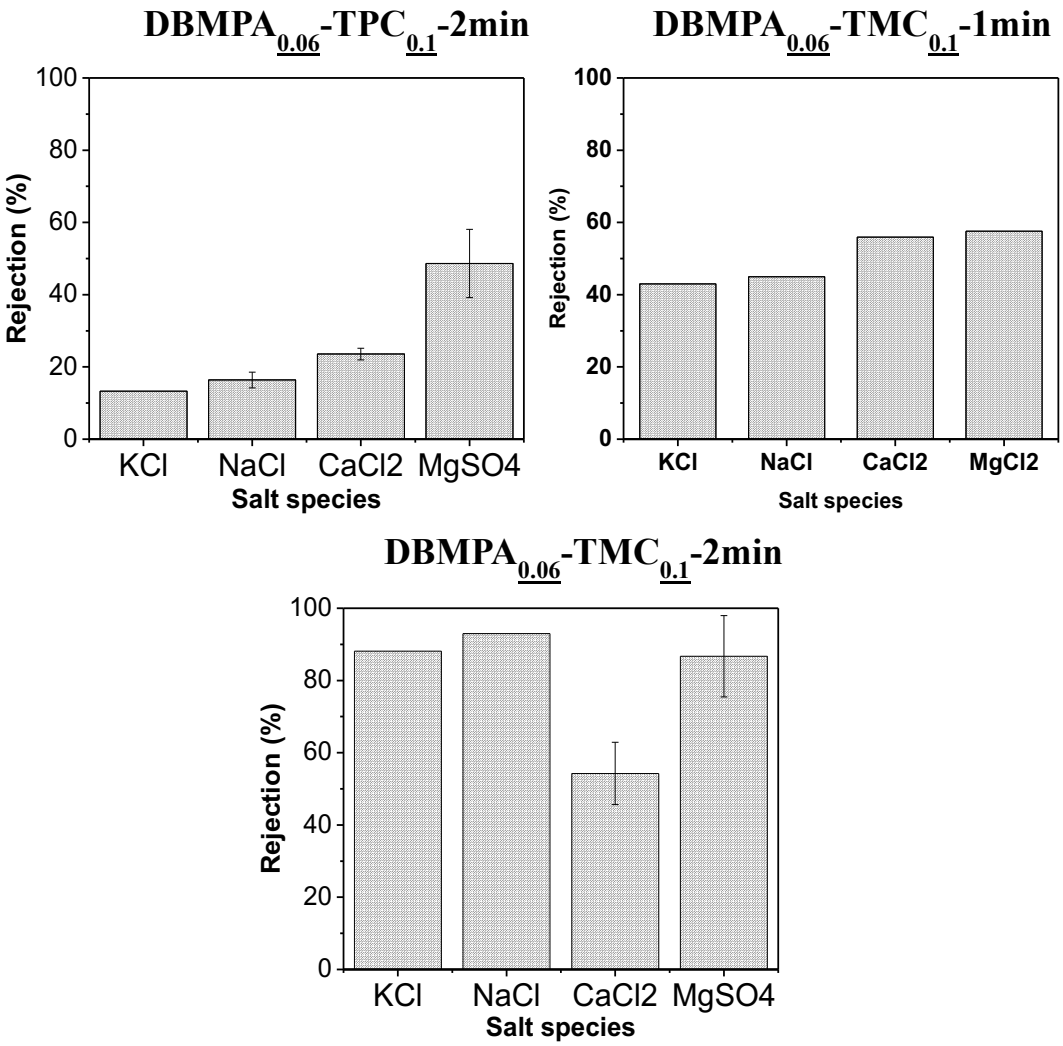
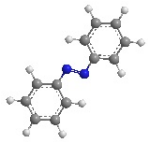
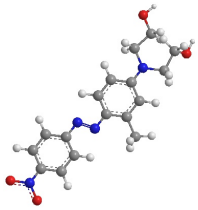
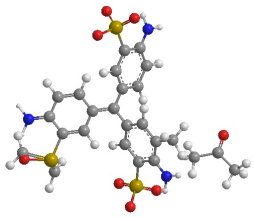
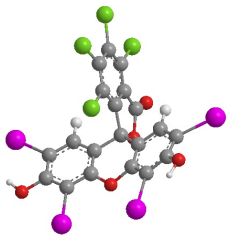


Figure S11. Salt rejections of SPA-1 and SPA-2 TFC membrane using PAN support in water.

SPA-2 membranes have higher salt rejections compared with SPA-1 membranes synthesized under same conditions. This could be due to hydrolysis of unreacted -COCl groups in tri-functional TMC monomer during IP reaction that demotivated ion permeation through SPA-2 membranes.

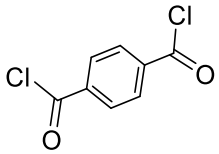
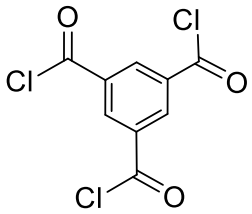
DBMPA has hydrophobic backbones and high carbon content, in comparison MPD is a small amine molecule with lower carbon content.

Table. S1 Properties of dye markers used in OSN.

Name	3-D structure	Molecular weight (g/mol)	Estimated dimensions (Å)
Acetone		58	4.6 × 3.7
Azobenzene (AZO)		182	10.7 × 5.7
Disperse Red (DR)		314	13.4 × 6.4
Sudan 7B (S7B)		379	14.2 × 8.9
Acid Fushin (ACF)		585	10.4 × 11.7
Rose Bengal (RB)		1017	11.1 × 11.0

To our knowledge TPC is the smallest multi-functional aromatic acyl chloride that is commercially available with decent reactivity. TPC also has smaller dimensions than TMC, hence to showcase our concept TPC is predominantly used to evaluate membrane structure and performances. On the other hand, TMC has similar molecular dimensions with TPC, but axial dynamic length of TMC molecule is larger than TPC which doesn't benefit crossover during IP film synthesis.

Table. S2 Properties of acyl chloride reagent used in polyamide film synthesis.

Name	Structure	MW (g mol^{-1})	Estimated dimension (Å)
Terephthaloyl chloride (TPC)		203	6.9 × 3.1
Trimesoyl chloride (TMC)		265	7.7 × 6.7

Functionalized SPA membranes for chiral separation:

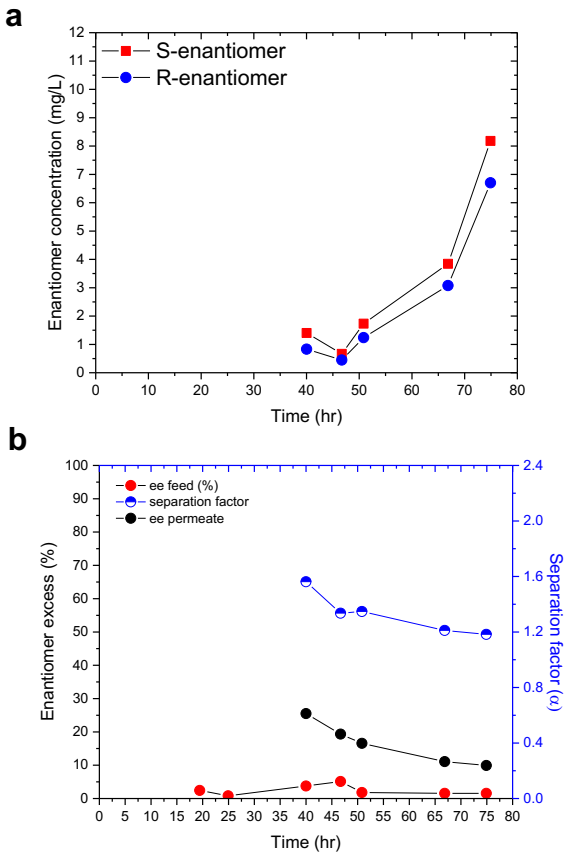
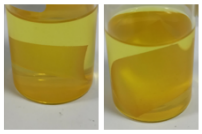
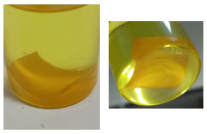
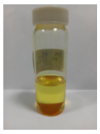
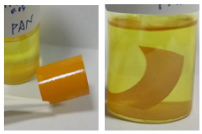
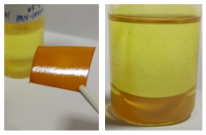
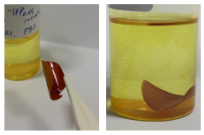


Figure S12. Reproduced chiral separation performances of NEA in static diffusion using chiral RBA-DBMPA-TPC membrane with PTFE support.

Despite chiral selectivity of RBA-DBMPA-TPC membranes was low ~ 16%, this result proved to be reproducible in static diffusion. Compared with enantiomer excess (ee) in feed solutions which didn't change significantly taking experimental and instrumental errors into consideration, small amount of both enantiomers permeated through the membrane while S-NEA diffused more rapidly than R-NEA.

Semi-crystalline thin-film composite membranes for energy storage devices:

Table S3. In situ TAPA-TFP film growth directly on supports. PAN, PAN-COOH and PBI supports were directly immersed in COF precursor solutions in DCM.

Support / Time (hr)	PAN	PAN-COOH	PBI sample
0 hr			
20 hr			
96 hr			
Remove solution after 96hr and store in EtOH.	-	-	-

Different ultrafiltration membranes were immersed in COF precursor solutions to observe TAPA-TFP layer growth. (Table. 4)

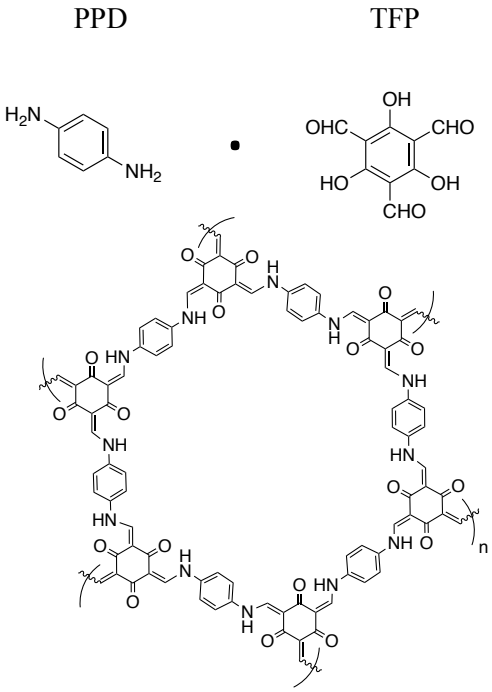


Figure S13. Chemical structures of PPD-TFP polymer synthesized from liquid-solid templated growth.

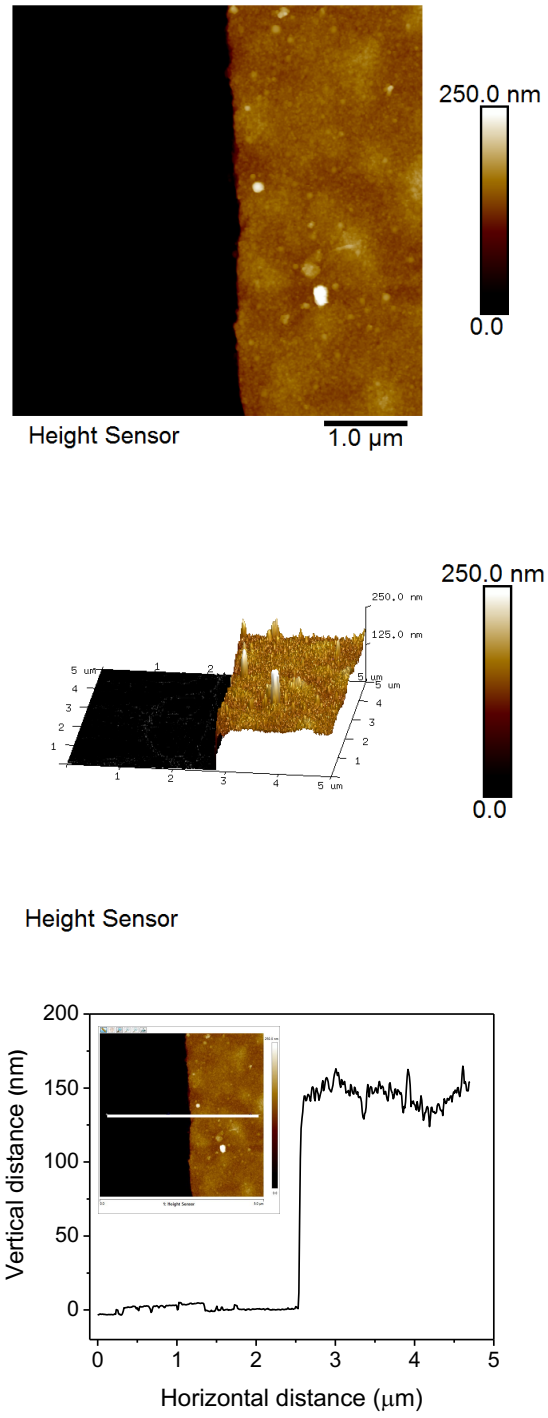
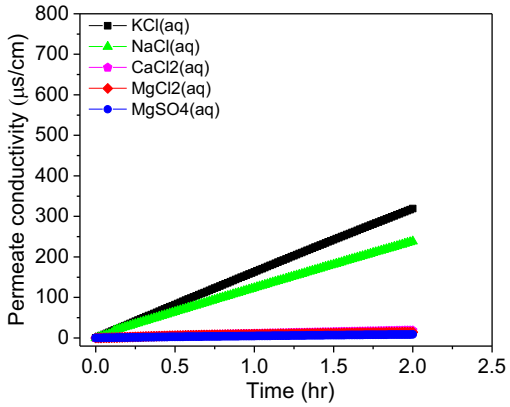
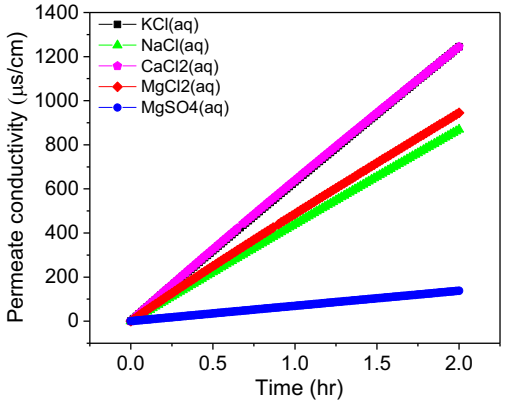


Figure S14. Top-view AFM image, 3-D AFM height profile analysis and height profile of PPD-TFP self-standing film captured on silicon wafer.

$TAPA_{0.05}$-$TFP_{0.05}$-48hr-PAN



Pristine PAN



$PPD_{0.1}$-$TFP_{0.1}$-72hr-PAN

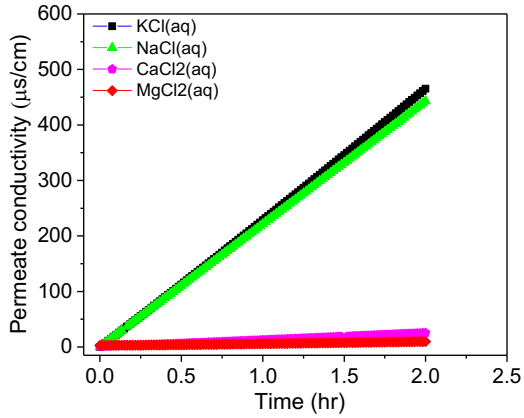


Figure S15. Ionic concentration development in permeate sides using TAPA-TFP-PAN TFC membranes, PAN support membranes and PPD-TFP-PAN membranes.

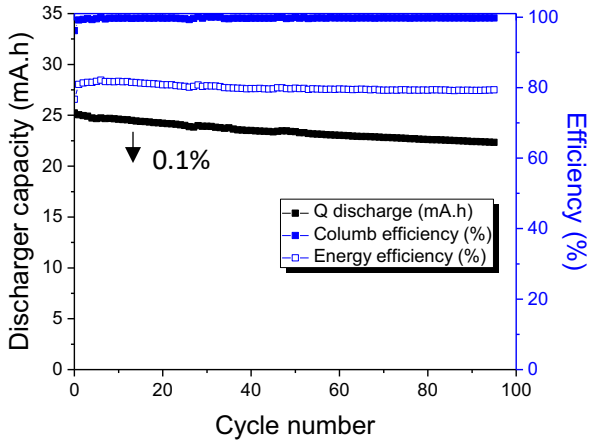


Figure S16. PPD0.1-TFP0.1-72hr-PAN-COOH RFB cycling performances in neutral pH RFB.

Synthesized PPD-TFP membrane had better discharger capacity retention than TAPA-TFP membranes.

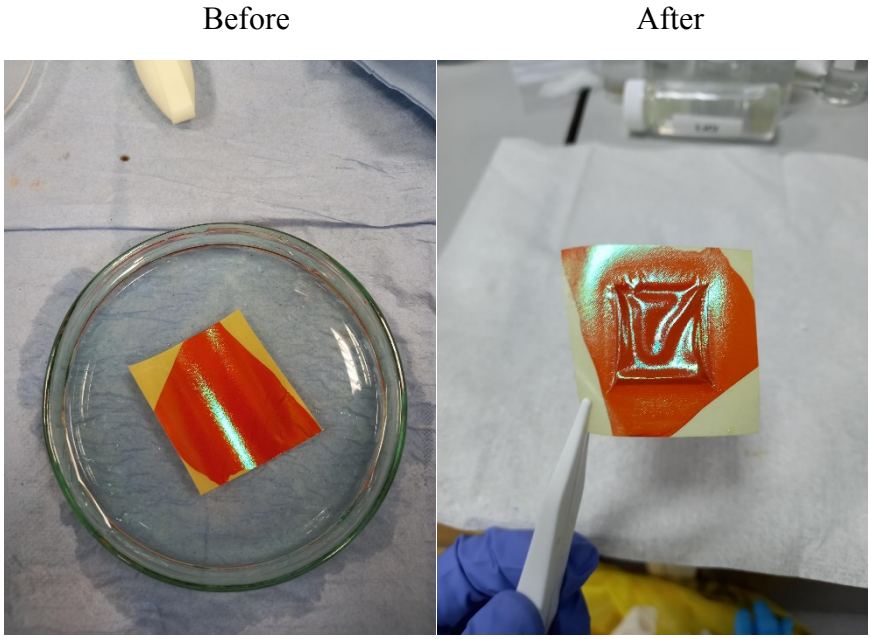
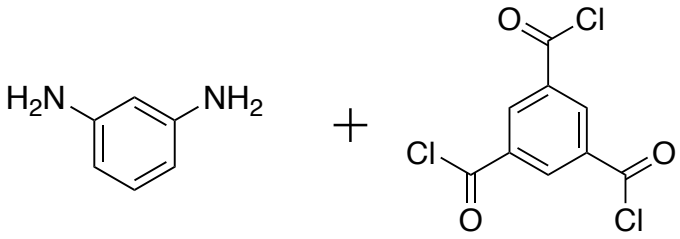
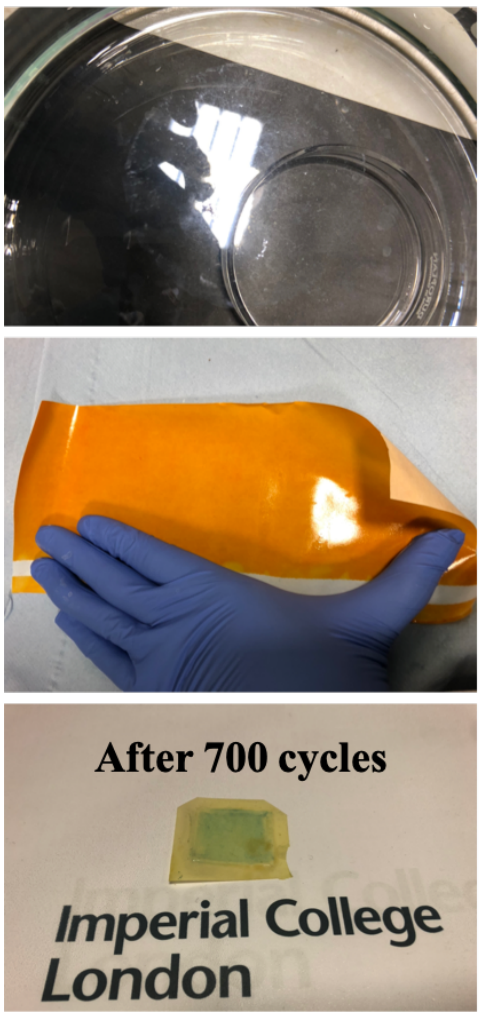


Figure S17. PPD0.1-TFP0.1-72hr-PAN-COOH TFC membrane appearance before and after running > 80 cycles in neutral pH RFB.

Polyamide composite membranes with ultra-thin skin layers for RFBs:



MPD TMC



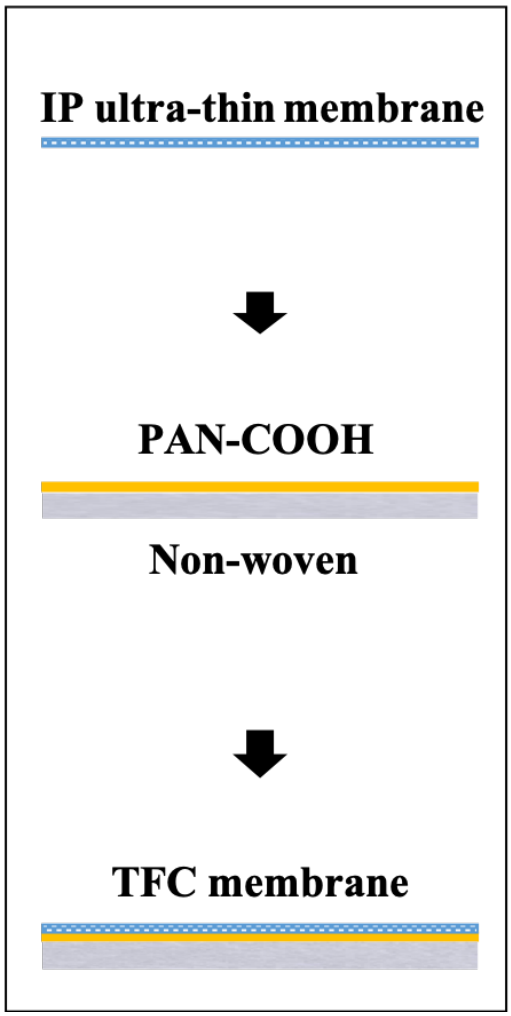


Figure S18. Self-standing MPD-TMC nanofilm synthesis was performed in a petri-dish reactor, synthesized films were transferred to water bath and captured using supporting substrates.

To investigate applicability of TFC membranes with ultra-thin skin layers in redox flow batteries, MPD-TMC-PAN-COOH membranes were prepared. MPD-TMC nanofilms were first synthesized from free-interface interfacial polymerization in a small petri-dish reactor then captured on top of

water bath. PAN support was immersed in 1wt% NaOH water-ethanol solution (volume ratio 1:1) for 1hr under 45 °C to convert nitrile groups into -COOH groups.

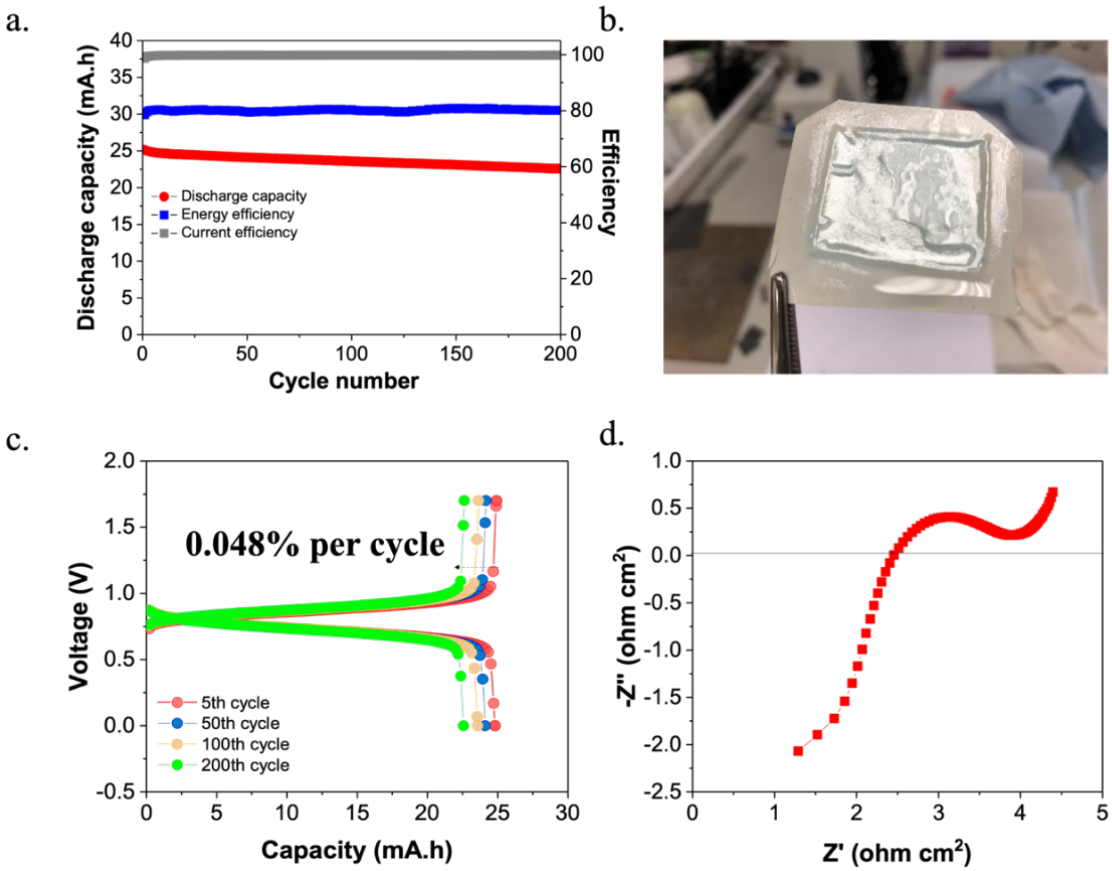


Figure S19. a. Neutral pH RFB battery performances using MPD-TMC-PAN-COOH membranes as separator. b. MPD-TMC nanofilm composite membrane appearance after battery cycling. c. Discharge capacities of RFB from 5th, 50th, 100th and 200th charge-discharge cycle. d. Resistance measurement of MPD-TMC-PAN-COOH membrane.

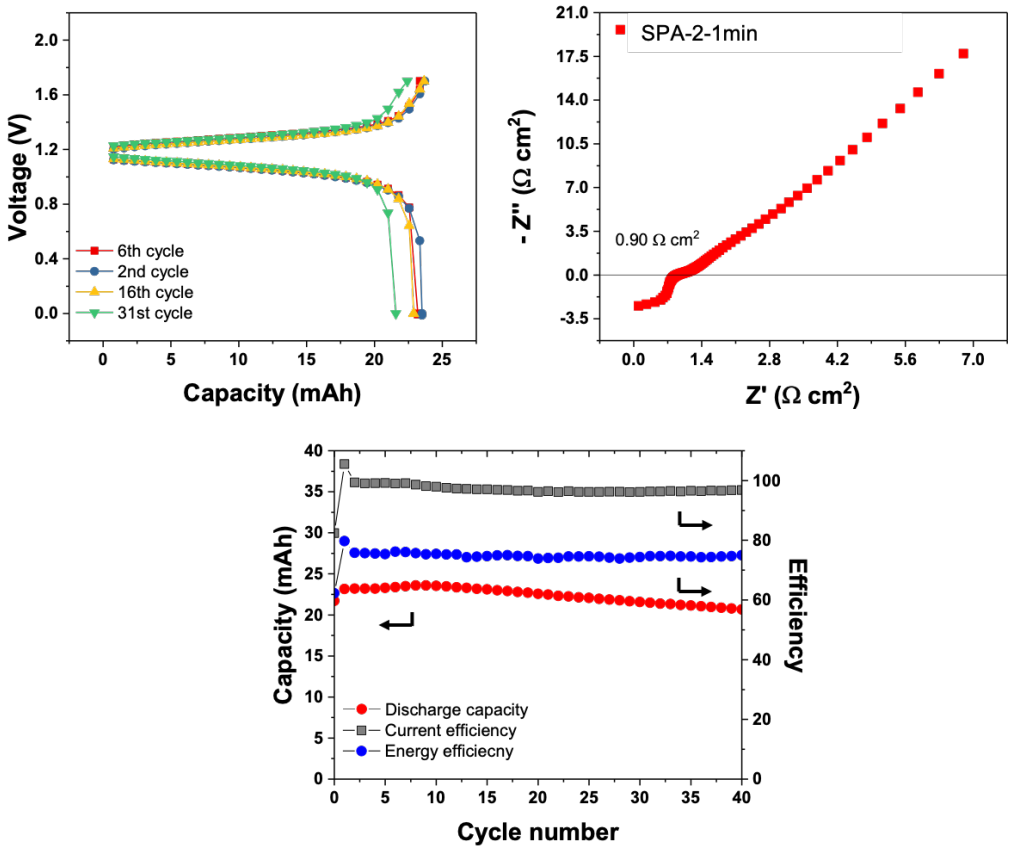


Figure S20. Alkaline redox flow battery performances using SPA-2 membrane synthesized for 1 minute with DHAQ and $K_4Fe(CN)_6$ as redox couples.

Crosslinked SPA-2 membranes still couldn't completely prevent crossover of redox couples. Discharge capacity slowly decreased over charge-discharge cycles. But during the first 16 cycles discharge capacity didn't decrease significantly, this can be credited to adsorption of redox couples into membranes which slightly prevented mixing.

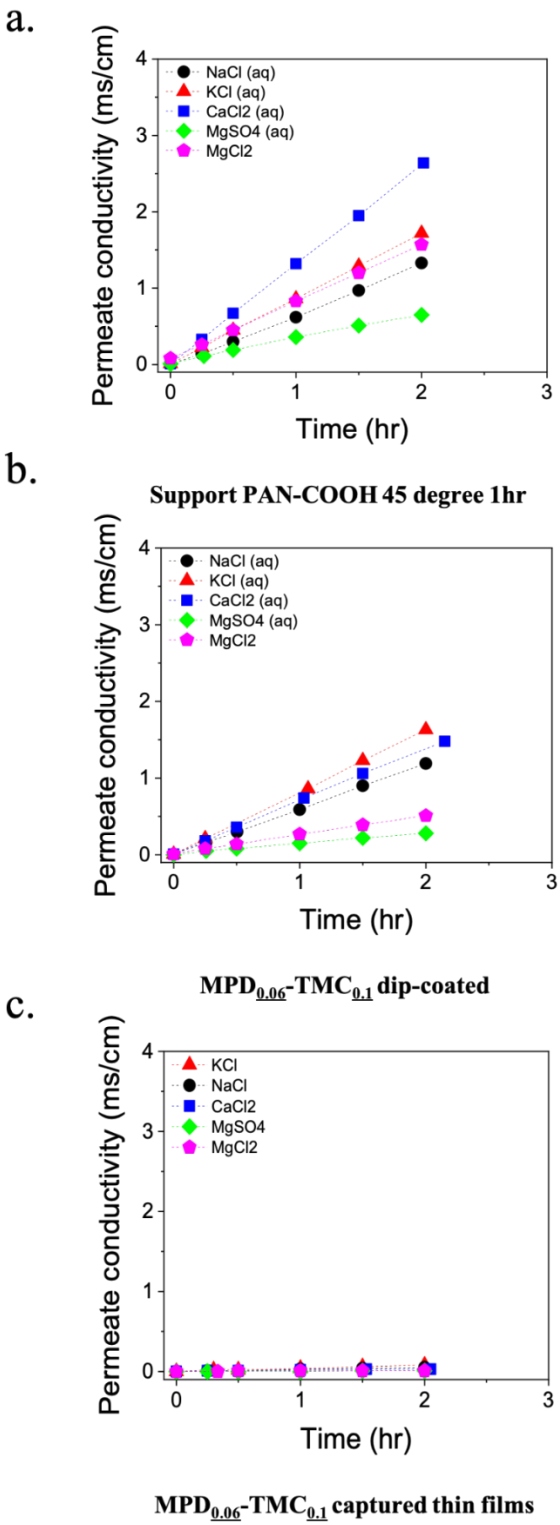


Figure S21. Ion permeation through MPD-TMC-PAN-COOH membrane in static dialysis using salt solutions as feed sides. a. Development of permeate side conductivity through PAN-COOH membrane. b. Development of permeate side conductivity through dip-coated MPD-TMC-PAN-COOH membrane. c. Development of permeate side conductivity through MPD-TMC-PAN-COOH membrane synthesized from IP at free interface.

Polyester thin film composite membranes for Li-S batteries:

Microporous polyester films were synthesized using commercial BHPF monomer and commercial TMC. Self-standing BHPF-TMC films were prepared according to previously reported method from the group, where NaOH was added into aqueous phase to boost solubility of BHPF in water.

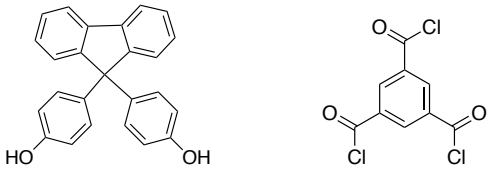


Figure S22. Chemical structures of BHPF and TMC monomers used in polyester thin film synthesis.

Top-view AFM images revealed that PE surface is smooth without nodule textures. BHPF-TMC film can grow up to ~ 800 nm when reacted up to 25 minutes. This result also suggests microporous polyester thin film synthesis using IP method at free-interfaces may not be confined.

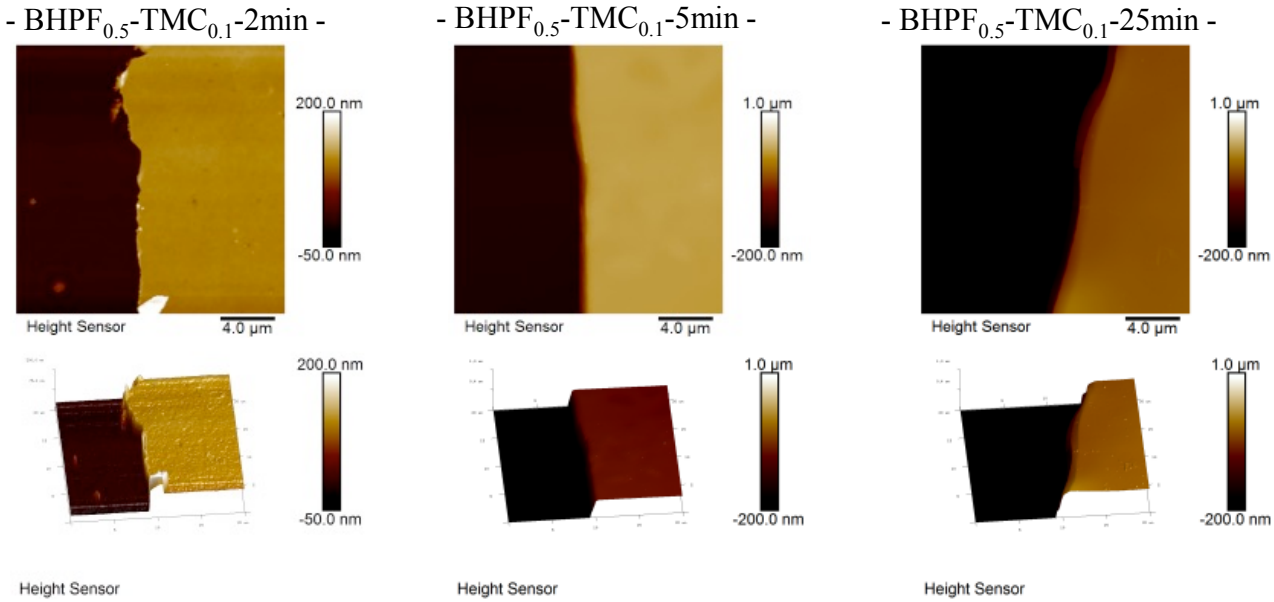


Figure S23. Top-view AFM images of BHPF-TMC membranes synthesized with different reaction time.

Table S5. Film properties of BHPF-TMC membranes synthesized with different reaction time.

	$BHPF_{0.5}$-$TMC_{0.1}$-2min	$BHPF_{0.5}$-$TMC_{0.1}$-5min	$BHPF_{0.5}$-$TMC_{0.1}$-25min
Thickness (nm)	108.3	622.2	880.5
Roughness R_q (nm)	3.9	5.8	6.1
Roughness R_a (nm)	3.1	4.1	4.9

BHPF-TMC film growth was not linearly proportionally to reaction time.

As IP reaction time progresses up to 25 minutes BHPF-TMC films grow up to ~ 880 nm, while BHPF-TMC-2min film had ~ 108 nm thickness. BHPF-TMC-2min-PAN membranes were used in Li-S coin cell battery tests, but performances were not as good as commercial Celgard membranes. (Fig. 26)

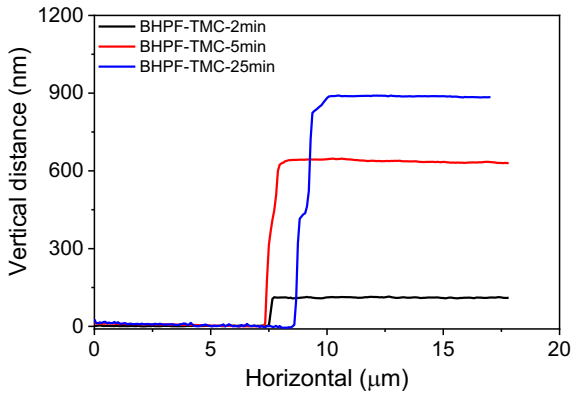


Figure S24. Film thicknesses of BHPF-TMC membranes synthesized with different reaction time.

BHPF-TMC-2min membrane was tested in dead-end filtration in acetonitrile. BHPF-TMC membrane showed high Rose Bengal retention up to 97% under high pressure. This result suggests synthesized BHPF-TMC membranes from IP were indeed defect-free.

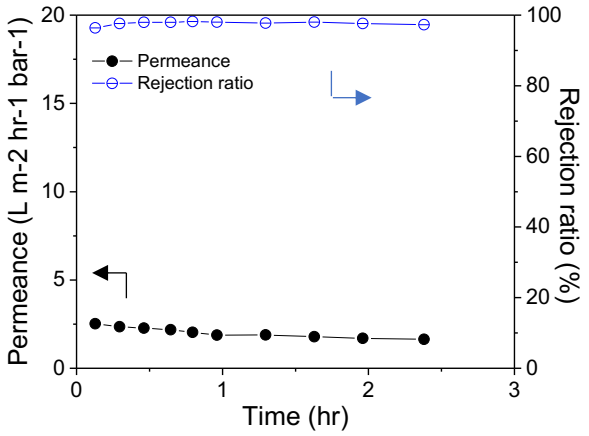


Figure S25. Acetonitrile permeance of BHPF-TMC-2min membrane on PAN support under 10 bar, and Rose Bengal rejections in same solvent.

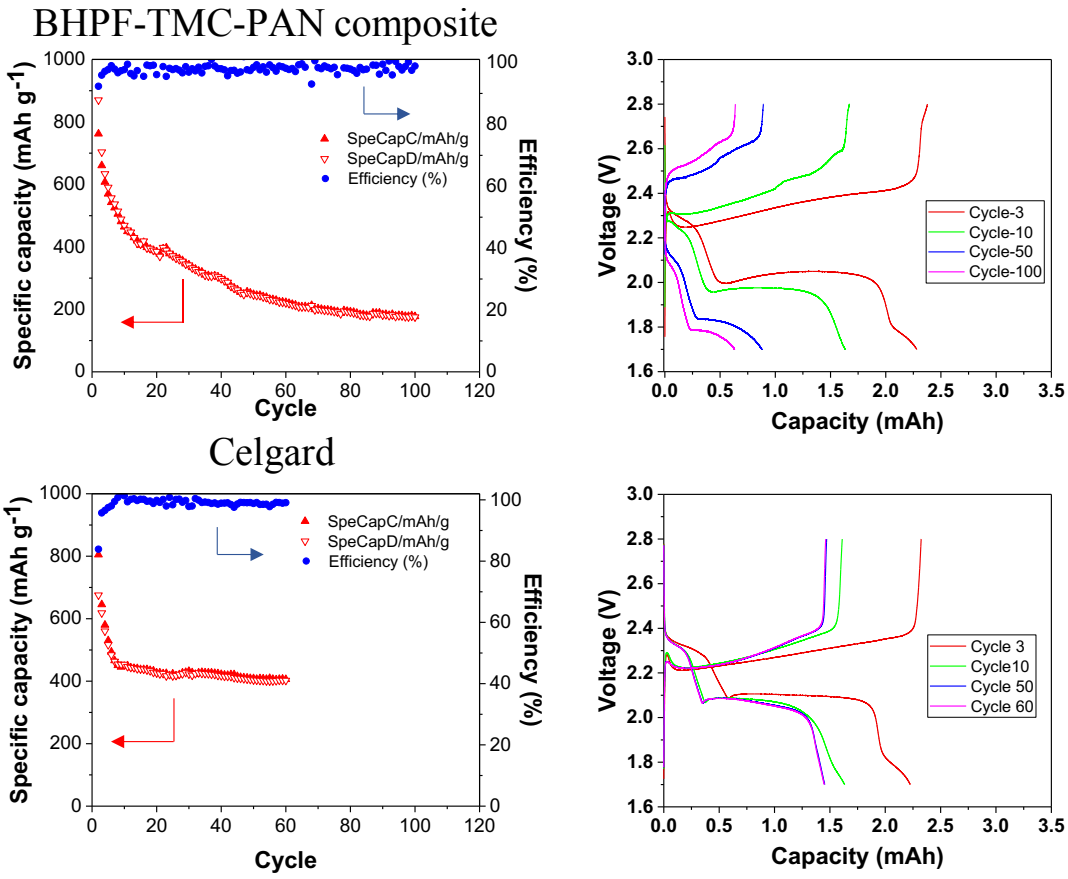
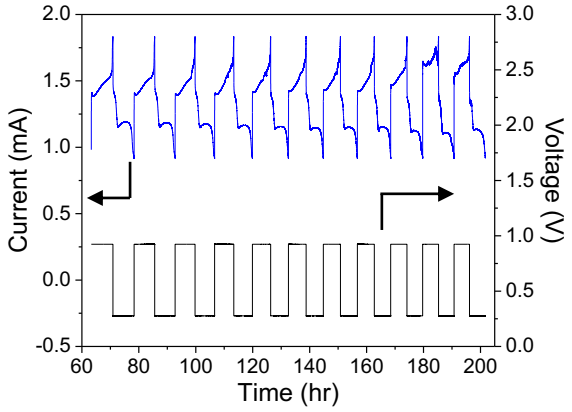


Figure S26. Charging-discharging performances in Li-S coin cell batteries using BHPF-TMC membranes and commercial Celgard membranes as separators.

Li-S coin-cell battery devices using microporous BHPF-TMC membranes had rapid specific capacity decay rate within < 100 cycles, this result implies microporous BHPF-TMC membranes could not prevent crossover of electrode materials especially S_4 in this case.



Figures S27. Current-voltage curves of Li-S coin cell batteries using BHPF-TMC as membrane separators.